A survey of cataclysmic variables from the Edinburgh-Cape Blue Object Survey

A thesis submitted to the Faculty

in partial fulfillment of the requirements

for the Degree of *Doctor of Philosophy*

by

An-Le Chen

Department of Astronomy

UNIVERSITY OF CAPE TOWN

1994 August

To my parents

Abstract

This thesis is based on the Edinburgh-Cape Blue Object Survey and includes a general review of blue star sky surveys, a detailed discussion of the selection techniques, the present status of the survey, and follow-up photometry and spectroscopy of the cataclysmic variable stars (CVs) found by the survey.

Because of the north-south imbalance in the number of blue objects, the Edinburgh-Cape Blue Object survey was designed to discover previously unknown blue objects with B≤~18 at high galactic latitude in the southern hemisphere. At present, all the planned fields (61 fields) in the North Galactic Pole region and 26 fields in the South Galactic Pole regions are complete, covering 2488 square degrees. The preliminary results show that the survey has an internal completeness of ~94% for objects with U-B bluer than the cutoff ~-0.3, and selects objects with an accuracy in photographic U-B of 0.16 mag. UBV measurements and spectra have been obtained for ~2000 objects. Half of these objects are hot subdwarfs which comprise the sdO, sdB, and sdOB stars. The white dwarfs account for about 17% of the total. About 18% of the objects are horizontal branch B and normal B stars. Cataclysmic variable stars and quasars comprise only a small fraction, 2 and 6 percent, respectively. Less than one percent are galaxies. The remaining ~5% have unknown spectral classes at present.

So far, 25 cataclysmic variable stars have been found by the survey. The space density was estimated to be 1.6×10^{-6} pc^{-3}. Among these cataclysmic variables, 6 dwarf novae and 8 nova-like variables are new discoveries; detailed study of their photometric and spectroscopic characteristics are discussed in Chapters 6-10.

One of the stars discovered, a close binary with large reflection effect, is a predecessor of the cataclysmic variables. Napier's (1968) method for the reflection effect in close binaries was used to model the light curve in order to solve for the physical properties of the system. Photometry, spectroscopy, and model fits for this system are discussed in Chapter 5.

Acknowledgments

In regard to the completion of this thesis, I have received all kinds of support and assistance from my supervisors, Dr D. O'Donoghue and Prof B. Warner: introducing the techniques of observations, providing the data reduction FORTRAN programs for photometry and spectroscopy, their useful discussions on the cataclysmic variable stars, and their patience to correct the English in this thesis.

Although Dr R.S. Stobie has not formally supervised my thesis work, he was very kind to give his expert guidance on my research work at the Royal Observatory, Edinburgh (ROE) (during 1990 August - 1991 April) and useful discussions on Chapters 2 and 5.

During my visit at ROE, the staff of the COSMOS facility provided efficient support in the plate measurement and digitization. Dr L. Miller allowed me to use his software for pairing the U,B plates.

The former Director, Prof M.W. Feast, and the present Director, Dr R.S. Stobie, of the South African Astronomical Observatory have allocated sufficient telescope time to my project during the course of my Ph.D. study. In addition to these, I thank Drs D. Kilkenny, R.S. Stobie, and D. O'Donoghue for their generous assistance in obtaining some data. Dr D.A.H. Buckley was very kind to obtain the CCD data for the estimate of the limiting magnitudes of the survey.

Financial support from the Foundation for Research Development of the Council for Scientific and Industrial Research, from the University of Cape Town, and from Prof B. Warner's research programme are gratefully acknowledged.

Contents

Chapter 1: *Review of Sky Surveys for Blue Objects*

§1.1 Introduction

Since the late 1940s, there has been great interest in the nature of the faint blue objects at high galactic latitude. The categories of blue objects include hot subdwarfs, white dwarfs, blue horizontal branch stars (HB), cataclysmic variables (CVs) and quasars. In the past forty years, small-scale (i.e. limited sky coverage) sky surveys in some particularly interesting regions, such as Savage et al. (1978), Morton et al. (1985), and Stobie et al (1985), and quite a few wide-area sky surveys such as Iriarte and Chavira (1957) and Chavira (1958,1959), Haro and Luyten (1962), Luyten (1952-1969), Jaidee and LyngÅ (1969), Slettebak and Brundage (1971), Berger and Fringant (1977,1980,1984), Noguchi et al. (1980), Green et al. (1986), and Downes (1986a) have been made. More recently, surveys such as Pesch and Sanduleak (1983,1984,1986,1988), Demers et al. (1986), and Stobie et al. (1988) are in progress. The small-scale surveys are deep surveys which usually cover ~25 square degrees and have limiting magnitudes ~17-20 Bmag or even fainter. The wide-area surveys do not penetrate as deeply, with a typical limiting magnitudes of 16-18 mag, because they cover a larger area of the sky (~thousands of square degrees) and would take excessive time and effort to complete if intended to search for objects as faint as those in small-scale surveys.

All the above surveys provide a means for searching for blue objects for further detailed studies of their physical properties and evolution. For example, Greenstein and Sargent (1974) colorimetrically selected 189 blue stars from various surveys such as Iriarte and Chavira (1957) and Chavira (1958,1959), Haro and Luyten (1962), and Luyten (1952-1969) and analyzed their spectra and colours to derive surface gravity and effective temperatures. They placed these objects, including HB B and A type stars, sdO, sdB, and white dwarfs, in the Hertzsprung-Russell diagram in order to compare with evolutionary tracks by Paczynski (1971) and suggested

evolutionary links between sdB, sdO stars and hot white dwarfs. Using a complete sample of quasars from the PG survey Schmidt and Green (1983) found that the increase in the space density of quasars with redshift depends strongly on their absolute magnitude. The surveys also provide a basis for statistical studies of galactic structure (e.g. Slettebak and Brundage 1971).

The basic attributes of the above surveys, including sky coverage, number of objects found, limiting magnitude, colour cutoff, and brief description of techniques, are given in Table I. The abbreviations of the surveys are

Table I. Basic Data of the Major Sky Surveys

survey	sky coverage	No. obj.	mag limit	colour cutoff	remarks
Ton	North Galactic Pole SGP: 20^h30^m~5^h30^m -21°~-34°	1588 419	17.1_{pg} 16.2_{pg}		UV,V,B three-image plates
Feige	$b>55^\circ$ $b<-45^\circ$ & $\delta>-15^\circ$	114	14_{pg}		blue, red, Hα three-image plates
PHL	21^h30^m~3^h30^m 0~-30°	8746	18.9_{pg}		UV,V,B three-image plates
LB	various area in sky	11444	$15\text{-}20_{pg}$		
JL	19^h~24^h;$<-70^\circ$ 0^h~2^h30^m;-45°~-58°	296	18_B	U-B≤-0.6	U,B two-image plates
SB	$29^\circ\times29^\circ$ centre on SGP	957	$14\text{-}15_B$		objective prism survey: dispersion 580Å/mm at Hγ
PB	9 fields near NGP with $6^\circ<\delta<48^\circ$ 26 fields near SGP: 22^h~2^h48^m 6°~-12°	4515 4495	19_B 19_B		same as PHL
KUV	22 fields scattered in northern sky	1186	$\sim18_V$		UGR three-image
CW	$b>30^\circ$;$\delta>30^\circ$	1030	18_B		objective prism survey: ~1500Å/mm at 4500Å
PG	$b>30^\circ$ & $\delta>-10^\circ$	1874	16.1_B	U-B<-0.4	U,B two-images plates
KPD	$\|b\|<11^\circ$ & $0^\circ<\delta<60^\circ$	159	15.3_B	U-B<-0.5	U,B plate pairs
MC	$b<-30^\circ$ & $\delta<-10^\circ$		17.5_B	U-B<-0.4	same as PG
EC	$\|b\|>30^\circ$ & $\delta<0^\circ$		18_B	U-B<-0.3	U,B plate pairs

defined as follows:

Ton: Iriarte and Chavira (1957) and Chavira (1958,1959),
Feige: Feige (1958),
PHL: Haro and Luyten (1962),
LB: Luyten (1952-1969),
JL: Jaidee and LyngÅ (1969),
SB: Slettebak and Brundage (1971),
PB: Berger and Fringant (1977,1980,1984),
KUV: Noguchi et al. (1980) and Kondo et al. (1984),
CW: Pesch and Sanduleak (1983,1984,1986,1988),
PG: Green et al. (1986),
KPD: Downes (1986a),
MC: Demers et al. (1986),
EC: Stobie et al. (1988).

The techniques used are discussed in section 1.2 and the surveys are discussed chronologically in section 1.3.

§1.2 Techniques

Two kinds of techniques, objective prism and colorimetry, are generally used to search for blue objects and are discussed below.

Objective prism surveys such as Slettebak and Brundage (1971) and Pesch and Sanduleak (1983) offer an efficient way to obtain spectra of individual objects in a wide field ($5^\circ \times 5^\circ$). Objective prism plates are taken with a prism providing low dispersion (e.g. 1500 Å/mm in Pesch and Sanduleak 1983) attached to a Schmidt telescope. The inspection of spectra can be made by using a binocular microscope and the objects with clear features are then classified. Pesch and Sanduleak (1983) have also estimated the B magnitudes of the objects from the density of the continuum near 4500Å and achieved an accuracy ~1 mag. Because selection criteria by visual inspection "are not specified numerically and cannot be expected to remain constant" (Clowes et al. 1984), an automated detection technique was developed: objective-prism plates were digitized by the COSMOS measuring machine at the Royal Observatory in Edinburgh to produce two-dimensional spectra for all objects. The selection was then performed by automated detection software which selected objects according to the options of emission lines, absorption lines, spectral discontinuities, ultraviolet excess, and red excess, within a specified numerical range (Clowes 1986).

Colorimetric surveys are based on the multiple image method which was first used by Haro and Herbig (1955): a double (e.g. U,B: Green et al. 1986) or triple (e.g. UV,B,V: Haro and Luyten 1962) exposure on each plate is made with Schmidt telescopes using filters designed to produce similar bandpasses to the Johnson system. In many such surveys, images in each colour are produced on the same plate but offset by a small displacement, achieved by moving the telescope between filters. In the early days, blue objects were selected from inspection of the image-size in different colours on plates (e.g. Haro and Luyten 1962): the exposures were timed so that the blue image of a blue object is larger than the red image. The magnitude of each object was estimated by visual inspection and had a typical error of ~0.5 mag (e.g in Ton, PHL, and PB surveys). More recently, the selection has been performed in a more objective and efficient way: the plates are digitized with a scanning microdensitometer (e.g. Green et al. 1986). The image's density is measured in the scanning procedure and then converted to an instrumental magnitude. The accuracy in the B-magnitude is typically better than about 0.3 mag (e.g. 0.27 Bmag in the PG survey and 0.24 Bmag in the MC survey). After the instrumental magnitudes in different bandpasses are determined, the colours can be obtained and those objects with colour excesses identified.

A comparison between the results of the two kinds of surveys shows that each has its own advantages and disadvantages. Colorimetry surveys provide a fast way to select blue objects but are not able to detect, for example, HB A-type stars, because such stars have large Balmer discontinuities and hence weak UV fluxes. As a consequence of the U-B cutoff and errors in the photographic U-B colour, some quasars will be missed in colorimetry surveys. For example, ~12% of quasars in Hewitt and Burbidge's quasar catalogue (1980) do not appear in the PG survey (Schmidt and Green 1983). The majority of blue objects such as white dwarfs, CVs and quasars lie near or above the blackbody line in the UBV two-colour diagram. Thus they are not distinguishable from the colours alone and determination of their nature requires follow-up spectroscopy. The objective-prism technique is very

useful for colour-independent surveys for objects with strong spectral features such as quasars (e.g. Osmer and Smith 1980) and studies of stellar populations (e.g. the SB survey). Although this technique gives better segregation of objects, the objects with weak spectral features can not be identified, e.g. hot sdO,B stars are not distinguished from O or early B main sequence stars (Slettebak and Brundage 1971). The resolution in prism spectra taken by Curtis and UK Schmidt telescopes decreases rapidly at longer wavelengths (Smith 1978). From the above, which technique to choose mainly depends on the aim of a survey: for example, it is better to use colorimetry for a search for CVs, because some CVs show very weak spectral features but the U-B colour for CVs is almost always very blue. Lyα is the strongest emission line in quasar spectra and will fall in the optical range $\lambda\lambda$3400-5400Å for $1.80<z<3.44$. Thus, objective-prism technique can directly detect quasars via identifying the Lyα line.

§1.3 Surveys and Coverage

In order to search for white dwarfs in clusters, which are of interest in studies of the evolution of clusters, Humason and Zwicky (1947) did the pioneering search for faint blue objects brighter than 15th photographic magnitude, in the Hyades cluster and in the neighbourhood of the North Galactic Pole (NGP). Of the forty-eight candidate blue objects found from the colorimetry, eight objects were spectroscopically identified as white dwarfs. More extensive surveys were undertaken by Iriarte and Chavira (1957) and Chavira (1958,1959) in the NGP with deeper limiting magnitude. Fifty bright objects were observed by UBV photometry (Iriarte 1959). The Ton survey is highly incomplete: a re-investigation of Tonantzintla plates by Iriarte (1959) showed that a large number of bright objects were missed in this survey. Feige (1958) pointed out that, up to that time, sky surveys had found a large number of blue stars which include horizontal branch stars, galactic halo stars, subdwarfs, and white dwarfs. He aimed to discover more blue stars in the NGP and SGP regions and thus found 114 blue objects.

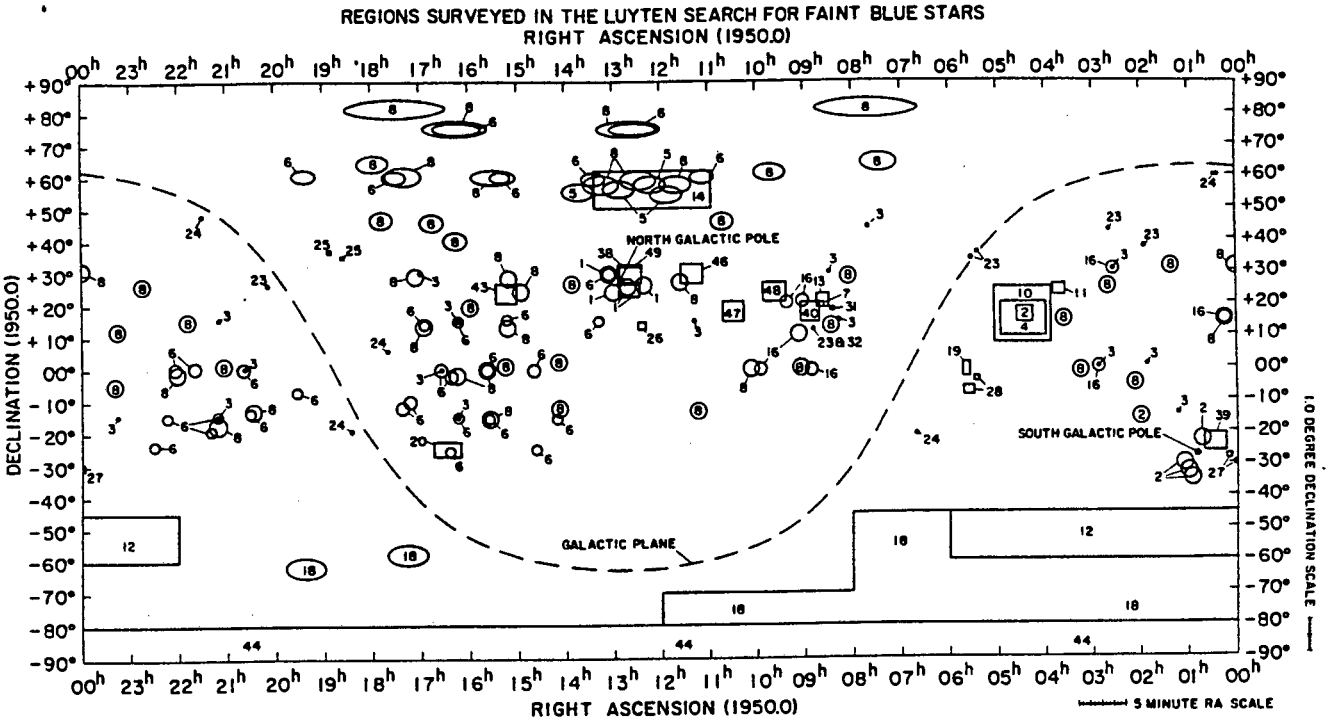

Figure 1. Regions surveyed in the LB survey (from Dixon and Sonneborn 1980).

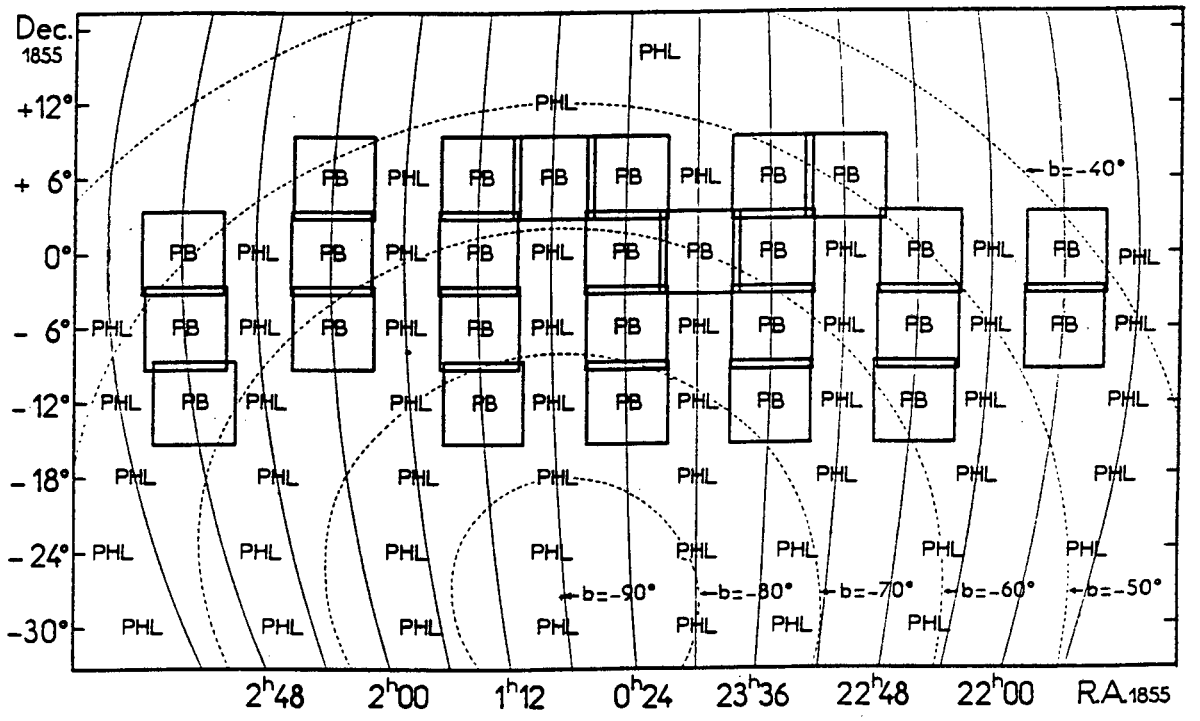

Figure 2. PHL and PB fields near SGP (from Berger and Fringant 1980). Dash lines represent constant galactic latitude b and the epoch is 1855.

Photoelectric colours and spectral types were obtained for only a small fraction (less than 20%). Luyten (1952-1969) has done a comprehensive survey in search of faint blue stars, but the LB survey's coverage is spotty over the sky except for the region, $22^h \geq \alpha \geq 7^h$ and $-45^\circ \geq \delta \geq -90^\circ$ (see Figure 1). The LB survey used the multi-image method to select blue objects from a large number of plate pairs from a number of different observatories (see Table 4 in the Appendix of Dixon and Sonneborn 1980). 11444 objects were found from a total area of 5832 square degrees. No follow-up spectroscopy and photometry were done in this survey. For the same purpose as Feige (1958), Haro and Luyten (1962) searched for faint blue objects at high galactic latitude (Figure 2). Although 8746 blue stars were found, no spectra and more precise photometry for these objects were obtained. Jaidee and LyngÅ (1969) completed a search for fairly blue stars in southern galactic latitudes and discovered 296 stars. They obtained UBV photometry for 43 of these stars and estimated that about 90% of them are white dwarfs. The remaining objects are halo stars and quasars. Wegner (1980) reported UBV observations of 54 JL stars and selected 24 candidate white dwarfs from these 54 stars using a criterion in which objects either had a colour of $-0.23 < B-V < 0.35$ (for $\log g > 7$) or they lay above the blackbody line in the two-colour diagram.

Slettebak and Brundage (1971) were interested in statistical studies of galactic structure and designed an objective prism survey to search for B-F0 type stars in an area of 840 square degrees centred at the SGP. From a total of 957 stars of spectral type B-F0 down to B=15, 10 peculiar stars of later type, and three galaxies showing emission lines were found in the survey. Their study showed that the distribution of stars earlier than A3 has a rapid increase towards faint apparent magnitudes, and that later than A5 it showed a rather flat maximum at a brighter apparent magnitude. This result suggests that the stellar population is dominated by halo stars for apparent magnitudes fainter than 11th or 12th mag, whereas disk population dominates for brighter apparent magnitudes (Slettebak and Brundage 1971).

The PB survey (Berger and Fringant 1977,1980,1984) searched for blue objects in 35 fields near the north and the south galactic pole, mainly for the purpose of examining distributions of redshifts and magnitudes for quasars. In fact, the PB survey is complementary to the PHL survey at $-12^\circ \leq \delta \leq 6^\circ$ (see Figure 2). About 9000 objects were found and the objects brighter than 14th mag were spectroscopically observed. Berger and Fringant (1985) studied statistics of the PHL and PB objects near the SGP and showed that (1) the PHL survey is very incomplete; (2) the redshift distribution of the PHL and PB quasars has a cutoff of z~2.4 which is consistent with the value z~2.5 used by Schmidt and Green (1983) in their models of the evolution of quasars. The quasars with redshift larger than the cutoff are not detected in colorimetry surveys, because of the faintness and the changes in colour due to the redshift of the spectrum.

The Kiso Schmidt ultraviolet excess survey has detected 1186 blue objects (Noguchi et al. 1980 and Kondo et al. 1984) by means of the UGR three-image method. Most of the KUV objects lie in a band at $l=180^\circ$ stretching from the north to the south galactic pole, and others scatter between $l=30^\circ$-180°. To date, 650 of these objects were spectroscopically observed but UBV photometry was obtained for only 106 objects with known spectral types (Wegner et al. 1990 and references therein).

An objective prism survey by Pesch and Sanduleak (1983,1984,1986,1988), over a large area, was designed to discover interesting blue objects in the northern hemisphere and is still in progress. So far, 1030 blue objects, which includes 469 blue/emission galaxies, 401 blue/emission stellar objects including QSOs, and 160 known and probable blue stars, were identified on objective-prism plates with a low dispersion of ~1500Å/mm at 4500Å.

Green et al. (1986) have successfully completed a survey which covered 10714 square degrees in the northern sky. 1874 blue objects were found in the PG survey. The follow-up photometry and spectroscopy for 1715 objects have been completed down to B~16.1 mag. The detailed results of the PG survey will be compared with that of the EC survey in Chapter 2.

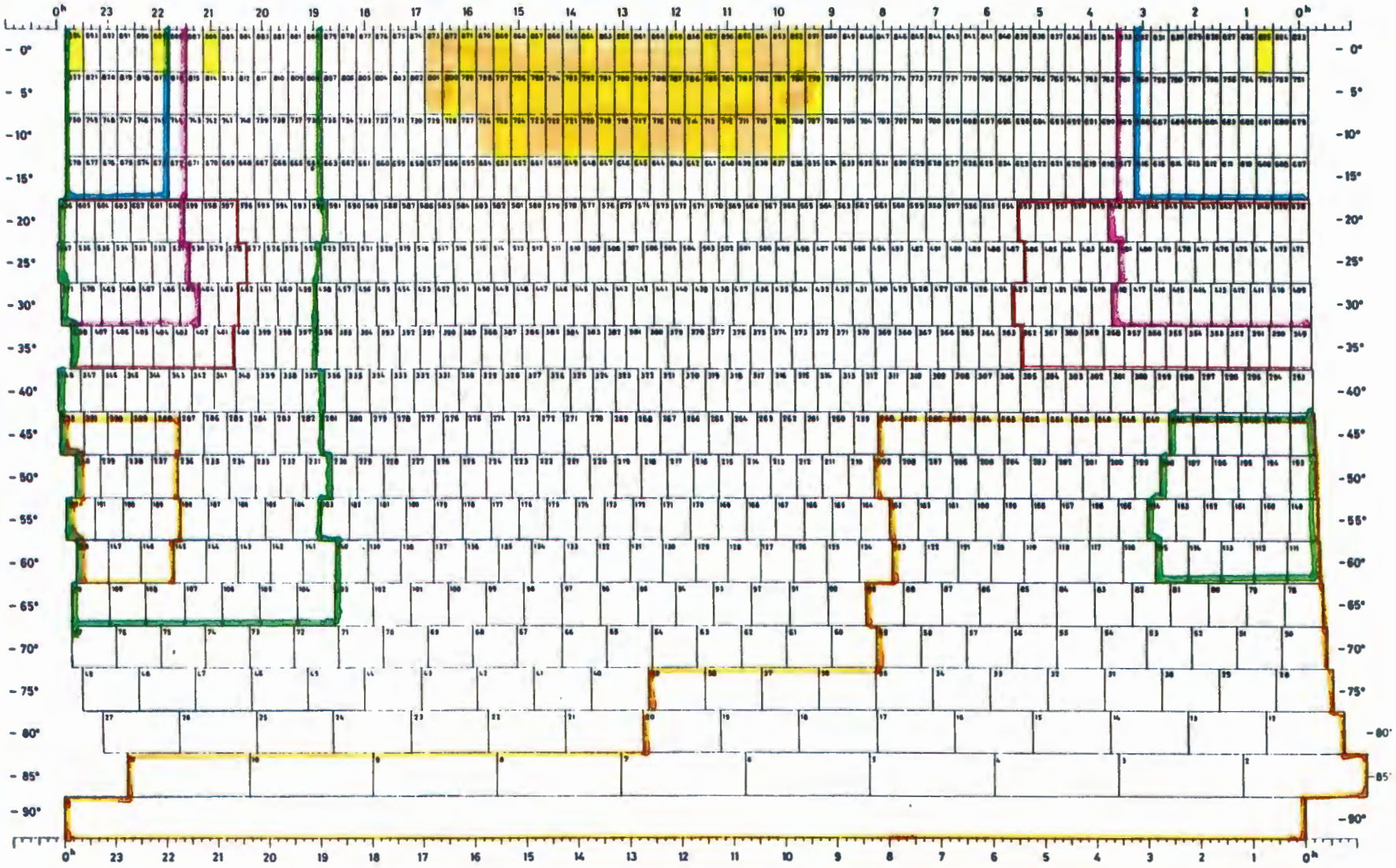

Figure 3. A sketch of the distribution of the major surveys in the southern sky. The fields of the PG survey lying between δ~0° and δ~-15° are painted in yellow. The boundary of the surveys are drawn in various colours: orange for the LB survey (the small area are not plotted), pink for the PHL survey, green for the JL survey, blue for the PB survey, and red for the Ton survey.

Downes (1986a) has searched for UV-excess objects over ~1000 square degrees of the Galactic plane. All candidate UV-excess objects (~700 objects) were spectroscopically observed. The majority of the objects are slightly redden B and A stars. The remaining objects comprise 60 hot subdwarfs, 34 hot white dwarfs, 41 Be stars, 9 cataclysmic variables, and 5 planetary nebulae. Photoelectric photometry was obtained only for the stars (white dwarfs, subdwarfs, and cataclysmic variables) used in the statistical analysis (Downes 1986ab).

In conclusion, a comprehensive colorimetric survey should include at least two distinct components: discovering candidate blue objects and follow-up spectroscopy. Of course, if detailed studies on interesting blue objects can also be done, then the survey would be perfect. Surveys such as the LB and PHL surveys provided only photographic photometry for all the objects. This kind of survey is of limited usefulness, because spectral types are unknown and no detailed follow-up work, such as estimates of the space density for various categories of blue objects, can be done. On the other hand, a survey such as the PG survey, which provided both photometric and spectroscopic data, is of much greater use.

From the above mentioned survey coverage, it is noticeable that the northern hemisphere is well covered by the surveys but the southern hemisphere is not (see Figure 3). This also can be seen in the number of blue objects such as white dwarfs, cataclysmic variables, and quasars (Table II): so far, 24 percent of white dwarfs in McCook and Sion's (1987) white dwarf catalogue, 38 percent of cataclysmic variables in Ritter's (1990) cataclysmic variable catalogue, and 41 percent of quasars in Hewitt and Burbidge's (1989) catalogue are in the southern hemisphere. Because of this imbalance, the MC survey (Demers et al. 1986) to search for hot subdwarfs and white dwarfs down to B~17.5, and the EC survey (Stobie et al. 1988) to discover various blue objects with a limiting magnitude of B~18 in the southern hemisphere were initiated. The details of the EC survey will be discussed in the next chapter.

Table II. Number of blue objects in North and South

Types	white dwarf[1]	cataclysmic variable[2]	quasar[3]
total	2420	168	4291
north	1835	103	2515
south	585	65	1776
S/N (%)	32	63	71

References: (1) McCook and Sion (1987); (2) Ritter (1990); (3) Hewitt and Burbidge (1989).

References:

Chavira, E. (1958). *Bol. Obs. Tonantzintla y Tacubaya*, 17, 15.

Chavira, E. (1959). *Bol. Obs. Tonantzintla y Tacubaya*, **18**, 3.

Clowes, R.G., Cooke, J.A., and Beard, S.M. (1984). *Mon. Not. R. astr. Soc.*, **207**, 99.

Clowes, R.G. (1986). *Mon. Not. R. astr. Soc.*, **218**, 139.

Demers, S., Kibblewhite, E.J., Irwin, M.J., Nithakorn, D.S., Béland, S., Fontaine, G., Wesemael, F. (1986). aj **92**, 878.

Dixon, R.S., and Sonneborn, G. (1980). *A Master List of Nonstellar Optical Astronomical Objects*, Ohio State University Press.

Downes, R.A. (1986a). *Astrophys. J. Suppl.*, **61**, 569.

Downes, R.A. (1986b). *Astrophys. J.*, **307**, 170.

Feige, J. (1958). *Astrophys. J.*, **128**, 267.

Green, R.F., Schmidt, M., and Liebert, J.(1986). *Astrophys. J. Suppl.*, **61**, 305.

Greenstein, J.L., and Sargent, A.I. (1974). *Astrophys. J. Suppl.*, **28**, 157.

Haro, G., and Herbig, G.H. (1955). *Bol. Obs. Tonantzintla y Tacubaya*, **12**, 33.

Haro, G., and Luyten, W.J. (1962). *Bol. Obs. Tonantzintla y Tacubaya*, **3**, 37.

Hewitt, A., and Burbidge, G. (1980). *Astrophys. J. Suppl.*, **43**, 57.

Hewitt, A., and Burbidge, G. (1989). *Astrophys. J. Suppl.*, **69**, 63.

Humason, H.L., and Zwicky, F. (1947). *Astrophys. J.*, **105**, 85.

Iriarte, B., and Chavira, E. (1957). *Bol. Obs. Tonantzintla y Tacubaya*, **16**, 3.

Iriarte, B. (1959). *Lowell Obs. Bull.*, **101**, 130.

Jaidee, S., and LyngÅ, G. (1969). *Arkiv för Astron.*, **5**, 345.

Kondo, M., Noguchi, T., Maehara, H. (1984). *Ann. Tokyo Astron. Obs.*, **20**, 130.

Luyten, W.J. (1952-1969). *Publications of the Observatory*, University of Minnesota.

McCook, G. and Sion, E.M. (1987). *Astrophys. J. Suppl.*, **63**, 605.

Morton, D.C., Krug, P.A., and Tritton, K.P. (1985). *Mon. Not. R. astr. Soc.*, **212**, 325.

Noguchi, T., Maehara, H., Kondo, M. (1980). *Ann. Tokyo Astron. Obs.*, **18**, 55.

Paczynski, B. (1971). *Acta Astr.*, **21**, 1.

Pesch, P., and Sanduleak, N. (1983). *Astrophys. J. Suppl.*, **51**, 171.

Pesch, P., and Sanduleak, N. (1984). *Astrophys. J. Suppl.*, **55**, 517.

Pesch, P., and Sanduleak, N. (1986). *Astrophys. J. Suppl.*, **60**, 543.

Pesch, P., and Sanduleak, N. (1988). *Astrophys. J. Suppl.*, **66**, 297.

Ritter, H. (1990). *Astron. Astrophys. Suppl.*, **85**, 1179.

Savage, A., Bolton, J.G., Tritton, K.P., and Peterson, B.A. (1978). *Mon. Not. R. astr. Soc.*, **183**, 473.

Schmidt, M., and Green, R.F. (1983). *Astrophys. J.*, **269**, 352.

Slettebak, A, and Brundage, R.K. (1971). *Astron. J.*, **76**, 338.

Smith, M.G. (1978). *Vistas in Astronomy*, **22**, 321.

Stobie, R.S., Sagar, R., Gilmore, G. (1985). *Astron. Astrophys. Suppl.*, **60**, 503.

Stobie, R.S., Morgan, D.H., Bhatia, R.K., Kilkenny, D., and O'Donoghue, D. (1988). in A.G. Davis Philip, D.S. Hayes and J.W. Liebert (eds.), IAU Colloq. **95**: *The Second Conference On Faint Blue Stars*, L. Davis Press, Schenectady, p493.

Wegner, G. (1980). *Astron. J.*, **85**, 538.

Wegner, G., Africano, J.L., and Goodrich, B. (1990). *Astron. J.*, **99**, 1907.

Chapter 2: *The Edinburgh-Cape Blue Object Survey*

In this chapter, the Edinburgh-Cape (EC) survey is described and an overview of the survey technique given (section 2.1). Details appear in later sections: the COSMOS machine and measuring process (section 2.2), star/galaxy separation (section 2.3), blue object selection (section 2.4). Evaluation of the technique is presented in section 2.5.

§2.1 Overview of The Edinburgh-Cape Blue Object Survey

§2.1.1 Introduction

The Edinburgh-Cape Survey (Stobie et al. 1988, 1992), a large area survey to discover ultraviolet excess (UVX) stellar objects brighter than 18th B magnitude in the southern sky, was commenced on the UK Schmidt Telescope in late 1984. The intended coverage of the sky is 10,000 square degrees at high galactic latitude $|b| > 30^\circ$ and $\delta < 0^\circ$. The survey may be separated into three phases: in phase 1, ultraviolet rich (UVX) stellar objects are extracted from U and B pairs of UK Schmidt Telescope plates digitised with the COSMOS machine. In phase 2, follow-up photometry and spectroscopy of candidate blue objects are being obtained with a variety of telescopes at the South African Astronomical Observatory (SAAO) to classify the objects brighter than B=16.5 into the principal categories: hot subdwarfs, white dwarfs, blue horizontal branch stars, cataclysmic variables and bright quasars. In phase 3, detailed study of the stars in these categories is conducted.

§2.1.2 Selection of Blue Objects (Phase 1)

U and B pairs of plates in each $6^\circ \times 6^\circ$ field are taken with the 1.2m UK Schmidt Telescope at the Anglo-Australian Observatory. The B plate is a 15-minute exposure on IIaO emulsion with a GG385 filter. The U plate is exposed

through a UG1 filter for 60 minutes on IIaO emulsion. The U plate is taken as soon after the B plate as possible to avoid selecting long period variables, but this doesn't exclude short period variables (e.g. RR Lyrae stars).

The U and B pairs of plates in each field are digitised with the COSMOS machine (MacGillivray & Stobie 1984) which outputs separate U and B catalogues of detected objects with a set of describing parameters,

B plate: RA, DEC, AREA, COSMAG, I_{sky}, a, b, θ, x_{cen}, y_{cen}
U plate: RA, DEC, AREA, COSMAG, I_{sky}, a, b, θ.

A brief summary of the use of these quantities is given now; much more detail will be presented in the next section, §2.2.3.

An error box of ±3 arcseconds in both RA and DEC is defined to pair images in the U and B catalogues and to produce a merged catalogue which retains the paired objects. Because the B plates are deeper, the number of paired objects is largely determined by the U plates. Of the brighter objects present on both the U and B plates, a small percentage do not pair. In practice, these discarded objects often appear as blended images on one plate and as separate images on the other plate; therefore the co-ordinates fail to match within the error box. The merged catalogue retains the paired objects with all the aforementioned parameters in the U and B catalogues and calculates the additional parameter COSMAG(U-B).

Stellar and galaxian photometry have different calibration relations between photoelectric and photographic magnitudes. Before selection of blue objects it is thus necessary to carry out star/galaxy separation, otherwise galaxies will scatter across the colour-magnitude diagram making it difficult to position the red boundary of the selection polygon (see the discussion of the selection technique in the following section). The star/galaxy discrimination is determined separately for each field by using a surface brightness criterion (Stobie et al. 1992) to eliminate galaxies from the merged catalogue. The discrimination criterion uses the fact that galaxian images occupy a larger area on the plate than stellar images of the same brightness, thus enabling them to be distinguished. The procedure is

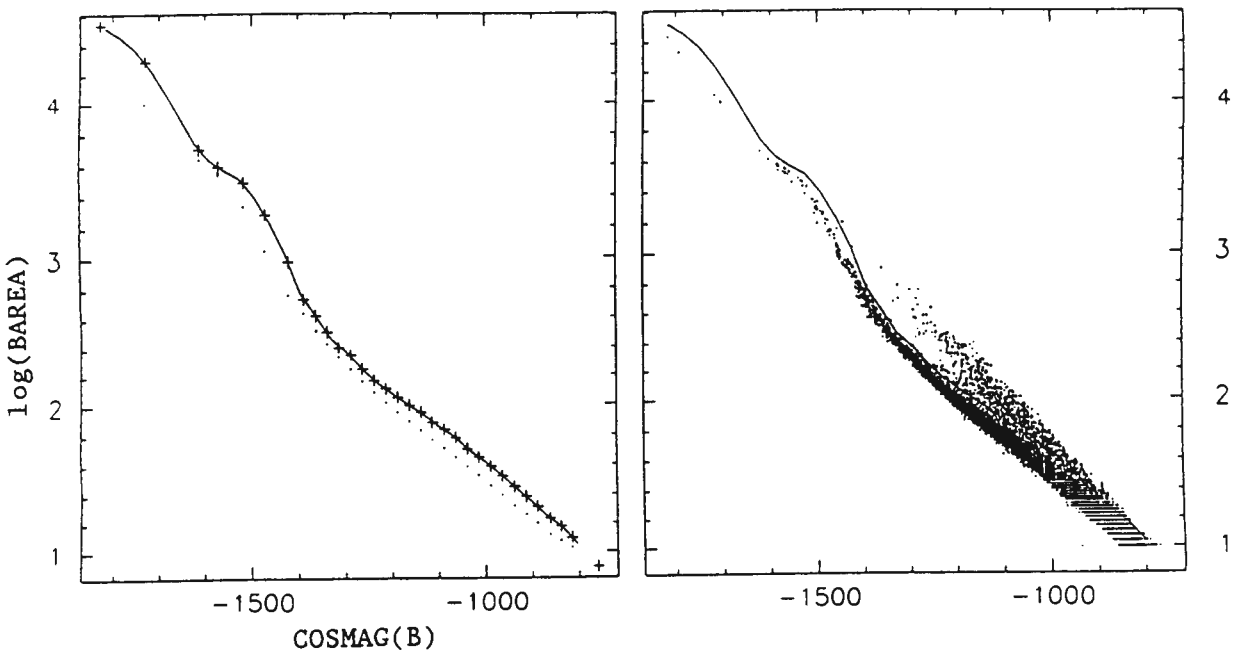

Figure 1. (Right diagram): Plot of log(*AREA*) of the B images vs. COSMAG (BMAG). Each point corresponds to an object in plate pair UB14051 for field 301. The solid line represents the star/galaxy discrimination line (see section 2.3).

Figure 1. (Left diagram): As for Fig. 1 (right). The dots indicate the modes of the distribution in the right panel of Figure 1. The plus sign (+) represents the "maximum stellar area" for each magnitude bin (see section 2.3 for details). The solid line is cubic spline interpolation between the (+) signs.

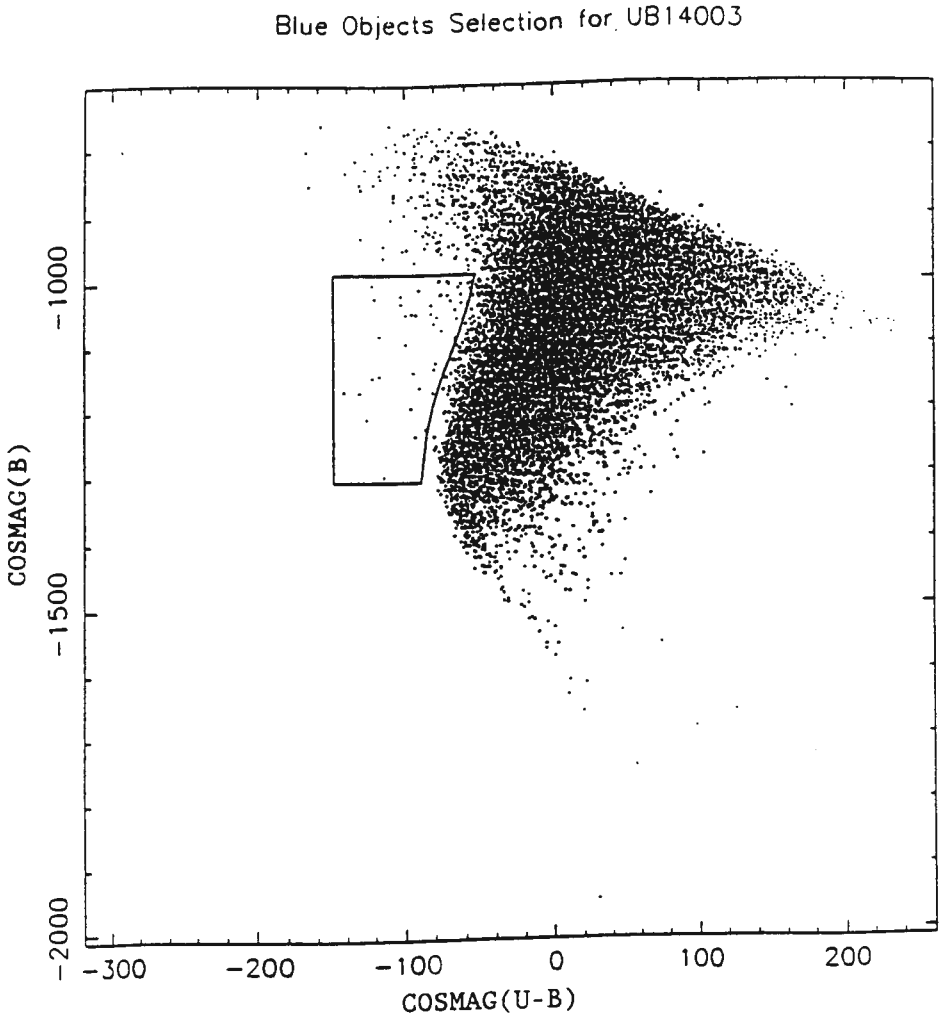

Figure 2. Plot of COSMAG(B) vs. COSMAG(U-B) for field 157. The blue objects selected for this field occur inside the polygon shown.

automatic and calculates the mode of the image-size distribution to define a discrimination curve (see the solid line in Figure 1 & section 2.3). The images above the discrimination curve are rejected as non-stellar objects. A clean separation can be achieved brighter than COSMAG ~ -1000 (B~18) but stellar and galaxian images merge at the faint end (COSMAG > -1000) as is obvious in the right part of Figure 1.

After the star/galaxy separation is completed, the blue object selection is carried out in the natural system COSMAG(B) versus COSMAG(U-B) diagram. In Figure 2, these quantities are plotted for Field 157. The plot shows a large concentration of F/G and late type stars, to the left of which are ultraviolet rich stars (negative COSMAG(U-B)). The polygon (in Figure 2) defines these candidate UV-rich objects. The limiting magnitude is set by the placement of the top boundary of the box (in this case ~ -1000). The position of the red COSMAG(U-B) boundary of the polygon is critical: interesting blue objects are missed if the COSMAG(U-B) boundary is positioned too blue; too many F/G stars are included if the COSMAG(U-B) boundary is positioned too red. The boundary of the polygon is determined subjectively on a field by field basis. Field effects, which comprise differential refraction, variable sky background, vignetting, and image profile variation (Gilmore 1983), on the plates also strongly affect the selection, missing blue objects or including F/G stars. Typically, the merged catalogue contains ~40000 objects from which about 50 candidate blue objects per field are selected. Finally, all candidate objects selected are visually inspected on both the original U and B plates to remove spurious objects, such as plate flaws, satellite trails, asteroid trails, blended stars, and star/galaxy merged images. Typically, a few of these per field are rejected. Finding charts for all candidate blue objects are machine-generated.

§2.1.3 Follow-up Photometry and Spectroscopy (Phase 2)

UBV photometry for all candidate blue objects brighter than B=16.5 is obtained with the 0.75-m or 1-m reflectors of the South African Astronomical

Observatory (SAAO) at the Sutherland site. The University of Cape Town photometer (UCTP) or the St. Andrews photometer (STAP) were used, equipped with UBV filters closely matching the standard filters. Blue-sensitive S-11 photomultiplier tubes were used as detectors. Observations of the program stars were obtained through each filter in the sequence VBUUBV with integration times sufficiently long to secure at least 10000 counts in each filter from the star alone, in order to approach one percent (~0.01 mag) accuracy. Sky measurements were made immediately after each program star measurement. The sky-subtracted intensity in each filter was converted to magnitudes and corrected for atmospheric extinction using the mean extinction coefficients for Sutherland, determined by routine observations with the 0.5-m reflector carried out by SAAO duty astronomers. Instrumental magnitudes were then transformed to the standard system using colour equations whose coefficients were determined by observations of several dozen E-region standard stars of a wide range of colour (Menzies et al. 1989).

If an object has photometric colours in the range of F/G type stars then no spectrum of this object is obtained. Otherwise, a low resolution spectrum is obtained for all stars in the survey. The spectroscopic observations were made with the Reticon Photon Counting System attached to the image tube spectrograph on the 1.88-m reflector. The spectra were obtained using grating #6 to yield a dispersion of 100 Å/mm at a resolution of 4 Å (FWHM) covering the range 3400 to 5200 Å. The object was detected using one array of the Reticon detector and the sky spectrum was simultaneously obtained with the other array. A second spectrum was obtained with the arrays swapped. A Cu/Ar arc spectrum was taken about every 20 minutes to minimize possible systematic wavelength shifts. Standard techniques of spectrum reduction were used: pixel to pixel sensitivity variations in the arrays of the Reticon detector were corrected by dividing by the flat-field spectrum which was obtained at the beginning or end of each night. The wavelength calibration was carried out by fitting a fifth-order polynomial to the sum of two arc spectra obtained before and after the observation of the star. The mean residual of

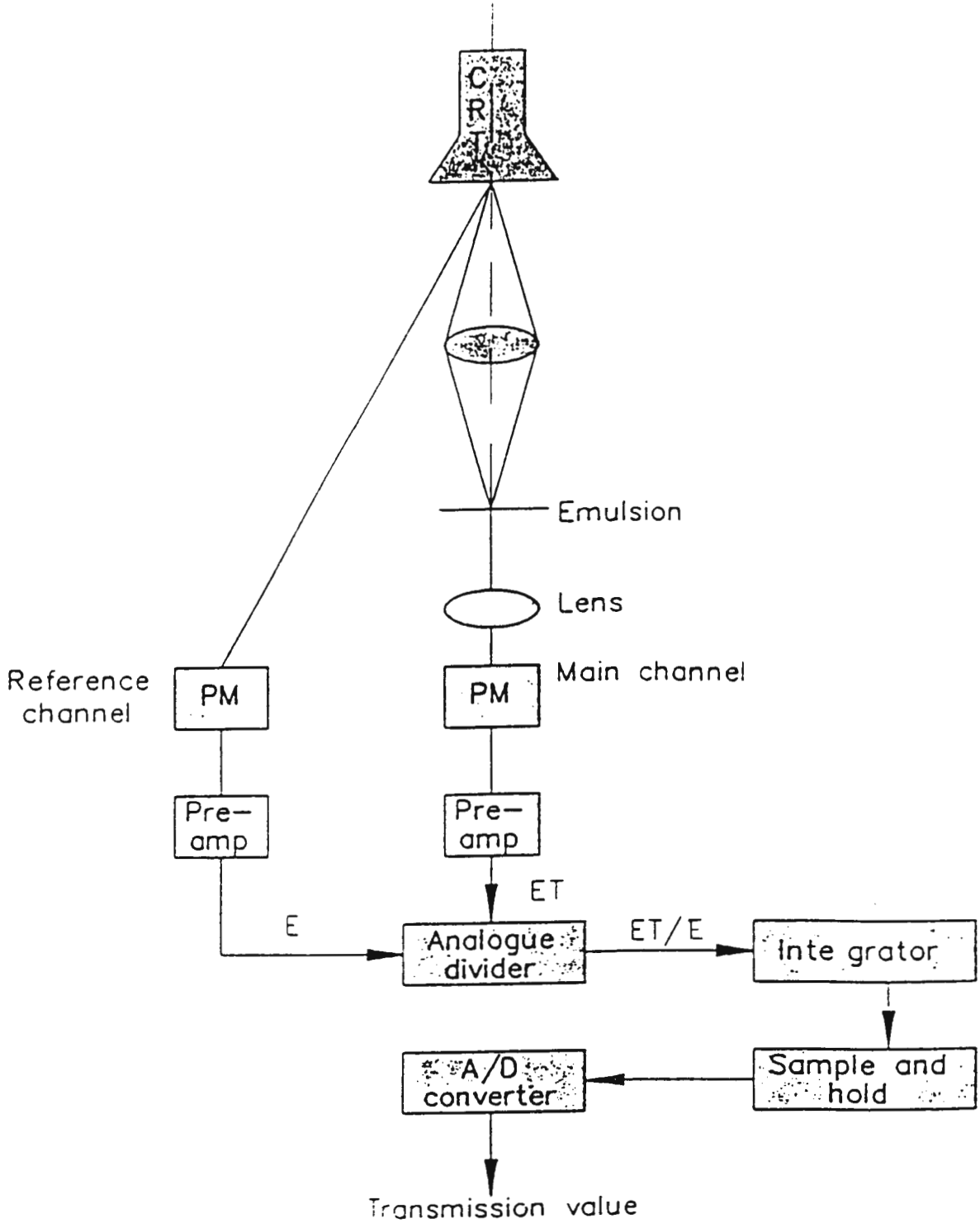

Figure 3. Schematic diagram of the scanning/detection system on COSMOS (from the COSMOS User Manual).

the fit and the shift from one arc to the next were found to be typically 0.2 pixels. Finally, the sky spectrum was subtracted from the object spectrum which was then converted to flux units using observations of spectrophotometric standard stars. Note that the object was observed through a slit, thus the estimate of B-magnitude from the continuum near λ4400Å is affected by guiding and atmospheric dispersion. A few experiments were made to compare with simultaneous photoelectric photometry: the error can be less than 0.1 mag under good seeing and guiding and is up to 0.3 mag under poor seeing and bad guiding.

This completes the overview of the Edinburgh-Cape survey. We now consider the techniques of Phase 1 in more detail.

§2.2 CO-ordinates, Sizes, Magnitudes, Orientations, and Shapes - Measurement

§2.2.1 General Description

The COSMOS machine is a high-speed microdensitometer, which is controlled in a fully-automatic way by computer. This photographic-plate scanning machine was built as a UK National Facility at the Royal Observatory Edinburgh. The basic principle of the scanning/detection is to illuminate the plate and to detect the amount of transmitted light. The scanning/detection system is sketched in Figure 3. A flying microspot produced by the Cathode Ray Tube (CRT) is focused onto the photographic emulsion. The transmitted light in the main channel is measured by a photomultiplier and compared with the direct light from the CRT to the reference channel. The result is digitised to yield the 8-bit transmission value (256 levels). These transmission values are converted to relative intensities by means of a look-up table derived from the sensitometer spots on each plate. The photographic plate is supported on the plate carriage with the emulsion up. A variety of plate holders is available to mount plates with dimensions less than 356×356 mm^2. For reasons of mechanical limitation, the largest scanned region in a single measurement is an area of 287×287 mm^2. The carriage drifts in the y-

direction by means of hydraulic rams while the CRT scans in the x-direction. The x-direction scanning control is achieved by a grating channel signal fed into a phase-locked-loop circuit which provides feedback to the CRT deflection coils. There is no gap or overlap at the boundary of the adjacent lanes, and the xy-precision is determined by Moiré fringe gratings to a resolution of 0.5 micron (Stobie 1982). Although the photographic plate can sag up to 250 microns from centre to edge due to the weight, an autofocus mechanism, which works on the principle of an optical depth probe, maintains the spot in perfect focus in the emulsion plane, irrespective of the position on the plate.

§ 2.2.2 Photograph Digitisation

As mentioned above, the CRT produces a scan parallel to the x-direction and the plate-carriage moves in the y-direction. The scan is divided into 128 pixels of sizes 8, 16 or 32 microns corresponding to lane widths of 1.024, 2.048 or 4.096 mm respectively (Stobie 1982). The basic operation of measurement is that a scan occurs in the direction of increasing x with a distance of 128 pixels and then successive scans proceed in the direction of increasing y. After completing a lane in the y-direction, the microspot will move to the next lane until the whole area of interest has been measured. For a 287×287 mm^2 plate, this requires 140 lanes and needs ~3.5 hours to be completed (MacGillivray and Stobie 1984).

There are two basic measuring modes of COSMOS, Mapping Mode(MM) and Threshold Mapping Mode(TM). In MM COSMOS digitizes the relevant area on the photographic plate and records the raw data of every pixel to disk. Such storage requires a large amount of disk space. For instance, a 287×287 mm^2 area measured with a 16-micron pixel size needs 612 Mbytes of disk storage at 14 bits per pixel. In general, this mode is used for studying small areas of interest or analysis of the UKST objective-prism plates. In TM mode, instead of storing every pixel as in MM, an isophotal threshold is applied to separate image pixels from background pixels. Let I_{sky} be the intensity of

sky and I_{thr} be the intensity of the threshold cut. Then an image pixel is defined by $I_i > I_{thr}$ and a background pixel by $I_i \leq I_{thr}$. The threshold can be defined from either an arithmetic cut, $I_{thr}-I_{sky}$=constant or a percentage cut, $(I_{thr}-I_{sky})/I_{sky}$ = constant. For an ideal flat-background it doesn't make any difference which method is used. The arithmetic cut for thresholding is the correct procedure if the background variations are mainly caused by real sky variations or by variations in the fog level of the plate. The percentage cut is better if the background variations are principally caused by emulsion sensitivity or vignetting effects. COSMOS image analysis uses the percentage cut threshold (Stobie 1982).

As noted above, the threshold is defined relative to I_{sky}. To obtain the value I_{sky} from the variable and noisy background, background cells of size 1 mm^2 are prescanned at low resolution (32 micron pixel). The intensity levels of the pixels within each cell are used to determine the background level in the intensity histogram. This histogram generally shows a Gaussian-shaped peak at low I values due to the sky background, with a tail at higher I values if images appear in the field. It may have a secondary peak at very high intensity caused by a saturated image. The sky background I_{sky} is carried out by calculating the median of the histogram. Of course, the presence of real images contaminates the estimation of sky values and biases the median towards higher intensity than the true sky level. However, this is not a large effect: the sky background pixels dominate in the majority of background cells except in crowded fields. To avoid biasing the median value of the sky background, a digital filter is required to remove the presence of contaminating objects (e.g. bright stars, clusters, galaxies). The filter most suitable for COSMOS analysis is a two dimensional weighted median filter (Stobie 1986 and Brownrigg 1984) with skeleton weights

```
1 1 1
1 3 1
1 1 1 .
```

The way the 2-D median filter works is to determine the median of a neighbourhood of background cells surrounding a given background cell; the

cell size is 128×128 pixels. Let I_m be the median of the neighbourhood of the background cells, I_i be the background intensity of the central background cell, and ΔI_f be the filter threshold. In the case of the scale length equal to one, the neighbouring cells surrounding a given background cell are chosen and its pattern is shown as following (each I represents a background value of a cell):

$$\begin{matrix} I_1 & I_2 & I_3 \\ I_4 & I_i & I_5 \\ I_6 & I_7 & I_8 \end{matrix}$$

The median I_m is determined from the series I_1, I_2, I_3, I_4, I_5, I_6, I_7, I_8, I_i, I_i, and I_i. If the value $|I_i-I_m|>\Delta I_f$ then replace I_i by I_m, otherwise leave the value I_i unchanged. This filter operates over a range of scale lengths, normally from one background cell up to five background cells in distance from the central cell, in order to remove the bright contaminating objects from affecting the sky background determination. The filtered background is calculated after every cellular grid has undergone the filtering and is subsequently used to provide exact isophotal thresholding on a pixel-by-pixel basis using bi-linear interpolation.

The thresholded data from TM mode are passed through a software pattern analyser which determines the pixel-connectivity and generates a set of parameters describing the objects. These parameters contain the information on astrometry, photometry and geometry of the detected objects. This is the category of data, Image Analysis Mode (IAM), which is used in this survey and from which the blue objects are extracted.

§ 2.2.3 Parameters of IAM Output

The IAM data provide the x-y coordinates, celestial coordinates, brightness, sizes and shapes of the detected objects, as well as the sky values. Most of these calculated parameters are based on the moments up to second order of the object-pixel distribution. The expressions for the moments are summarized as follows. Let x_i, y_i be the coordinates of a pixel and w_i is a weighting function with two possible definitions: (a) unit-

weighting $w_i \equiv 1$ and (b) intensity-weighting $w_i = I_i - I_{sky}$. Thus the intensity-weighting function is proportional to the number of photons from the object which impact the pixel on the emulsion. The centralised and normalised moments (Stobie 1980, 1986) are

$$M_x = \Sigma x_i w_i / \Sigma w_i,$$

$$M_y = \Sigma y_i w_i / \Sigma w_i,$$

$$M_{xx} = \Sigma (x_i - x_{cen})^2 w_i / \Sigma w_i,$$

$$M_{yy} = \Sigma (y_i - y_{cen})^2 w_i / \Sigma w_i,$$

$$M_{xy} = \Sigma (x_i - x_{cen})(y_i - y_{cen}) w_i / \Sigma w_i,$$

where the sum Σ is over all the pixels of an object and $x_{cen}=M_x$, $y_{cen}=M_y$. The parameters describing the detected objects can be derived from the above moments; the astrometric parameters and the sky background I_{sky} are intensity-weighted and the geometric parameters are unit-weighted.

(1) Astrometry: x_{cen}, y_{cen}, RA, Dec

The Cartesian coordinates x_{cen}, y_{cen} on the plate for the objects are calculated from the first moments. Furthermore, the Celestial coordinates are obtained from the relative positions (x_{cen}, y_{cen}) of the bright stars on the plate. These relative positions, in conjunction with standard bright star catalogues, are used to determine a transformation to convert x-y coordinates into spherical coordinates RA and Dec. In the Edinburgh-Cape survey, COSMOS provides Celestial coordinates for epoch 1950 with positional accuracy of ~1 arcsecond.

(2) Photometry: I_{max} and COSMAG

Photometric data are obtained from the zeroth order moments. I_{max} is the intensity of the brightest pixel in an object; a detailed discussion of this parameter will be given in the following section. The magnitude parameter COSMAG is the volume integral of the intensity in the object on a logarithmic scale and is defined as $-250 \cdot \log(\Sigma(I_i - I_{sky}))$ (Stobie 1982).

(3) Geometry: *AREA*, a, b, and θ.

The parameter *AREA* estimates the size of an object and is measured by the number of 16-micron pixels in the object. The normalised and centralised

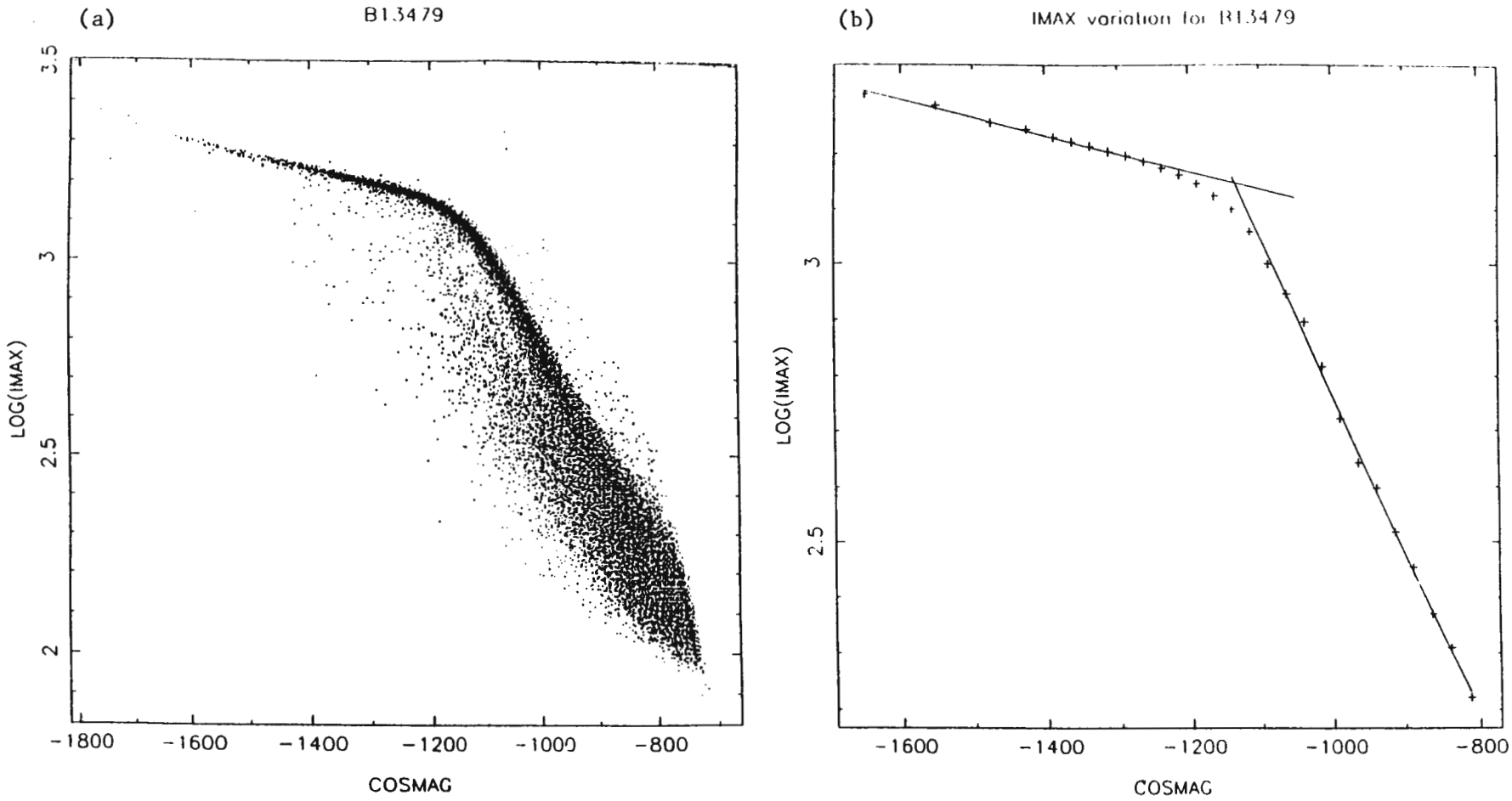

Figure 4a. Plot of $\log(I_{max})$ vs COSMAG(B) for the B plate of field 296. Each point corresponds to an object on this plate . Images with COSMAG > -1100 are unsaturated, those with COSMAG < -1200 are saturated.

Figure 4b. As for Fig. 4a but with the points replaced by the plus sign (+) representing the mode of $\log(I_{max})$ for that magnitude. The straight lines are regressions used to determine the saturation point.

second order moments can be used to determine the semi-major axis a, semi-minor axis b, and orientation θ of a generalised ellipse (Stobie 1980, 1986), where

$$a^2 = 2(M_{xx}+M_{yy}) + 2[(M_{xx}-M_{yy})^2+4(M_{xy})^2]^{\frac{1}{2}},$$

$$b^2 = 2(M_{xx}+M_{yy}) - 2[(M_{xx}-M_{yy})^2+4(M_{xy})^2]^{\frac{1}{2}},$$

$$\tan\theta = 2M_{xy}/(M_{xx}-M_{yy}).$$

Therefore the ellipticity, e, can be simply derived from the above parameters as $e = 1-b/a$. e and θ are useful quantities for the visual checking of the image-classification, especially for identifying merged and spurious objects.

In addition to these, the values of I_{sky} at the centroid of the objects are also given in the output catalogue.

§2.2.4 Measurable Maximum Density of COSMOS

The profile of the COSMOS microspot comprises two parts, the core and the halo. The intensity profile of the core of the microspot is described by a Gaussian distribution and contains 95 percent of the total light. The remaining 5 percent is distributed over the spot halo which is non-Gaussian and very extensive (Stobie 1982). As a result, the measurable density range is restricted to $\Delta D=1.3$ above the sky background. Thus bright stars appear saturated in intensity space with flat-topped profiles. A sample of 14 U and B pairs of plates have been used to investigate the saturation of COSMOS measurements. A plot of $\log(I_{max})$ against COSMAG is shown in Figure 4a from which it is clear that $\log(I_{max})$ and COSMAG are correlated in a manner described by two straight lines of different slope. The intersection occurs where image saturation begins. At this point, the correlation changes smoothly from one line to the other. All the images fainter than COSMAG about -1100 are unsaturated while all images brighter than COSMAG about -1200 (see Figure 4a) are totally saturated. All the objects in Figure 4a were placed in bins corresponding to their COSMAG values and then the mode of $\log(I_{max})$ was determined for each bin (crosses in Figure 4b). A fit of two line segments (Figure 4b) was used to determine the measurable maximum

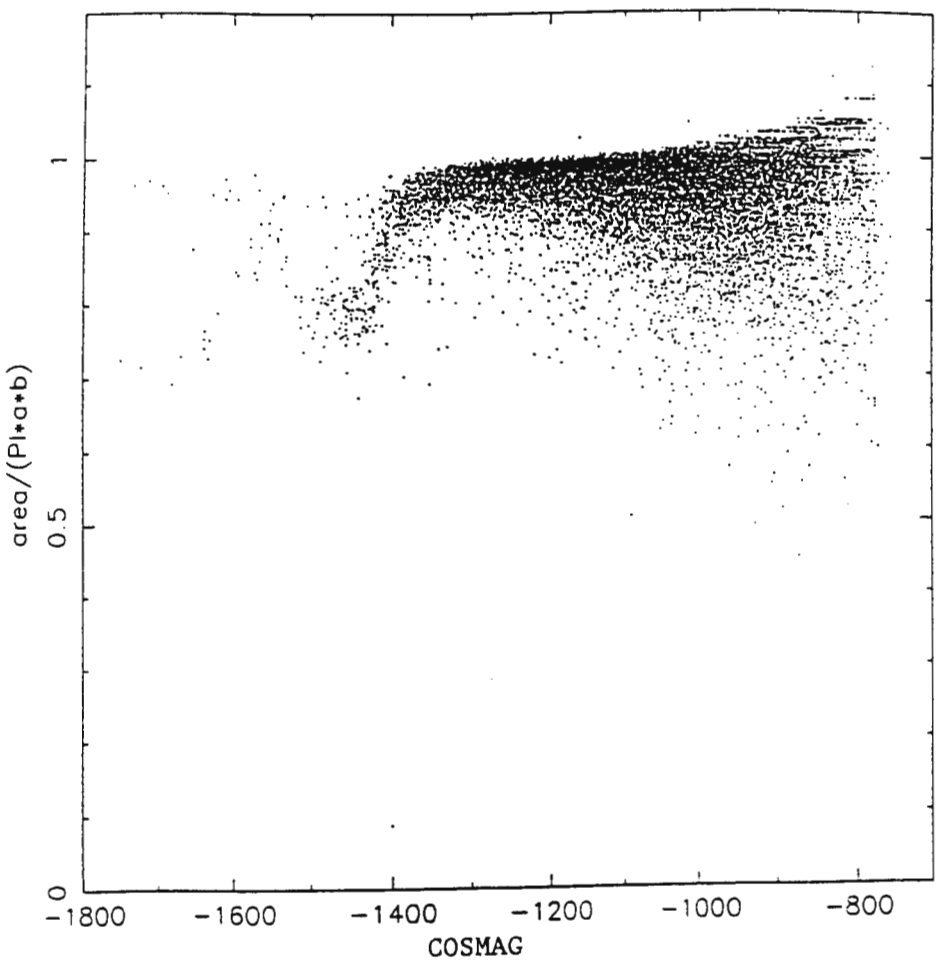

Figure 5. Plot of *AREA*/(πab) vs COSMAG(B) for field 358. Star/galaxy separation can only be achieved using this plot for objects with COSMAG(B) < -1400.

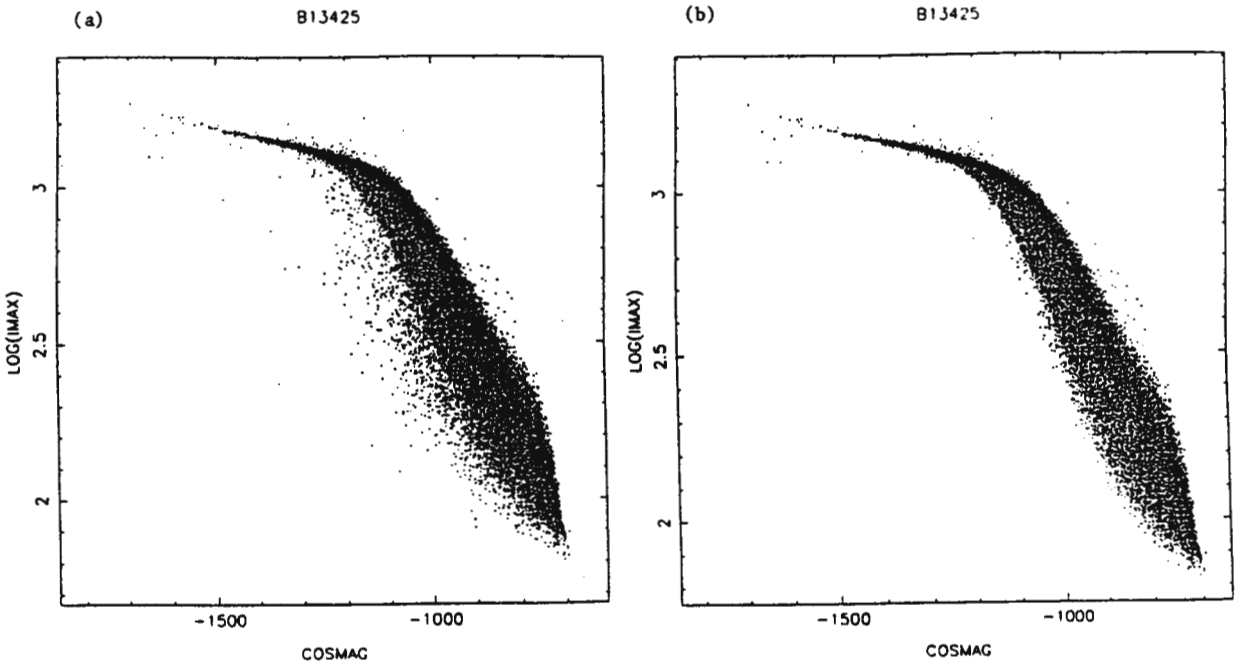

Figure 6a. Plot of $\log(I_{max})$ vs COSMAG(B) for the B plate of field 347 before separating stars and galaxies. Each point corresponds to an object on this plate.

Figure 6b. As for Figure 6a but only stars appear in this plot. This plot shows that $\log(I_{max})$ is strongly affected by field effects (see section 2.2.4 for details).

intensity from the intersection of the saturated I_{max}-mode line and the unsaturated I_{max}-mode line. As the brightness of objects on the saturated relation increases the image size increases (but the density does not).

The combination of this behaviour and field effects makes some of the photometry very unreliable, because field effects show notably in the "saturated" magnitude range. The details of this will be discussed in section 2.4 on the selection of blue objects.

§2.3 Star/Galaxy Separation

There are many different ways of performing image classification: to distinguish stars and galaxies efficiently, the most discriminating parameters should be used. Three parameters (1) *AREA/(πab)*, (2) LOG(I_{max}), and (3) LOG(*AREA*) are frequently used to classify images. (1) The ratio *AREA/(πab)* is a "compactness" parameter, being close to 1 if an image corresponds to a filled ellipse. For bright galaxies, this ratio is always greater than a value of 0.9. Figure 5 shows a plot of COSMAG versus *AREA/(πab)*: the distinction between stars and galaxies is clear only in the bright magnitude range for COSMAG(B) <-1400, about 600 COSMAG units above the magnitude limit of the plate. This parameter is thus not particularly useful and will not be considered further.

(2) The parameter I_{max} is the maximum intensity of the image profile measured by COSMOS. For the same brightness, the I_{max} of a star is higher than that of a galaxy. Thus, this parameter might be used to separate stars and galaxies. In the COSMAG versus log(I_{max}) diagram (Figure 4a), the images above and near the log(I_{max})-mode locus are stellar objects and the images scattering below that locus are galaxies. However, the star/galaxy boundary is not distinct. Furthermore, the parameter I_{max} is strongly affected by field effects. Figure 6 shows a plot of COSMAG vs log(I_{max}) for a plate with strong field effects. In this case, the total image intensity of many of the objects (both stars and galaxies) is spread over a larger area, leading to a lower I_{max} at a given COSMAG. This gives rise in Figure 6 to the "broad band"

of objects for COSMAG > -1200. Using the successful star/galaxy separation technique to be described below, the galaxies in Figure 6a were removed leaving only stellar objects in Figure 6b, showing that most of the objects in the "broad band" are stars. Thus, the use of I_{max} to distinguish stars and galaxies is very difficult in the presence of field effects.

(3) The parameter *AREA* is not as sensitive to field effects as I_{max}. The COSMAG versus log(*AREA*) diagram was adopted as the image classification technique for the Edinburgh-Cape survey and is based on MacGillivray and Stobie's (1984) technique. Stars and galaxies occupy different regions in the magnitude-size scattergram. For images of the same brightness, galaxies always have larger sizes. In other words, galaxies are low surface brightness objects, obvious examples of which are seen in the right panel of Figure 1 at BAREA=2.8, BMAG=-1300. The following quantitative technique was developed to discriminate stars and galaxies. First, all the objects within a given field were placed in bins corresponding to their magnitudes. Then, for each bin, the mode, $\log(AREA)_{mode}$, and standard deviation, σ, of the distribution of the parameter log(*AREA*) were determined. These modes appear as dots in the left panel in Figure 1.

Next, the quantity $\log(AREA)_{max}$ for each magnitude bin was defined using $\log(AREA)_{max} = \log(AREA)_{mode} + (1+C)\sigma$; C is $\Sigma|\log(AREA)_i - \log(AREA)_{mode}|/N\sigma$ and N is the total number of objects of each magnitude bin. The coefficient C is empirically defined as the "mean probability" in the one-sigma width of the peak of the image-area histogram about the log(*AREA*) mode. These values of $\log(AREA_{max})$ are shown as crosses in the left panel of Figure 1 and are estimates of the maximum size of a <u>stellar</u> object of that magnitude. Cubic spline interpolation was used to define the discrimination curve for all magnitudes which is shown as the solid line through the crosses. An object was classified as a galaxy if its log(*AREA*) lay above the discrimination curve. This curve corresponds closely to the stellar locus since for B < 18 the number counts of stars completely dominate over galaxies.

The photographic photometry is unreliable within about 200 COSMAG units of the plate magnitude-limit, fainter than -1000 in Figure 1. This is also the brightness at which the star and galaxy loci merge. Consequently, the uncertainty of star/galaxy separation at faint magnitudes doesn't influence the subsequent extraction of blue objects.

Blended stars, merged star/galaxy pairs, stars joined with a satellite trail and elongated images frequently show on the plates. These objects usually have the axial ratio b/a between 0.4 and 0.7, and appear near the upper edge of the star-locus. These spurious stellar-objects are sometimes classified as stars by the present software. However, the selected candidate objects were visually inspected on the original plates to reject spurious stellar objects and to ensure that the remainder are stellar objects. From these inspections, very few galaxies were found to have escaped detection; thus, the star/galaxy separation technique described above is adequate for the purpose of classifying images.

§2.4 Selection of Blue Objects

Because only uncalibrated U and B plates are available, blue object selection is carried out in the natural system colour-magnitude diagram. The COSMAG(U-B) versus COSMAG(B) diagram (Figure 2) is displayed on a graphics terminal and the candidate blue objects within the manually determined polygon are selected. The process is subjective and tricky, and there are some uncontrollable field effects which affect the distribution of the colour index COSMAG(U-B) in the colour-magnitude diagram. This is the chief difficulty in identifying blue objects by machine algorithm only.

Field effects cause the main complication in the selection. These field effects primarily arise if the profile of a point source (star) varies systematically across the plate. If the images are grossly distorted, this, combined with the saturation problem of measurable maximum density on COSMOS, will enhance the brightness for objects with saturated images. For instance,

Figure 7a. The fuzzy blue-red boundary in the colour-magnitude (COSMAG(U-B) vs COSMAG(B)) diagram for field 194 is caused by field effects occurring on the U plate. This leads to difficulty in blue object selection (see details in section 2.4).

Figure 7b. X-Y distribution of the objects lying in the box (Fig. 7a) on the U plate of field 194; namely, the region where field effects occurred. The orientation is that North is at the bottom and East is at the right.

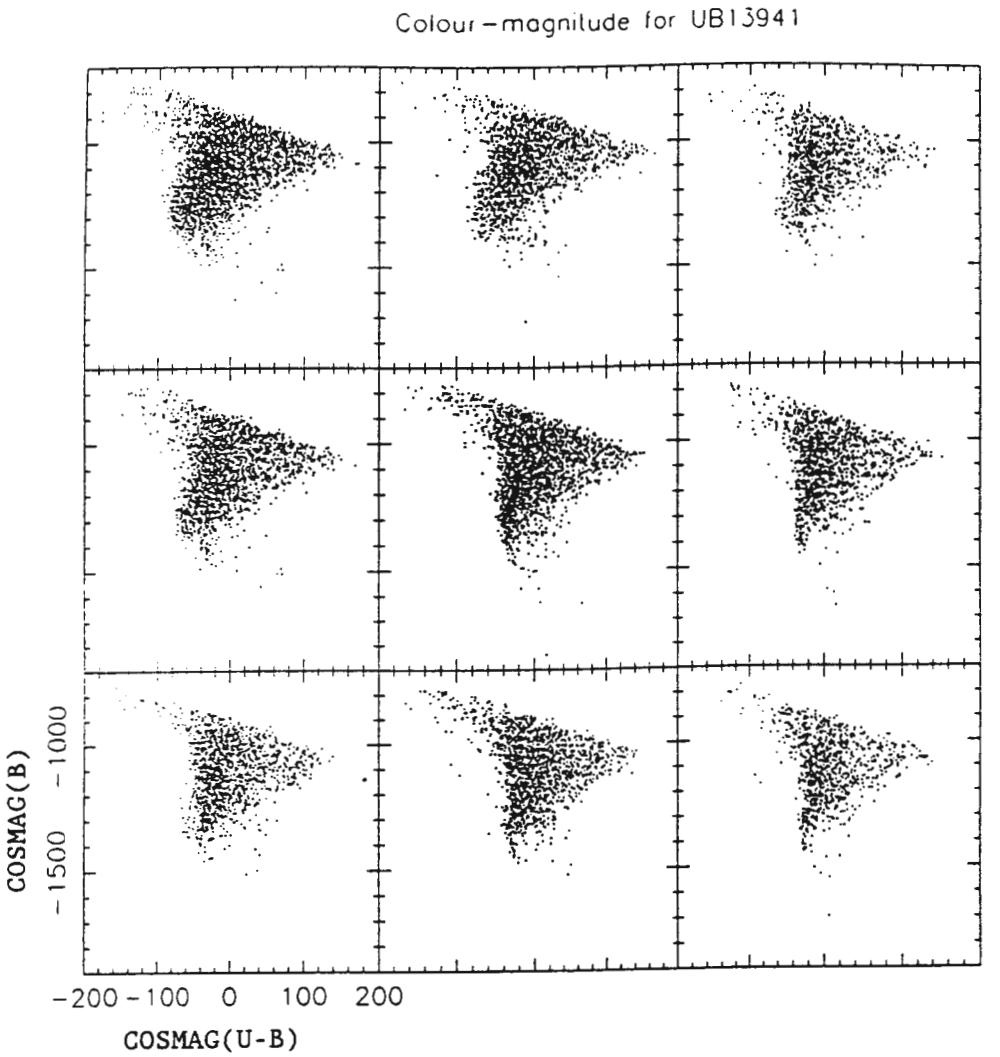

Figure 7c. The colour-magnitude diagrams for different regions on the U plate of field 194.

if such field effects occurred on the U plate, the COSMAG(U) will be brighter so that the value of COSMAG(U-B) decreases. Thus lots of F-G type stars will be pushed towards the blue side in the colour-magnitude diagram. For unsaturated objects, the image is spread out over a larger area due to the deformation. Those pixels having an intensity below the threshold will be regarded as part of the background, so the object's brightness will get fainter and the COSMAG(U-B) indices of these objects will become redder. Therefore some interesting blue objects may be missed. Owing to these effects, the blue boundary of the majority of stars can be fuzzy as shown in Figure 7a with the result that it is difficult to extract only genuine blue objects. In such cases the objects lying near the blue boundary should be sampled and their distribution on the plate examined. Figure 7b shows the x-y distribution of objects within the polygon in Figure 7a. Strong field effects obviously occurred in the South, the West and the South-West corner of the plate. To determine how field effects influence the colour-magnitude distribution, the whole plate was divided into nine equal areas and local colour-magnitude diagrams were plotted as shown in Figure 7c. The orientation in Figure 7c is the same as in Figure 7b. These plots evidently show that the colour-magnitude diagram with a fuzzy blue boundary gives rise to spurious blue objects. Obviously, the region on the plate with a high space density of spurious blue objects must be excluded, and then the colour-magnitude diagram has to be plotted again to select the genuine blue objects. Note that ~0.1 percent of area of survey was lost because of field effects.

If the field effects occurred on the B plate, the COSMAG(U-B) indices of the objects becomes redder/bluer for saturated/unsaturated images. In practice, it is unavoidable to gain some F-G type stars or to lose some interesting blue objects whenever field effects occur.

§2.5 Results

The results of the techniques described above will now be presented.

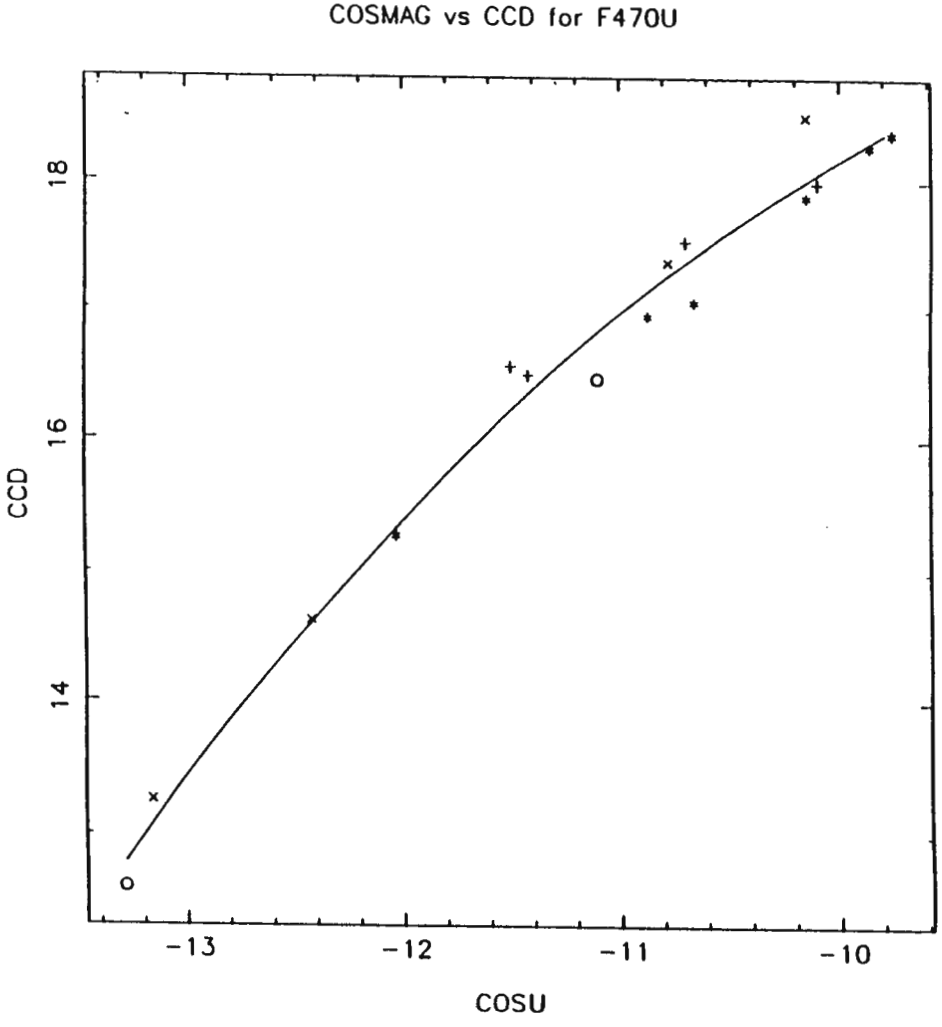

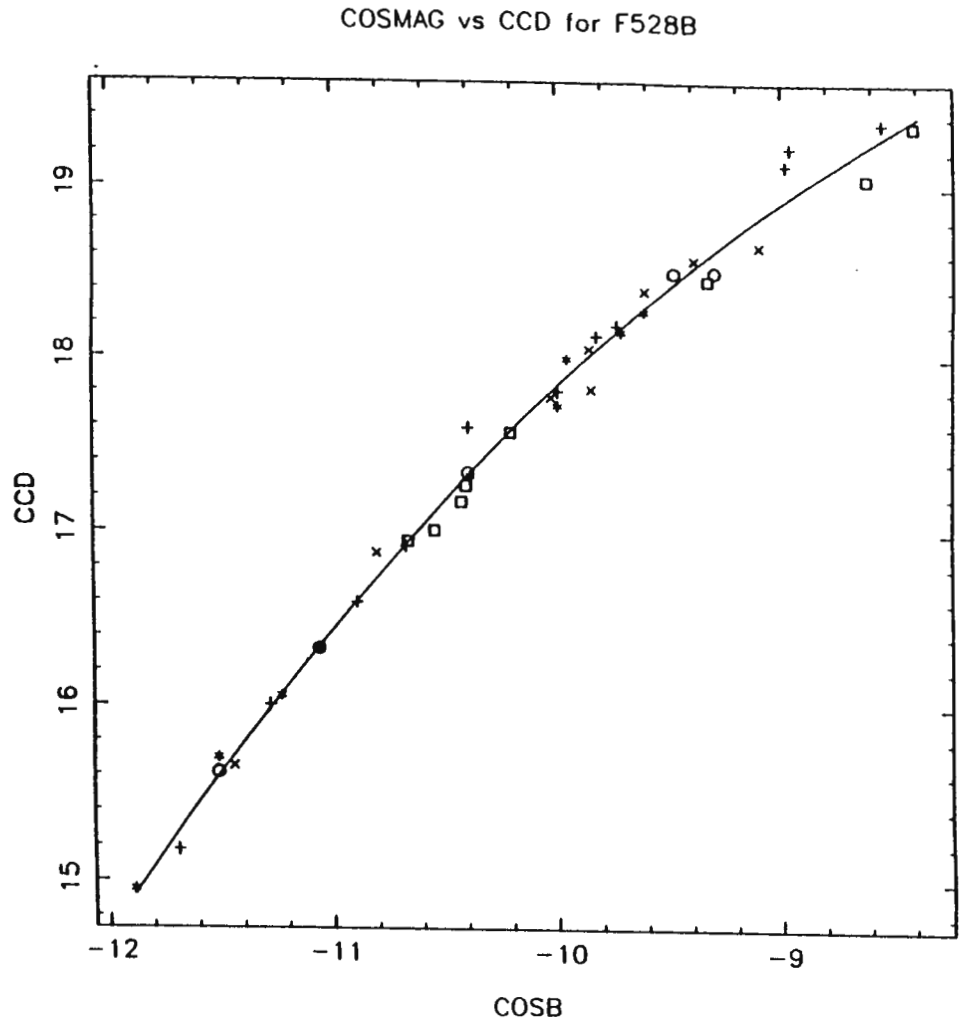

Figure 8. The U and B magnitude limits of the survey's plates were obtained by CCD frames of field 470 and field 528, respectively. The abscissa is in units of 100 COSMAG.

§2.5.1 Limiting Magnitude

The typical limiting magnitude of the survey was determined by CCD calibrations in a few fields in which five frames (near the centre and four corners) were taken. The CCD frames were obtained through U and B filters with the RCA CCD on the 1.0-m reflector at the SAAO. The U and B exposures were 110 and 15 minutes respectively. The CCD data were analysed by using the CCD reduction software package DAOPHOT (Stetson 1987) at the Royal Observatory Edinburgh. After reduction the frames of the same field were corrected for zero-point difference and then combined together. The results show that a magnitude cutoff of COSMAG(B)=-1000 corresponds approximately to B=18 (Figure 8). The B plate is much deeper than the U plate (which reaches ~18th mag), achieving a magnitude limit of ~20. Thus star/galaxy separation and blue object selection can be reliably done to 18th B magnitude.

§2.5.2 Accuracy and Non-Gaussian Errors in Photographic Photometry

By 1993 February, photoelectric photometry of nearly 90 fields was complete to B~16.5, the limiting magnitude of phase 2 UBV photometry in the EC survey. From previous experience (Reid and Gilmore 1982; Stobie and Ishida 1987) with UK Schmidt plates and the COSMOS measuring machine, the errors in photographic photometry are expected to be ~0.1 mag (1σ) for stellar objects with magnitudes at least 2.5 mag brighter than the plate limit. This leads to an expected accuracy of ~0.15 mag for photographic (U-B) colour (hereafter COS U-B). O'Donoghue et al. (1993) have assessed the accuracy of the photographic photometry on the basis of the above-mentioned 90 fields. For each of these fields, the calibrations of the photoelectric (hereafter U and B) and photographic (hereafter COS U and COS B) photometry were calculated. There were some fields showing tight parabolic relationships between COS U and U, and COS B and B with residuals with σ~0.1 mag. For the majority of fields, σ ~0.2 mag with some fields having a scatter as large as σ ~0.3-0.4 mag. These results would seem to imply that the accuracy in COS U-B is worse than 0.3 mag.

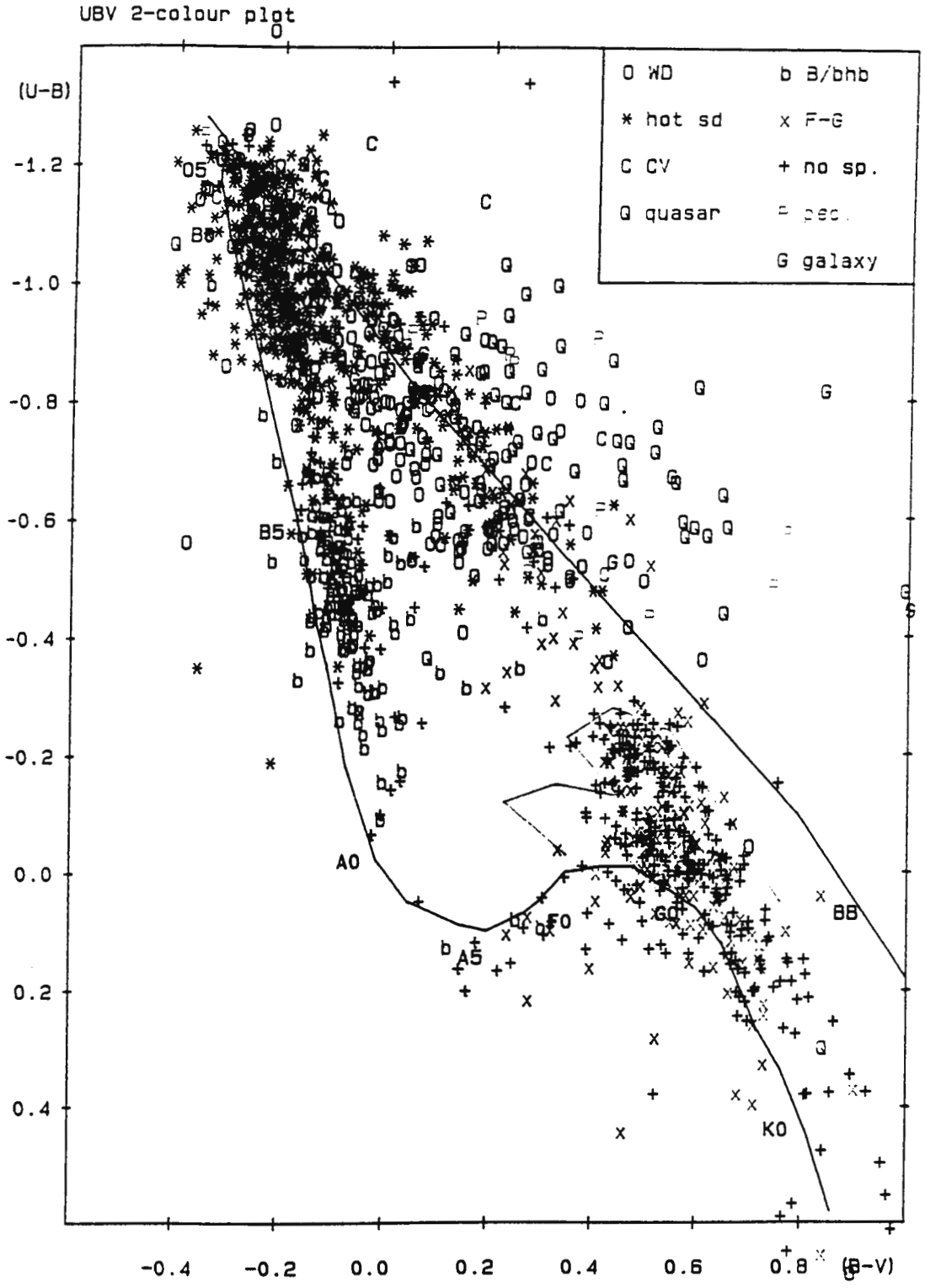

Figure 9. The (U-B, B-V) two colour diagram for all selected blue objects with photoelectric photometry (from O'Donoghue et al. 1993).

The presence of variable stars contributes to the scatter, especially in those fields with a small number of selected blue stars (≤7). In order to reduce this influence, all completed fields were combined to obtain an overall assessment of the accuracy of the photographic photometry. This was achieved by determining the different zero points for each field: a parabola with fixed linear and quadratic coefficients was fitted to the COS B vs B plot and also to the COS U vs U plot for each field separately. The zero points derived from these fits were subtracted from all the stars within the corresponding field to enable all the objects to be combined in a single plot of COS B vs B (and COS U vs U). Parabolae with all coefficients variable were then fitted to the combined data of COS B vs B and COS U vs U separately. The scatters in the residuals derived from these parabolic fits were found to be 0.21 and 0.30 mag for COS B vs B and COS U vs U respectively. This scatter in the residuals is still much larger than expected.

The (U-B, B-V) two colour diagram (Figure 9) for all selected blue objects with photoelectric photometry in the survey shows a significant contamination of ~18% of the survey sample by sdF and sdG stars with colours U-B≥-0.2 and B-V≥0.4; very few objects with U-B~0.1 and B-V~0.1 were selected. This might imply that there exists a colour term in the COS U-B vs U-B relation that results in objects with redder B-V being selected at redder U-B. O'Donoghue et al. (1993) tried to find a colour term in the relationship between photographic and photoelectric magnitudes but could find no consistent colour term.

Gilmore (1983) and Stobie & Henley (1983) showed that the error distribution in photographic photometry is non-Gaussian and shows an extended tail. This is an important effect that leads to the occurrence of spurious objects in surveys for variables or objects of extreme colour. The U-B distribution of stars with $12 \leq V \leq 20$ in the North Galactic Cap obtained by Yoshi et al. (1987) shows a peak at U-B~0.0, i.e. there is a large number of sdF and sdG stars in the range of $-0.2 \leq U-B \leq 0.1$. Assuming that the EC

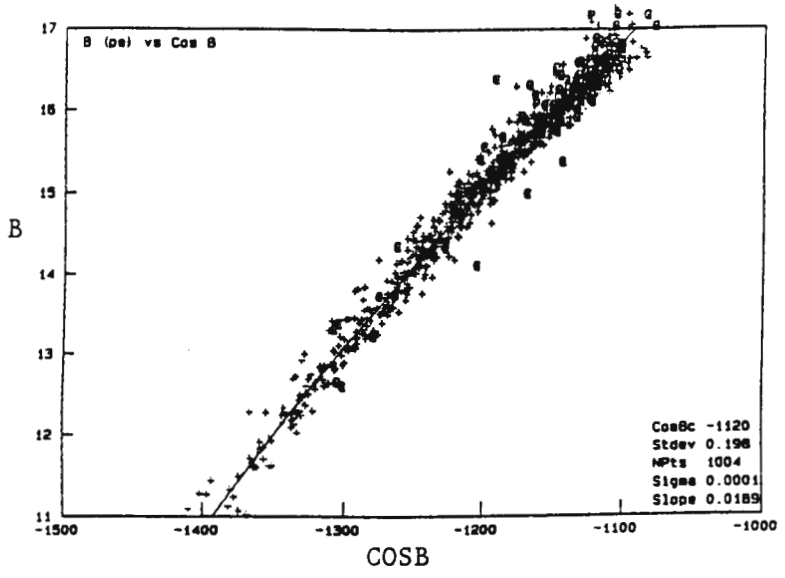

Figure 10. Combined plot of B vs COS B (from O'Donoghue et al. 1993).

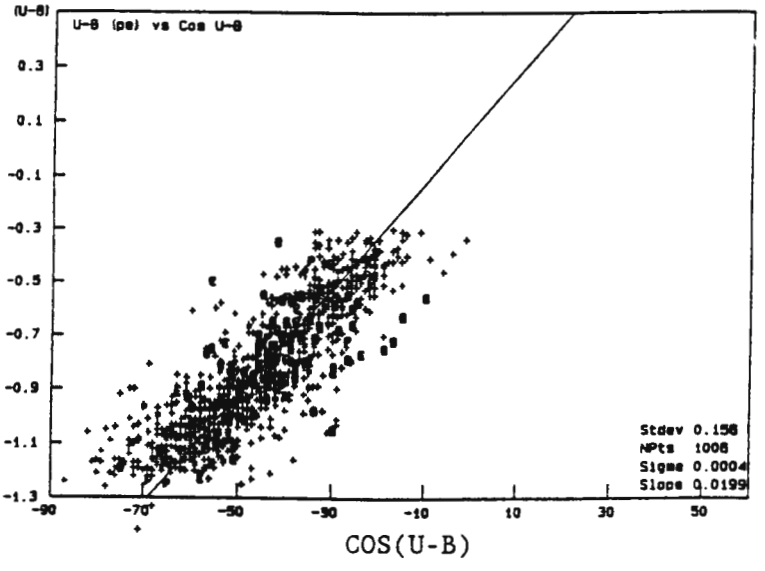

Figure 11. Combined plot of U-B vs COS U-B (from O'Donoghue et al. 1993).

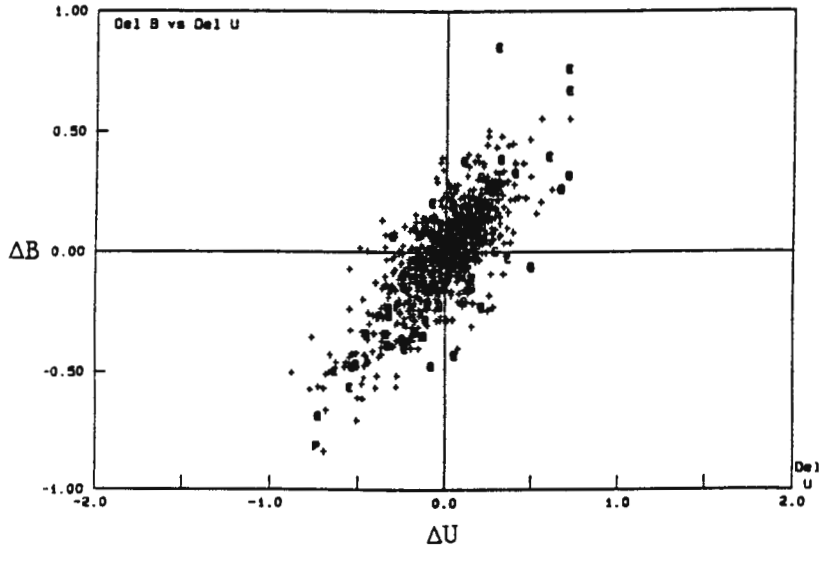

Figure 12. Plot of residuals in COS B (ordinate) vs COS U (abscissa) (from O'Donoghue et al. 1993).

survey has the same U-B distribution as that obtained by Yoshi et al. (1987), and the error distribution is the same as that found by Stobie and Henley (1983), it is possible to calculate the number of selected stars scattered into the range U-B $\leq$ -0.4. Because the F/G stars with U-B in the above-mentioned range so outnumber the genuine blue stars, even if only ~1% are scattered into the ultraviolet-rich region with U-B < -0.4, the contamination of blue objects by sdF/G stars can be explained.

Since the sdF and sdG stars scattered into the ultraviolet-rich region have anomalously large errors in the photographic photometry, such objects should be excluded from the COS B vs B and COS U vs U calibrations. Thus, parabolae were again fitted to the combined COS B vs B and COS U vs U data but with all stars with U-B >-0.3 excluded. The results show that the standard deviation of the residuals for the COS B vs B calibration (Figure 10) is 0.20 mag, only slightly improved. However, that for the COS U vs U calibration (not shown but similar to Figure 10) is 0.22 mag, much smaller than the previous error of 0.30 mag. This now suggests an expected error of 0.30 mag in the relation between COS U-B and U-B. In order to derive an error in COS U-B colour directly, a linear regression between COS U-B and U-B was calculated and showed a standard deviation of the residuals of 0.16 mag (see Figure 11). The reason for the smaller error in U-B is because the residuals in the COS B vs B and COS U vs U relations are correlated (Figure 12). The correlation of the residuals in Figure 12 strongly suggests that the cause of the large scatter in the COS B vs B relation is the same as that in the COS U vs U relation. In order to investigate the cause of the correlation in Figure 12, O'Donoghue et al. (1993) tried to find correlations between the residuals and the apparent magnitude, U-B colour, and position on the plate but no relationship was discovered. The residuals also did not depend on the seeing at the time the plates were taken.

Although the cause of the correlation of the residuals is unknown, the blue objects in the Edinburgh-Cape survey are being selected with an accuracy in photographic U-B of 0.16 mag, which is more precise than that of 0.38 mag for

the Palomar-Green survey (Green et al. 1986). The individual photographic U and B magnitudes are measured with a lower accuracy of ~0.20 mag.

§2.5.3 Repeatability and Results of Selection

In order to test the repeatability of blue object selection, three fields, F503, F640, and F710, in the North Galactic Pole area were repeated. Photometry and spectroscopy for these duplicate fields are available, so the objects brighter than B=16.5 in each pair could be checked to see if they were selected in both sets of plates of the field. The results are listed below:

Field No.	Plate No.	Found Twice	Found Once		
			F/G	B/bhb	A
503	UB10694	5	12	1	1
	UB12577	5	1	0	0
640	UB11613	12	6	0	0
	UB12474	12	0	0	0
710	UB11819	11	6	0	0
	UB12351	11	1	0	1

Apparently, the majority of the objects selected only once in the above table are F/G type stars. Even the horizontal branch stars selected only once occur near the red edge of the selection polygon. The discrepancy of the selection in the duplicate fields is possibly caused by non-Gaussian errors in the photographic photometry and field effects. Although the selection technique causes some F/G stars to contaminate the sample of blue objects, a high percentage of blue objects is being found twice. So this evidently shows the repeatability of our selection technique.

§2.5.4 Survey Completeness

The completeness of a survey is an important measure of its success. Incompleteness results from a number of causes: (1) failure in the pairing of the U and B catalogues. This arises because the image on one of the plates is affected by a plate flaw or a satellite/asteroid trail, or is blended with

a nearby star or galaxy; (2) the object is close to the limiting magnitude of the survey; (3) the object is close to the colour cutoff for the survey.

The completeness may be estimated internally by checking the repeatability of blue object detection in repeated fields or in the overlap area between neighbouring fields. External checks on completeness can be made by comparison with a variety of catalogues containing known blue objects (e.g. Palomar-Haro-Luyten survey).

With the exception of incompleteness arising from the limiting magnitude of the survey, we shall discuss the above sources of incompleteness in turn. As mentioned in §2.5.1, the approximate limiting magnitude of the survey was shown to be ~18 in B. However, this may vary by ~0.5 mag from field to field but we have no information to make this claim more precise.

§2.5.4.1 Losses in Pairing

Five pairs of neighbouring fields were selected to estimate the loss of objects due to non-repeatable errors in pairing. The overlap region between the plates was determined by cross-correlating <u>all</u> the objects in a given field with <u>all</u> the objects in the neighbouring field (without regard for U-B colour). This yielded a subset of objects for each field which should have been measured in the neighbouring field. In order to eliminate the difference in limiting magnitude as a cause of losses, only objects brighter than 16.5 Bmag in a given field were selected and checked for in the neighbouring field. The results show that less than 4% of objects were paired in one field but missed in the neighbouring field. Note that this does not estimate losses due to repeatable pairing errors which could cause the objects to be detected in neither field.

§2.5.4.2 Internal Completeness

In an ideal survey, the overlap region between two neighbouring fields should result in two detections of a blue object that lies in this region.

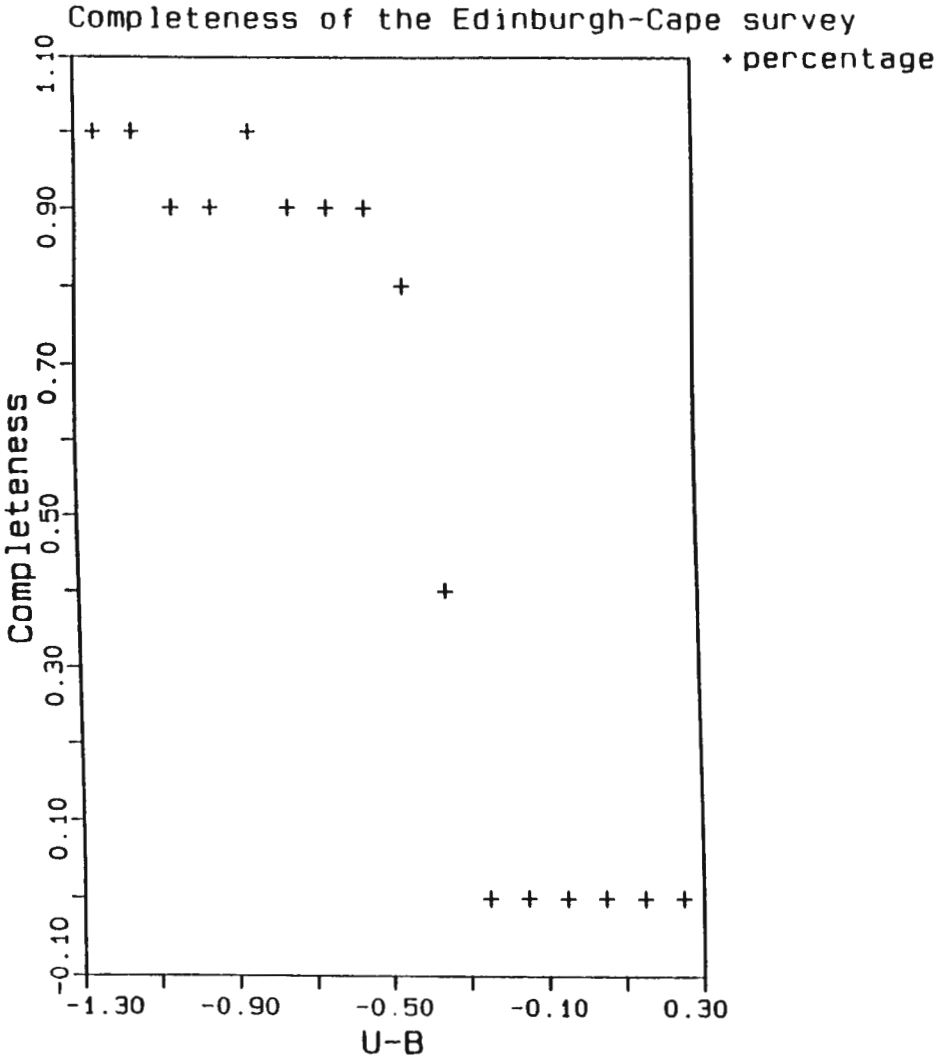

Figure 13. Plot of colour U-B vs completeness for the objects brighter than B~16.5 mag found in overlap regions.

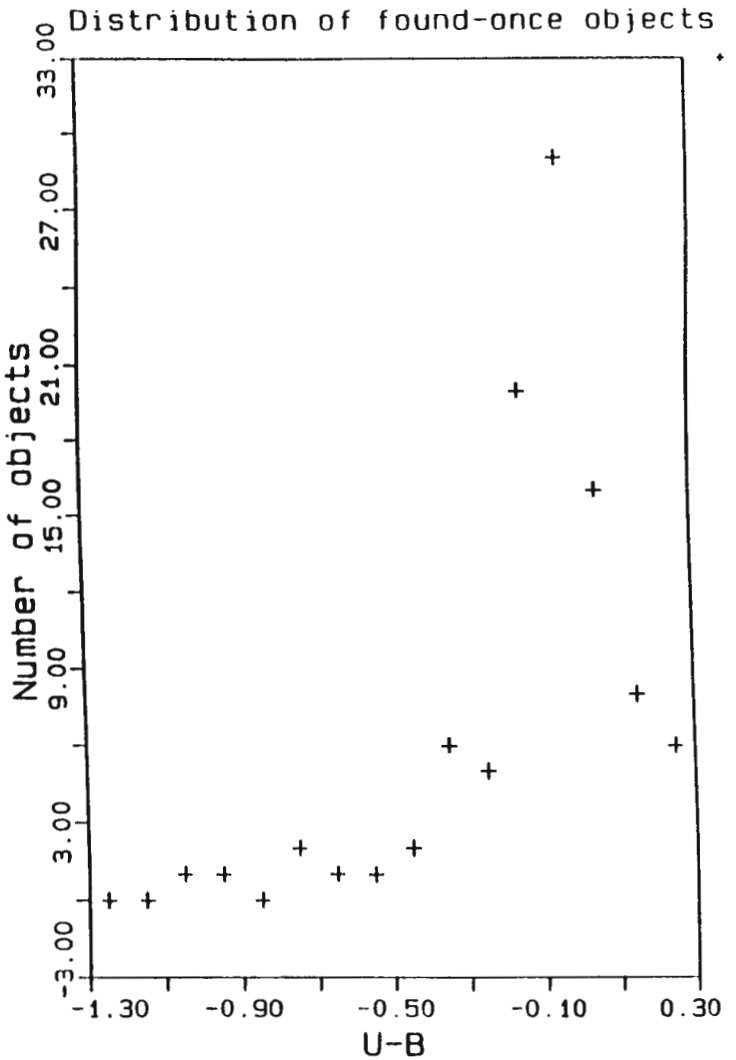

Figure 14. Plot of colour U-B vs number of objects for the found-once objects brighter than B~16.5 mag in overlap regions.

We used the method of Green et al. (1986) to check this property of the EC survey. Let a be the number of objects found twice and b be the number of objects found once in an overlap region. If p is the probability of discovering a blue object in a single plate pair, p is $2a/(2a+b)$. The completeness, c, of the survey is the sum of the fraction of objects found once in a non-overlap region, the fraction of objects found twice in an overlap region, and the fraction of objects found once in an overlap region. Let f be the fraction of the total area surveyed which lies in an overlap region, then $c = (1-f)p + f[2p(1-p)+p^2]$. Note that triple overlaps were neglected in this calculation.

Seventy fields with a coverage of 2002 square degrees were used to evaluate the survey completeness. These fields provide 88 overlap regions with total coverage of 211 square degrees. Thus the overlap region is 10% of the coverage of the above seventy fields, i.e. f = 10%. In the above overlap regions, 215 objects were found twice and 371 objects were found once. Thus the survey seems to have p~54 percent. This yields a completeness of ~56 percent which is much smaller than expected and disappointingly low. In order to understand the reasons which cause such incompleteness, a detailed analysis was carried out: the objects brighter than B~16.5 with photoelectric photometry in overlap regions were selected and placed in colour U-B bins with a bin width of 0.1 mag. The results are tabulated in Table I and plotted in Figure 13 and 14. The completeness for individual U-B bins is shown in Figure 13: the completeness of the bins with U-B < -0.4 is greater than 80 percent and drops to zero at U-B > -0.3 mag. This shows, not surprisingly, that the survey completeness is dependent on U-B colour and that the selection cutoff is U-B ~ -0.3. Therefore the overall completeness of 55% is not representative of the success of the EC survey. Instead, the average completeness of 94 percent, which was calculated for the objects with a colour U-B $\leq$ -0.3, is a more reasonable estimate of the completeness of the Edinburgh-Cape survey.

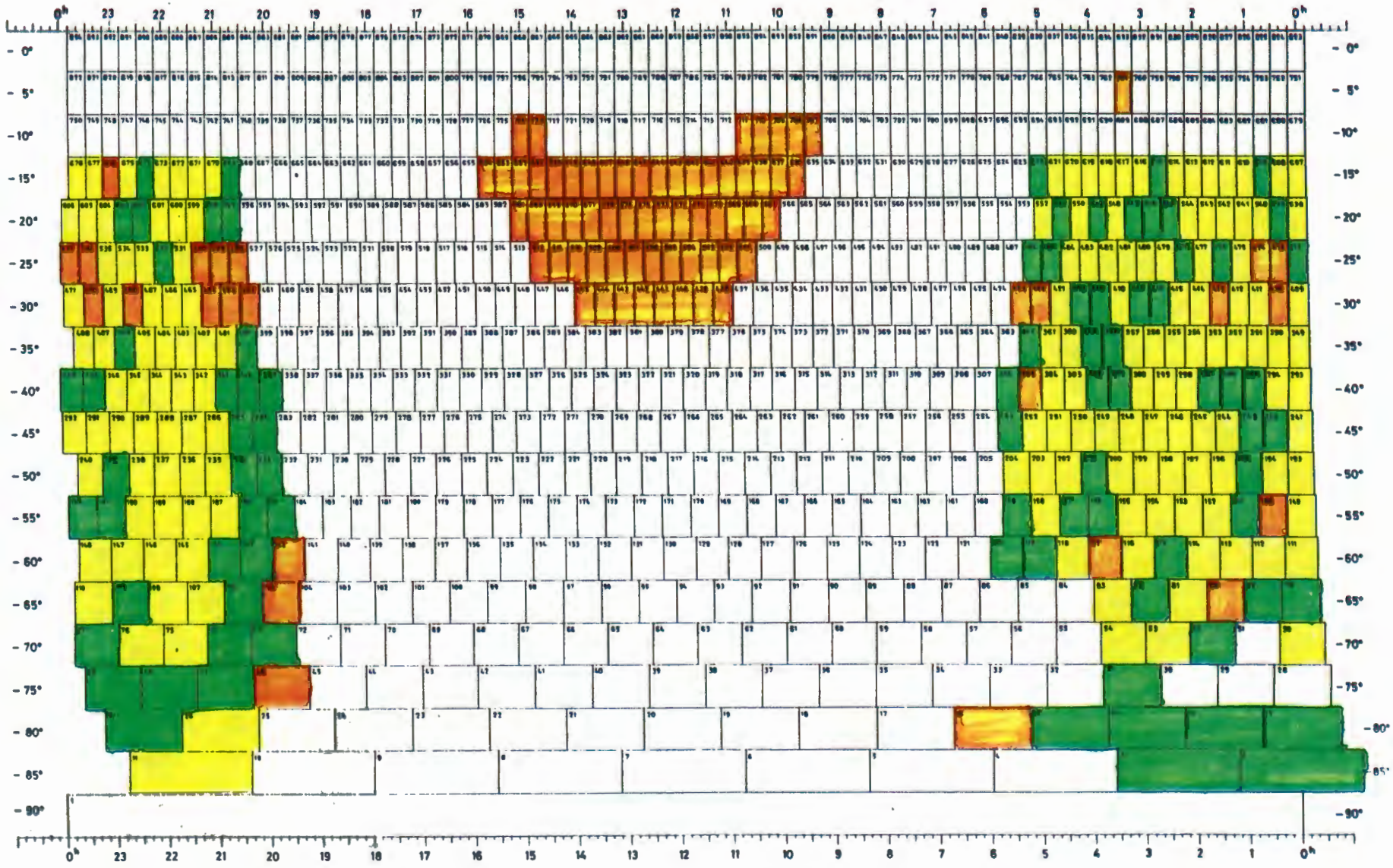

Figure 15. The field distribution of the EC survey: the "green" fields represent the fields whose blue object selection have been done; the "orange" fields represent the fields with photometry and spectroscopy completed to B=16.5 mag; the "yellow" fields are the planned fields whose blue object selection haven't been done.

the white dwarfs in the EC survey to compare with McCook and Sion's (1987) white dwarf catalogue; their results show a completeness of 82 percent. From the statistical view point, these results may be influenced by small numbers in the samples. The number of quasars missed was only three. The white dwarf numbers were larger, but these results should be viewed with caution until better statistics are available.

§2.5.5 The EC Survey Statistics

The present status (1994 August) of the survey is that there are currently about 200 pairs of plates which have been taken and shipped to the Royal Observatory Edinburgh, and 176 of these (including 3 duplicate fields) have been processed for blue object selection. Compared to the total of 380 planned fields phase 1 of the survey is 46% complete. The field distribution is shown in Figure 15. In the whole survey, it is expected to discover ~5000 objects brighter than B~16.5. Typically about 50 objects brighter than B=18 are being selected per field (28.6 square degrees), and 15 of these selected objects are brighter than B~16.5, corresponding to a number density of ~0.5 per square degree. This number density is about twice that of the Palomar-Green Survey (0.2 per square degree) because of the deeper magnitude limit and the U-B cutoff of about -0.3, slightly redder than the Palomar Green Survey's (U-B) cutoff ~ -0.4.

UBV photometry has been obtained for 2025 objects, and spectra (covering 3400-5200Å) for 1832 objects. The (U-B, B-V) two colour diagram (Figure 9) is shown for objects with photoelectric photometry. The colours may be used to discriminate between some categories of stars: e.g. hot subdwarfs, and cool F/G subdwarfs. Spectroscopy is essential for distinguishing between quasars, cataclysmic variables, and white dwarfs which are found near the blackbody line. The statistics of the survey and comparison with the Palomar-Green Survey (Green et al. 1986) appear below:

Type of Object	EC No.	Survey %	PG No.	Survey %
hot subdwarfs	776	50.7	913	53.7
white dwarfs	261	17.0	448	26.4
cataclysmic variables	28	1.8	81	4.7
horizontal branch B stars	129	8.4	99	5.8
B stars	148	9.7	-	-
sdF/G stars	304	-	-	-
quasars	97	6.3	116	6.8
galaxies	10	0.6	35	2.1
peculiar	34	2.2	-	-
other	48	3.1	6	0.4

The presence of a large number of sdF/G stars is not surprising, the explanation has been fully discussed in section 2.5.2 and 2.5.4. In comparison to the Palomar-Green survey, the EC survey has a higher percentage of horizontal branch B stars because of the redder U-B cutoff for the selection of objects. Although star/galaxy separation has been carried out, a small number of galaxies still appear in the survey because of their large nuclear surface brightness which makes them appear stellar.

References:

Brownrigg, D.R.K.(1984). *Communications ACM* **27**, 807.

Gilmore, G. (1983). in Occ. Rep. Roy. Obs. Edinburgh No. **10**, *Workshop on Astronomical Measuring Machine*, eds Stobie, R.S., McInnes, B., p259.

Green, R.F., Schmidt, M., and Liebert, J.(1986). *Astrophys. J. Suppl.*, **61**, 305.

Hewitt, A., and Burbidge, G. (1987). *Astrophys. J. Suppl.*, **63**, 1.

McCook, G. and Sion, E.M. (1987). *Astrophys. J. Suppl.*, **63**, 605.

MacGillivray, H.T., and Stobie, R.S. (1984). *Vista in Astronomy*, **27**, 433.

Menzies, J.W., Cousins, A.W.J., Banfield, R.M., and Laing, J.D.(1989). S. Afr. astr. Obs. Circ., **13**, 1.

O'Donoghue, D., Chen, A., Kilkenny, D., and Stobie, R.S. (1993). in *Proceedings of the 8th European Workshop on White Dwarfs*, ed. M. Barstow, NATO Advanced Study Institute Series, Kluwer, p39.

O'Donoghue, D., Stobie, R.S., Chen, A., Kilkenny, D., and Koen, C. (1993). in *Precision Photometry Conference Proceedings*, eds. D. Kilkenny, E. Lastovica and J. Menzies, p72.

Reid, N., and Gilmore, G.(1982). *Mon. Not. R. astr. Soc.*, **201**, 73.

Savage, A., Cannon, R.D., Stobie, R.S., Kilkenny, D., O'Donoghue, D., and Chen, A. (1993). *Proc. astr. Soc. Austr.*, **10**, 265.

Stetson, P.B.(1987). *Publ. astr. Soc. Pac.*, **99**, 191.

Stobie, R.S.(1982). *COSMOS User Manual* (Royal Observatory, Edinburgh).

Stobie, R.S.(1986). *Pattern Recognition Letter*, **4**, 317.

Stobie, R.S., and Henley, R.C.(1983). in Occ. Rep. Roy. Obs. Edinburgh No. **10**, *Workshop on Astronomical Measuring Machine*, eds Stobie, R.S., McInnes, B., p49.

Stobie, R.S., Morgan, D.H., Bhatia, R.K., Kilkenny, D., and O'Donoghue, D. (1988). in A.G. Davis Philip, D.S. Hayes and J.W. Liebert (eds.), IAU Colloq. **95** : *The Second Conference On Faint Blue Stars*, L. Davis Press, Schenectady, p493.

Stobie, R.S., Chen, A., O'Donoghue, D., and Kilkenny, D. (1992) in B. Warner (ed.), *Variable Stars and Galaxies*, *Astr. Soc. Pac. Conf. Series*, **30**, p87.

Stobie, R.S., Chen, A., O'Donoghue, D., and Kilkenny, D. (1993) "*Description of the Edinburgh-Cape Blue Object Survey*", in preparation.

Yoshi, Y., Ishida, K., and Stobie, R.S.(1987). *Astron. J.*, **93**, 323.

Chapter 3: *Cataclysmic Variable Stars and Close Binaries --- discovered by the Edinburgh-Cape Survey*

In this chapter, a general review of cataclysmic variables (CVs) is given in section 3.1. Section 3.2 describes the selection of cataclysmic variables and the results. The external completeness and space density estimated from the Edinburgh-Cape cataclysmic variable stars (hereafter EC CVs) are respectively discussed in section 3.3 and 3.4. The EC CVs are introduced in the Appendix. The detailed studies of individual objects will be discussed in chapters 6-10.

§3.1 Cataclysmic Variables

Cataclysmic variables are all semi-detached, strongly interacting binary stars consisting of a white dwarf (hereafter primary) and a cool secondary (Robinson 1976; Wade and Ward 1985; Warner 1994) which is usually a cool dwarf of spectral type G, K, or M, but may be a red giant as in the recurrent novae T CrB (Kraft 1958) and RS Oph (Barbon et al. 1968), or a degenerate star as in AM CVn (Faulkner et al. 1972). The secondary star fills its Roche lobe and transfers mass through the inner Lagrangian point to the white dwarf. In a weak magnetic field ($\leq 10^5$G), the gas flow from the secondary's atmosphere does not accrete directly onto the white dwarf due to the conservation of angular momentum; instead it orbits the white dwarf in an accretion disk formed by viscous processes in the gas flow which radiate away the gravitational potential energy. Note that the accretion luminosity from the disk is about 0.01-10 $L_\odot$ (although it can fall to 0.001 $L_\odot$, see Patterson 1984) which is higher, and usually much higher than the combined luminosity ($< \sim 0.01$ $L_\odot$) of a white dwarf-red dwarf pair. Thus if a CV terminates mass transfer, it will be much less obvious in most kinds of surveys. The region in which the gas flow impacts the outer rim of the accretion disk is termed the "bright spot" which has been observed in light curves of many systems

such as UX UMa (Frank et al. 1981), VW Hyi (Vogt 1974), and Z Cha (Warner 1974).

If the primary has a strong magnetic field ($\geq 10^7$G), the gas stream from the secondary is captured by the magnetic field and falls onto the magnetic pole along the field lines and forms an accretion column. The gas stream is accelerated by the primary's gravitational field to supersonic velocities near the magnetic poles. So a strong shock is formed in the accretion flow close to the surface of the white dwarf and emits hard X-rays. The X-rays incident upon the atmosphere of the white dwarf (about half of the total) are absorbed and re-emitted as soft X-rays and UV radiation. Systems of this kind are called polars (e.g. Cropper 1990), and include AM Her and EF Eri. For a moderate magnetic field, the field is not strong enough to prevent formation of the disk. Thus, an accretion disk still exists but its interior is disrupted. An accretion column is fed by gas channelled from the inner edge of the disk. These objects, such as V1223 Sgr and AO Psc, are termed intermediate polars (Warner 1983 and 1985). The magnetic field of the primary in polars is sufficiently strong that the secondary enforces corotation of the primary at the binary orbital period. In contrast, in the intermediate polars the field is weaker and the rotation period of the primary is shorter than the orbital period. Thus, two or more photometric periods (Warner 1986a) are seen in intermediate polars whereas only the orbital period is seen in polars.

§3.1.1 Taxonomy of Cataclysmic Variables

The canonical classification is essentially based on morphology of long-term light variation; of course, spectroscopic characteristics are the auxiliary criterion as in the distinction between (recurrent) novae and dwarf novae, or in that between the UX UMa and RW Tri subclasses of nova-like variables. The spectroscopic differences between the outbursts of novae and dwarf novae have been crucial in the understanding of the former as a thermonuclear runaway on the primary (with subsequent mass ejection), and the

latter as an increase in the mass accretion rate through the accretion disk. Cataclysmic variables include classical novae (CN), recurrent novae (RN), dwarf novae (DN), and nova-like variables (NL). The definitions of the subtypes of CVs are stated as follows and the detailed properties of these stars are discussed in Warner (1994).

Classical Novae have been observed to undergo only one eruption with very large amplitude of 6-19 magnitudes. The decline rate of eruption has a correlation with the absolute amplitude at maximum; the brighter amplitude eruptions have shorter duration.

Recurrent Novae have been observed to undergo more than one eruption with smaller amplitude than classical novae eruptions.

Dwarf Novae have outbursts recurring on timescales of weeks to years, with typical amplitudes 2-5 magnitudes, lasting for 2-100 days. There are three subclasses of DN: Z Cam stars, SU UMa stars, and U Gem stars with distinct characters of outbursts: (1) Z Cam stars show standstills at brightness about less than 1 mag below the maximum during early decline, lasting for tens of days to years. (2) SU UMa stars exhibit two kinds of outbursts, "normal" (lasting ~days) and "super" outbursts (lasting ~weeks), and show superhumps in the light curve during superoutbursts. The superoutbursts have larger amplitudes and recur less frequently than normal outbursts. (3) U Gem stars include the dwarf novae which are neither Z Cam stars nor SU UMa stars.

Nova-like Variables, by definition (Warner 1994), are all "non-eruptive" CVs which include UX UMa stars, RW Tri stars, SW Sex stars, VY Scl stars, nova remnants (NRs), polars, and intermediate polars (IPs). The definitions of the subclasses are based on photometric and spectroscopic behaviour. UX UMa stars have a long-term brightness variation of no more than ~1 mag, low amplitude flickering activity, and broad Balmer absorption lines. The NLs having photometric behaviour similar to UX UMa stars but showing pure emission line spectra are called RW Tri stars.

Although NLs are defined as a group of CVs which do not show eruptive behaviour, this does not mean that NLs undergo no changes in long-term

brightness. In particular, the VY Scl stars may spend most of their time varying little about a mean magnitude (the "high state"), but occasionally drop in brightness by a magnitude or more for weeks to years (the "low state"). Note that a VY Scl star may belong to either the UX UMa category or the RW Tri category.

The SW Sex stars are a group of eclipsing NLs with orbital periods in the range 3.24-3.74 hrs and show single-peaked emission lines which have narrow central absorptions at certain orbital phases. Their radial velocity curves reveal large phase shifts relative to photometric ephemerides.

Nova remnants show a variety of spectra: from broad, shallow Balmer and helium absorption lines with weak emission cores to pure emission lines of H, HeI, HeII, and λ4650Å. The high excitation lines are remarkably strong in some NRs, such as CP Pup (O'Donoghue et al. 1988) and RR Pic (Wyckoff and Wehinger 1977). Some of the emission lines present in the optical spectra of NRs, such as OIII λ3429Å, HeII λλ4199Å, 5411Å, MgII λ4481Å, and FeII λλ4550Å, 4731Å (Warner 1994), are not seen in the spectra of NLs.

Polars exhibit both high and low states in their long-term light variations, with gradual transitions between them (Warner 1983). The optical spectra of polars are characterized by strong Balmer series, HeI, HeII, the CIII/NIII λ4650Å blend, and the Balmer jump in emission. Typically the strength of HeII λ4686Å is comparable to that of Hβ. These objects also show strong, variable circular and linear polarization at optical wavelengths and emit soft and hard X-rays.

IPs are hard X-ray emitters and multi-periodic (Warner 1994). The optical spectra of IPs resemble those of polars but HeII λ4686Å is weaker relative to Hβ. The polarization is much weaker than in the polars being usually unobservable. The long-term brightness variations of IPs are similar to that of polars, but with less time spent in the high state.

§3.1.2 Origin of Cataclysmic Variables

In very wide binaries with massive primaries, the primary evolves to a red giant (or a red supergiant). Once the giant expands sufficiently to fills its Roche lobe, it begins mass transfer on a dynamical time scale at a rate of ~0.1 $M_{\odot}$/yr. The accreting secondary, a low mass main sequence star, can not adjust its structure at that high rate. Thus, the transferring material, instead of accreting onto the secondary, passes through the outer Lagrangian point (L_2) and fills the outer Roche lobe (Warner 1994). At this stage, the binary is embedded in a "common envelope". The common envelope gives frictional resistance to the orbital motion of the secondary. Thus the two components transfer angular momentum and energy to the envelope and gradually spiral in with decreasing orbital period and separation. Eventually, the common envelope is ejected when the energy deposited in the envelope exceeds its binding energy. By this time the binary will have reduced its orbital period to be $\leq$ ~1 days and may appear as a nucleus of a planetary nebula (PN) such as LSS2018 (Drilling 1985), MT Ser (Grauer and Bond 1983; Green et al. 1984), and V477 Lyr (Bond 1980 and 1987). After the planetary nebula has dissipated, the hot primary gradually cools down and evolves into a white dwarf. The secondary has not yet filled its Roche lobe (Paczynski 1985). Thus, the system is still detached, such as GK Vir (Green, Richstone and Schmidt 1978) and V471 Tau (Bond 1985 and references therein).

These short-period binaries consisting of a white dwarf or a precursor of a white dwarf, and a lower main sequence star are generally believed to be progenitors of cataclysmic variables (hereafter PCV) (e.g. Ritter 1986a and Patterson 1984). Each PCV will become a CV as soon as the secondary fills its Roche lobe. This will occur when the orbital separation and period have decreased by means of orbital angular momentum loss due to: (1) magnetic braking; (2) gravitational radiation. Another cause of Roche lobe overflow is expansion of the secondary due to nuclear evolution.

§3.1.3 Evolution of Cataclysmic Variables

After the mass transfer begins, the accretion onto the primary may proceed in different ways which depend on the strength of the primary's magnetic field as discussed in section 3.1. The mass transfer rate plays a crucial role in the behaviour of CVs: (1) VY Scl stars and polars show high states and low states which are due to changes in mass transfer rate (M_{tr}); (2) DN and Novae show outbursts. At present, there are two theories to explain DN outbursts: one is the Mass Transfer Instability model (Bath and Pringle 1982) in which the secondary suddenly increases its mass transfer rate due to an instability in the secondary's atmosphere near the inner Lagrangian point; the other is the Disk Instability model in which the material in the disk falls rapidly onto the surface on the white dwarf when the disk exceeds a critical surface density (Cannizzo and Kaitchuck 1992). In contrast, nova eruptions have a completely different mechanism: it is certain that they are due to thermonuclear runaway on the surface of the white dwarf due to accumulation of H-rich material (see section 3.1.3.2). Note that within a few years of a nova eruption, the underlying binary usually appears very similar, both photometrically and spectroscopically, to DN in outburst. Thus, the disks in these systems seem to be 'stuck' permanently in outburst. However, there is theoretical reason (Shara et al. 1986) and some observational support (e.g. CK Vul: Shara et al. 1985) for the view that NRs do not stay in this condition for all the time between successive nova eruption, which are thought to recur on a time scale of 10^3-10^5 years.

§3.1.3.1 Stability of Mass Transfer

The absolute magnitude (M_v) of DN are 6-11 mag at quiescence and 4-5 mag during outburst (Warner 1994). As mentioned above, M_v of NLs are similar to that of DN in outburst. From the M_{tr}-M_v relation computed by Smak (1989), the mass transfer rate of various subclasses of CVs can be roughly estimated to be: for NRs, NLs, and DN during outburst, M_{tr}~10^{-9}-10^{-8} $M_\odot$/yr and for DN at quiescence, M_{tr}~10^{-11}-10^{-10} $M_\odot$/yr. Assuming that the mass transfer is steady,

the lifetime of CVs is about 10^7-10^{10} yrs for a system containing a secondary of a mass ~0.5 $M_\odot$. One may ask whether or not the mass transfer is stable during the above time scale. In fact, the mass transfer is self-sustaining only in systems with $q(\equiv M_2/M_1)>1$, which is due to decreasing orbital separation and period as M_2 is steadily reduced (Eq(9.5) of Warner 1994: $\dot{a}/a=2(q-1)\cdot\dot{M}_2/M_2$ and $\dot{P}_{orb}/P_{orb}=3(q-1)\cdot\dot{M}_2/M_2$). For systems with $q<1$, the mass transfer is not self-sustaining because R_2 contracts faster than $R_{2,lobe}$ does (Eq(9.6) of Warner 1994: $\dot{R}_{2,lobe}/R_{2,lobe}=(2q-5/3)\cdot\dot{M}_2/M_2$). Thus, in order to keep the main sequence secondary in contact with its Roche lobe, there must be some mechanism to drain orbital angular momentum from CVs. If the system contains an evolved or relatively massive secondary, the secondary's radius may expand to fill its Roche lobe due to nuclear evolution, on a nuclear time scale. Otherwise, orbital angular momentum and separation must be reduced via magnetic braking and/or gravitational radiation.

Gravitational quadrupole radiation is a possible mechanism for the evolution of CVs, as pointed out by Kraft et al. (1962), Paczynski (1967), and Faulkner (1971). Gravitational radiation removes both energy and orbital angular momentum from the binary system. As a result of this, the orbital separation and period decrease if the secondaries are main sequence stars. For a lobe-filling main sequence secondary, the corresponding mass transfer rate derived by Warner (1994) is

$$dM_2/dt = -3.4\times10^{-11}\cdot(1-15q/19)^{-1}\cdot(1+q)^{-1/3}\cdot(M_1)^{2/3}\cdot(P_{orb})^{-1/6}\ M_\odot/yr \text{ for } P_{orb}\leq 9 \text{ hrs},$$

where M_1 is in $M_\odot$ and P_{orb} is in hrs. From the above equation, the mass transfer rate derived by gravitational radiation is of the order 10^{-11}-10^{-10} $M_\odot$/yr which is much lower than observed rates of mass transfer in NLs and NRs (see above) but may be the dominant braking mechanism for short period DN at quiescence and polars (Warner 1994).

The above estimate indicates that braking by gravitational radiation alone cannot drive the mass transfer rates in all kinds of CVs. Thus, magnetic braking is also considered important as an efficient way of extracting

orbital angular momentum: a lobe-filling secondary loses its rotational angular momentum via a stellar wind which streams out along the secondary's magnetic field lines. In order to keep synchronous rotation by spin-orbit coupling in the close binary, orbital angular momentum is transferred to the rotation of the secondary. Verbunt and Zwaan (1981) applied the rotational braking law observed in single G-stars to the much faster rotating late type secondaries in CVs and have derived a semi-empirical relation for the rate of loss of orbital angular momentum. Rappaport et al. (1983) used this braking law to obtain a dM_2/dt-P_{orb} relation for $P_{orb} > 2.7$ hrs:

$$dM_2/dt = -2.0\times10^{-11}\cdot(P_{orb})^{3.2\pm0.2}.$$

The mass transfer rate estimated from the above equation shows a range of $\sim5\times10^{-10}$-10^{-8} $M_\odot$/yr which matches reasonably well the observed mass transfer rates in NRs and NLs.

This completes the overview of the mechanisms of mass transfer. We now consider the consequences of mass transfer in CVs. Long term mass transfer, driven by magnetic or gravitational braking, changes the secondary's structure and orbital elements. These changes affect the CV's evolution as discussed in the following sections.

§3.1.3.2 Hibernation and Cyclical Evolution

Continuous accretion of mass onto the compact primary (white dwarf) will eventually ignite hydrogen burning in various ways (Ritter 1986b): (1) for high mass transfer rates, $M_{tr} \geq 10^{-7}$ $M_\odot$/yr, stable hydrogen burning occurs in a shell; (2) for mass transfer rate, 10^{-7} $M_\odot$/yr $\geq M_{tr} \geq 10^{-9}$ $M_\odot$/yr, hydrogen is burnt in shell flashes; (3) for low mass transfer rates, $M_{tr} \leq 10^{-9}$ $M_\odot$/yr, the accreted hydrogen becomes degenerate before the nuclear reaction ignite. When the nuclear burning starts, a thermonuclear runaway occurs on the surface of the white dwarf and produces a nova eruption. Theoretically, ejecting most or all the accreted mass on the white dwarf should result in sufficient loss of angular momentum to increase the orbital separation for $P_{orb} \geq 8$ hrs but to decrease that for shorter periods (Warner 1994). This

effect is supported by the observed increase in orbital period of BT Mon after its 1939 eruption (Schaefer and Patterson 1983). The mass transfer is maintained at a high rate for 50-200 yrs after nova explosion, because the secondary is heated by the now much hotter white dwarf primary which expands its outer layers to overflow the Roche surface. A few hundred years after the nova eruption, the secondary decreases its radius and underfills its Roche lobe as the white dwarf gradually cools down (Kovetz et al. 1988). This results in reducing or even cutting off mass transfer from the secondary, as observed in RR Pic (Warner 1986b) and CK Vul (e.g. Shara et al. 1985). If the mass transfer from the secondary ceases, a post-nova would become unobservable due to its faint brightness. Shara et al. (1986) suggested that post-novae may "hibernate" for 10^3-10^5 yrs and at this time these objects will appear as detached white dwarf-red dwarf binaries with much lower luminosity than the pre-nova. The magnetic braking and/or gravitational radiation will eventually drain sufficient orbital angular momentum to bring the secondary back to filling its Roche lobe again, with mass accretion onto the white dwarf resuming. Once critical envelope mass is achieved, another thermonuclear runaway occurs at the base of the degenerate envelope. This completes the cycle hypothesized in the "cyclical evolution" model (e.g. Vogt 1989; Shara et al. 1986).

§3.1.3.3 Distribution of Orbital Periods

The majority of CVs with known orbital periods have periods shorter than 15 hrs. There exists a minimum orbital period of ~80 mins for a CV with a normal hydrogen-rich secondary. The systems with orbital periods < 80 mins are AM CVn stars which contain a degenerate helium-rich secondary (DB white dwarf). CVs are deficient in the period range $2.3 \leq P_{orb} \leq 2.8$ hrs. This is the so-called "period gap".

The model of Robinson et al. (1981) is generally accepted as an explanation of the period gap and proposes that the period gap arises from the temporary

cessation of mass transfer from the secondary so the system fades from view, becoming a low luminosity detached pair.

The reason for the cessation of mass transfer (or equivalently the detachment of the secondary from its Roche lobe) is not well understood. In a scenario which has been favoured for some years, the secondary changes from having a radiative core to being fully convective at a mass of less than ~0.3 $M_\odot$ (e.g. Copeland et al 1970; Grossman et al. 1974). The binary will have a period near the upper edge of the gap, which can be verified from the secondary mass-period relation (Warner 1994) for a lobe-filling secondary, $M_2=0.065\cdot(P_{orb})^{5/4}$, where M_2 is in $M_\odot$ and P_{orb} is in hrs. When fully convective, the secondary's magnetic field is supposed to weaken or collapse reducing the magnetic braking needed to sustain mass transfer. The reduction of braking will allow the secondary, which was out of thermal equilibrium because its thermal time scale was longer than the mass-loss time scale, to shrink to the thermal equilibrium radius and detach from its Roche lobe. The detached system will take ~2-5$\times10^8$ yrs to re-establish contact via gravitational braking (Warner 1994) and resume mass transfer at the lower edge of the period gap.

In regard to the minimum orbital period, Paczynski and Sienkiewicz (1981), Rappaport et al. (1982), and D'Antona and Mazzitelli (1982) independently showed that continuous mass loss will eventually lead the very low mass secondaries to leave the lower main sequence and become fully degenerate joining the white dwarf mass-radius relation. The low-mass degenerate secondary will increase its radius and its orbital period (Warner 1994), as the mass transfer continues. Therefore the P_{orb} must pass through a minimum, ~80 mins, during the transformation from a contracting non-degenerate secondary to an expanding degenerate secondary.

§3.2 Motivation for Searching for CVs in the EC survey and Results

The Catalogue of Cataclysmic Variables with Determined Orbital Periods (Ritter 1990) reveals a north-south imbalance in the number of cataclysmic

variables; 103 in the north and 65 in the south. Howell and Szkody (1990) pointed out that only 14% (60 of 426) and 8% (8 of 113) of CVs, respectively, in the 3rd edition of the General Catalogue of Variable Stars and Patterson's (1984) list of all the CVs known at that time with determined orbital periods, are possible galactic halo CVs. The studies of high Galactic latitude CVs by Howell and Szkody (1990) and Szkody and Howell (1992) showed that the distribution of orbital periods has a tendency toward shorter periods and the halo DN below the period gap exhibit a larger outburst amplitude. This may be caused by a selection effect: because the halo CVs have fainter apparent magnitudes, DN with larger amplitudes are easily detected. The halo CVs are believed to be either population II CVs with lower metal abundance (which may affect the mechanism of DN outburst, period gap, and evolutionary scenario) or intrinsically faint disk CVs (which may alter the currently accepted space density and estimated mass transfer rate) (Howell 1993). The EC survey is thus expected to discover previously unknown CVs at high galactic latitude in the southern hemisphere and thereby rectify the north-south imbalance. As mentioned in Chapter 2 (§2.5.4), there are 28 candidate CVs spectroscopically identified in the EC survey thus far. Their spectra are characterised by either Balmer lines in emission or broad shallow Balmer absorption lines. After the follow-up work (high-speed photometry and spectroscopy), 22 of these stars were confirmed to be CVs and one was found to be a close binary. This close binary system, EC11575-1845, doesn't show flickering in its light curve but instead shows a smooth sinusoidal variation with a period of ~8 hrs, deduced to be the orbital period. The detailed study of EC11575-1845 is discussed in Chapter 5. The CVs are tabulated in Table I and generally described in the appendix. Table I gives coordinates (epoch 1950.0) (accuracy ~1 arcsec), Bmag ranges detected in the period of 1991-1993, orbital periods, and subtypes. Among these twenty-two CVs, ten of them are already known and were rediscovered by the EC survey (marked "#" in Table I). These already known CVs are not discussed in this thesis.

Table I. The Edinburgh-Cape Cataclysmic Variables

Objects	RA (1950.0) h m s	Dec ° ′ ″	Bmag	P_{orb} (hrs)	Type	Distance (pc)
#01396-6808 (BL Hyi)	01 39 36.4	-68 08 37		1.89[d]	NL	
#03120-2246 (EF Eri)	03 12 00.3	-22 46 49		1.35[a]	NL	200[a]
04030-5801	04 03 05.3	-58 01 35	14.7->18		DN	
04224-2014	04 22 29.6	-20 14 01	11.6-13.0	4.2	NL	
05114-7955	05 11 25.1	-79 55 02	15.1	3.1	DN?	
05287-5857	05 28 44.8	-58 57 01	14.3->18	2.57:	NL	
#05340-5803 (TW Pic)	05 34 03.4	-58 03 33		6.5:[d]	NL	
05301-4626	05 30 11.4	-46 26 13			NL	
05565-5935	05 56 32.8	-59 35 40	14.2	3.4	NL	240
#06169-8148 (H0551-819)	06 16 54.3	-81 48 23		3.34[e]	NL	
#10174-0826 (RW Sex)	10 17 27.2	-08 26 50		5.93[c]	NL	150[a]
10560-2902	10 56 03.8	-29 02 57	14.0		NL	
10565-2858	10 56 32.6	-28 58 35	14.9-16.3	8.0 or 12.0	DN?	
10566-3120	10 56 36.2	-31 20 29	17.9		CV	
10578-2935	10 57 53.7	-29 35 52	15.6	2.8:	NL?	
11588-3142	11 58 50.6	-31 42 44	13.1		NL	
#12497-2858 (EX Hya)	12 49 42.3	-28 58 38		1.63[a]	NL	125[a]
#13290-2925 (1329-294)	13 29 05.5	-29 25 34		1.795[d]	DN	
19314-5915	19 31 26.3	-59 15 00	14.1	4.75	NL	600[b]
#19442-4207 (V3885 Sgr)	19 44 12.7	-42 07 54		4.94[c]	NL	130[a]
20335-4332	20 33 31.5	-43 32 59	14.9-15.9		DN?	
23128-3105	23 12 50.0	-31 05 09	16.6	1.40	DN	
#23262-3003 (VY Scl)	23 26 21.2	-30 03 19		3.99:[c]	NL	
#23475-2639 (VZ Scl)	23 47 33.8	-26 39 34		3.47[c]	NL	250[a]
23593-6724	23 59 21.7	-67 24 28	14.3	1.99:	DN	

previously known system; DN: dwarf novae; NL: Nova-like variables. references: (a) Patterson (1984); (b) Buckley et al. (1992); (c) Warner (1987); (d) Warner (1994) and references therein; (e) Buckley et al. (1993).

§3.3 External Completeness

As mentioned in Chapter 2 (§2.5.5), blue object selection for forty-six percent of the survey area is complete. The present EC catalogue comprising objects brighter than B~18th mag was cross-correlated with Ritter's (1990) cataclysmic variables catalogue to estimate the survey's completeness for CVs. Ten known CVs in the completed fields of the EC survey were found and two CVs, TX Col and V4140 Sgr, were missed. This leads to an estimate of the external completeness of 83%, consistent with the external completeness of the EC white dwarfs (O'Donoghue et al. 1993). The sample used to estimate the completeness is small. Thus, this result should be viewed with caution. The causes of incompleteness were investigated and the results are that TX Col was missed due to the pairing and V4140 Sgr was not detected, probably, due to photographic photometry-error, because of its faint brightness ($U \geq 17$: Baptista et al. 1989) close to the limiting magnitude ($17 < U < 18$) of the U plate.

§3.4 Local Space Density of CVs from the EC Survey

Patterson (1984) has shown that the observed space density of CN is much lower than the value deduced from nova theory (Bath and Shaviv 1978) and the observed eruption frequency of novae in M31. The hibernation hypothesis (see section 3.1.3.2) was then proposed by Shara et al. (1986) to explain the above discrepancy. Thus, the space density is a crucial parameter for understanding the long-term evolution and interrelation of the subclasses of CVs.

In order to estimate the space density of CVs detected in the survey, the $1/V_{max}$ method (Schmidt 1968; Green 1980) was used: first, the limiting magnitude to which the survey is complete must be determined in order to obtain the maximum volume, V_{max}, defined by the maximum distance at which the object would still appear in the magnitude-limited sample. The V/V_{max} method (Schmidt 1968) is a powerful test of the completeness limit. If V is the

volume defined by the observed distance to an object, then the average of V/V_{max} values for a complete sample would be 0.5 with an uncertainty of $(12n)^{-1/2}$ (Green 1980), assuming a uniform distribution for n objects. Because the number of EC CVs is small, the limiting magnitude for the DA white dwarfs in the EC survey (O'Donoghue et al. 1993) was adopted. A statistically complete sample of 17 CVs (Table II), including 14 NLs and 3 DN, to a limiting magnitude of B_{lim}=16.4 (quoted from O'Donoghue et al. 1993) was selected from ~2000 square degrees (which covers all the NGP fields and some fields in the SGP region). Because the majority of CVs have a colour around B-V=0.0, the limiting magnitude in B can be approximately converted to $m_{v,lim}$=16.4. For the objects located in those fields for which photometry and spectroscopy are not yet complete to B=16.5, the faintest brightnesses measured in the fields are listed for the corresponding objects in Table II. The V and V_{max} for each CV were then calculated. The (maximum) distance can be obtained from the distance modulus: $m_v - M_v = 5 \cdot \log(d) - 5$, where d is in pc and the mean absolute magnitude M_v is 4.1 for NLs (Warner 1994) and 8.4 for DN (Warner 1987). However, CVs are not uniformly distributed in space, because of the concentration of stars to the Galactic plane. To correct for the nonuniform distribution, a z-distance weighting factor $\exp(-z/z_0)$ (Schmidt 1968) was applied to calculate the volume:

$$V' = \int_0^z \exp(-z/z_0) \cdot dV \quad , \text{ where z is the height above the Galactic plane}$$

and z_0 is the Galactic scale height of CVs. The unit volume $dV = 4\pi \cdot z^2 \cdot dz/(\sin b)^3$, where b is galactic latitude. Thus, the above integral yields

$$V' = (4\pi/3) \cdot (z/\sin b)^3 \cdot \{6(z_0/z)^3 \cdot [1-\exp(-z/z_0)] - 6(z_0/z)^2 \cdot \exp(-z/z_0) - 3(z_0/z) \cdot \exp(-z/z_0)\} .$$

Because $d=z/\sin b$ and $V=(4\pi/3) \cdot d^3$,

$$V' = V \cdot \{6(z_0/z)^3 \cdot [1-\exp(-z/z_0)] - 6(z_0/z)^2 \cdot \exp(-z/z_0) - 3(z_0/z) \cdot \exp(-z/z_0)\}.$$

As mentioned above, complete samples were selected from ~2000 square degrees which is corresponding to 4.8% of the whole sky (41253 square degrees). Therefore, the above equation should be modified as

$$V' = 0.048 \cdot V \cdot \{6(z_0/z)^3 \cdot [1-\exp(-z/z_0)] - 6(z_0/z)^2 \cdot \exp(-z/z_0) - 3(z_0/z) \cdot \exp(-z/z_0)\}.$$

Note that the distances of the EC CVs are not well determined, thus the scale height can not be derived from the sample. Three values of the scale height z_0 were used (100, 150, and 200 pc) in order to investigate the dependence of the space density on the scale height. The observed local space density is then $\rho = \Sigma\ 1/V_{max}$. The results show that ρ is sensitive to z_0: an increase in z_0 will result in a decrease in ρ (see Table II). Table II lists the galactic coordinates, m_v, $1/V_{max}$, $m_{v,lim}$, ρ, and $\langle V/V_{max} \rangle$. The ρ for z_0=100

Table II. Complete Sample of CVs from the EC survey

Object	*l*	*b*	m_v	$1/V_{max}$ ($\times 10^{-7}$ pc^{-3})			$m_{v,lim}$
				z_0=100	150	200 pc	
Nova-like variables:							
04224-2014	216.7	-41.0	11.5	2.3	0.69	0.29	
05287-5857	267.5	-33.5	14.3	1.4	0.41	0.18	15.8
05340-5803	266.4	-32.8	14.1	1.3	0.39	0.17	15.8
05565-5935	268.3	-29.9	14.2	1.0	0.31	0.14	15.8
06169-8148	293.8	-28.2	13.5	0.87	0.26	0.11	
10174-0826	251.8	38.7	10.5	2.0	0.59	0.25	
10560-2902	275.2	27.4	14.3	0.8	0.24	0.1	
10578-2935	275.9	27.1	15.9	0.78	0.23	0.1	
11588-3142	290.7	29.7	13.1	1.0	0.30	0.13	
12497-2858	303.2	33.6	13.5	1.4	0.41	0.18	
19314-5915	337.9	-28.6	13.7	0.9	0.27	0.12	
19442-4207	357.5	-27.8	9.6	0.83	0.25	0.11	
23262-3003	19.8	-71.7	12.9	7.0	2.1	0.88	
23475-2639	32.6	-76.3	15.6	7.5	2.2	0.94	
ρ(NLs)				29.0	8.7	3.7	
$\langle V/V_{max} \rangle$ (±0.08)				0.53	0.38	0.28	
Dwarf Nova:							
05114-7955	292.3	-31.2	15.0	3.3	2.1	1.7	
10565-2858	275.3	27.5	16.0	2.9	1.9	1.5	
20335-4332	357.5	-36.9	15.4	5.5	3.5	2.8	16.0
ρ(DN)				12.0	7.5	6.0	
$\langle V/V_{max} \rangle$ (±0.17)				0.53	0.48	0.45	

pc compared with the values in Warner (1994) is rather high, so this scale height may be too small. Patterson (1984) determined the scale height for CVs

to be 150 pc and Warner (1994) derived the scale height for U Gem and SU UMa stars to be 103 and 176 pc respectively. Thus, the ρ derived for z_0=150 pc is likely to yield the best value of the space density of the EC CVs. The local space density of DN is roughly equal to the value in Table 9.4 of Warner (1994) and that of NLs is slightly lower than Warner's (1994) results, 1.6×10^{-6} pc^{-3}.

If the sum of the space densities of the EC NLs and DN (1.6×10^{-6} pc^{-3}) is used to represent the space density of the EC CVs, then the observed space density is much lower than the predicted space density ~$1\text{-}4\times10^{-5}$ pc^{-3} (Warner 1994), obtained from the theoretical work of De Kool (1992) who used a Monte Carlo technique to derive a CV birth rate of $0.5\text{-}2.0\times10^{-14}$ $pc^{-3}yr^{-1}$. Over the age of our Galaxy, this yields ~$0.5\text{-}2.0\times10^{-4}$ pc^{-3} and ~80% of them have evolved beyond the orbital period minimum (Ritter and Burkert 1986), becoming unrecognisable as CVs. Hertz et al. (1990) have derived a lower limit on the space density for X-ray-selected, faint CVs, $2\text{-}3\times10^{-5}$ pc^{-3}, which is consistent with the predicted value. They also suggested that a large number of low $\dot{M}$ CVs, which release the majority of their accretion energy as X-rays and therefore will be invisible in UV surveys, have not been found. Thus, the space density of CVs may be grossly underestimated. Identification of more low $\dot{M}$ CVs in company with those found in UV and X-ray sky surveys is needed to test the evolution theory of CVs just mentioned.

Appendix: General Description of the New EC CVs

Object	Spectral features	Details
EC04030-5801:	narrow Balmer emission lines at quiescence	Ch6
EC04224-2014:	shallow, broad Balmer lines and HeI λ4471Å in absorption	Ch7
EC05114-7955:	broad, double-peaked Balmer lines in emission	CH8
EC05287-5857:	Balmer lines, weak HeI λ4471Å and HeII λ4686Å in emission	Ch9
EC05301-4626:	a polar, were discovered by both the Edinburgh-Cape and ROSAT surveys. This object will not be discussed in this thesis.	
EC05565-5935:	shallow broad absorption or very weak emission spectrum	Ch7
EC10560-2902:	strong, broad Balmer emission lines with weak absorption in the wings. The CIII/NIII λ4650Å blend was present in emission as well as HeII λ4686Å.	Ch7
EC10565-2858:	broad, double-peaked emission lines	Ch10
EC10566-3120:	very weak Balmer emission lines. Because of its faint brightness ~18th Bmag, no follow-up observations were made.	
EC10578-2935:	Balmer lines, CIII/NIII λ4650Å blend, HeII λ4686Å in emission and unusual emission line CaI λ4227Å.	Ch10
EC11588-3142:	shallow broad Balmer lines, HeI λ4471Å, and HeII λ4686Å in absorption with an emission core.	Ch7
EC19314-5914:	a bright ecliping nova-like variable, showed eclipses and has an orbital period 4.75 hrs. Its spectra shows weak Balmer, HeII λ4686 Å in emission and HeI λ4771 Å, metallic lines in absorption (Buckley et al. 1992).	
EC20335-4332:	weak Balmer lines, HeI, and HeII λ4686Å in emission	Ch8
EC23128-3105:	broad, double-peaked Balmer, HeI λ4471Å, and weak HeII λ4686Å in emission	Ch6
EC23593-6724:	strong, narrow Balmer lines, weaker HeI and HeII λ4686Å in emission	Ch6

References:

Baptista, R., Jablonski, F.J., Steiner, J.E. (1989). *Mon. Not. R. astr. Soc.*, **241**, 631.

Barbon, R., Mammano, A., and Rosino, L. (1968). in L. Detre (ed.), *I.A.U. Colloq. No. 4, Non Periodic Phenomena in Variable Stars*, Reidel, Dordrecht, 257.

Bath, G.T., and Shaviv, G. (1978). *Mon. Not. R. astr. Soc.*, **183**, 515.

Bath, G.T., and Pringle, J.E. (1982). *Mon. Not. R. astr. Soc.*, **199**, 267.

Bond, H.E. (1980). *IAU Circ. No.* 3480.

Bond, H.E. (1985). in D.Q. Lamb and J. Patterson (eds.), *Cataclysmic Variables and Low-Mass X-Ray Binaries*, D. Reidel Publishing Company, p15.

Bond, H.E., and Grauer, A.D. (1987). in A.G. Davis Philip, D.S. Hayes, and J.W. Liebert (eds.), IAU Colloqium No. **95**, *The Second Conference on Faint Blue Stars*, L. Davis press, p221.

Buckley, D.A.H., O'Donoghue, D., Kilkenny, D., Stobie, R.S., and Remillard, R.A. (1992). *Mon. Not. R. astr. Soc.*, **258**, 285.

Buckley, D.A.H., Remillard, R.A., Tuohy, I.R., Warner, B., and Sullivan, D.J. (1993). *Mon. Not. R. astr. Soc.*, **265**, 926.

Cannizzo, J.K., and Kaitchuck, R.H. (1992). *Scientific American*, **266**, No.1, 42.

Copeland, H., Jensen, J.O., and Jorgensen, H.E. (1970). *Astron. Astrophys.*, **5**, 12.

Cropper, M. (1990). *Space Science Reviews*, **54**, 195.

D'Antona, F., and Mazzitelli, I. (1982). *Astron. Astrophys.*, **113**, 303.

Drilling, J.S. (1985). *Astrophys. J. Lett.*, **294**, L113.

Faulkner, J. (1971). *Astrophys. J. Lett.*, **170**, L99.

Faulkner, J., Flannery, B.P., and Warner, B. (1972). *Astrophys. J. Lett.*, **175**, L79.

Frank, J., King, A.R., Sherrington, M.R., Jameson, R.F., and Axon, D.J. (1981). *Mon. Not. R. astr. Soc.*, **195**, 505.

Grauer, A.D., and Bond H.E. (1983). *Astrophys. J.*, **271**, 259.

Green, R.F. (1980). *Astrophys. J.*, **238**, 685.

Green, R.F., Richstone, D.O., and Schmidt, M. (1978). *Astrophys. J.*, **224**, 892.

Green, R.F., Liebert, J., and Wesemael, F. (1984). *Astrophys. J.*, **280**, 177.

Grossman, A.S., Hays, D., and Graboske, H.C., Jr. (1974). *Astron. Astrophys.*, **30**, 95

Hertz, P, Bailyn, C.D., Grindlay, J.E., Garcia, M.R., Cohn, H., and Lugger, P.M. (1990). *Astrophys. J.*, **364**, 251.

Howell, S.B., and Szkody, P. (1990). *Astrophys. J.*, **356**, 623.

Howell, S.B. (1993). in O. Regev and G. Shaviv (eds.), *Cataclysmic variables and Related Physics*, p67.

Kovetz, A., Prialnik, D., and Shara, M.M. (1988). *Astrophys. J.*, **325**, 828.

Kraft, R.P. (1958). *Astrophys. J.*, **127**, 625.

Kraft, R.P., Mathews, J., Greenstein, J.L. (1962). *Astrophys. J.*, **136**, 312.

O'Donoghue, D., Chen, A., Kilkenny, D., and Stobie, R.S., in *Proceedings of the 8th European Workshop on White Dwarfs*, ed. M. Barstow, NATO Advanced Study Institute Series, Kluwer, 1993, p39.

O'Donoghue, D., Warner B., Wargau, W., and Grauer, A.D. (1988). *Mon. Not. R. astr. Soc.*, **240**, 41.

Paczynski, B. (1967). *Acta Astr.*, **17**, 287.

Paczynski, B. (1985). in D.Q. Lamb and J. Patterson (eds.), *Cataclysmic Variables and Low-Mass X-Ray Binaries*, D. Reidel Publishing Company, p1.

Paczynski, B. and Sienkiewicz, R. (1981). *Astrophys. J. Lett.*, **248**, L27.

Patterson, J. (1984). *Astrophys. J. Suppl.*, **54**, 443.

Rappaport, S., Joss, P.C., Webbink, R.F., (1982). *Astrophys. J.*, **254**, 616.

Rappaport, S., Verbunt, F., Joss, P.C. (1983). *Astrophys. J.*, **275**, 713.

Ritter, H. (1986a). *Astron. Astrophys.*, **169**, 139.

Ritter, H. (1986b). in J. Truemper et al. (eds.), *The Evolution of Galactic X-Ray Binaries*, D. Reidel Publishing Company, p271.

Ritter, H., and Burkert, A. (1986). *Astron. Astrophys.*, **158**, 161.

Ritter, H. (1990). *Astron. Astrophys. Suppl.*, **85**, 1179.

Robinson, E.L. (1976). *Ann. Rev. Astron. Astrophys.*, **14**, 119.

Schmidt, M. (1968). *Astrophys. J.*, **151**, 393.

Shara, M.M., Moffat, A.F.J., and Webbink, R.N. (1985). *Astrophys. J.*, **294**, 271.

Shara, M.M., Livio, M, Moffat, A.F.J., and Orio, M. (1986). *Astrophys. J.*, **311**, 163.

Schaefer, B.E., and Patterson, J. (1983). *Astrophys. J.*, **268**, 710.

Szkody, P., and Howell, S.B. (1992). *Astrophys. J. Suppl.*, **78**, 537.

Verbunt, F., and Zwaan, C. (1981). *Astron. Astrophys.*, **100**, 7.

Vogt, N. (1974). *Astron. Astrophys.*, **36**, 369.

Vogt, N. (1989). in M.F. Bode and A. Evans (eds.), *Classical Novae*, John Wiley and Sons Ltd, Ch12, p225.

Wade, R.A., and Ward, M.J. (1985). in *Interacting Binary Stars*, p129, ed. J.E. Pringle and R.A. Wade, Cambridge University Press.

Warner, B. (1983). in M. Livio and G. Shaviv (eds.), *Cataclysmic Variables and Related Objects*, D. Reidel Publishing Company, p155.

Warner, B. (1985). in D.Q. Lamb and J. Patterson (eds.), *Cataclysmic Variables and Low Mass X-Ray Binaries*, D. Reidel Publishing Company, p269.

Warner, B. (1986a). *Mon. Not. R. astr. Soc.*, **219**, 347.

Warner, B. (1986b). *Mon. Not. R. astr. Soc.*, **219**, 751.

Warner, B. (1987). *Mon. Not. R. astr. Soc.*, **227**, 23.

Warner, B. (1994). *Cataclysmic Variable Stars*, Cambridge University Press, in press.

Wyckoff, S., and Wehinger, P.A. (1977). in R. Kippenhahn, J. Rahe, and W. Strohmeier (eds.), IAU Colloq. No. 42, *The Interaction of Variable Stars with Their Environment*, p201.

Chapter 4: *Observations and Data Reductions*

All the follow-up observations on the Edinburgh-Cape CVs were made during 1991-1993 at the Sutherland site of the South African Astronomical Observatory (SAAO). For this work, the 0.75-m and 1.0-m reflectors were used to do high speed photometry (HSP) and UBV photometry, and the 1.88-m was used to do spectroscopy and infrared photometry.

The techniques of observations and data reduction used in this work are described in the following sections (except the UBV photometry and low-resolution spectroscopy which have been described in section 2.1.3): high speed photometry in section 4.1, infrared photometry in section 4.2, time-resolved spectroscopy in section 4.3, and the extensively used cross-correlation technique in section 4.4.

§4.1 High Speed photometry

The HSP observations were made with the University of Cape Town photometer (UCTP) or the St. Andrews photometer (STAP) both of which are aperture photometers with offset guiding capability so that guiding corrections do not interrupt the program star measurements. Each HSP-run was obtained with 10-sec integrations in "white light" (no filter used). Thus the effective wavelength and bandpass of the system was determined by the detector which was always a blue-sensitive, S-11, photomultiplier tube. Such devices are only sensitive over the standard UBV bandpasses. Thus, bearing in mind that CVs are ultraviolet-rich stars, the 'white light' measurements may be thought of as corresponding to a 'broad B' magnitude, B_w i.e. with effective wavelength similar to that of Johnson B but with a much broader bandpass. Because of the faintness of the program stars, small apertures were used, ranging from 11 arcsec diameter in good seeing to 34 arcsec when the seeing was poor.

Sky background measurements were obtained at least every half an hour and more frequently in substantial moonlight by observing a nearby patch of sky for 30-60 seconds. The data reduction was performed using a cubic spline to interpolate the sky background values, thus subtracting the sky background from the star measurements on a point-by-point basis. A mean extinction coefficient, κ, was used to correct for atmospheric extinction using the formula $I = I_0 \cdot 10^{0.4 \cdot \kappa \cdot \sec z}$ where z is the zenith distance. The HSP-runs were reduced to zero mean and normalized by the mean intensity of the star during the run. In order to obtain the corresponding B_w for each run, blue E-region standard stars were observed to obtain a crude zero-point. Thus the approximate B_w-magnitude is obtained simply using $B_w = ZP - 2.5 \cdot \log(I_w)$, where ZP and I_w are the B_w zero-point and mean intensity in "white light" respectively. This magnitude system is certainly crude, taking no account of many of the techniques of standard photometry. However, its purpose is to enable rough estimates to be made of the brightness of a given star and allow a long-term light curve to be constructed. Experience of this approach accumulated by other members of the UCT Astronomy Department shows that systematic errors are less than 0.1 mag.

§4.2 Infrared JHK Photometry

JHK measurements were made using the Mk III photometer with the F50 chopping secondary on the 1.88-m reflector of the SAAO on 1993 March 16/17. The 1.88-m infrared photometer requires both 'chopping' and 'nodding'. A first estimate of the signal from the star is obtained by chopping: two nearby patches of sky, one of which contains the object, are alternatively measured through two apertures by the detector at a chopping frequency of 12.5 Hz (Glass 1983). In the ideal case, where the background in the two patches of sky are identical, the pure signal from the source can be obtained by subtracting one signal from the other. However, the background is not uniform and contains a gradient. To overcome this problem, the telescope is moved so that the object is placed in the other aperture. This beam-switching

is called nodding and repeated every 10 seconds. Thus, the background gradient between the two patches of sky is cancelled out. Automatic telescope nodding is available on the 1.88-m reflector and controlled by the hardware in the CAMAC crate (Glass 1983; Whitelock 1988) which drives the telescope back and forth along the N-S direction with a separation of up to 36-arcsecs between the two nodding positions. The observing procedure used modules comprising four 10-sec integrations on the same filter. The module was repeated five times to achieve an error of less than 0.02 mag. IR standard stars (Carter 1990) were observed to calculate the zero points. The data were reduced using standard atmospheric extinction coefficients, J=0.1, H=0.06, and K=0.1 (Whitelock 1988).

§4.3 Time-Resolved Spectroscopy

Time-resolved spectroscopy (TRS), continuously monitoring the spectral variation of a program star, was carried out with the same instrument used for the general survey spectroscopy (see section 2.1.3). The spectra were obtained using grating #8 which provides a dispersion of 75 Å/mm and a resolution of 3 Å (FWHM). Integration times of 600-900 seconds were used for program stars brighter than 15th Bmag; grating #6 (100 Å/mm, 4Å resolution) was used for the objects fainter than 15th Bmag. In order to obtain accurate radial velocities, the object was detected using only one array of the Reticon detector and sky spectrum was simultaneously obtained with the other array. A Cu/Ar arc spectrum was taken about every 20-25 minutes to minimize possible systematic wavelength shifts. The reduction techniques used for TRS were the same as for the general survey spectroscopy discussed in section 2.1.3 except that the resulting spectra were not converted to flux units.

§4.4 Cross-Correlation Technique

Relative radial velocities were measured using the cross-correlation technique of Tonry & Davis (1979). First, a template was constructed;

usually, this was made by simply summing all the spectra of a given series of time-resolved spectra. This template was then rebinned onto a logarithmic scale (so that radial velocity shifts will result in a constant displacement across the spectrum). The continuum and any residual large-scale variations were then removed by polynomial fitting and high-pass digital filtering. Each individual spectrum of the series was processed in the same way as the template, and its relative radial velocities was determined from the shift required to bring the spectrum into register with the template spectrum. Finally, the relative radial velocity could be transformed onto an absolute scale by correcting for the heliocentric velocity of the template.

References:

Carter, B.(1990). *Mon. Not. R. astr. Soc.*, **242**, 1.

Menzies, J.W., Cousins, A.W.J., Banfield, R.M., and Laing, J.D.(1989). S. Afr. astr. Obs. Circ., **13**, 1.

Glass, I.S. (1983). *MK III I.R.P. Instruction Manual*, SAAO.

Tonry, J., and Davis, M. (1979). *Astron. J.*, **84**, 1511.

Whitelock, P.A. (1988). *Infrared Photometry Manual*, SAAO.

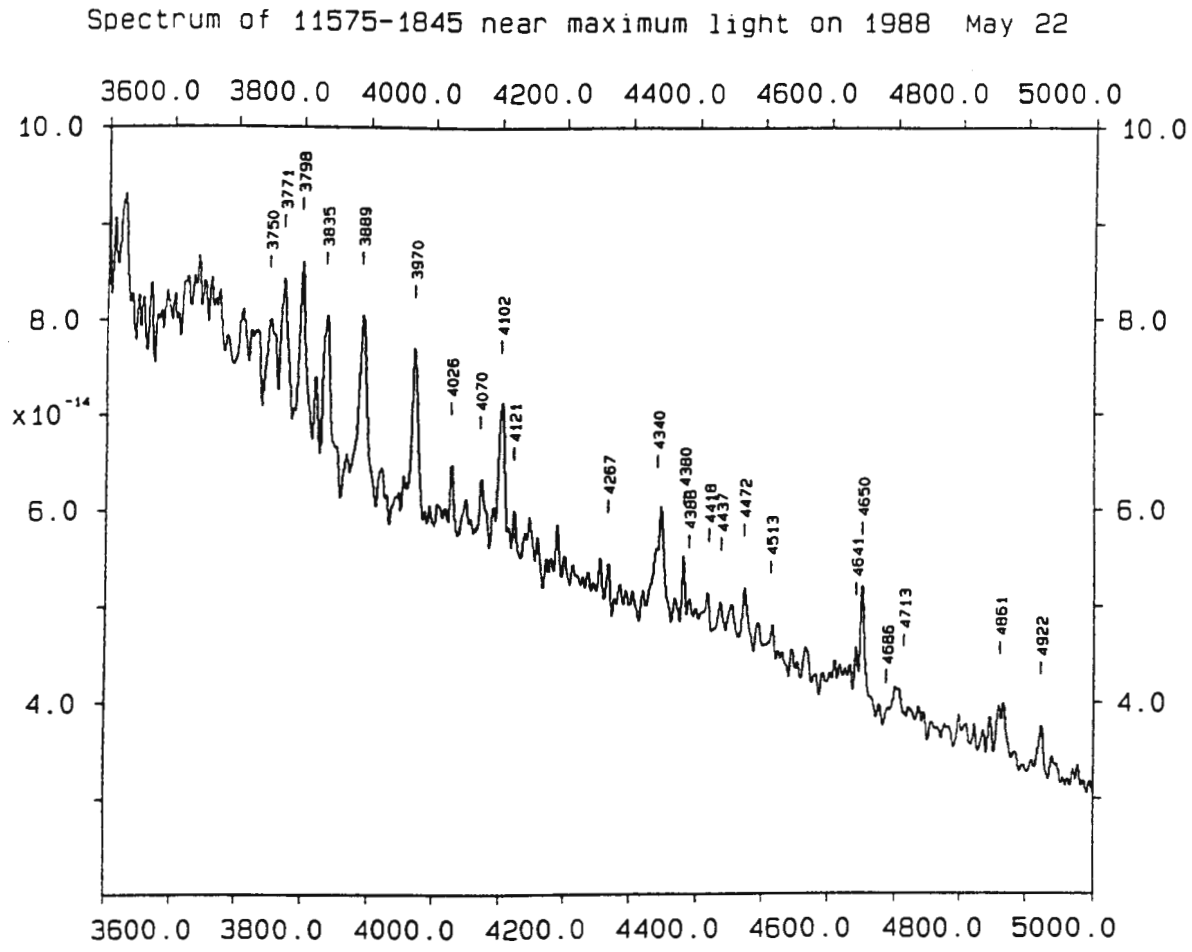

Figure 1. Spectrum taken near maximum light on 1988 May 22. Detailed discussion of the spectral features appears in section 5.3.1 and 5.5.1.

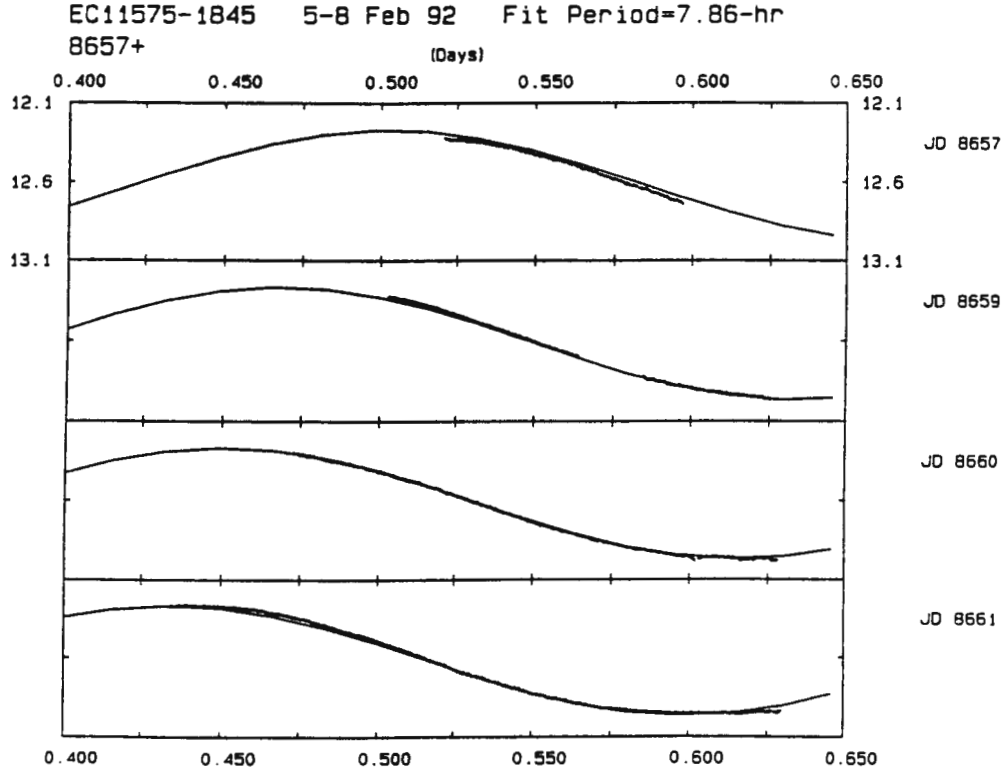

Figure 2. Light curves in "white light" obtained during 1992 February 5-8. The solid lines are a least squares fit of the orbital period 7.86-hr derived in section 5.2.2.

Chapter 5: *EC11575-1845 - A New Close Binary with Large Reflection Effect*

§5.1 Introduction

EC11575-1845 was spectroscopically observed on 1987 February 9 and 1988 May 22 for the purposes of classification. The spectra (e.g. Figure 1) showed the CIII/NIII blend and broad Balmer lines in emission. Interestingly, HeII λ4686Å is not seen. Even so, this object was regarded as a cataclysmic variable (CV) until the first run of high-speed photometry (hereafter HSP) was obtained in "white light" (no filter used). This first HSP-run (top panel of Figure 2) revealed a very smooth decline of 0.43 mag over 1.86 hrs. This photometric behaviour, in particular the absence of flickering, doesn't resemble the light curves of CVs. Therefore intensive time-resolved spectroscopy, UBV(RI)$_c$ (hereafter UBVRI) and high-speed photometry were obtained during 1992 February-May to study the photometric and the spectroscopic variations. Infrared (JHK) photometry was also obtained on 1993 March 16/17. The photometric results showed that EC11575-1845 is a non-eclipsing close binary system with a period of 7.86-hr, deduced from the reflection effect. The spectroscopic results revealed the CIII/NIII λ4650Å blend and the Balmer lines in emission near maximum light, and HeII λ4686Å and the Balmer lines in absorption at minimum light. The spectrum at minimum light is that of an sdO star. This behaviour can be explained by a system consisting of an sdO primary and a cool secondary whose atmosphere is illuminated by the primary and produces the photometric and emission/absorption line variations.

An upper limit on the mass ratio of the system is about 0.33, derived from the ratio of the semi-amplitudes of the radial velocity curves. Napier's (1968) model was used to construct the monochromatic light curves and to constrain the masses, radii, inclination and the effective temperature of the primary.

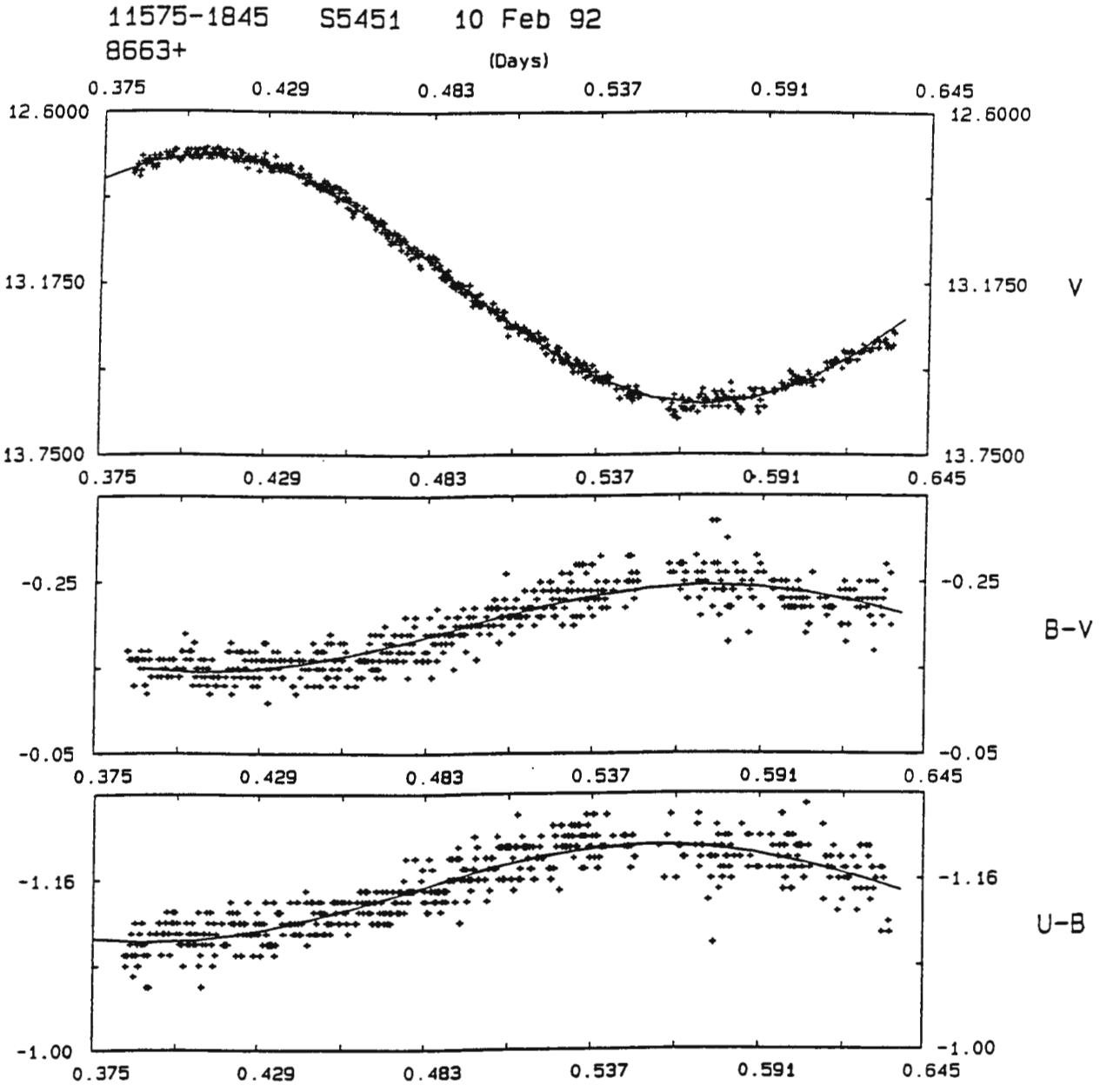

Figure 3. UBV light curves obtained on 1992 February 10.

§5.2 Photometric Characteristics

§5.2.1 High Speed Photometry

The HSP observations (see Table I) were made during 1992 February 5-10. The "white light" data were obtained with 10-sec integrations. The sequential UBV HSP-run S5451 had an effective sampling time of 33 seconds: 10-sec integrations in each of Johnson U, B, and V filters with 1-sec "dead" time in between. For run S5451, the E-region standard star E303, whose magnitude and colours are V=7.562, B-V=-0.030, and U-B=-0.063, was observed to measure the zero-points in the UBV system. Thus, the UBV data of run S5451 were converted to instrumental magnitudes and plotted in Figure 3, which shows that the light and colour indices vary almost sinusoidally. The colours are reddest at maximum light.

Table I. Observing Log of High Speed Photometry

Run No.	UT Date	Start HJD 2440000.+	Duration (hrs)	Bandpass
S5440	050292	8657.51993	1.8	white light
S5442	060292	8659.50196	2.9	"
S5445	070292	8660.47241	3.7	"
S5447	080292	8661.43336	4.7	"
S5451	100292	8663.38192	6.0	UBV

§5.2.2 Multicolour UBV(RI)$_c$ Photometry

Multicolour UBVRI photometry was obtained during 1992 February-May. The A0 star HD104640 (V=10.092, B-V=0.308, U-B=0.093, V-R=0.184, V-I=0.366) was chosen to be the comparison to check the stability of the sky every 10-15 minutes. E-region standards were observed about every hour to determine the colour equations (for details of photometry reduction see section 2.1.3). The results are tabulated in Table II; the third column specifies the telescope that was used. The UBVRI light curves show the same behaviour as the HSP but give more accurate estimates of amplitudes and the orbital period; the amplitudes of the brightness variations are 0.646±0.003 mag in U, 0.736±0.002 mag in B, 0.846±0.002 mag in V, 0.932±0.004 mag in R, 1.02±0.01 mag in I. Table III shows the range of the V magnitude and colours. An amplitude

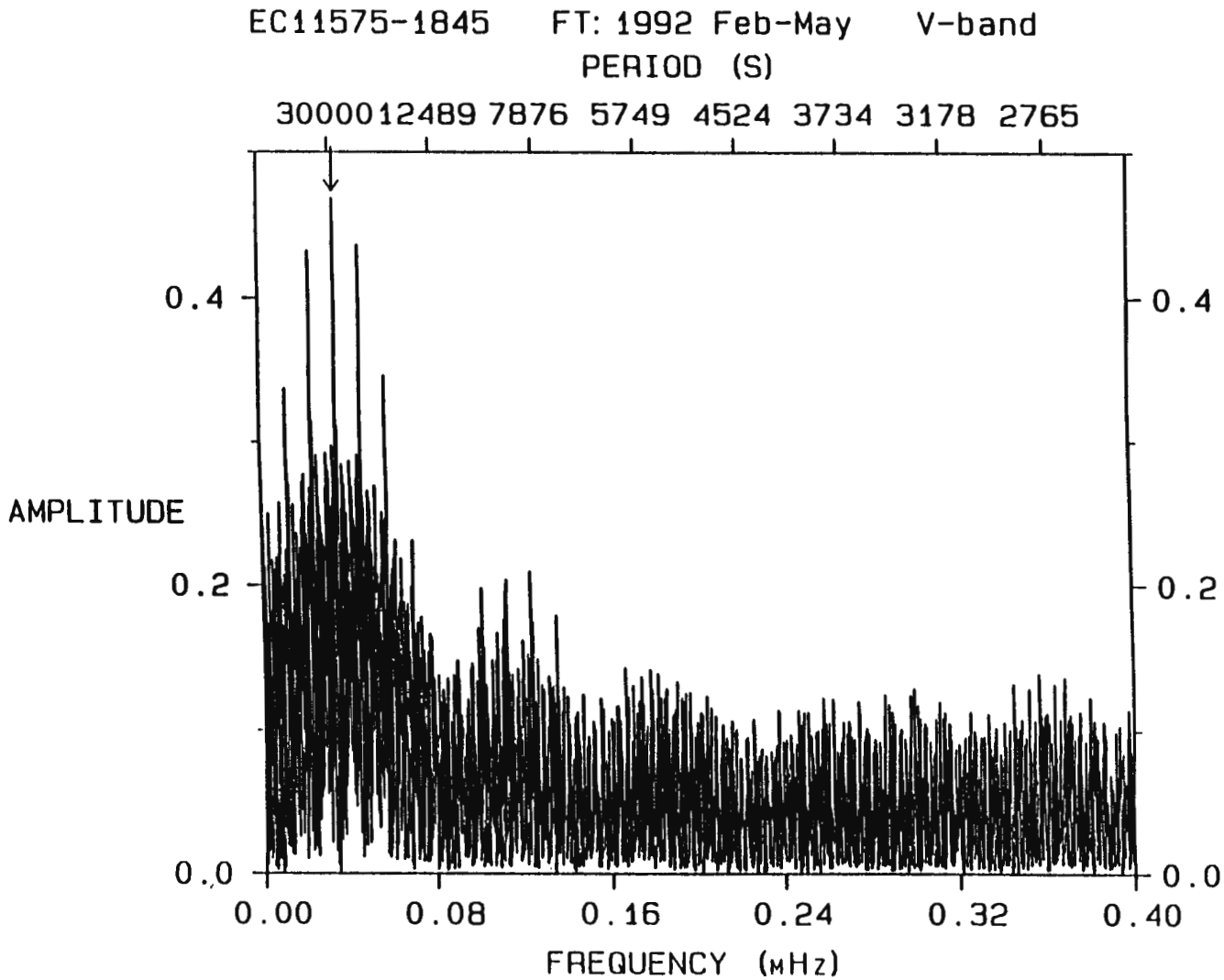

Figure 4. Fourier amplitude spectrum calculated for the V data collected during 1992 February-May.

spectrum (Deeming 1975) was calculated for the V data and is shown in Figure 4. The three highest peaks (at 0.02374, 0.035328 and 0.04692 mHz) are of similar amplitude. From the longest HSP-run S5451 (Figure 3), which lasted for ~6 hrs and showed more than half of a cycle, the orbital period must be longer than 6 hrs and much shorter than 12 hrs. Thus the frequencies 0.04692 mHz (5.9 hrs) and 0.02374 mHz (11.7 hrs) can be excluded. The highest peak (0.035328 mHz) arrowed in Figure 4 is then the correct period (7.86-hr). In order to derive an ephemeris corresponding to minimum brightness, a sinusoid of period 7.86-hr was fitted to the data by least-squares and gave

$$T_{min}(HJD) = \underset{\pm 0.0003}{2448661.6049} + \underset{\pm 0.00003}{0^d.32762}\ E \ .$$

From the above least-squares fit, the standard deviations of the residuals for the UBVRI measurements are 0.02 mag in U, 0.02 mag in B, 0.02 mag in V, 0.03 mag in R, and 0.09 mag in I.

Table II. UBVRI photometry of EC11575-1845

HJD 2440000.+	Phase	Tel (m)	V	B-V	U-B	V-R	V-I
8661.60520	0.00	0.5	13.53	-0.26	-1.21	-0.15	-0.29
8662.56070	0.91	0.5	13.51	-0.27	-1.23	-0.09	-0.16
8663.49240	0.76	0.5	13.16	-0.19	-1.16	-0.08	-0.17
8663.49780	0.77	0.5	13.22	-0.21	-1.16	-0.05	-0.18
8665.55930	0.07	0.5	13.49	-0.28	-1.19	-0.09	-0.21
8665.56870	0.09	0.5	13.48	-0.28	-1.21	-0.10	-0.15
8666.50310	0.95	0.5	13.52	-0.28	-1.21	-0.13	-0.24
8666.51410	0.98	0.5	13.52	-0.27	-1.22	-0.09	-0.10
8671.58280	0.45	0.5	12.74	-0.16	-1.13	-0.11	-0.07
8671.58800	0.47	0.5	12.68	-0.13	-1.11	-0.06	0.14
8675.53810	0.52	0.5	12.69	-0.19	-1.10	-0.02	0.04
8675.54350	0.54	0.5	12.71	-0.18	-1.11	0.01	0.13
8681.44680	0.56	0.5	12.72	-0.16	-1.13	0.00	0.07
8681.45380	0.58	0.5	12.76	-0.17	-1.13	-0.02	-0.02
8682.47450	0.70	0.5	13.01	-0.21	-1.15	-0.03	0.03
8682.48140	0.72	0.5	13.08	-0.22	-1.15	-0.02	0.02
8684.54560	0.02	0.5	13.54	-0.27	-1.22	-0.07	-0.22
8684.55250	0.04	0.5	13.52	-0.27	-1.22	-0.10	-0.21
8706.42170	0.79	0.5	13.27	-0.24	-1.19	-0.05	-0.06
8706.42720	0.81	0.5	13.29	-0.21	-1.20	-0.07	-0.14
8713.38740	0.06	0.5	13.52	-0.27	-1.21	-0.09	-0.22
8713.39390	0.08	0.5	13.52	-0.29	-1.21	-0.08	-0.21
8714.30760	0.86	0.5	13.42	-0.26	-1.19	-0.04	-0.08
8714.32060	0.90	0.5	13.49	-0.28	-1.20	-0.05	-0.09
8714.47770	0.38	0.5	12.81	-0.16	-1.15	-0.01	-0.09
8714.48920	0.42	0.5	12.76	-0.18	-1.13	0.00	-0.02
8714.50100	0.45	0.5	12.72	-0.16	-1.13	-0.01	-0.02
8715.34160	0.02	0.5	13.53	-0.29	-1.20	-0.14	-0.17

HJD 2440000.+	Phase	Tel (m)	V	B-V	U-B	V-R	V-I
8715.36350	0.08	0.5	13.53	-0.27	-1.22	-0.13	-0.17
8715.47370	0.42	0.5	12.76	-0.14	-1.17	-0.02	-0.08
8715.49830	0.50	0.5	12.70	-0.17	-1.12	0.00	0.00
8715.51320	0.54	0.5	12.74	-0.19	-1.12	0.00	0.01
8716.38260	0.20	0.5	13.29	-0.23	-1.21	-0.05	-0.02
8716.39310	0.23	0.5	13.18	-0.20	-1.19	-0.02	0.00
8716.40420	0.26	0.5	13.10	-0.20	-1.17	-0.03	-0.08
8716.54890	0.70	0.5	13.03	-0.21	-1.12	-0.10	-0.21
8716.55740	0.73	0.5	13.13	-0.26	-1.12	-0.09	-0.44
8717.36740	0.20	0.5	13.25	-0.20	-1.21	-0.04	-0.02
8717.37790	0.23	0.5	13.17	-0.20	-1.20	-0.01	-0.04
8717.39080	0.27	0.5	13.05	-0.19	-1.17	0.00	-0.06
8717.45100	0.46	0.5	12.71	-0.16	-1.14	-0.01	-0.03
8717.46530	0.50	0.5	12.70	-0.16	-1.13	-0.02	-0.09
8717.47720	0.54	0.5	12.72	-0.17	-1.13	-0.02	-0.12
8719.38560	0.36	0.5	12.83	-0.15	-1.15	-0.01	0.01
8719.39750	0.40	0.5	12.78	-0.16	-1.13	-0.01	-0.01
8719.40920	0.43	0.5	12.74	-0.18	-1.13	-0.01	-0.04
8734.26970	0.79	0.5	13.24	-0.21	-1.16	-0.10	-0.18
8734.27510	0.81	0.5	13.28	-0.21	-1.18	-0.11	-0.38
8734.47900	0.43	0.5	12.78	-0.19	-1.15	0.04	0.01
8734.48430	0.45	0.5	12.71	-0.17	-1.14	0.04	0.06
8734.42030	0.25	1.0	13.13	-0.21	-1.16	-0.03	-0.02
8734.42744	0.27	1.0	13.07	-0.20	-1.16	-0.01	-0.03
8734.43477	0.30	1.0	13.01	-0.20	-1.15	-0.00	-0.02
8734.44663	0.33	1.0	12.91	-0.17	-1.16	-0.00	-0.02
8734.45325	0.35	1.0	12.88	-0.19	-1.13	-0.01	0.03
8734.46017	0.37	1.0	12.83	-0.17	-1.15	-0.01	-0.07
8734.47205	0.41	1.0	12.77	-0.16	-1.16	-0.00	-0.03
8734.47905	0.43	1.0	12.74	-0.19	-1.13	-0.01	-0.09
8734.48589	0.45	1.0	12.71	-0.17	-1.14	0.00	-0.01
8734.50228	0.50	1.0	12.70	-0.17	-1.13	-0.02	-0.02
8734.50899	0.52	1.0	12.70	-0.15	-1.12	-0.00	-0.00
8734.51581	0.54	1.0	12.74	-0.18	-1.15	-0.00	-0.00
8734.52918	0.59	1.0	12.82	-0.22	-1.17	-0.03	-0.07
8735.31056	0.97	1.0	13.55	-0.29	-1.22	-0.11	-0.22
8735.37167	0.16	1.0	13.40	-0.26	-1.18	-0.04	-0.14
8735.44610	0.38	1.0	12.80	-0.16	-1.15	-0.00	-0.01
8735.51523	0.59	1.0	12.77	-0.16	-1.11	-0.00	-0.01
8741.26820	0.15	0.5	13.36	-0.26	-1.18	-0.08	-0.03
8742.36570	0.50	0.5	12.69	-0.16	-1.13	0.03	0.14
8742.37290	0.53	0.5	12.72	-0.18	-1.12	-0.03	-0.09
8743.42290	0.73	0.5	13.12	-0.23	-1.14	-0.06	-0.18
8743.42980	0.75	0.5	13.16	-0.22	-1.17	-0.06	-0.06
8747.38680	0.83	0.5	13.36	-0.26	-1.18	-0.10	-0.08
8747.39380	0.85	0.5	13.40	-0.26	-1.18	-0.06	-0.17
8741.30558	0.27	1.0	13.05	-0.19	-1.15	-0.01	0.03
8741.35902	0.43	1.0	12.74	-0.18	-1.13	-0.01	0.00
8747.29777	0.56	0.75	12.72	-0.15	-1.17	0.00	-0.00
8747.30104	0.57	0.75	12.74	-0.15	-1.17	-0.00	-0.03
8747.30451	0.58	0.75	12.76	-0.16	-1.17	0.00	-0.04
8747.31139	0.60	0.75	12.78	-0.16	-1.16	-0.00	-0.01
8747.31431	0.61	0.75	12.80	-0.15	-1.17	-0.02	0.00
8747.31723	0.62	0.75	12.80	-0.14	-1.17	-0.03	-0.02

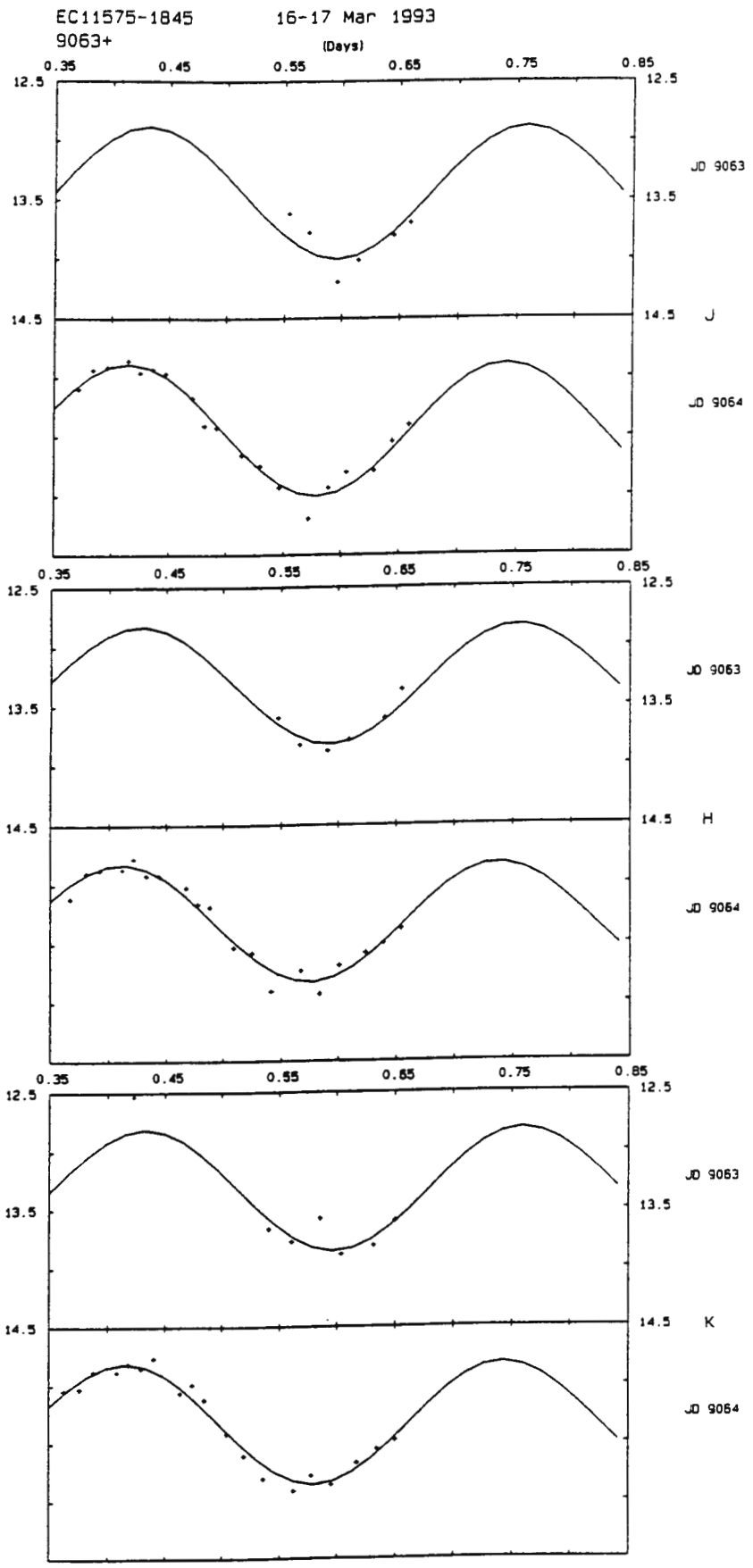

Figure 5. Infrared light curves in JHK obtained on 1993 March 16-17.

HJD 2440000.+	Phase	Tel (m)	V	B-V	U-B	V-R	V-I
8747.32376	0.64	0.75	12.85	-0.16	-1.18	-0.01	0.00
8747.32679	0.65	0.75	12.88	-0.15	-1.18	-0.03	-0.03
8747.32983	0.66	0.75	12.89	-0.17	-1.17	-0.02	-0.01
8747.35017	0.72	0.75	13.04	-0.16	-1.19	-0.03	-0.01
8747.35341	0.73	0.75	13.08	-0.18	-1.20	-0.04	0.00
8747.35646	0.74	0.75	13.10	-0.18	-1.20	-0.03	-0.00
8747.36269	0.76	0.75	13.15	-0.20	-1.19	-0.07	-0.17
8747.36563	0.77	0.75	13.18	-0.20	-1.20	-0.07	-0.20
8747.36864	0.78	0.75	13.20	-0.20	-1.20	-0.07	-0.12
8747.37524	0.80	0.75	13.27	-0.23	-1.20	-0.06	-0.13
8747.37845	0.81	0.75	13.32	-0.26	-1.21	-0.07	-0.21
8747.38143	0.81	0.75	13.34	-0.25	-1.21	-0.09	-0.37
8747.40606	0.89	0.75	13.46	-0.25	-1.24	-0.04	-0.22
8747.40939	0.90	0.75	13.45	-0.23	-1.22	-0.03	-0.17
8747.41231	0.91	0.75	13.46	-0.22	-1.25	-0.06	-0.20
8747.41911	0.93	0.75	13.53	-0.29	-1.21	-0.05	-0.16
8747.42230	0.94	0.75	13.55	-0.29	-1.24	-0.07	-0.17
8747.42519	0.95	0.75	13.52	-0.27	-1.22	-0.05	-0.04
8747.44227	0.00	0.75	13.54	-0.27	-1.22	-0.08	-0.24
8747.44521	0.01	0.75	13.53	-0.28	-1.23	-0.09	-0.24
8747.44829	0.02	0.75	13.53	-0.27	-1.24	-0.07	-0.26
8747.45504	0.04	0.75	13.54	-0.30	-1.22	-0.08	-0.07
8747.45819	0.05	0.75	13.53	-0.28	-1.23	-0.09	-0.07
8747.46110	0.06	0.75	13.52	-0.25	-1.23	-0.13	-0.11
8747.46788	0.08	0.75	13.49	-0.27	-1.21	-0.04	-0.00
8747.47082	0.09	0.75	13.45	-0.20	-1.23	-0.08	-0.07
8747.47381	0.10	0.75	13.42	-0.21	-1.21	-0.04	0.07
8747.48028	0.12	0.75	13.43	-0.23	-1.23	-0.07	-0.00
8747.48315	0.13	0.75	13.42	-0.22	-1.24	-0.06	-0.00

Table III. Colour Range of EC11575-1845

Colour	Max Light	Min Light
V	12.71	13.55
B-V	-0.16	-0.27
U-B	-1.13	-1.22
V-R	-0.00	-0.09
V-I	0.00	-0.17
J	12.88	14.00
J-H	0.05	0.18
J-K	0.07	0.15
H-K	0.02	-0.03

§5.2.3 Infrared JHK Photometry

Infrared photometry was obtained on the nights of 1993 March 16-17. The results are listed in Table IV and plotted in Figure 5. The JHK variations

are similar to the optical variations but with larger scatter. A sinusoid (the solid lines in Figure 5) of period 7.86-hr was fitted to the data of 1993 March 17 by least-squares and gave the amplitudes of the brightness variations: 1.12±0.03 mag in J, 0.99±0.02 mag in H, and 1.04±0.02 mag in K. The standard deviations of the residuals for the JHK measurements were 0.066 mag in J, 0.073 mag in H, and 0.066 mag in K. The JHK values at minimum and maximum light are shown in the second half of Table III.

Table IV. Infrared Photometry for EC11575-1845

HJD	Phase	J	HJD	Phase	H	HJD	Phase	K
9063.55363	0.8861	13.61	9063.54732	0.8668	13.60	9063.54051	0.8461	13.66
9063.57167	0.9412	13.77	9063.56642	0.9251	13.83	9063.56055	0.9072	13.77
9063.59617	0.0160	14.19	9063.59062	0.9990	13.88	9063.58559	0.9837	13.57
9063.61428	0.0712	14.01	9063.60926	0.0559	13.78	9063.60355	0.0385	13.88
9063.64463	0.1639	13.80	9063.63974	0.1489	13.60	9063.63135	0.1233	13.81
9063.65908	0.2080	13.69	9063.65454	0.1941	13.36	9063.64967	0.1793	13.60
9064.37149	0.3825	13.09	9064.36704	0.3689	13.11	9064.36269	0.3556	13.04
9064.38401	0.4207	12.93	9064.38058	0.4102	12.89	9064.37617	0.3968	13.03
9064.39621	0.4580	12.91	9064.39262	0.4470	12.87	9064.38792	0.4326	12.88
9064.41457	0.5140	12.85	9064.41144	0.5044	12.87	9064.40779	0.4933	12.88
9064.42485	0.5454	12.96	9064.42121	0.5343	12.78	9064.41785	0.5240	12.81
9064.43617	0.5799	12.93	9064.43227	0.5680	12.92	9064.42878	0.5574	12.85
9064.44737	0.6141	12.96	9064.44374	0.6030	12.92	9064.44011	0.5919	12.77
9064.47065	0.6852	13.17	9064.46736	0.6751	13.02	9064.46372	0.6640	13.06
9064.48122	0.7174	13.40	9064.47778	0.7069	13.16	9064.47408	0.6956	12.99
9064.49204	0.7505	13.42	9064.48842	0.7394	13.19	9064.48480	0.7284	13.12
9064.51358	0.8162	13.65	9064.50942	0.8035	13.53	9064.50429	0.7878	13.41
9064.52954	0.8649	13.75	9064.52489	0.8507	13.58	9064.51907	0.8330	13.60
9064.54597	0.9151	13.93	9064.54128	0.9008	13.90	9064.53605	0.8848	13.80
9064.57197	0.9944	14.19	9064.56721	0.9799	13.73	9064.56243	0.9653	13.91
9064.58937	0.0475	13.93	9064.58374	0.0304	13.92	9064.57797	0.0127	13.78
9064.60519	0.0958	13.80	9064.60066	0.0820	13.69	9064.59539	0.0659	13.86
9064.62870	0.1676	13.79	9064.62347	0.1516	13.58	9064.61710	0.1322	13.67
9064.64423	0.2150	13.54	9064.63890	0.1987	13.49	9064.63408	0.1840	13.55
9064.65880	0.2595	13.40	9064.65422	0.2455	13.37	9064.64982	0.2321	13.48

§5.3 Spectroscopic Characteristics

The spectrum in Figure 1 was obtained with 4Å resolution near maximum light. As mentioned in section 5.1, the CIII/NIII λ4650Å blend and Balmer lines in emission are the dominant features in Figure 1. In fact, the CIII/NIII blend can be resolved into NIII/OII λ4640Å and CIII/NIII λ4650Å.

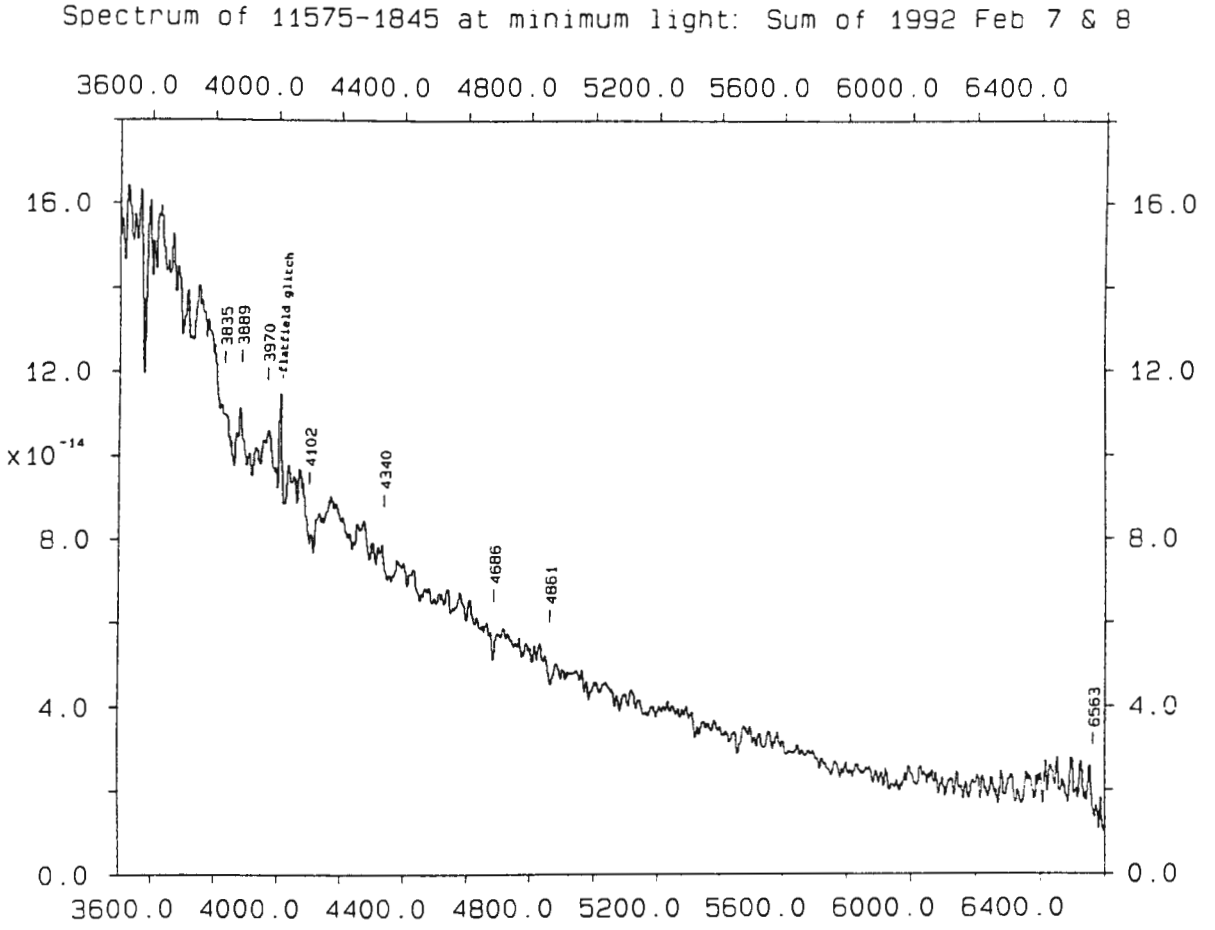

Figure 6. Sum of the spectra of 1992 February 7 and 8 at minimum light.

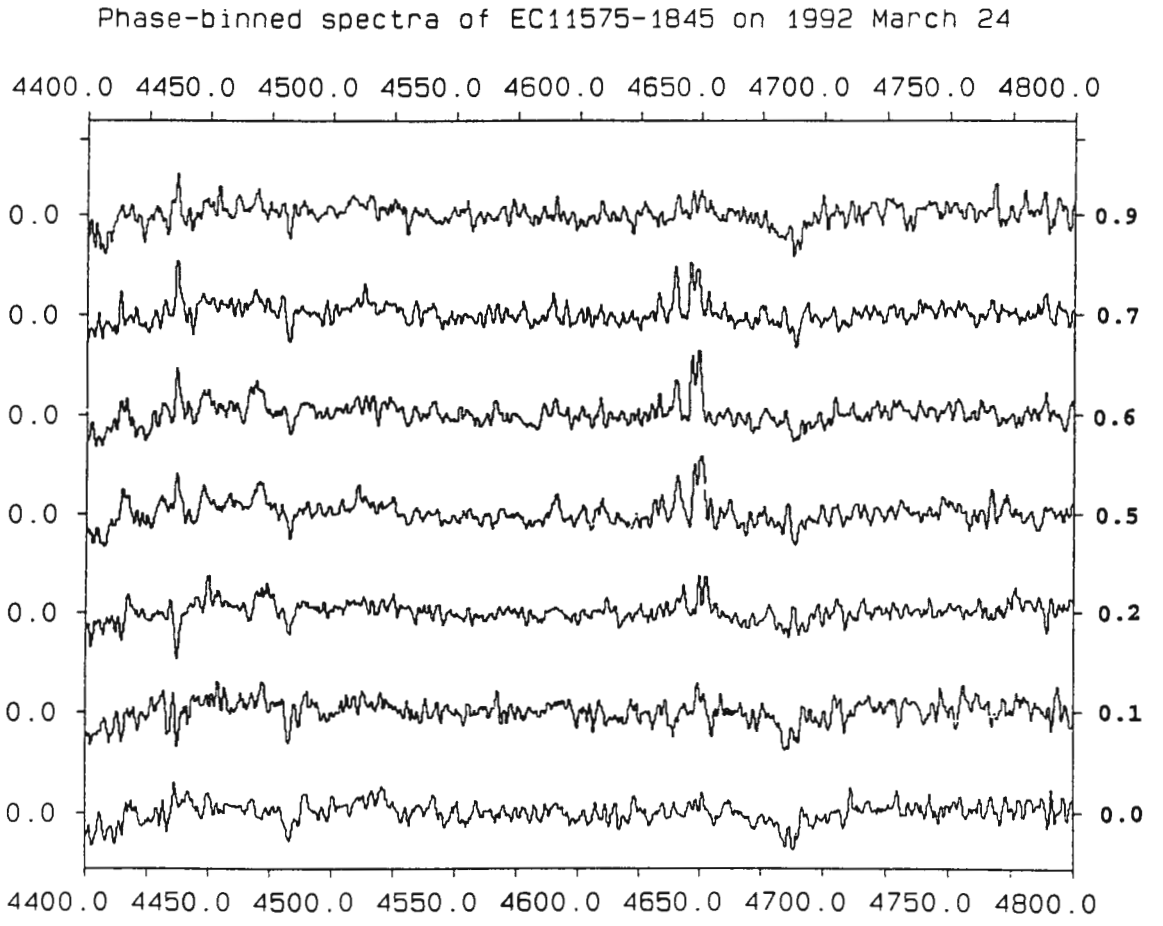

Figure 7a. A sequence of spectra binned in orbital phase for 1992 March 24. The right ordinate indicates the orbital phase and the left ordinate gives the continuum level.

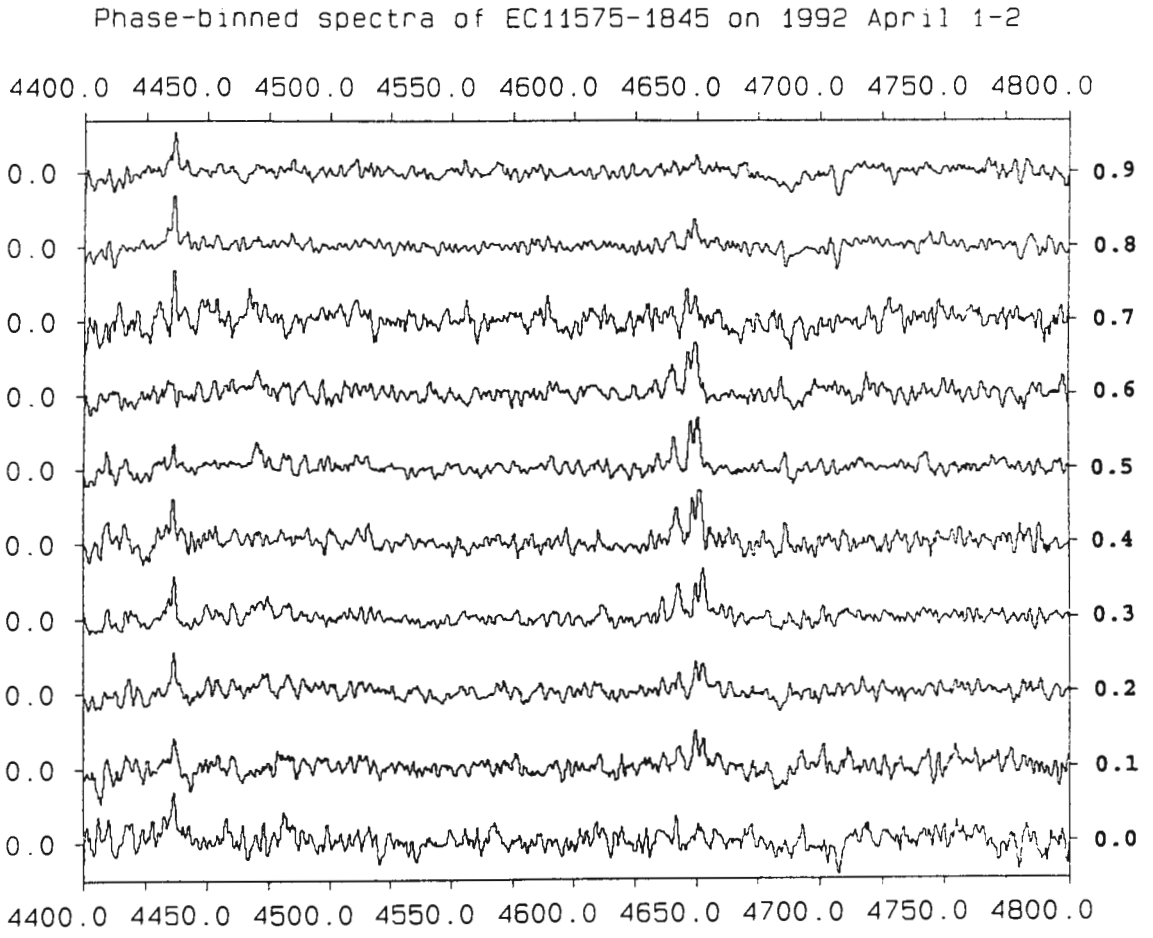

Figure 7b. A sequence of spectra binned in orbital phase for 1992 April 1-2.

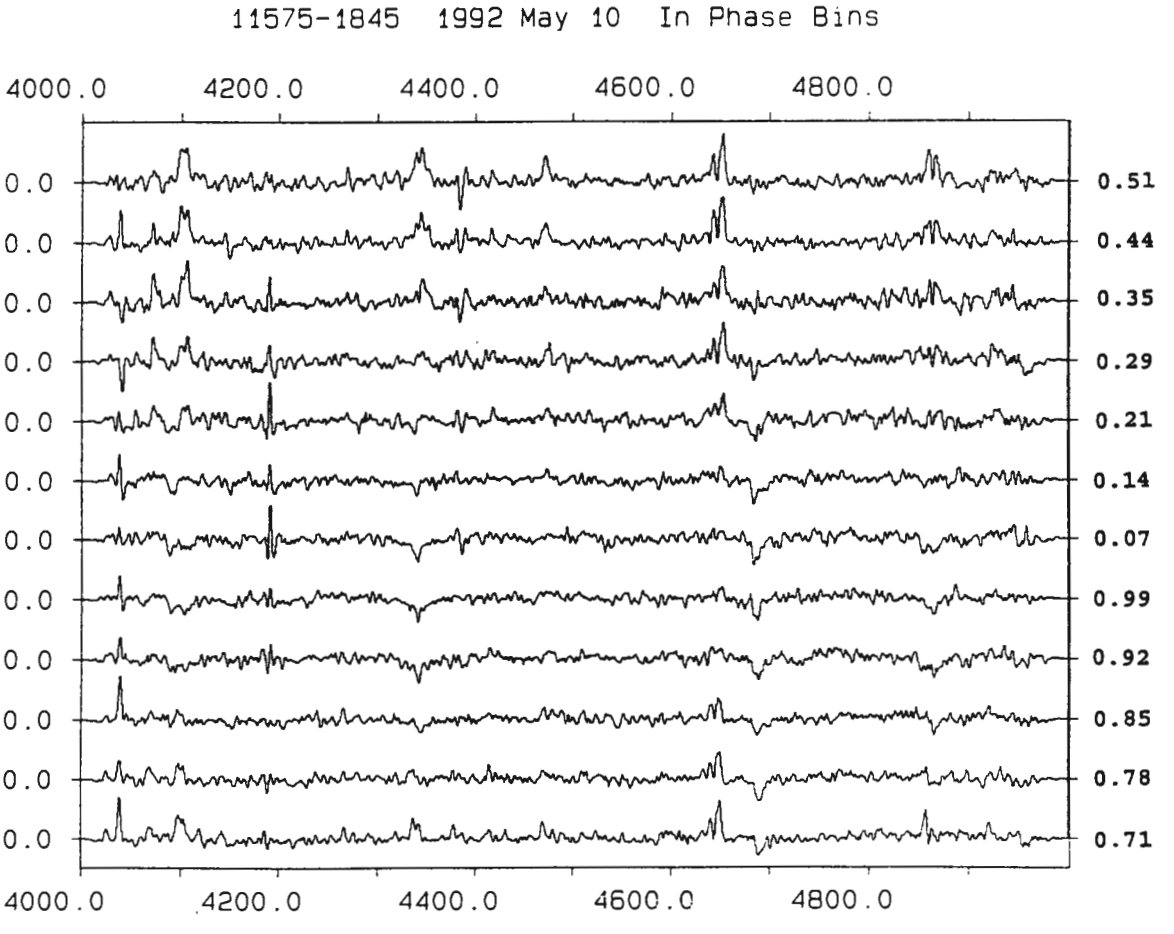

Figure 7c. A sequence of spectra binned in orbital phase for 1992 May 10. Note that the emission lines near λ4200Å at phase 0.07-0.35 are flat-field glitches.

The Balmer lines are seen up to H12 and show broad widths of FWZI~35Å. In addition to these, HeI λ4026Å, λ4121Å, λ4437Å, λ4472Å, and λ4922Å in emission are clearly visible. CII λ4267Å, NII/FeII λ4418Å blend, and NII λ4610Å are possibly present in emission as well as CIII λ4070Å, λ4380Å, and λ4513/4516Å.

Spectra with 8Å resolution covering λλ3500-6600Å were obtained at minimum light on 1992 February 7 and 8. The sum of the two spectra is shown in Figure 6 and exhibits weak Hβ, Hγ, Hδ, and HeII λ4686Å in absorption. Hα and the high Balmer series can not be seen. No other features are visible.

In order to investigate spectral and radial velocity variations, time-resolved spectroscopy was obtained with a range of wavelength resolution (see Table V) during 1992 March-May. The sequences of spectra were binned into orbital phase corresponding to the photometric ephemeris obtained in section 5.2.2 and are shown in Figure 7 with the continuum removed. These spectra (Figure 7) indicate that the strength of the CIII/NIII λ4650Å blend and the Balmer emission lines gradually decrease from maximum to minimum light. The Balmer lines change to absorption lines at minimum light but the CIII/NIII λ4650Å does not. In contrast to the above behaviour of the emission lines, the strength of the HeII λ4686Å absorption increases from maximum light to minimum light but is filled in by emission and disappears completely at maximum light. This suggests that the emission and absorption lines may come from different components in the system. Note that Figure 6 and 7c show that the spectra at minimum light are typical of that of an sdO star.

Table V. Observing Log of Time-resolved Spectroscopy

UT Date	Start UT h m	Duration (hrs)	Resolution FWHM(Å)	Coverage (Å)
24 Mar 92	19:26	6	1.2	4400-4900
01 Apr 92	18:36	6	1.2	"
02 Apr 92	17:56	1	1.2	"
10 May 92	17:24	7	3.0	3800-5000

§5.4 The Model

The photometric and spectroscopic behaviour can be understood in terms of the following model: the system is a close binary with an orbital period of 7.86-hr. The primary is a very hot ($10^{4.5-5.0}$ K) sdO star illuminating the inside face of a late G, K, or M dwarf which produces the light and emission/absorption line variations. The photometric variations can be regarded as a simple "reflection" effect. Note that the colours U-B and B-V of this object are "reddest" at maximum light and are "bluest" at minimum light (see Figure 3). This is because the atmosphere of the cool secondary absorbs the incident radiation from the primary and re-emits at a lower temperature than the primary. The CIII/NIII λ4650Å blend and the Balmer emission components are produced in the heated hemisphere of the secondary. The Balmer and HeII λ4686Å absorption components arise in the photosphere of the primary.

Based on the above model, the radial velocity variations and dynamical solutions will be discussed in the following sections.

§5.5 Radial Velocities

§5.5.1 Radial Velocity Variation of the Secondary

In the spectra of 1992 Mar 24 (Figure 7a) and April 1-2 (Figure 7b), the CIII/NIII blend at λ4650Å is the dominant feature. Although the strength of the CIII/NIII emission varies in phase with the brightness of the system and nearly vanishes at minimum light, it was selected to determine the radial velocity. The best signal-to-noise spectrum taken near maximum light was chosen to be the template. The relative radial velocities were measured using the cross-correlation technique of Tonry and Davis (1979) (§4.3). The spectra at minimum light, having poor signal-to-noise at λ4650Å, were excluded. The relative radial velocities were then transformed to heliocentric velocities by correcting for the heliocentric velocity of the template, -25.2 and -28.1 km/s for March 24 and April 1-2 respectively. The resulting heliocentric velocities are listed in Table VI and binned into

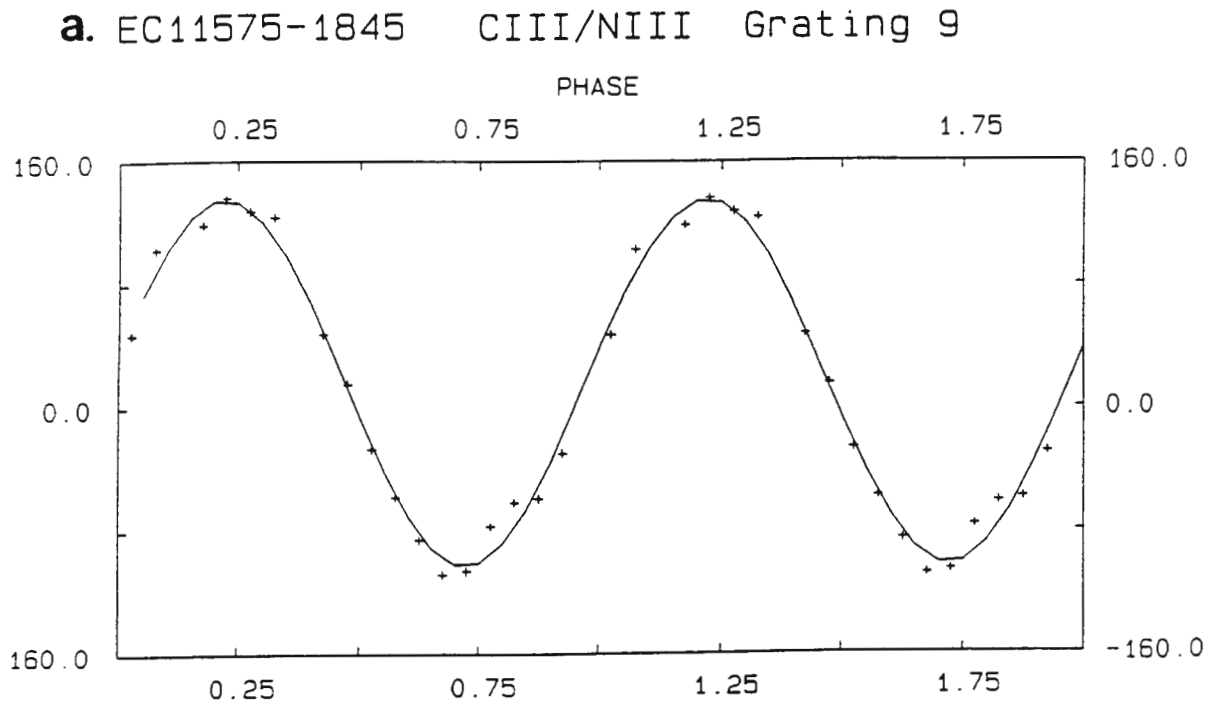

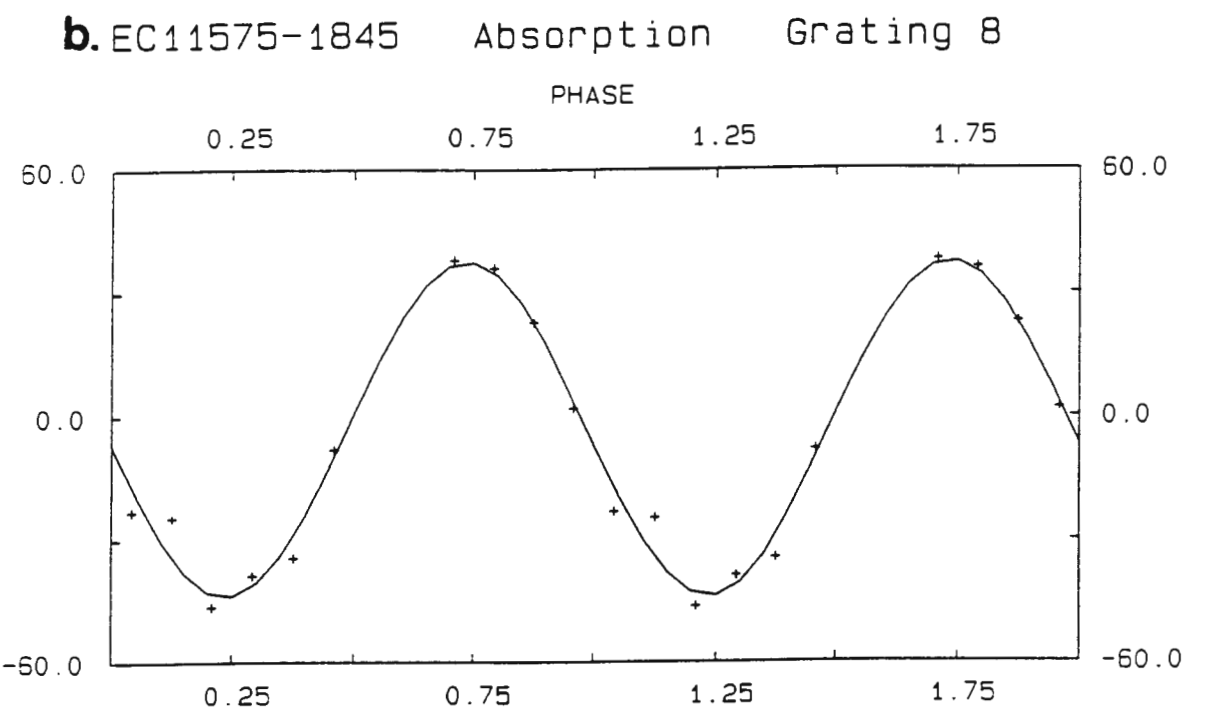

Figure 8. Radial velocity variations vs. orbital phase: (a) for the secondary and (b) for the primary.

orbital phase (Figure 8a). A sinusoid of period 7.86-hr was fitted to the data in Figure 8a by least-squares and gave a semi-amplitude of 119 ± 4 km/s and γ-velocity of 17 ± 3 km/s.

Table VI. Radial Velocities of the Secondary*

HJD	km/sec	HJD	km/sec
8706.31565	14	8714.31326	-57
8706.33190	-25	8714.40059	131
8706.34766	-61	8714.41667	113
8706.36326	-102	8714.43233	131
8706.37900	-108	8714.44797	127
8706.39851	-105	8714.46371	124
8706.44176	-48	8714.49770	48
8706.46288	-20	8714.51349	17
8706.50156	48	8714.52904	-28
8706.52073	103	8714.54470	-54
8706.53983	112	8714.56029	-68
8706.55898	142	8715.25288	-83
8714.28086	-70	8715.28631	-71
8714.29701	-61	8715.30190	-38

*obtained on the nights of 1992 Mar 24, Apr 1, and Apr 2.

As mentioned in section 5.3, the strengths of the CIII/NIII λ4650Å emission blend and HeII λ4686Å absorption vary in opposite phase. In order to measure the absorption line velocities, HeII λ4686Å was used to determined the relative radial velocity. The spectrum at minimum light was chosen to be the template. The results (not plotted) show that although the radial velocity variation of HeII λ4686Å has the opposite phase to that of the CIII/NIII curve, there is large scatter due to the complex profile in which a variable emission core is superposed on the absorption line.

§5.5.2 Radial Velocity Variation of the Primary

Because of the emission components superposed on the absorption lines in the HeII λ4686Å and Balmer lines, it is difficult to determine the radial velocities of the primary. In order to obtain a well-determined radial velocity curve of the primary, the emission components must be removed. A few assumptions are needed to achieve this: (1) The observed spectra are the sum of the spectra of the sdO primary (assumed constant) and the heated inside hemisphere of the secondary. The contribution of the outside

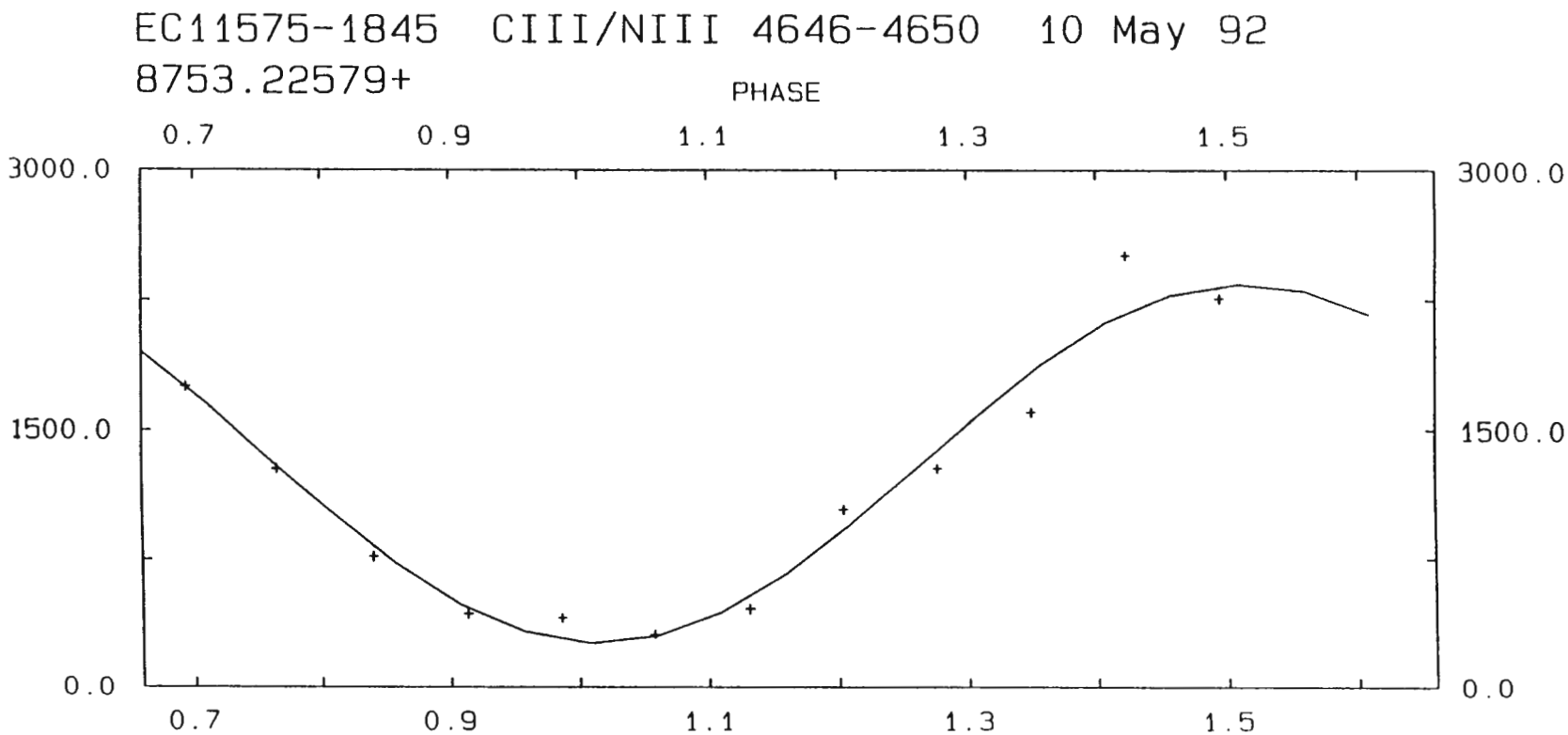

Figure 9. The light intensity of the CIII/NIII λ4650Å blend above the continuum vs. orbital phase.

hemisphere is negligible. (2) The intrinsic spectrum of the heated hemisphere is constant. Its contribution to the observed spectra varies because of the varying visibility of the heated hemisphere resulting from the orbital motion. (3) The spectrum of the heated hemisphere is uniformly produced over the heated hemisphere. Thus, the spectrum of the heated hemisphere can be found by subtracting the spectrum at minimum light from the spectrum at maximum light. If this spectrum, suitably scaled, is subtracted from a spectrum observed at any arbitrary phase, then the spectrum of the primary sdO at that time can be obtained. This approach enables us to measure the radial velocities of the primary: let E_1 be the spectrum of the primary and E_r be the intrinsic spectrum of the heated hemisphere of the secondary. Therefore the observed spectrum E_x at arbitrary phase x can be expressed as $E_1+f_x \cdot E_r$, where f_x is a scaling factor varying with orbital phase. From the above expression, $E_r = (E_{0.5}-E_{0.0})/(f_{0.5}-f_{0.0})$ where x=0.0 at minimum light. As mentioned above, the strength of the CIII/NIII λ4650 Å emission varies in phase with the brightness of the system and does not change to absorption at minimum light. Thus it is a useful measure of the factor f_x. A bandpass, λλ4645-4656Å, was applied to the 12 phase-binned spectra (Figure 7c) to calculate the CIII/NIII intensity in counts above the continuum. Each of these spectra was produced from the sum of three 600s exposures. The results (Table VII) are well fitted by the photometric period and shown in Figure 9.

Table VII. Parameters used to derive the primary's Radial velocity

HJD	Phase	Counts (λλ4645-4656Å)	Counts*	f_x*	RV_r* (km/s)
8753.23736	0.71	1750	1750	0.747	-118
8753.26092	0.78	1279	1295	0.553	-125
8753.28546	0.85	766	824	0.352	-107
8753.30923	0.92	435	467	0.199	-68
8753.33323	0.99	409	279	0.119	-15
8753.35663	0.07	312	302	0.129	38
8753.38071	0.14	462	531	0.227	85
8753.40455	0.21	1035	918	0.392	113
8753.42850	0.29	1278	1386	0.592	117
8753.45228	0.35	1604	1834	0.783	96
8753.47630	0.44	2508	2176	0.929	54
8753.49978	0.51	2258	2335	0.997	1

*obtained from least squares fit

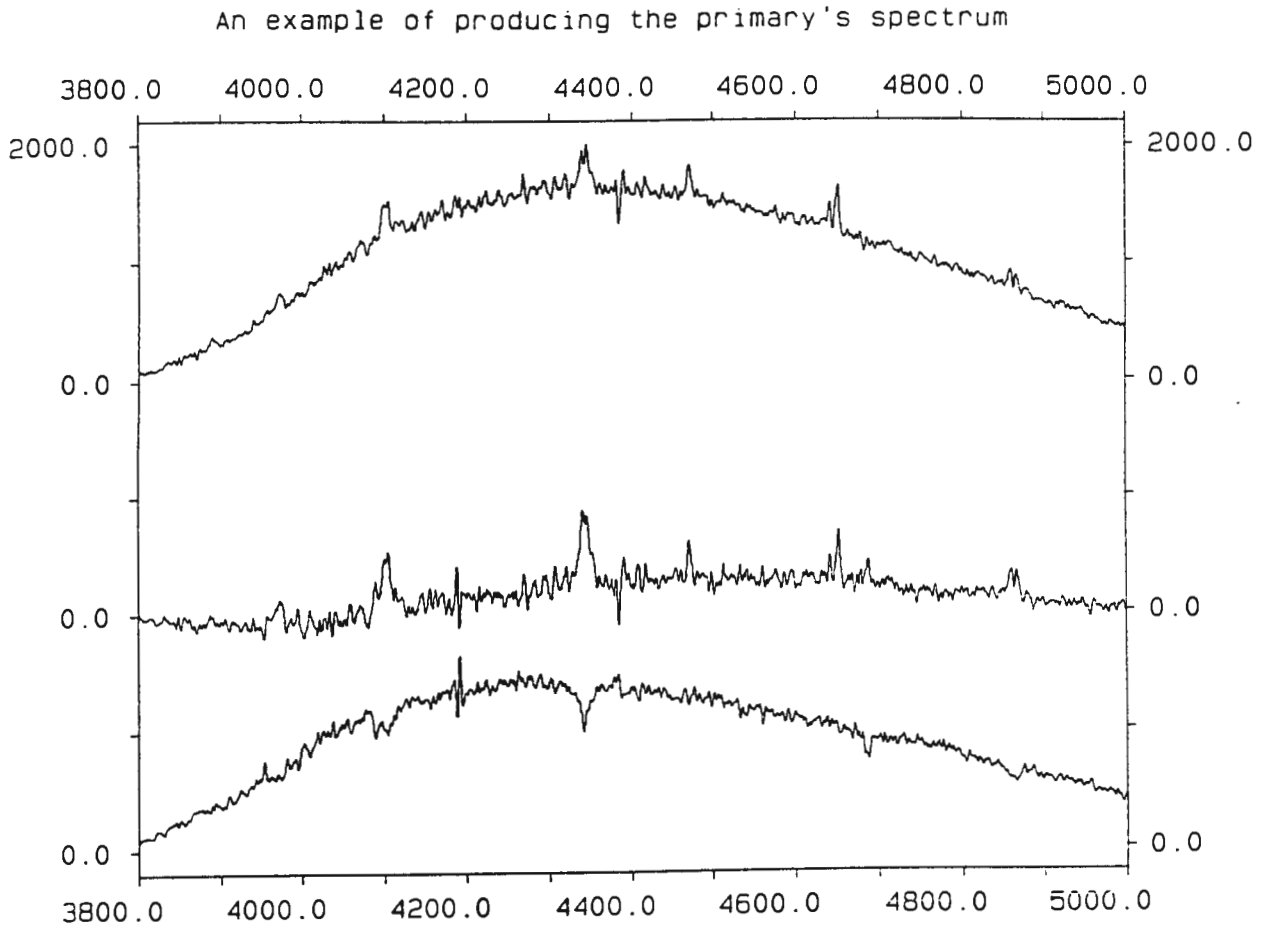

Figure 10. Plot of the original spectrum at maximum light (top), the spectrum of the reflecting face of the secondary (middle), and the primary's spectrum (at maximum light) after removing the middle spectrum from the top spectrum. (see the details in section 5.5.2)

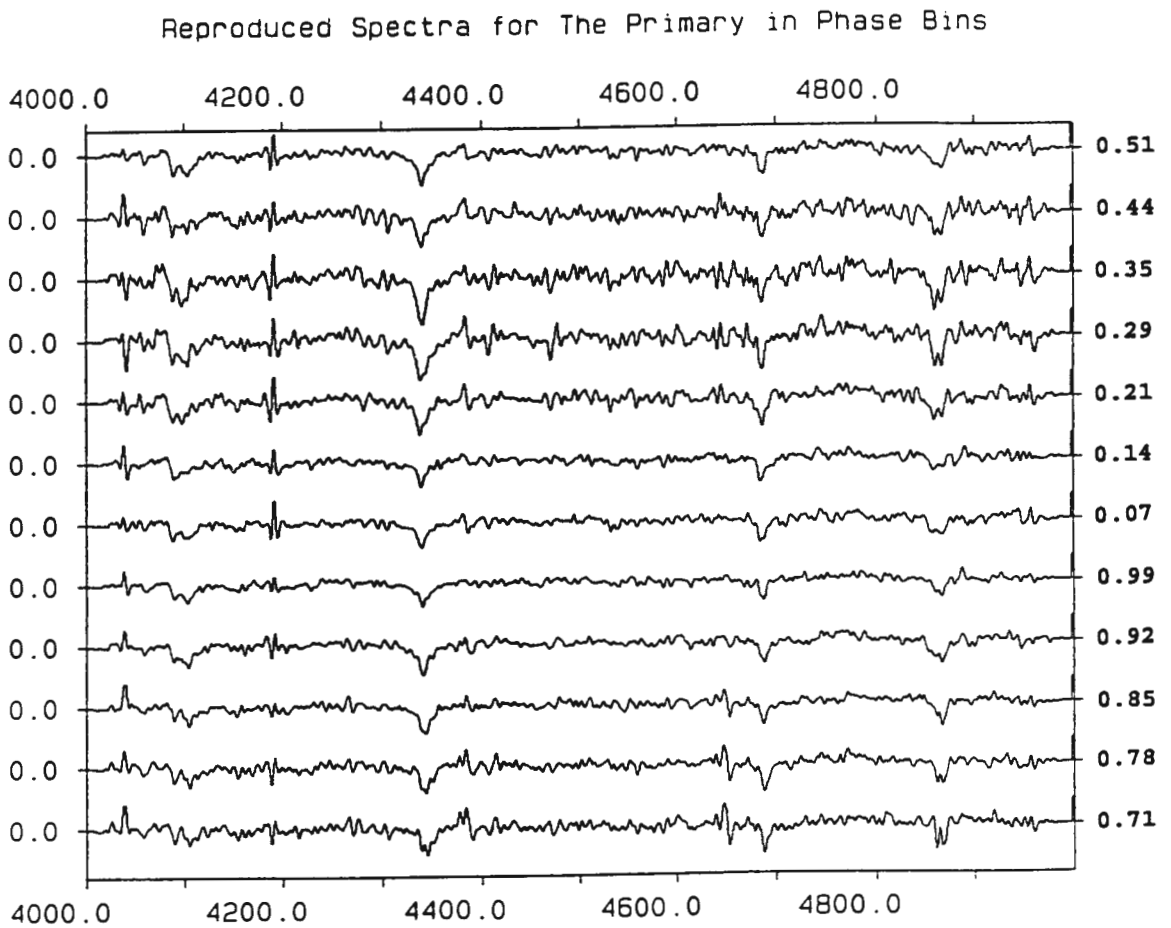

Figure 11. The spectra of the primary after removing the middle spectrum of Figure 10 from the spectrum in Figure 7c.

To simplify the problem, $f_{0.5}$=1 was assumed. In the present case, E_r is obtained at zero-velocity shift (superior conjunction of the secondary). Thus the velocity shift of the heated hemisphere at different phases should be taken into account when deriving E_1 from $E_1+f_x \cdot E_r$. The velocity shifts of the heated hemisphere were derived from the CIII/NIII λ4650Å blend in the same spectra and are listed in Table VII.

Figure 10 shows an example of removing the emission spectrum. The middle spectrum of Figure 10 is the emission spectrum of the heated hemisphere. This spectrum was scaled by factor f_x, velocity shifted and then subtracted from the observed spectrum (top in Figure 10) to yield the bottom spectrum in Figure 10. After removing $f_x \cdot E_r$ from the original spectra, the twelve resulting spectra are shown vs orbital phase in Figure 11. The absorption features at Hγ and HeII λ4686Å are much clearer than at Hβ and Hδ. This is probably because the factor f_x is not uniform at all wavelengths due to wavelength-dependent light losses at the spectrograph slit and/or wavelength-dependent changes in the spectrum from the heated hemisphere. Thus there are still emission components in Hβ and Hδ. These 12 spectra (Figure 11) were used to measure the primary's radial velocity curve by cross-correlating with the template in the spectral range λλ4000-5000Å. The template was obtained using the same procedure as demonstrated in Figure 10: the emission spectrum was scaled by the factor $f_{0.99}$ and then subtracted from the spectrum near minimum light (at phase 0.99). The relative radial velocities were transformed to heliocentric velocities by correcting for the heliocentric velocity of the template, -7.8 km/s. The resulting heliocentric velocities of the primary are tabulated in Table VIII and plotted in Figure 8b. The

Table VIII. Radial Velocities of the Primary*

HJD	km/sec	HJD	km/sec
8753.23736	38	8753.38071	-25
8753.26092	36	8753.40455	-46
8753.28546	31	8753.42850	-39
8753.30923	14	8753.45228	-34
8753.33323	2	8753.47630	-7
8753.35663	-23	8753.49978	-9

*obtained on the night of 1992 May 10.

The sum of a_1 and a_2 is equal to the separation of the two components. From Kepler's Third Law with P_{orb}=7.86-hr

$$a = 1.391\times10^{6}\cdot(M_1+M_2)^{1/3} \text{ km}$$

where M_1 and M_2 are in solar masses, then we have

$$1.391\times10^{6}\cdot(M_1+M_2)^{1/3} = P_{orb}\cdot(K_1+K_2)/(2\pi\cdot\sin i) + 0.424\cdot r_2\cdot a$$

From the above equation, the total mass of the system can be obtained as follows:

$$M_1+M_2 = 3.716\times10^{-19}\cdot\{(K_1+K_2)\cdot P_{orb}/[2\pi\cdot(1-0.424\cdot r_2)\cdot\sin i]\}^3 \qquad (4)$$

In order to solve for M_1 and M_2 in equation (4), the mass ratio M_2/M_1 must be derived. Equations (2) and (3) are re-expressed as

$$K_1\cdot P_{orb}/(2\pi\cdot\sin i) = M_2/(M_1+M_2)\cdot a \qquad (5)$$

and

$$K_2\cdot P_{orb}/(2\pi\cdot\sin i) = M_1/(M_1+M_2)\cdot a - 0.424\cdot r_2\cdot a \qquad (6)$$

Dividing equation (6) by equation (5), we have

$$q\ (\equiv M_2/M_1) = (1-0.424\cdot r_2)/(K_2/K_1+0.424\cdot r_2) \qquad (7)$$

Therefore the dynamical solution can be obtained by substituting the parameters determined from the model fit into Equation (4) and (7). These solutions, including the mass ratio of the system, the masses in $M_\odot$, the radii (R) in $R_\odot$, and the surface gravity (log g) of the two components, are listed in the 7th-13th columns of Table IX.

Figure 14 presents an example of the best fit with an inclination of 35°, an effective temperature T_1 of 105000 K for the primary, and the primary and secondary having radii of 0.025 and 0.16 in units of their separation, respectively.

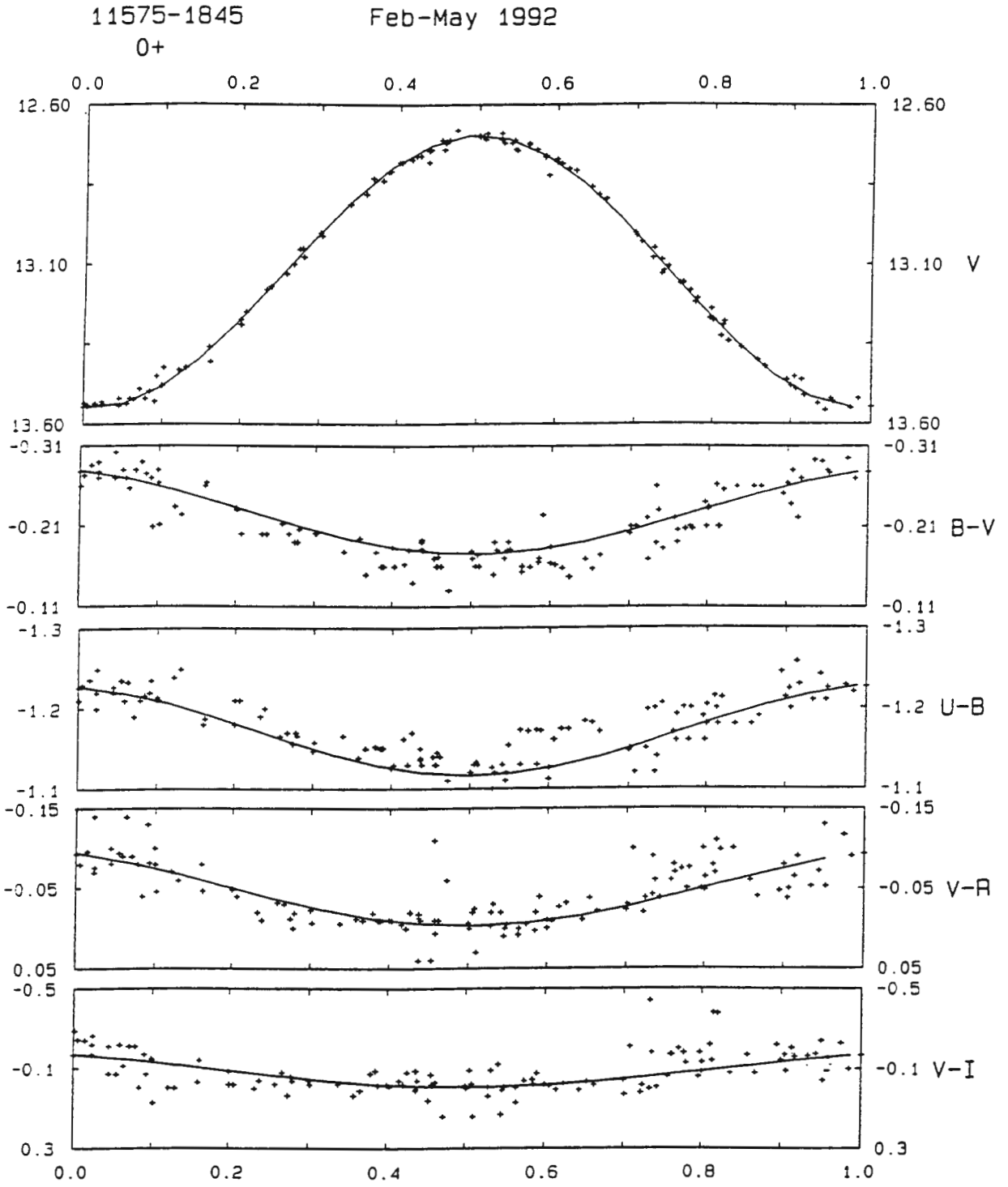

Figure 14. V-magnitude and colours variations vs. orbital phase. The solid lines are an example of a best model fit at T_1=105000K with i= 35° and q=0.31.

lower T_1 is required to produce the same amplitude of the reflection effect as observed.

From the results shown in Figure 13, it is certain that there are fitted models in the 'gap' of the solutions in Table IX. Thus, further calculations with fine increments (0.001 for r_1 and r_2, 1° for i, and 1000K for T_1) were made to search for more fitted models. 9347 fitted models were obtained and the ranges of the parameters are $0.017 \leq r_1 \leq 0.060$, $0.110 \leq r_2 \leq 0.310$, $27^\circ \leq i \leq 60^\circ$, and $63000K \leq T_1 \leq 135000K$. Note that the value 135000K is not the upper limit on T_1 (see discussion in §5.7.2).

The mass ratio of a binary system is equal to the ratio of the velocity semi-amplitudes, i.e. $M_2/M_1 = K_1/K_2$. In the present case, a correction is needed in using the ratio of semi-amplitudes to derive the mass ratio, because the centre of light for the region producing the CIII/NIII λ4650Å blend does not coincide with the centre of mass of the secondary. Assuming synchronous rotation for the secondary and that the CIII/NIII λ4650Å blend is produced uniformly over the heated hemisphere of the secondary, the separation of these two points is 0.424 times the radius of the secondary (Drilling 1985). Let a_1 and a_2 be respectively the distances of the primary and secondary from the centre of mass of the system. The semi-amplitudes of the radial velocity curves are:

$$K_1 = (2\pi a_1/P_{orb}) \cdot \sin i$$

and

$$K_2 = (2\pi \cdot (a_2 - 0.424 \cdot r_2 \cdot a)/P_{orb}) \cdot \sin i$$

where r_2 is the radius of the secondary in units of the orbital separation (a). The values of a_1 and a_2 can be obtained from the above equations and expressed as

$$a_1 = K_1 \cdot P_{orb}/(2\pi \cdot \sin i) \qquad (2)$$

and

$$a_2 = K_2 \cdot P_{orb}/(2\pi \cdot \sin i) + 0.424 \cdot r_2 \cdot a \qquad (3)$$

Table IX. Examples of The Results of Model Fits

r_1	r_2	r_2/r_1	i	T_1	Limit i	q	M_1 $M_\odot$	M_2 $M_\odot$	R_1 $R_\odot$	R_2 $R_\odot$	$\log(g_1)$	$\log(g_2)$
0.020	0.120	6.0	40	130000	82	0.31	0.46	0.14	0.02	0.14	7.3	5.3
0.025	0.115	4.6	55	130000	82	0.31	0.22	0.07	0.01	0.07	7.5	5.6
0.025	0.120	4.8	50	130000	81	0.31	0.27	0.08	0.02	0.09	7.4	5.5
0.025	0.125	5.0	50	120000	81	0.31	0.27	0.09	0.02	0.09	7.4	5.5
0.025	0.130	5.2	45	120000	81	0.31	0.35	0.11	0.02	0.12	7.3	5.3
0.025	0.145	5.8	40	110000	80	0.31	0.48	0.15	0.03	0.18	7.1	5.1
0.025	0.155	6.2	35	110000	79	0.31	0.68	0.21	0.04	0.27	7.0	4.9
0.025	0.160	6.4	35	105000	79	0.31	0.68	0.21	0.04	0.29	7.0	4.8
0.030	0.160	5.3	40	105000	79	0.31	0.49	0.15	0.04	0.20	7.0	5.0
0.030	0.165	5.5	40	100000	78	0.31	0.49	0.15	0.04	0.21	7.0	5.0
0.035	0.180	5.1	40	95000	77	0.30	0.50	0.15	0.05	0.23	6.8	4.9
0.035	0.195	5.5	35	95000	76	0.30	0.72	0.22	0.07	0.37	6.7	4.6
0.035	0.200	5.7	35	90000	76	0.30	0.73	0.22	0.07	0.38	6.7	4.6
0.045	0.280	6.2	30	70000	71	0.28	1.24	0.35	0.14	0.89	6.2	4.1
0.050	0.240	4.8	40	75000	73	0.29	0.55	0.16	0.07	0.34	6.5	4.6
0.050	0.305	6.1	30	65000	69	0.28	1.29	0.36	0.17	1.01	6.1	4.0
0.055	0.250	4.5	40	75000	72	0.29	0.56	0.16	0.08	0.36	6.4	4.5

investigate this, a total of 121 additional models at fixed radii (r_1=0.025 and r_2=0.125) was calculated for the U-band data in a fine grid: T_1 was varied between 115000 and 125000 K in steps of 1000K and i between 45° and 55° in steps of 1°. The result is shown in a plot of T_1 vs i (Figure 13). The acceptable models with $\sigma \leq \sigma_{obs}$ (marked '+' in Figure 13) show an amplitude (A) in the range A_{obs}-5s $\leq A \leq A_{obs}$+8s, where s is the error in amplitude (section 5.2.2). Those with $\sigma > \sigma_{obs}$, i.e. unacceptable, were marked ',' in Figure 13 if their amplitudes were greater than A_{obs}+3s, and marked '.' if their amplitudes were smaller than A_{obs}-3s. Thus, the distribution of ',' and '.' in Figure 13 shows that the former models were unacceptable because their amplitudes were too large, and the latter because their amplitudes were too small. Four models marked ',' at lower right-hand corner in Figure 13 show reasonable amplitudes but the shapes of their curves do not fit the observed curves well. In addition to these, Figure 13 also shows a correlation between T_1 and i for the acceptable models (marked '+'): T_1 shows a tendency towards lower temperatures at higher inclinations. This can be easily understood from the difference of the visible area of the heated hemisphere of the cool component between maximum and minimum light: for a high-inclination system, the difference of the visible area of the heated hemisphere is larger than that for a low-inclination system. Thus, a

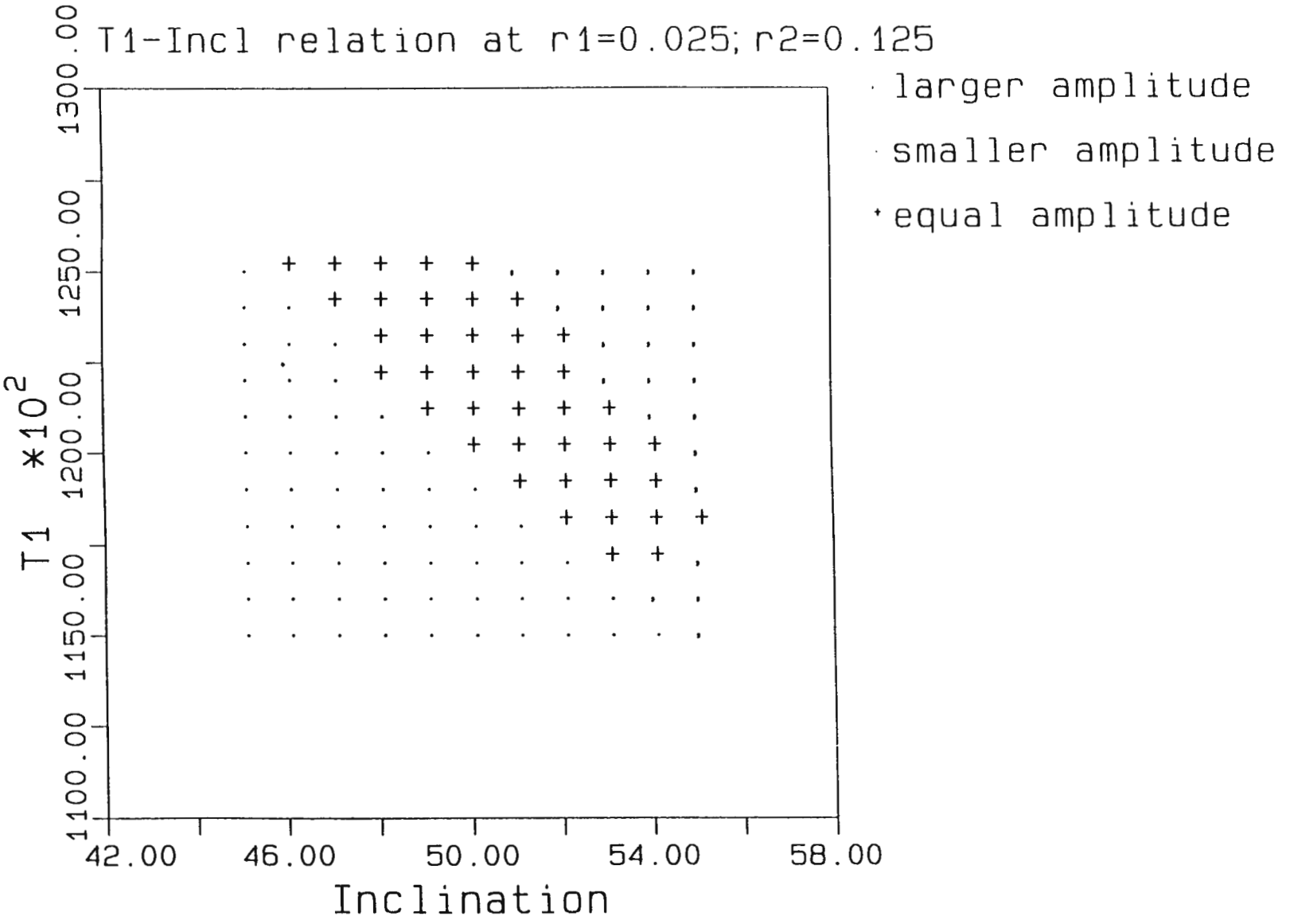

Figure 13. A plot of T_1-i relation. The symbol (+) represents the acceptable solutions from the model fits. For details, see text.

as a blackbody at temperature T_r. The total flux of light $L(\lambda,x)$ consists of light from the illuminating primary ($L_1(\lambda)$) and reflecting ($L_r(\lambda)$) hemisphere of the secondary: $L(\lambda,x) = L_1(\lambda) + L_r(\lambda,x)$. Replacing $L_1(\lambda)$ and $L_r(\lambda,x)$ by Planck's Law and normalizing the above equation by $L_1(\lambda)$, then we have

$$L'(\lambda,x) = 1 + (r_2/r_1)^2 \cdot \pi^{-1} \cdot \Sigma\, A_i \cdot [\exp(hc/\lambda kT_1)-1]/[\exp(hc/\lambda kT_r(i))-1] \quad (1)$$

where r_1 and r_2 are respectively the radius of the primary and secondary in units of their separation; the coefficients A_i specify the relative contributions of each annulus and depend on orbital phase, inclination, and angular distance δ (Figure 12). A range of models were computed in which the parameters, r_1, r_2, i, and T_1 in equation (1) covered the following ranges:

parameter	lower limit	upper limit	step
r_1	0.005	0.995	0.005
r_2	0.005	0.995	0.005
i	30	80	5
T_1(K)	10000	130000	5000

Thus, ~4.8 million combinations were calculated excluding unphysical models with $r_1+r_2>1$. Each set of parameters was used to construct a light curve for each of the UBVRI filters which was then fitted to the observed data. If the standard deviation (σ) of the residuals was smaller than observed (σ_{obs}) (section 5.2.2 and 5.2.3), the set of parameters was accepted as a possible solution. Overall, the model fit is good at UBVRI and is poor at H. None of the models fits the JK curves satisfactorily. This is not surprising because assumption (5) may not be correct at JHK wavelengths. Seventeen solutions from the grid defined above were found in the model fits for all five UBVRI light curves. The solutions, including r_1, r_2, r_2/r_1, i, T_1 and an upper limit on the inclination for the absence of eclipses, are listed in the first 6 columns of Table IX. However, the solutions in Table IX are expected to fall continuously in a range. For example, a range of T_1 near 120000K should be acceptable for those models with r_1=0.025, r_2=0.125, and i=50°. Instead, a unique value for T_1, 120000K, was acceptable. Thus, fewer solutions were found in the above calculation than expected and this may be due to the coarse increments used in the above calculations. In order to

solid line in Figure 8b is a least-squares fit of a sinusoid of the orbital period 7.86-hr and yielded a semi-amplitude of 40 ± 2 km/s and a γ-velocity of -3 ± 1 km/s.

Comparing Figures 8a and 8b, it is clear that these two curves are 180° out of phase. This is exactly what is expected from the model: the CIII/NIII λ4650Å emission is produced by reprocessing in the atmosphere of the cool secondary, and the HeII λ4686Å absorption comes from the hot primary's atmosphere. The emission core appearing in the HeII λ4686Å absorption is also contributed by the secondary.

§5.6 Light-Curve Analyses

Napier's (1968) model gives a thorough analysis of the light curves for the reflection effect in close binary systems. It has been applied to analyze the light curves of LSS2018 by Drilling (1985) and Landolt & Drilling (1986), and gives the radii (r) of the components in units of their separation, the inclination of the orbital plane (i), and the effective temperature (T_1) of the primary. Napier's algorithm was adopted to model the light curve of EC11575-1845. A few assumptions were needed: (1) both stars are spherical, (2) multiple reflections are neglected, (3) the irradiating star is treated as a disk-source, (4) the atmosphere of both stars show no limb-darkening, (5) the secondary has no self-luminosity and (6) the heated hemisphere of the secondary absorbs and re-emits the radiation from the primary acting as a blackbody. The surface brightness distribution over the heated hemisphere is represented by a set of concentric annuli with respect to the point H, the point closest to the primary (see Figure 12). The temperature (T_r) is assumed constant within each annulus, each of which has a width of 5°, and decreases outwards from H. T_r is a function of T_1, the separation of the two components, and the angular distance from the point H. Note that T_r is set to 0K outside the heated hemisphere. The flux at wavelength λ from the heated hemisphere received by observers at an arbitrary phase x is then obtained by adding the contributions from each visible annulus which radiates

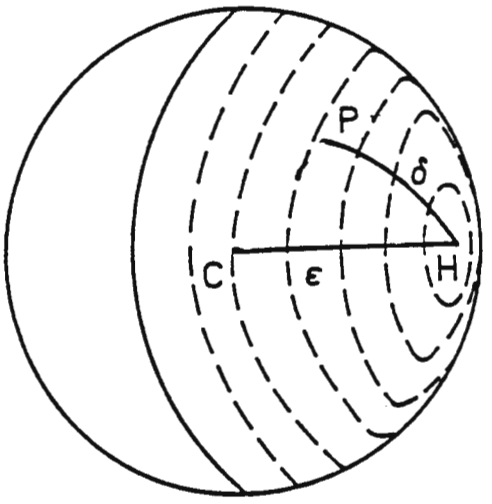

Figure 12. Schematic diagram of the system. The normal to the surface at H points to the centre of the primary. The annuli defined by dash lines are isotherms of the temperature (T_r) distribution: the T_r at point P is higher than that at the point C.

§5.7 Discussion

§5.7.1 Emission Lines from the Secondary

As mentioned above, the Balmer emission lines are broad with velocities of up to 1200 km/s (FWZI~35Å) in the wings of the lines which greatly exceed the binary orbital velocity (<200 km/s). The lines show no evidence for P Cygni profiles which would be indicative of a high velocity wind from the system. Such a large line width is usually seen in spectra of CVs, and arises from emission from the inner part of the accretion disk. This is not tenable in this case, because the object is not a CV.

Note that the line widths in other emission lines, such as the CIII/NIII λ4650Å blend and HeI, are much narrower (FWZI~15Å) than those in the Balmer lines. The widths of the Balmer lines show an increase from Hβ to Hδ, which can be seen in the middle spectrum of Figure 10. This suggests that the line broadening is caused by the Stark effect (Struve 1970). However, the lines produced in the photosphere of a lower main sequence star can not have such large widths, because the surface gravity is not large enough.

Let us consider another possible cause: rotational broadening. The equatorial velocity of the secondary of a CV is $V_{eq}=140\cdot(M_2\cdot R_\odot/R_L)^{1/2}$ km/s, where R_L is the radius of the Roche lobe. From the above equation, Warner (1994) derived that the spectral lines of secondaries generally have total widths ~280·sin *i* km/s. This is an upper limit if the line broadening is mainly caused by the rotational effect. In fact, the hydrogen lines and CIII/NIII λ4650Å blend are, respectively, at least four times and twice as broad as predicted by the above estimate. The cause of the large line widths in EC11575-1845 is currently unknown.

§5.7.2 Physical Properties of the System

The results of model fits (Table IX) suggest that the secondary is of spectral type not earlier than ~M5, because the mass is less than 0.5 $M_\odot$. According to the formula for the Roche lobe radius of the secondary (Eggleton 1983),

$$R_L/a=0.49\cdot q^{2/3}/[0.6\cdot q^{2/3}+\ln(1+q^{1/3})],$$

the Roche lobe radii R_L for various mass ratios in Table IX are then 0.276 for q=0.28, 0.278 for q=0.29, 0.281 for q=0.30, and 0.283 for q=0.31. Thus, the secondaries with $r_2 \geq 0.28$ already fill their Roche lobe. This is inconsistent with the photometric behaviour (section 5.2.1) which lacks flickering activity. Therefore, the solutions with $r_2 \geq 0.28$ should be discarded. About 7% (631 out of 9347) of solutions showing $0.28 \leq q \leq 0.29$ are excluded for this reason. The ranges of the parameters for the acceptable models are slightly different from those in section 5.6: $0.017 \leq r_1 \leq 0.060$, $0.110 \leq r_2 \leq 0.278$, $28^\circ \leq i \leq 60^\circ$, and $68000K \leq T_1 \leq 135000K$. Thus, the radii ratios for all the acceptable models fall in the range, $8 > r_2/r_1 > 4$. Assuming the secondary is a M5 dwarf with a radius $\sim 0.32R_\odot$ and the primary is a white dwarf which has a typical radius $\sim 0.01R_\odot$, the value of r_2/r_1 will be greater than 32. Thus, the model fits show that the primary is not a white dwarf, which is consistent with the spectral features of the primary.

At minimum light, let us assume that the primary dominates the energy distribution at short wavelengths. Thus the (θ_{eff},Q)-calibration (Greenstein and Sargent 1974) can be used to estimate the effective temperature T_{eff} of the hot primary. θ_{eff} and Q were defined as $\theta_{eff} = 5040/T_{eff}$ and Q = (U-B)-0.72(B-V) (Johnson and Morgan 1953), respectively. The parameter Q is -1.03 calculated from Table III and yields $\theta_{eff} \sim 0.09$ using the (θ_{eff},Q)-relation from Figure 1 of Greenstein and Sargent (1974). This gives an effective temperature of the primary of about 56000K. Note that the UBV colours are insensitive to determination of T_{eff} in very hot stars, because the UBV bandpasses all fall on the Rayleigh-Jeans tail of the energy distribution. Thus, the T_{eff} obtained above is a lower limit on T_1. The resulting temperatures of the model fits (in Table IX) are higher than this limit. Although the results show that T_1 falls in between 68000 and 135000 K, it doesn't imply that 135000K is the upper limit. Instead, that value is a T_1 cutoff used in the numerical simulation chosen by the author. It is possible

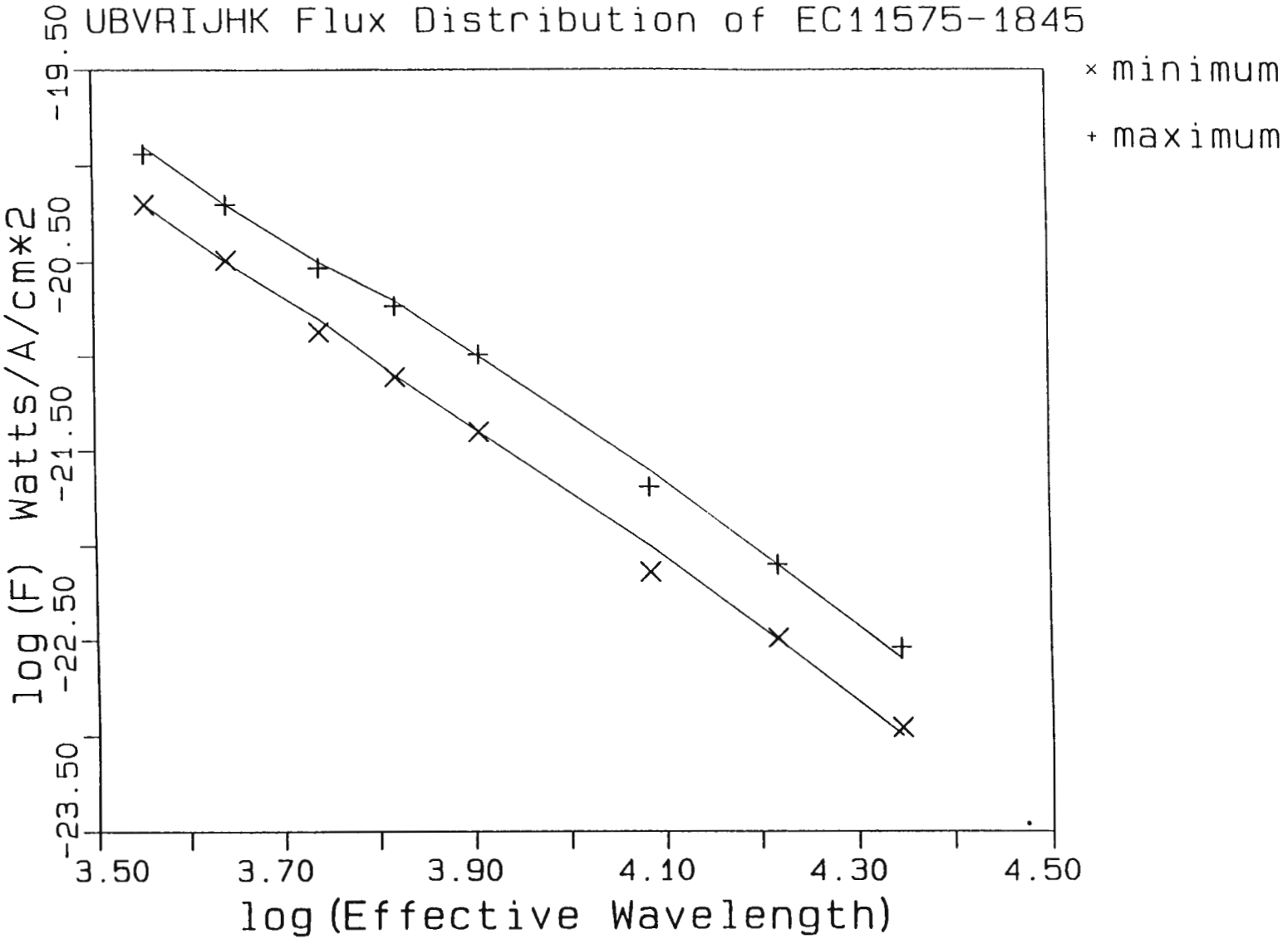

Figure 15. A plot of the flux distribution of EC11575-1845 from UBVRIJHK photometry. The asterisk (*) and plus (+) symbols represent the flux obtained at maximum light and minimum light respectively.

to get fitted models with higher temperature. Thus, no upper limit on T_1 can be derived.

The UBVRIJHK magnitudes at minimum and maximum light (Table III) were converted to fluxes by adopting the zero points, $\log(F_\lambda(U))=-15.37$, $\log(F_\lambda(B))=-15.18$, $\log(F_\lambda(V))=-15.44$, $\log(F_\lambda(R))=-15.65$, $\log(F_\lambda(I))=-15.91$ (Bessell 1979), $\log(F_\lambda(J))=-16.54$, $\log(F_\lambda(H))=-16.97$, and $\log(F_\lambda(K))=-17.42$ in Watts$\cdot$cm$^{-2}\cdot$Å^{-1} (Wilson et al. 1972). The flux distributions are shown in Figure 15. From the results of model fit, T_{eff} of the secondary can be assumed to be ~2500K. According to Wien's Displacement Law, $\lambda_{max}\cdot T = 0.28973$ cm$\cdot$K, the flux distribution may show a peak at ~11000Å if T_{eff} ~2500K is correct. In fact, that peak is invisible in the flux distribution at minimum light (the bottom of Figure 15) which is probably because the secondary has a low luminosity. The two fitted curves in Figure 15 are blackbody curves which were calculated from the model ($r_1=0.046$, $r_2=0.278$, $i=32^\circ$, and $T_1=68000$K). Now, assume that the amount of energy arriving above the atmosphere of the Earth per cm^2 at wavelength λ is F_λ. The total energy leaving the star per second is given by

$$L(\lambda,T) = 4\pi\cdot d^2\cdot F_\lambda \qquad (8)$$

where d is the distance between the star and the Earth. The total energy $L(\lambda,T)$ can also be expressed as

$$L(\lambda,T) = 4\pi\cdot R^2\cdot B(\lambda,T) \qquad (9)$$

where R is the radius of the star and $B(\lambda,T)$ is Planck's function. Combining Eq(8) and Eq(9), we find

$$F_\lambda = (R/d)^2\cdot B(\lambda,T) \qquad (10)$$

In the present case, Equation (10) can be rewritten as

$$\begin{aligned} F_\lambda &= [L_1(\lambda,T_1) + L_r(\lambda,T_r)]/4\pi d^2 \\ &= L_1(\lambda,T_1)\cdot[1 + L_r(\lambda,T_r)/L_1(\lambda,T_1)]/4\pi d^2 \end{aligned} \qquad (11)$$

Substituting Equation (1) into Equation (11) yields

$$F_\lambda = (R_1/d)^2 \cdot B_1(\lambda,T_1) \cdot L'(\lambda,T_1,T_r,i,r_1,r_2) \qquad (12)$$

Let us choose one of the solutions (not shown in Table IX), r_1=0.046, r_2=0.278, i=32°, T_1=68000K, and R_1=0.12$R_\odot$, then d is the only variable in Eq(12). Thus, the distance of the system (d) can be determined by substituting the observed fluxes and the above parameters into Eq(12). The resulting distances calculated at different wavelengths are not equal to each other (see Table X). In order to solve this problem, the distances (d) in Table X were separately substituted into Eq(12) to derive the theoretical fluxes (F_λ) and then fitted to the observed fluxes. The distance, d=557 pc, which gives the smallest deviation of the residuals in the fit is the best value for the distance of the system. In fact, this value is an upper limit, because the model with the largest R_1 at the lowest T_1 was used in the above calculation. The blackbody curves at maximum and minimum light are shown in Figure 15. The blackbody curves fit well at UBVRIH but poor at JK.

Table X. Distances derived from the fluxes at maximum and minimum light

λ (Å)	L'		d (pc)	
	min	max	min	max
3600	1.087	1.930	557	552
4400	1.140	2.272	552	555
5500	1.213	2.678	574	577
6600	1.279	3.012	548	548
8100	1.357	3.372	536	528
12200	1.507	4.008	593	577
16550	1.601	4.385	506	534
22180	1.676	4.676	496	513

The flux ratio diagram (Figure 2 of Berriman et al. 1985) which is based on the flux ratios $F_\nu(J)/F_\nu(K)$ and $F_\nu(H)/F_\nu(K)$ can be used to verify the origin of the infrared flux observed at minimum light. From Table III, the JHK-magnitudes at minimum light are 14.0, 13.82, and 13.85, respectively. These were transformed into the CTIO system (Carter 1993) to allow use of the flux ratio diagram which is on the CTIO system. The resulting magnitudes are J=13.97, H=13.82, and K=13.84, which were then converted to fluxes by adopting the zero points, $\log(F_\nu(J))$=-22.82, $\log(F_\nu(H))$=-23.01, and

$\log(F_\nu(K))=-23.21$ Watts$\cdot m^{-2}\cdot Hz^{-1}$ (Wilson et al. 1972). This yields $F_\nu(J)/F_\nu(K)=2.18$ and $F_\nu(H)/F_\nu(K)=1.61$ which falls very close to the locus of the upper main sequence at temperature ~8000K. This temperature is much too high for the secondary and may represent T_{eff} of the partially heated hemisphere of the secondary which has been seen at minimum light. From the model fits, in the case of a system which has a primary with T_{eff}~68000K (lowest fitted T_1) illuminating the inside face of the secondary's atmosphere, the temperature of the heated face of the secondary is greater than 8000K which is consistent with the above estimate.

§5.7.3 Possible Evolution of the System

In very wide binaries with massive primaries, the primary evolves to a red giant (or a red supergiant). Once the giant expands sufficiently to fill its Roche lobe, it begins mass transfer on a dynamical time scale at a rate of ~0.1 $M_\odot$/yr. The accreting secondary, a low mass main sequence star, can not adjust its structure at that high rate. Thus, the transferring material, instead of accreting onto the secondary, passes through the outer Lagrangian point (L_2) and fills the outer Roche lobe (Warner 1994). At this stage, the binary is embedded in a "common envelope". The common envelope gives frictional resistance to the orbital motion of the secondary. Thus the two components transfer angular momentum to the envelope and gradually spiral in with decreasing orbital period and separation. Eventually, the common envelope is ejected when the energy deposited in the envelope exceeds its binding energy. By this time the binary will have reduced its orbital period to be $\leq$ ~1 days and may appear as a nucleus of a planetary nebula (PN) such as LSS2018 (Drilling 1985), MT Ser (Grauer and Bond 1983; Green et al. 1984), and V477 Lyr (Bond 1980 and 1987). After the planetary nebula has dissipated, the hot primary gradually cools down and evolves into a white dwarf. The secondary has not yet filled its Roche lobe (Paczynski 1985). Thus, the system is still detached, such as GK Vir (Green, Richstone and Schmidt 1978) and V471 Tau (Bond 1985 and references therein).

These short-period binaries consisting of a white dwarf or a precursor of a white dwarf, and a lower main sequence star are generally believed to be progenitors of cataclysmic variables (PCV) (e.g. Ritter 1986 and Patterson 1984). Each PCV will become a CV as soon as the secondary fills its Roche lobe by means of orbital angular momentum loss due to magnetic braking or/and gravitational radiation.

From visual inspection of the images of EC11575-1845 on UKST plates taken in the U, B, and R bands, no nebulosity is visible. Thus the object emerged from the common-envelope phase at least 10^4 years ago, because planetary nebulae are only visible for $\sim 10^4$ yrs (Ritter 1986; Warner 1994). Let us take $M_1=0.68M_\odot$, $M_2=0.21M_\odot$, and $R_2=0.29R_\odot$ and assume that the system loses its angular momentum via gravitational radiation to achieve a semi-detached state. According to Equation (7) of Ritter (1986), the secondary will fill its Roche lobe and begin mass transfer in the next $\sim 1\times10^{10}$ yrs at an orbital period ~3 hrs. If the angular momentum is lost via magnetic braking, the dynamic time scale for the system to reach the semi-detached state can be estimated using equation (11) of Ritter (1986). The system will take about 1.5×10^8 yrs, which is shorter than that for gravitational radiation, to reduce its P_{orb} to be ~3 hrs.

Among the known PCVs, a selection of those showing a significant reflection effect are listed in Table XI. A comparison between these objects show that

Table XI. Pre-cataclysmic Variables with Reflection Effect

Object	Spectral types	P_{orb} (hrs)	T_1 (K)	Amplitude of reflection effect U	B	V	R	I	Ref
MT Ser	sdO+dM	2.72	50000	0.15	0.15				1,2
V477 Lyr		11.32	60000		0.5				3,4
UU Sge	sdO+dK-M	11.16	>30000		0.28	0.26			5,6
VW Pyx		16.1			1.5				4
HFG1		13.95			1.1				4
LSS2018	sdO+dM	8.57	77000	0.437	0.486	0.563	0.609	0.668	7
EC11575 -1845	sdO+dM	7.86		0.646	0.736	0.846	0.932	1.020	
BE UMa	DO+dM1-5	2.d3	80000			1.5			8

References: (1) Grauer and Bond (1983); (2) Green et al. (1984); (3) Bond (1980); (4) Bond and Grauer (1987); (5) Budding and Kopal (1980); (6) Bond et al. (1978); (7) Londolt and Drilling (1986); (8) Ferguson et al. (1987).

(1) the secondaries are generally K-M dwarfs, (2) T_{eff} of the primaries are higher than ~30000K, (3) narrow emission lines are visible in their spectra except EC11575-1845 which shows broad emission lines (see section 5.7.1), (4) the orbital periods are shorter than 1 day except for BE UMa, and (5) EC11575-1845 and BE UMa are not surrounded by nebulosity but the rest are nuclei of PN. From the above discussion of PCV's evolution, EC11575-1845 is older than the first six objects in Table VIII and is probably younger than BE UMa.

§5.8 Summary

EC11575-1845 is a non-eclipsing binary consisting of an sdO primary and a late M type secondary showing a large reflection effect. The system is not further than ~600pc away from the Earth. The physical properties of the system are summarized as follows: (1) the effective temperature of the primary is at least 68000K; (2) the effective temperature of the heated hemisphere of the secondary is higher than ~8000K; (3) the masses of the primary and secondary are about 0.18-1.50 $M_{\odot}$ and 0.06-0.43$M_{\odot}$ respectively; (4) the system has an inclination 28-60° and a mass ratio 0.29-0.32.

If the effective temperatures of the primary and secondary are determined, the other parameters can then be fixed. This requires IUE and IR observations to obtain the flux distribution in order to determine the T_{eff} of both components.

References:

Berriman, G., Szkody, P., and Capps, R.W. (1985). *Mon. Not. R. astr. Soc.*, **217**, 327.

Bessell, M.S. (1979). *Publ. astr. Soc. Pac.*, **91**, 589.

Bond, H.E., Liller, W., and Mannery, E.J. (1978). *Astrophys. J.*, **223**, 252.

Bond, H.E. (1980). *IAU Circ. No.* 3480.

Bond, H.E. (1985). in D.Q. Lamb and J. Patterson (eds.), *Cataclysmic Variables and Low-Mass X-Ray Binaries*, D. Reidel Publishing Company, p15.

Bond, H.E., and Grauer, A.D. (1987). in A.G. Davis Philip, D.S. Hayes, and J.W. Liebert (eds.), IAU Colloqium No. **95**, *The Second Conference on Faint Blue Stars*, L. Davis press, p221.

Budding, E. and Kopal, Z. (1980). *Astrophys. Space Sci.*, **73**, 83.

Carter, B. (1993). in *Precision Photometry*, eds. D. Kilkenny, E. Lastovica and J. Menzies, p100.

Deeming T.J. (1975). *Astrophys. Space Sci.*, **36**, 137.

Drilling, J.S. (1985). *Astrophys. J. Lett.*, **294**, L107.

Eggleton, P.P. (1983). *Astrophys. J.*, **268**, 368.

Ferguson, D.H., Liebert, J., and Cutri, R. (1987). *Astrophys. J.*, **316**, 399.

Glass, I.S. (1983). *MK III I.R.P. Instruction Manual*, SAAO.

Grauer, A.D., and Bond H.E. (1983). *Astrophys. J.*, **271**, 259.

Green, R.F, Richstone, D.O., and Schmidt, M. (1978). *Astrophys. J.*, **224**, 892.

Green, R.F., Liebert, J., and Wesemael, F. (1984). *Astrophys. J.*, **280**, 177.

Greenstein, J.L., and Sargent, A.I. (1974). *Astrophys. J. Suppl.*, **28**, 157.

Johnson, H.L., and Morgan, W.W. (1953). *Astrophys. J.*, **117**, 313.

Johnson, H.L. (1966). *Ann. Rev. Astron. Astrophys.*, **4**, 193.

Landolt, A.U., and Drilling, J.S. (1986). *Astron. J.*, **91**, 1372.

Napier, W.McD. (1968). *Astrophys. Space Sci.*, **2**, 61.

Paczynski, B. (1985). in D.Q. Lamb and J. Patterson (eds.), *Cataclysmic Variables and Low-Mass X-Ray Binaries*, D. Reidel Publishing Company, p1.

Patterson, J. (1984). *Astrophys. J. Suppl.*, **54**, 443.

Ritter, H. (1986). *Astron. Astrophys.*, **169**, 139.

Stobie, R.S., Morgan, D.H., Bhatia, R.K., Kilkenny, D., and O'Donoghue, D. (1988). in A.G. Davis Philip, D.S. Hayes and J.W. Liebert (eds.), IAU Colloq. **95** : *The Second Conference On Faint Blue Stars*, L. Davis Press, Schenectady, p493.

Stobie, R.S., Chen, A., O'Donoghue, D., and Kilkenny, D. (1992). in B. Warner (ed.), Variable Stars and Galaxies, *Astr. Soc. Pac. Conf. Series*, **30**, p87.

Struve, O. (1970). in G.H. Herbig (ed.), *Spectroscopic Astrophysics*, University of California press, p83-105.

Tonry, J., and Davis, M. (1979). *Astron. J.*, **84**, 1511.

Warner, B. (1994). *Cataclysmic Variable Stars*, Cambridge University Press, in press.

Whitelock, P.A. (1988). *Infrared Photometry Manual*, SAAO.

Wilson, W.J., Schwartz, P.R., Neugebauer, G., Harvey, P.M., and Becklin, E.E. (1972). *Astrophys. J.*, **177**, 523.

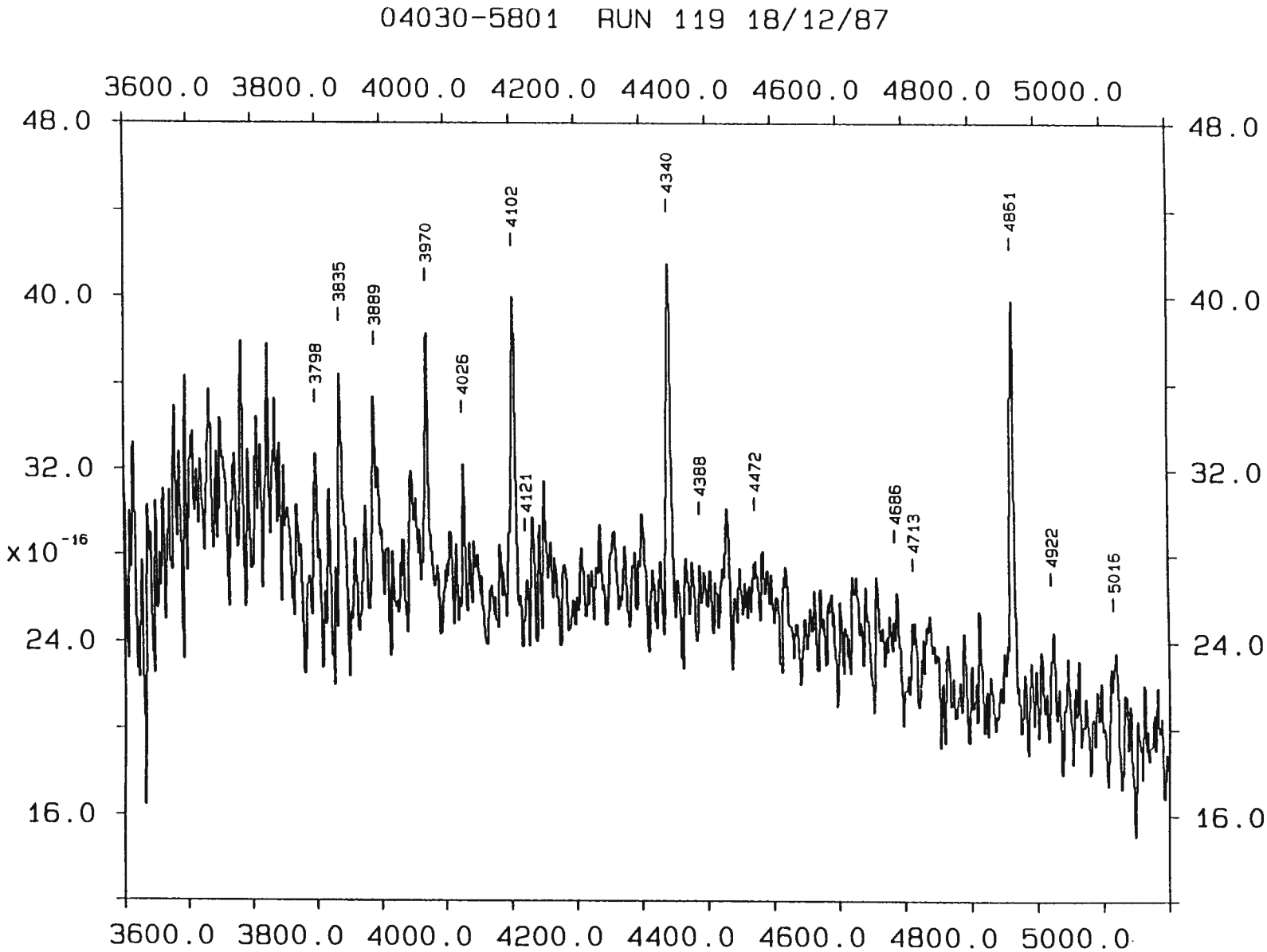

Figure 1. The spectrum of EC04030-5801 at 15th Bmag was taken on 1987 December 18.

Chapter 6: *Dwarf Novae - EC04030-5801, EC23128-3105, and EC23593-6724*

§6.1 Introduction

Dwarf Novae (DN), a subtype of CVs, have outbursts recurring on a time scale of weeks to years, with a typical amplitude 2-5 mag, lasting for 2-100 days. At present, there are two theories to explain DN outburst: one is the Mass Transfer Instability model in which the secondary suddenly increases its mass transfer rate due to an instability in the secondary's atmosphere; the other is the Disk Instability model in which the material in the disk falls rapidly onto the surface on the white dwarf when the disk exceeds a critical surface density (Cannizzo & Kaitchuck 1992). The spectroscopic character of the outburst is a transition from an emission line spectrum to an absorption line spectrum. The emission lines dominant at quiescence are gradually superposed by the rising continuum. At maximum light absorption lines appear with an emission core in most DN (eg. RX And: Kaitchuck et al. 1988; TW Vir: Mansperger & Kaitchuck 1990). During the decline, the emission components become stronger and stronger on the way back to quiescence.

Three dwarf novae, EC04030-5801, EC23128-3105, and EC23593-6724, are presented in this Chapter. The details of these DN are discussed in the following sections: EC04030-5801 in section 6.1, EC23128-3105 in section 6.2, and EC23593-6724 in section 6.3.

§6.2 EC04030-5801

EC04030-5801 was selected from the UB plate pair which was taken with the UKST on 1986 November 9 and was spectroscopically observed and identified as a CV in 1987. The first spectrum with 4Å resolution shows strong Balmer lines in emission with a FWHM ~6Å and no obvious Helium lines except HeI λ4026 Å (Figure 1). CaII λ3934Å is also seen. Three years later, follow-up photometry was commenced in 1991. Two outbursts were caught in 1991 December

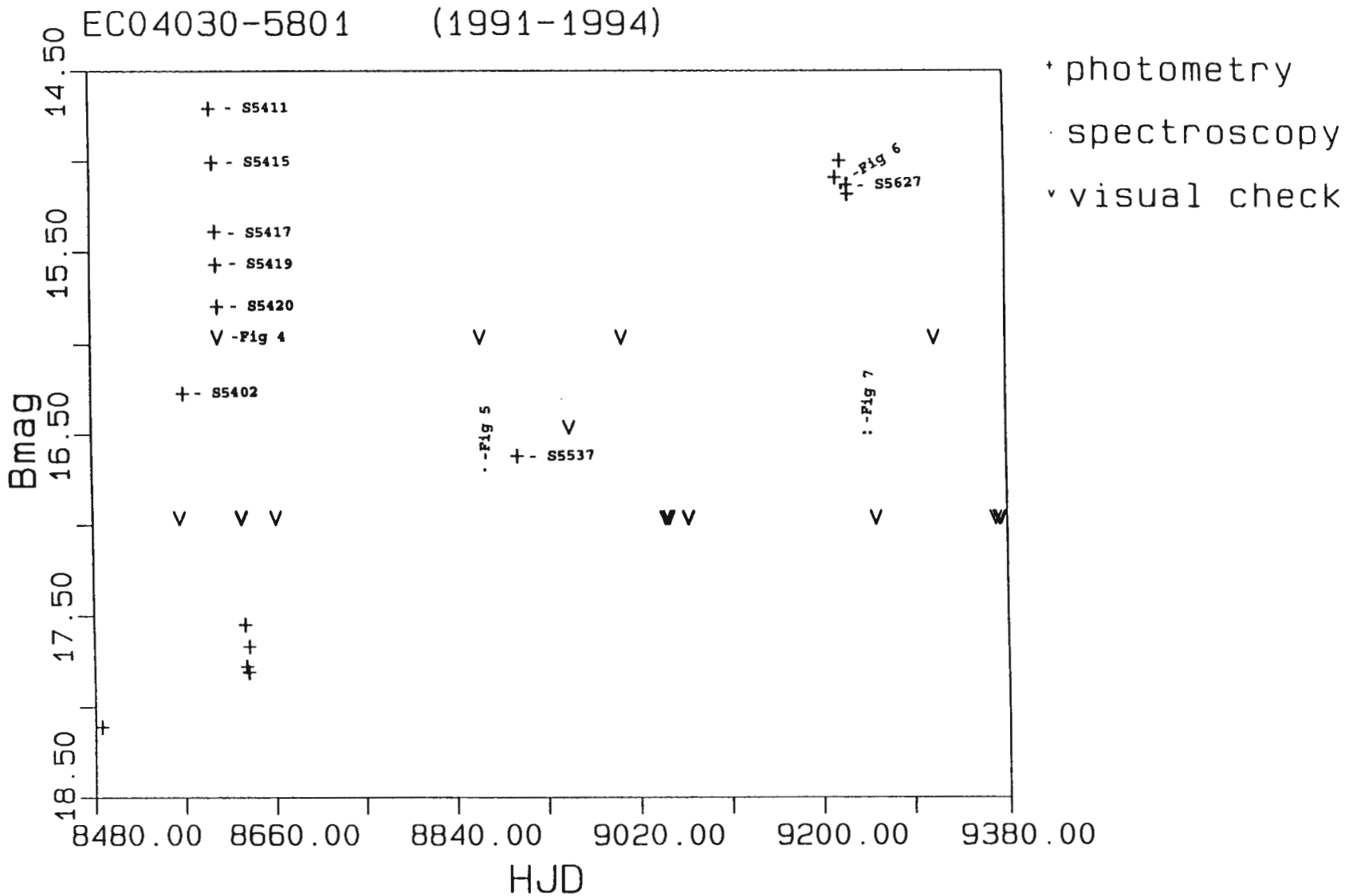

Figure 2. Long term light-variation of EC04030-5801 during 1991-1993. The (+) signs represent the magnitudes obtained by UBV measurements or the mean magnitudes of HSP; if the magnitude is obtained by HSP, the run number of the light curve is labelled in the right-hand side of the (+) sign. The dots represent the magnitudes derived from the spectroscopic flux; the spectrum is shown in the plot whose Figure number is beside the dot.

§6.2.2 Results

§6.2.2.1 Photometric Characteristics

The photometric data, obtained from photography, visual checks, photoelectric photometry, and spectroscopy during 1986-1994, are collected in Table II; only the 1991-1994 data are plotted in Figure 2. Figure 2 shows that EC04030-5801 underwent outburst with a slow decline of ~0.18 mag/day in early December of 1991 (JD8594-JD8601). The interval between the rising branch and the declining branch at ~16.4 Bmag (hereafter Full Width at Half Maximum of outburst) is about 36 days. Note that from visual inspection the object was found to be fainter than 17th mag on 1991 October 31 (JD8561) and was detected at 16.3 Bmag on 1991 November 5 (JD8565), leading us to assume that the object was on the rise in early November. In 1992, the object was found at 16.7 Bmag, at least one magnitude above quiescence, on August 31 (JD8865) and October 2 (JD8897); the time interval between these two measurements is ~32 days, very close to the FWHM of the 1991 outburst. Thus there was probably an outburst in the period August 31 - October 2. Ten months later, an outburst was observed in 1993 August. During the outburst, the colours showed no significant variation (Table III). The outburst in 1993 differed from the outburst in 1991: the brightness was almost unchanged over 12 days (August 12-24: JD9211-JD9223). This may imply that the EC04030-5801 was in "standstill", a characteristic of the Z Cam stars. On the other hand, the HSP-run on 1993 August 24 (Figure 3c) showed no flickering, different from the behaviour of Z Cam at standstill (see Figure 3 of Robinson 1973). Eventually the object faded to ≥17th Bmag in 1993 September (JD9238). A visual inspection made during 1994 Jan 11-16 (JD9364-JD9369) showed that the object was still fainter than 17th Bmag. From the 1991-1994 observations (Figure 2), it is apparent that outbursts recurred approximately every 10 months, or shorter if outbursts which occurred between observing seasons were missed.

The HSP during the 1991 outburst reveals that the flickering activity became stronger as the system returned towards quiescence (Figure 3ab and

Table II. Brightness Variations of EC04030-5801 During 1986-1993

UT Date	HJD	B mag	Measuring Method
9 Nov 86	6743.36007	14.9	UKST plate
12 Oct 87	7081.5530	15.5	UBV photometry
18 Dec 87	7147.50850	15.9	spectroscopic flux
12 Aug 91	8480.62974	18.2	HSP
31 Oct 91	8561.56	>17.	visual inspection
5 Nov 91	8565.50155	16.3	HSP
3 Dec 91	8594.42051	14.8	"
5 Dec 91	8596.41311	15.1	"
8 Dec 91	8598.51370	15.4	"
8 Dec 91	8599.41200	15.6	"
9 Dec 91	8600.45197	15.8	"
10 Dec 91	8601.3096	>16.	visual inspection
31 Dec 91	8622.45	>17.	visual inspection
1 Jan 92	8623.34	>17.	visual inspection
2 Jan 92	8624.32560	17.6	HSP
3 Jan 92	8625.38477	17.8	"
5 Jan 92	8627.33078	17.9	"
6 Jan 92	8628.33116	17.7	"
4 Feb 92	8657.3	>17.	visual inspection
28 Aug 92	8862.65	>16.	visual inspection
31 Aug 92	8865.64773	16.7	spectroscopic flux
2 Oct 92	8897.55566	16.7	HSP
23 Nov 92	8949.64	≥16.5	visual inspection
23 Jan 93	9001.31	>16.	visual inspection
23 Feb 93	9042.29	>17.	visual inspection
25 Feb 93	9044.29	>17.	visual inspection
27 Feb 93	9046.29	>17.	visual inspection
18 Mar 93	9065.27083	>17.	visual inspection
12 Aug 93	9211.5990	15.1	UBV photometry
17 Aug 93	9216.6581	15.1	"
18 Aug 93	9217.6443	15.2	spectroscopic flux
23 Aug 93	9222.6284	15.2	UBV photometry
24 Aug 93	9223.6163	15.2	"
24 Aug 93	9223.6614	15.1	spectroscopic flux
8 Sep 93	9238.6384	~16.5	"
14 Sep 93	9244.5970	~16.5	"
19 Sep 93	9249.48	>17.	visual inspection
15 Nov 93	9307.47	>16.	visual inspection
11 Jan 94	9364.38	>17.	visual inspection
14 Jan 94	9367.38	>17.	visual inspection
15 Jan 94	9368.38	>17.	visual inspection
16 Jan 94	9369.38	>17.	visual inspection

Table III. UBV photometry at Outburst for EC04030-5801

UT Date	HJD	V	B-V	U-B
12 Oct 87	7081.5530	15.48	0.071	-0.805
12 Aug 93	9211.5990	15.14	0.005	-0.824
17 Aug 93	9216.6581	15.00	0.045	-0.803
23 Aug 93	9222.6284	15.12	0.064	-0.875
24 Aug 93	9223.6163	15.19	0.045	-0.853

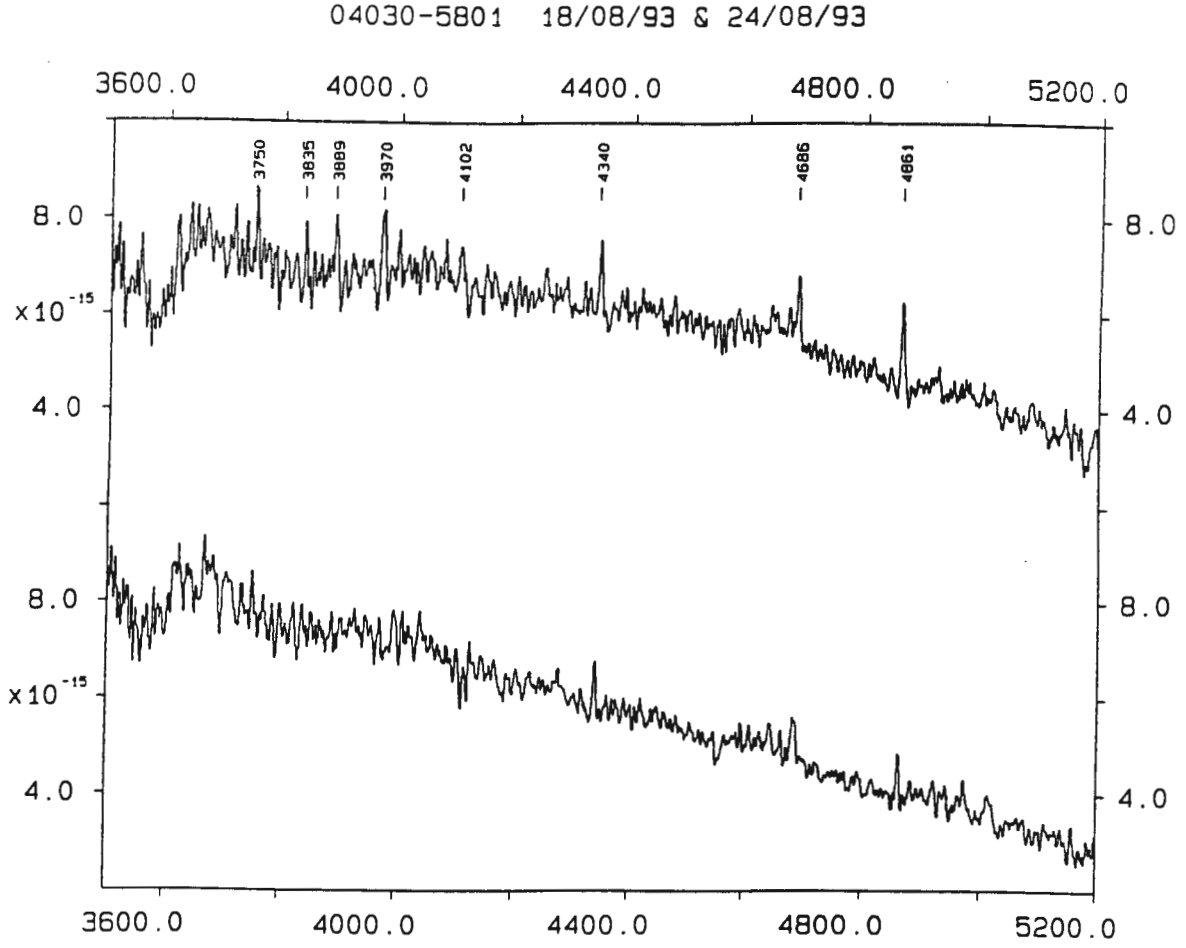

Figure 6. The spectra of EC04030-5801 in the outburst of 1993. The bottom panel was taken on 1993 August 18 and top panel was taken on 1993 August 24.

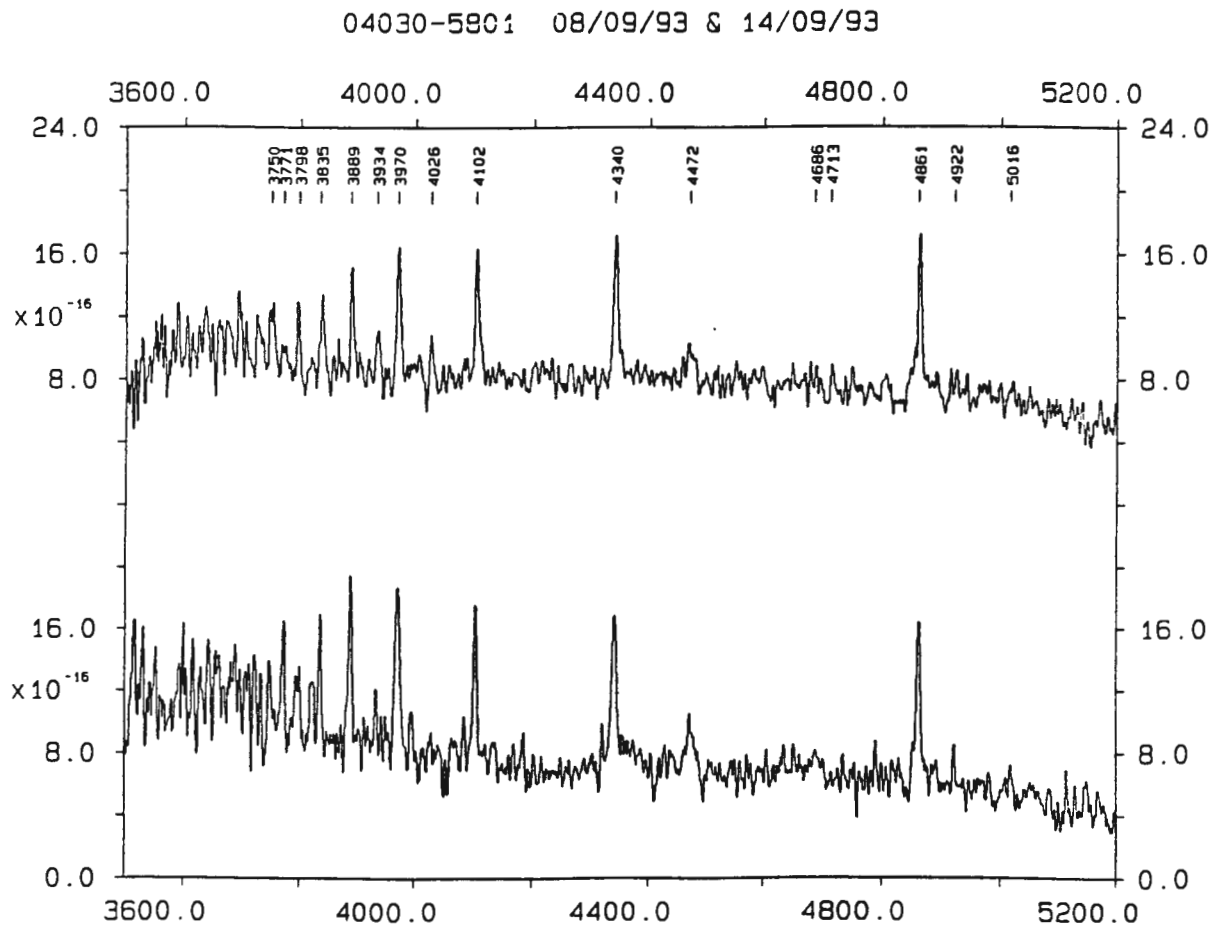

Figure 7. The spectra of EC04030-5801 in the late decline of 1993 outburst. The bottom panel was taken on 1993 September 8 and top panel was taken on 1993 September 14.

stronger emission features, with the CIII/NIII blend λ4650Å, HeII λ4686Å, and the Balmer series resolved up to H12 λ3750Å. The Balmer lines are narrow (FWHM ~6 Å) and show very weak absorption in the wings on both nights (Figure 6). The emission lines are stronger in the spectrum of 1993 August 24 than that in 1993 August 18 as though the system was on the declining branch of a DN outburst (see Figure 4 & 5 of Kaitchuck et al. 1988). However, the Bmag was unchanged during August 13-24. Unfortunately there are insufficient observations to define the profile of the declining branch of the outburst. Two weeks later (in September), the object had faded to 16th Bmag and stayed at approximately the same brightness during 1993 September 8-14. Two spectra with 4Å resolution were obtained and are shown in Figure 7. These two spectra in Figure 7 have similar spectral features. Comparing the spectra of September (Figure 7) with that of August (Figure 6), it is apparent that (1) strong Balmer lines and weak HeI lines emission are present in late decline (at ~16th Bmag), (2) HeII λ4686Å is stronger at 15th Bmag and very weak in late decline, (3) CaII λ3934Å emission appeared in the late decline, (4) the line widths of Figure 7 are broader than those of Figure 6 (see Table IV), (5) the slope of the flux distribution in late decline (Figure 7) is flatter than that at 15th Bmag (Figure 6). The system was visually inspected and found to be fainter than 17th Bmag on 1993 September 19. Thus these spectral characteristics suggest that the accretion disk is transitting from optically thick to optically thin and the disk is cooling down. These properties are typical of dwarf novae.

Table IV. Width of Balmer lines for EC04030-5801

UT Date	Hβ FWZI(±3Å)	Hγ	Hδ
18 Aug 93	10	12	-*
24 Aug 93	17	15	-*
8 Sep 93	25	25	19
14 Sep 93	26	28	20

*It's difficult to measure due to weak line profile.

The relative radial velocities in the 1993 outburst were measured. The spectrum of 1993 September 14 was chosen to be the template because it shows the strongest signal-to-noise ratio among the spectra in Figure 6 and 7. The

relative radial velocities were determined using the cross-correlation technique. The results are listed below:

UT Date	HJD 2440000.+	RV km/sec
18 Aug 93	9217.63274	-49
24 Aug 93	9223.65448	9
8 Sep 93	9238.63843	-6
14 Sep 93	9244.59702	0

The RV measurement for the night of August 18 is not very accurate due to the poor S/N ratio. The radial velocities of the other nights show that the system seems to have slow orbital motion. This supports the possibility that EC04030-5801 may have an orbital period ≥6 hrs, as suggested by the T_d-P_{orb} relation in section 6.2.2.1.

§6.2.3 Summary

The results of the preliminary study of EC04030-5801 are summarized as follows: (1) EC04030-5801 is a new dwarf nova; (2) the outburst of 1991 had an amplitude of ~3 magnitudes; (3) the outburst in 1993 lasted for at least 12 days at almost constant brightness, 15th mag. During this time, the spectra show that the strength of the emission is on the increase, typical of the spectral behaviour of DN in the decline phase from an outburst; (4) from the data of 1991-1994, the outburst frequency is estimated to be ~10 months. Perhaps the most unusual behaviour of this object is its tendency to stay at brightness levels intermediate between quiescence and outburst for several days or more. This was seen in 1993 August and September and possibly 1992 August and October.

Useful further work might include: (1) time-resolved spectroscopy to obtain the orbital period; (2) UBV photometry and high-speed photometry at quiescence to get the colours and flickering activity; (3) obtaining the long term light curve from sky patrol plates is critical to determine more accurately the outburst amplitude, outburst frequency, and subclass of EC04030-5801.

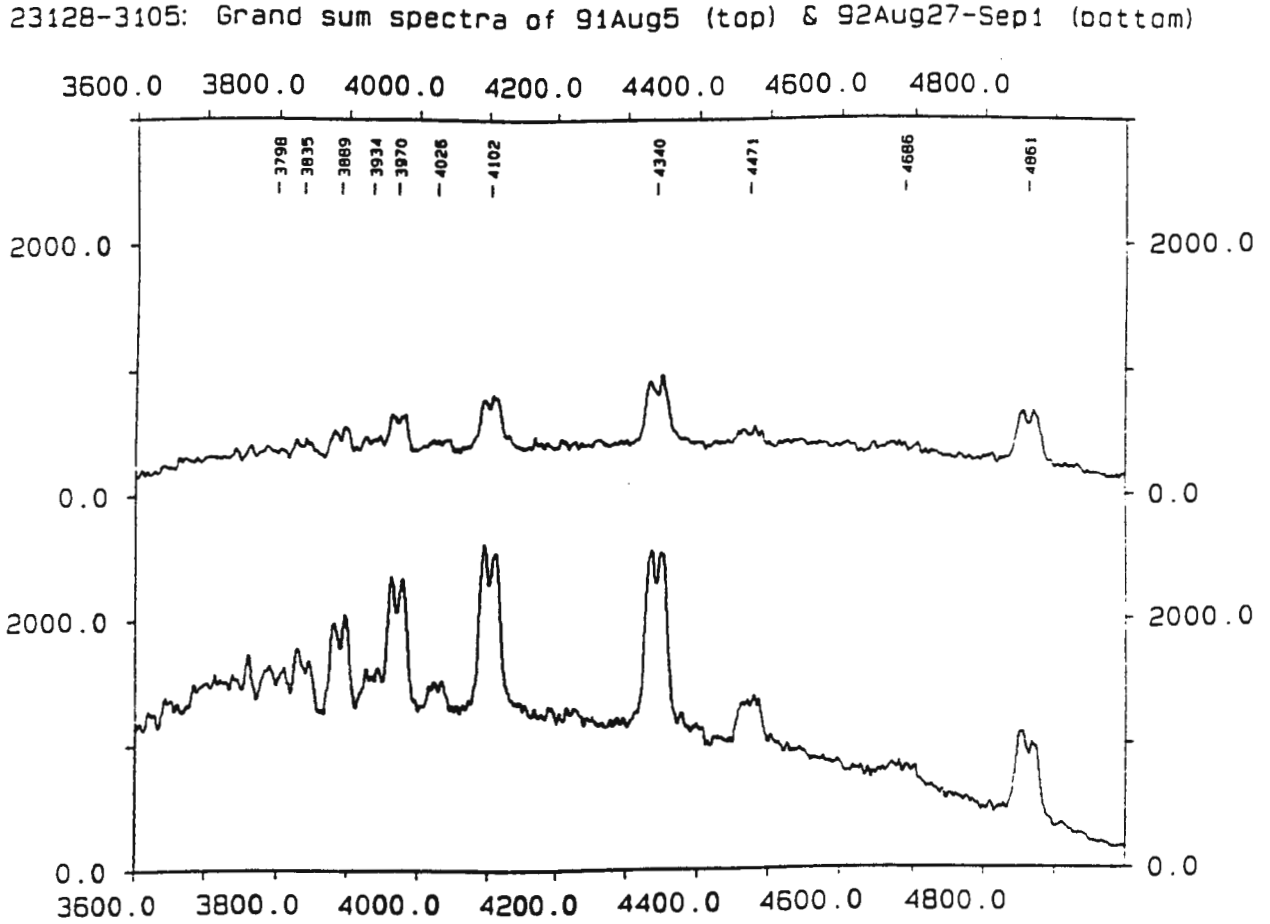

Figure 8. Grand sum spectra of EC23128-3105. The ordinate is in counts; the abscissa is in Angstroms.

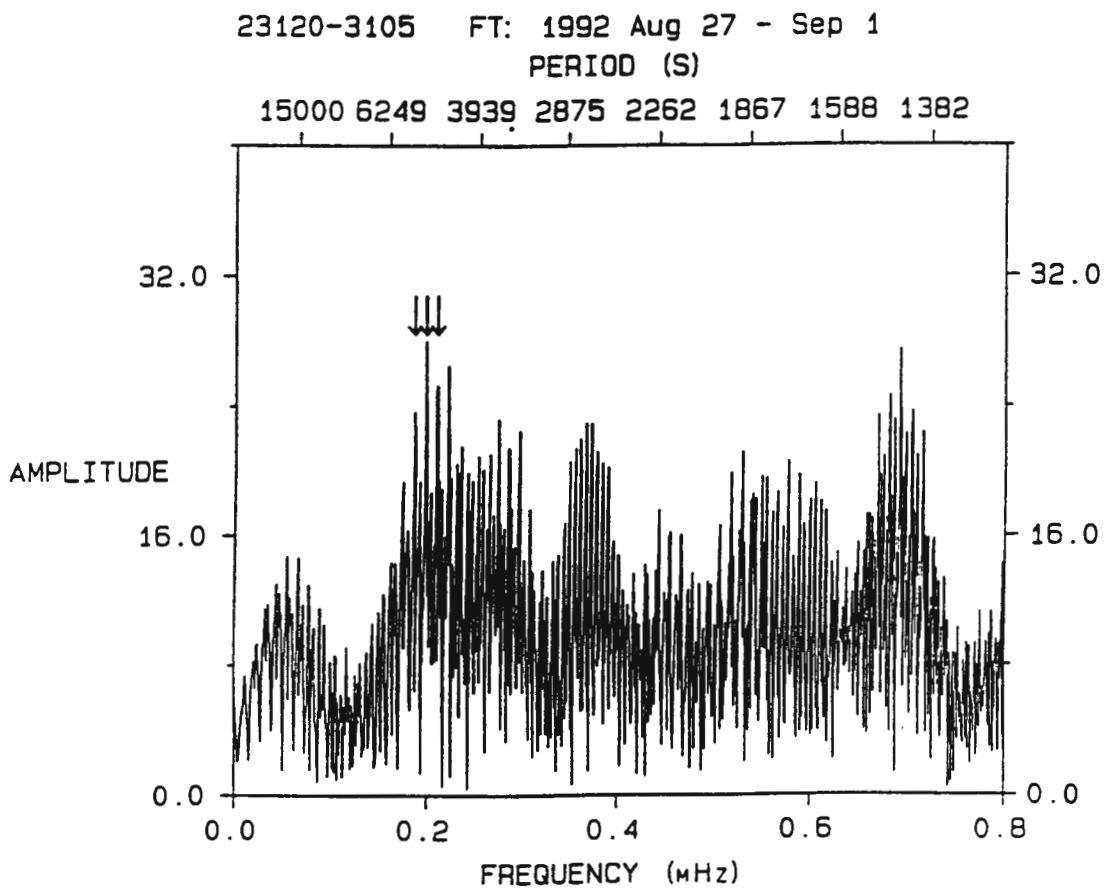

Figure 9. Amplitude spectrum of EC23128-3105 calculated from the data of radial velocities in 1992 August 27-September 1 showing an orbital period of 84-min.

§6.3 EC23128-3105

EC23128-3105 was selected to be a candidate blue object from the UB plate pair on 1986 September 18 and was spectroscopically observed on 1986 October 22 showing broad, double-peaked Balmer lines in emission. From the absence of CIII/NIII λ4650Å, it is likely that the object is a dwarf nova. UBV measurements taken on 1987 October 14 showed that the object was faint and blue (V=16.67, B-V=-0.14, and U-B=-1.17) and fell near the blue end of the blackbody relation in the two-colour diagram.

§6.3.1 Radial Velocity Curves

Time-resolved spectroscopy with 4Å wavelength resolution was obtained with 600 seconds time resolution in 1991 August and with 1200 seconds time resolution in 1992 August. These data are listed in Table V. The grand sum

Table V. Observing Log of Time-Resolved Spectroscopy for EC23128-3105

UT Date	Start UT Time h m	Duration hrs	Resolution (FWHM Å)	Coverage Å
91 Aug 5	22 31	5.33	4	3700-5000
92 Aug 27	00 04	2.00	4	3700-5000
92 Aug 28	23 24	4.00	4	3700-5000
92 Aug 30	23 04	4.00	4	3700-5000
92 Sep 1	00 40	2.66	4	3700-5000

spectra of 1991 August 5 (top) and 1992 August 27-September 1 are plotted in Figure 8 and show broad, double-peaked Balmer emission lines with full width at continuum level (FWZI) ~64Å. The lines are resolved up to H10 and are superimposed on a blue continuum. CaII λ3934Å blended with Hε is clearly present as well as HeI λ4026Å and HeI λ4471Å. In addition to these lines, HeII λ4686Å is barely visible. The grand sum spectra in Figure 8 were used as templates. The relative radial velocities of individual spectra were measured using the cross-correlation technique. The results are listed in Table VI. An amplitude spectrum (shown in Figure 9) was calculated for the data of HJD8862-8867 in Table VI. Its highest peak at 0.1980 ± 0.0006 mHz is not very significant because there are other features of similar amplitude. The radial velocity curves, solid lines in Figure 10, are a least squares fit

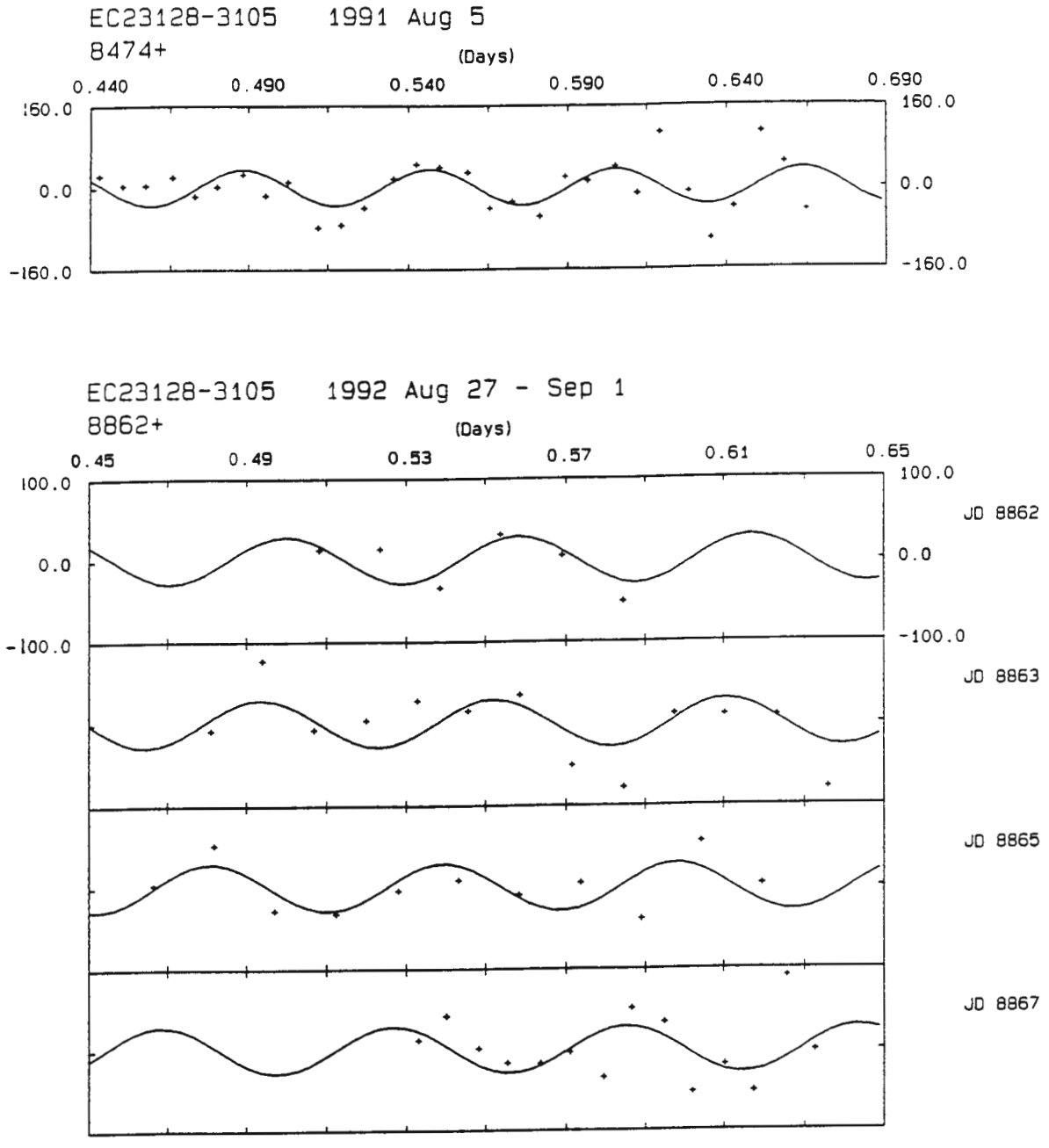

Figure 10. Radial velocity curves of EC23128-3105 for 1991 Aug 5 (top) and 1992 Aug 27 - Sep 1 (bottom).

Table VI. Relative Radial Velocity of EC23128-3105

HJD 2440000.+	RV km/s	HJD	RV	HJD	RV
8474.44277	24	8474.63518	-101	8865.48185	49
8474.45011	6	8474.64224	-39	8865.49708	-30
8474.45718	5	8474.65061	107	8865.51235	-34
8474.46574	22	8474.65768	47	8865.52796	-6
8474.47282	-15	8474.66475	-46	8865.54320	5
8474.47989	3	8862.50815	10	8865.55849	-12
8474.48838	26	8862.52339	11	8865.57372	2
8474.49545	-14	8862.53863	-36	8865.58898	-41
8474.50250	12	8862.55386	28	8865.60421	52
8474.51197	-77	8862.56912	2	8865.61944	0
8474.51916	-72	8862.58437	-53	8867.53315	8
8474.52632	-38	8863.48100	-11	8867.54018	39
8474.53544	17	8863.49397	74	8867.54850	-1
8474.54250	46	8863.50690	-10	8867.55554	-19
8474.54966	40	8863.51981	1	8867.56388	-20
8474.55844	30	8863.53275	24	8867.57098	-5
8474.56551	-40	8863.54567	12	8867.57943	-36
8474.57266	-27	8863.55859	31	8867.58647	47
8474.58132	-57	8863.57150	-54	8867.59479	30
8474.58916	21	8863.58443	-81	8867.60190	-56
8474.59626	13	8863.59735	7	8867.61024	-21
8474.60499	42	8863.61028	6	8867.61728	-55
8474.61207	-11	8863.62319	5	8867.62569	87
8474.61914	107	8863.63612	-82	8867.63273	-4
8474.62812	-8	8865.46649	0		

of a sinusoid of frequency equal to the highest peak in Figure 9, assuming that peak is the correct orbital period (see discussion in next section). The results of the above least squares fit give an ephemeris corresponding to largest redshift T_0 and semi-amplitude K_1 to be

Run	T_0(HJD) 2440000.+	K_1 km/sec	Fitted Period (days)
1991 August 5	8474.4296 ± 0.0028	35 ± 10	0.0584 ± 0.0002
1992 Aug27-Sep1	8862.4998 ± 0.0021	29 ± 7	0.0584 ± 0.0002

The double-peaked profile is principally caused by Doppler broadening in an accretion disk and usually appears in highly inclined dwarf novae such as OY Car (Bailey and Ward 1981), Z Cha (Marsh et al. 1987), and TY PsA (O'Donoghue and Soltynski 1992). The central absorption in the line profiles of EC23128-3105 is not as deep as those of OY Car and Z Cha but is comparable to that of TY PsA. The line width in lines of EC23128-3105 is also comparable to that of TY PsA. Therefore values of semi-amplitude larger than the above K_1 are expected to be observed. Eclipses may also be expected. In fact, there is no eclipse found in the light variations (see next section) and the K_1 is

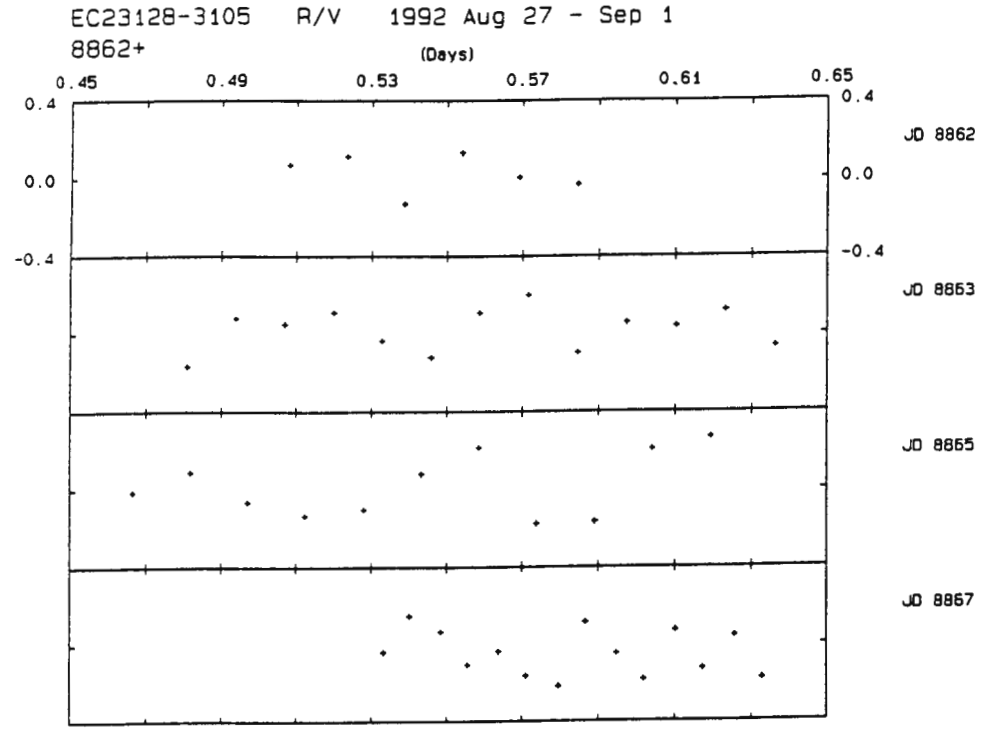

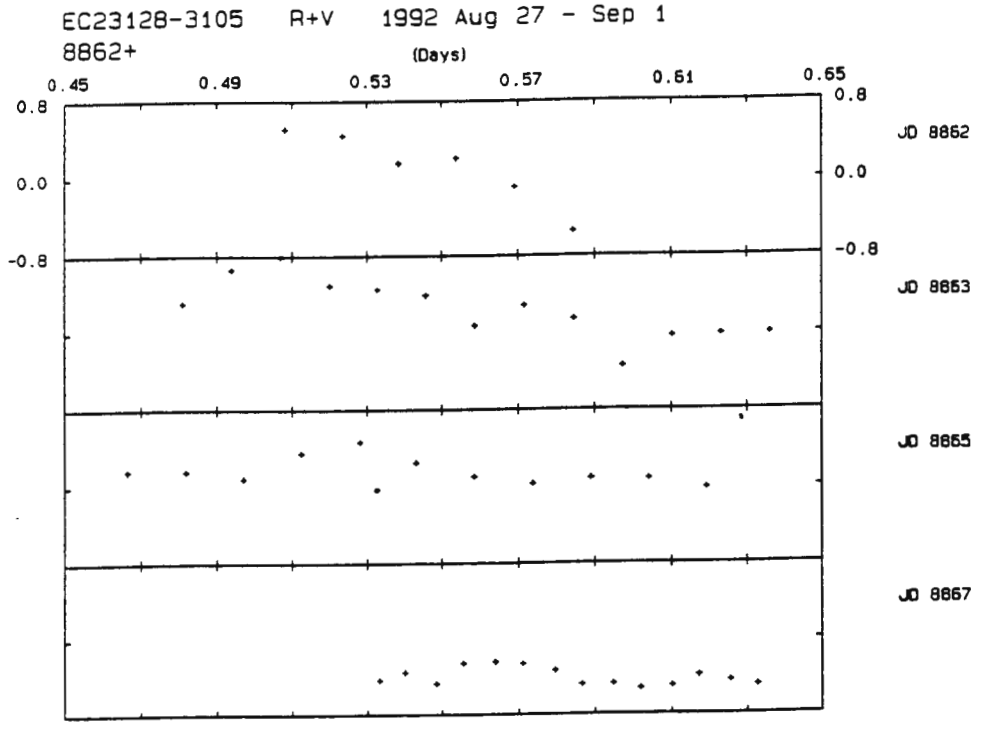

Figure 11. EC23128-3105: Line profile variations of R/V (top) and R+V (bottom). No systematic variations are found.

about 35 km/s in 1991 August and 29 km/s in 1992 August. This leads us to doubt the reliability of the above measurements of radial velocity and suspect that they may be contaminated by periodic variations in the line profiles, unrelated to orbital motion.

In cataclysmic variables, the profiles of the emission lines frequently show variations unrelated to orbital motion. This variation is caused by asymmetric distribution of emission over the accretion disk. A region of enhanced emission will wander back and forward in the line profile and is often called an 'S-wave'. In order to investigate this possibility, the red/violet (R/V) ratio was measured for Hβ, Hγ, Hδ, and Hϵ separately. The technique of O'Donoghue and Soltynski (1992) was used to evaluate the ratio (R/V) and total equivalent width (R+V): first, a fifth order polynomial was fitted to the continuum. The spectrum was normalized by the fitted continuum which was then subtracted. Next, each line was divided into halves about its rest wavelength shifted by the above velocity ephemeris in order to avoid the influence by the apparent orbital motion, and the counts of the red and violet halves were summed separately. The summation range was set equal to the whole line profile. The results are shown in Figure 11; neither R/V nor R+V reveals periodic variations.

Since the radial velocity curves obtained in the previous section are not obviously contaminated by S-waves, the low semi-amplitude of the radial velocity curves may simply be due to a low mass ratio ($q=M_2/M_1$) in the system, a possibility which will now be explored. Let i be the inclination, M_2 be the mass of secondary, and M_1 be the mass of white dwarf. The semi-amplitude, K_1, of the primary's radial velocity curve is given by the mass function:

$$(K_1)^3 = 2\pi G\cdot(M_2\cdot\sin i)^3/[P_{orb}\cdot(M_1+M_2)^2] \qquad (1)$$

where P_{orb} is the orbital period in seconds. The empirical M_2-P_{orb} relation derived by Warner (1994) is

$$M_2 = 4.63\times10^{27}\cdot(P_{orb})^{5/4}\ \text{gm, for } 1.3 \le P_{orb} \le 9\ \text{hrs} \qquad (2)$$

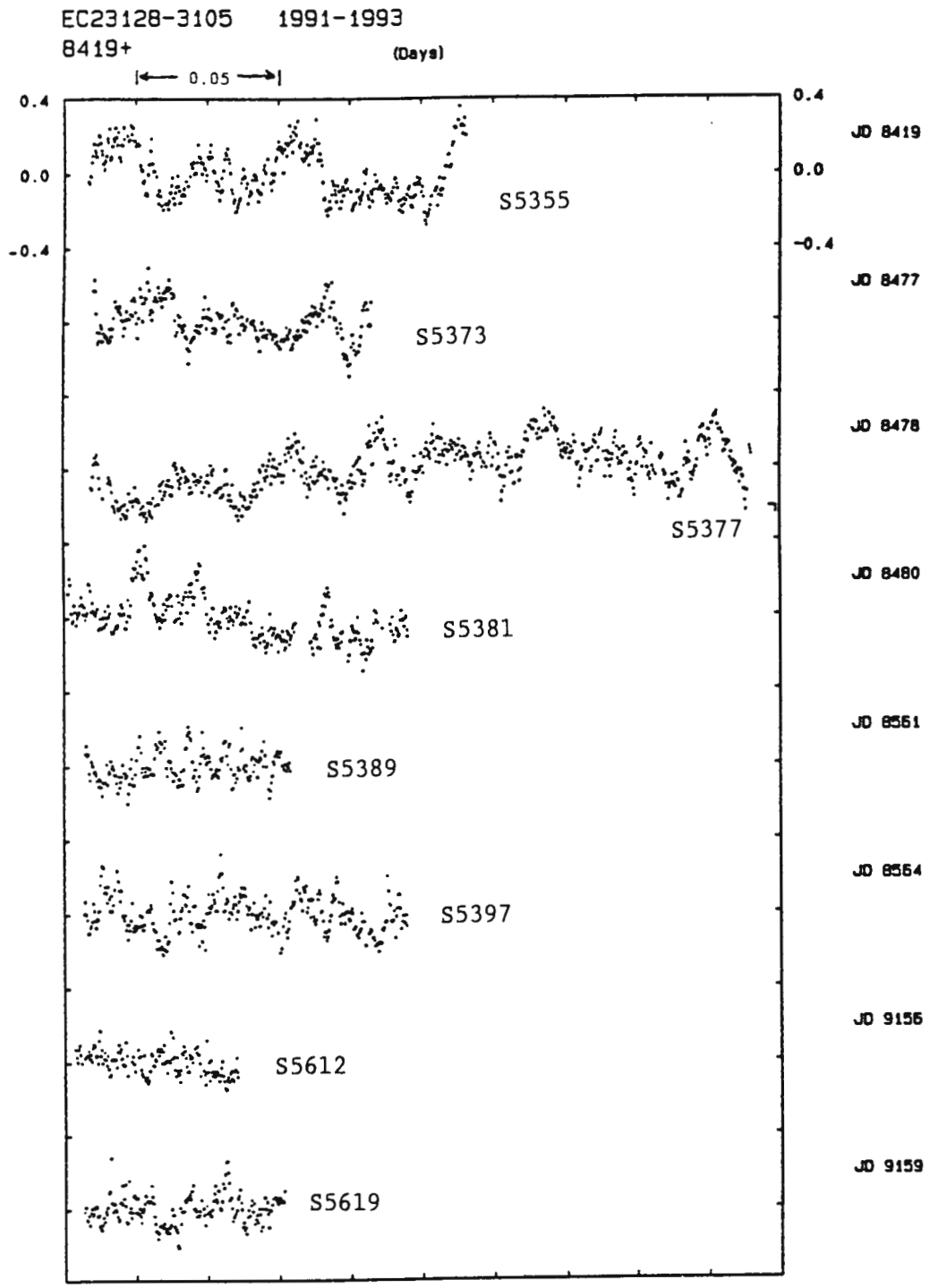

Figure 12. Light curves of EC23128-3105.

In order to obtain a K_1-q relation, equation (2) was substituted into equation (1) yielding

$$K_1 = 125 \cdot (P_{orb})^{1/12} \cdot \sin i/(1+1/q)^{2/3} \quad km/s \qquad (3)$$

Equation (3) can be rewritten in the form:

$$q = [1394 \cdot (\sin i/K_1)^{3/2} \cdot (P_{orb})^{1/8} - 1]^{-1} \qquad (4)$$

Let us assume that the inclination of EC23128-3105 is in the range of 45°-65°, because the line width and central depth in lines are comparable to TY PsA but the system doesn't show eclipses in the light curve. Substituting i = 45° and 65°, P_{orb}=5050 s, and K_1=35 km/s into equation (4) yields a range for the mass ratio, $0.09 \geq q \geq 0.06$. Using equation (2), the mass of the secondary is likely to be about 0.1 $M_\odot$. This yields a value of M_1 greater than 1.1 $M_\odot$ (Note that the lower limit of q implies $M_1 > 1.44\ M_\odot$). Because K_1 and i are not well-determined, these values should be treated with caution. Nevertheless, this result should inspire further spectroscopy to check whether the system does have such a high mass white dwarf.

§6.3.2 Light Variations

The majority of the HSP observations were made in 1991 and the rest were taken in 1993. The observing log is tabulated in Table VII. No outbursts were

Table VII. Observing Log of High-Speed Photometry for EC23128-3105

Run	UT Date	HJD	Duration (hrs)	B_w	ΔB_w
S5355	120691	8419.54733	3.2	16.6	0.73
S5373	090891	8477.57965	2.3	16.7	0.73
S5377	090891	8478.43905	5.5	16.8	0.79
S5381	110891	8480.50091	2.8	16.7	0.86
S5389	311091	8561.26679	1.7	16.8	0.54
S5397	031191	8564.26621	2.7	16.8	0.65
S5612	180693	9156.58307	1.4	16.6	0.48
S5619	210693	9159.59605	1.7	16.7	0.49

detected. The HSP data are plotted in Figure 12. Humps resembling the orbital humps in SU UMa stars such as Z Cha (Bailey 1979 and Wood et al.

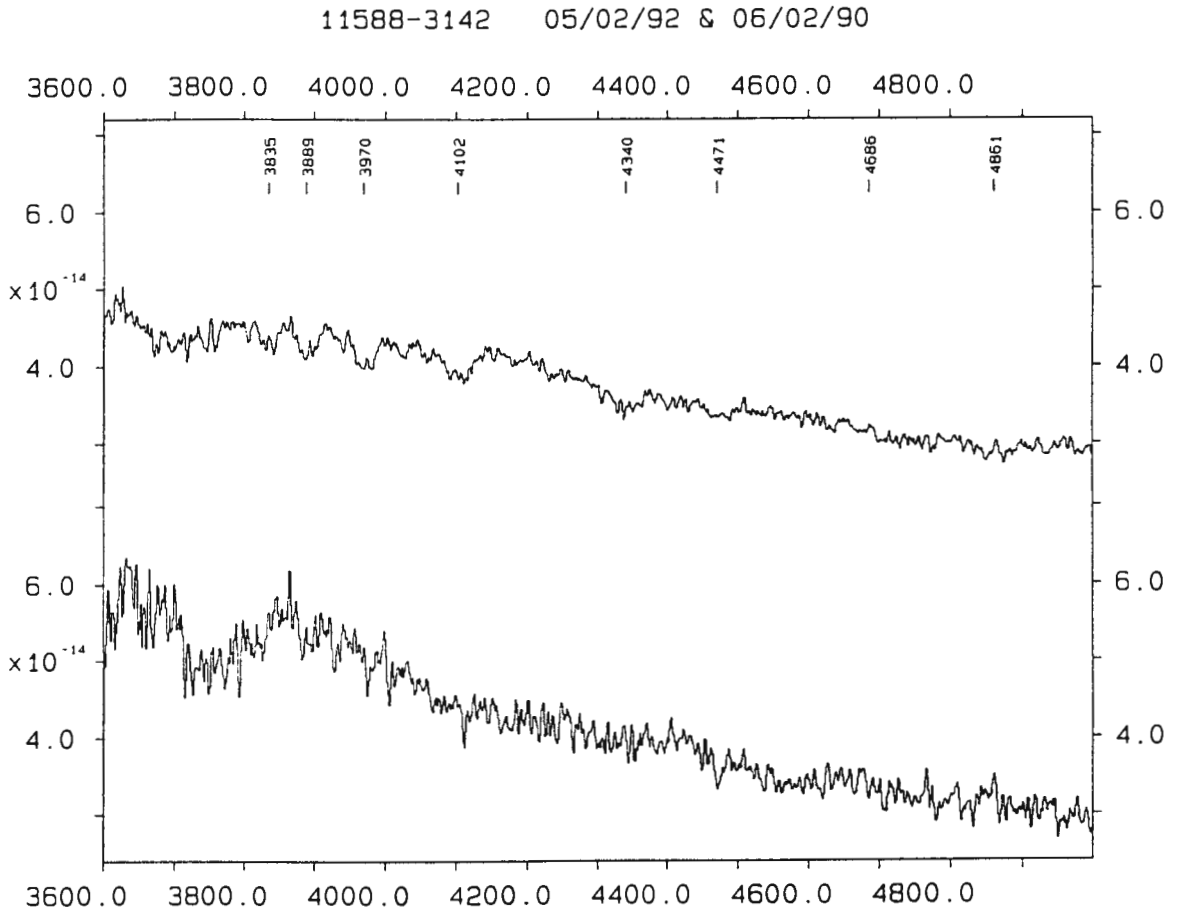

Figure 13. Spectra of EC11588-3142 on 1990 February 6 (top) and 1992 February 5 (bottom).

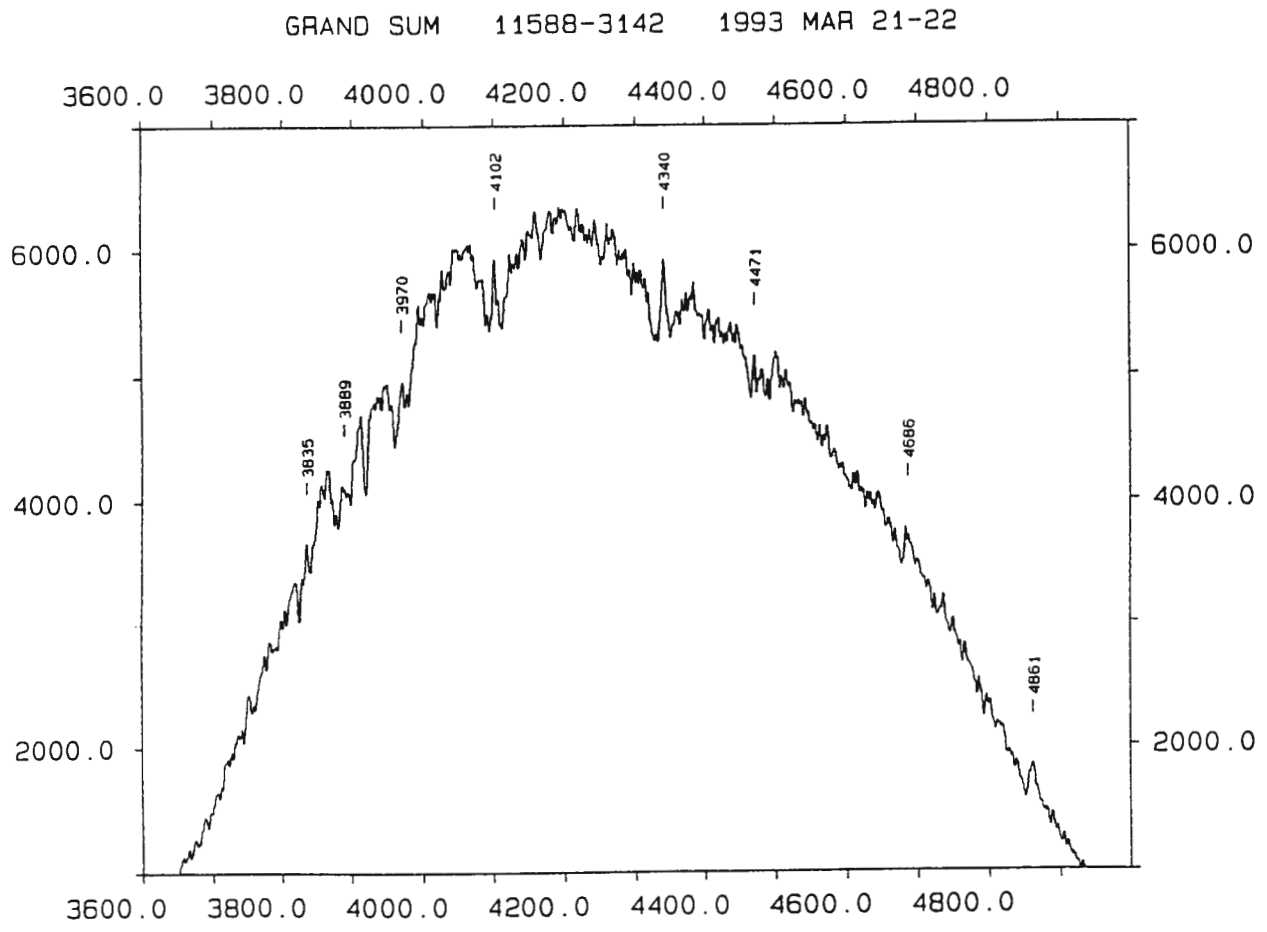

Figure 14. Grand sum spectrum of EC11588-3142 of 1993 March 21-22.

respectively. The results are plotted in Figure 11; the highest peaks for the three groups are consistent with each other:

Group	Frequency (mHz)	Period (hrs)
92Jan	0.0803±0.0014	3.46±0.06
92Feb	0.0816±0.0009	3.40±0.04
93Jan	0.0790±0.013	3.52±0.6

The gaps in the 92Jan and 92Feb groups give rise to the aliases in the lower two amplitude spectra in Figure 11; the nearest one cycle/day aliases cannot be excluded as candidate periods. Assuming, however, that the highest alias is correct, the most precise frequency estimate comes from the longest data set, 92Feb, and gives 3.40 hours for the orbital period.

A K-band magnitude of 13.76 was obtained from the IR observations on 1993 March 17. Bailey (1981) has given a method of determining distances to CVs from their IR photometry. His formula was re-written by Warner (1987) in the form:

$$\log(d) = K/5 - 0.93 + 1.073 \cdot \log(P_{orb}), \quad P_{orb} < 6.5 \text{ hrs}$$

where d, K, and P_{orb} are the distance in pc, the K-band magnitude, and the orbital period in hours respectively. This equation yields a distance of ~240 pc. Because of a possible contribution to the IR measurements from the extensive outer cool regions of the accretion disk, this distance must be regarded as a lower limit.

§7.4 EC11588-3142

EC11588-3142 has UBV colours of V=13.14, B-V = 0.07, and U-B= -0.78, similar to those of EC04224-2014 and EC05565-5935. Nine HSP-runs were obtained which are listed in Table VI and plotted in Figure 12. The photometric behaviour of EC11588-3142 resembles that of EC04224-2014 and EC05565-5935, showing low amplitude (~10%) flickering variations on a time scale of a few minutes. It is thus certain that this object is a CV. No evidence for eclipses or any orbital brightness modulation was found in the

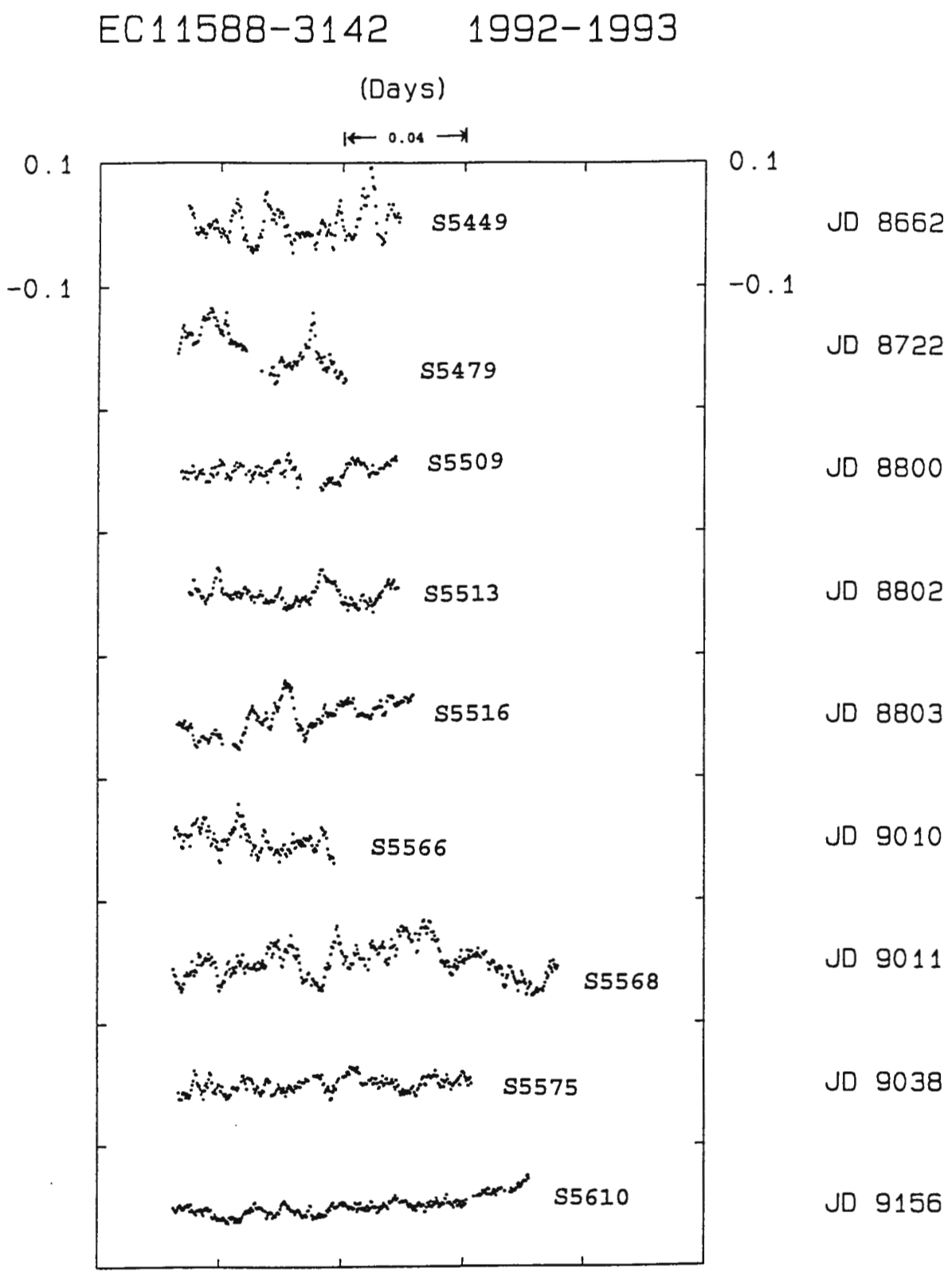

Figure 12. Light curves of EC11588-3142 during 1992-1993.

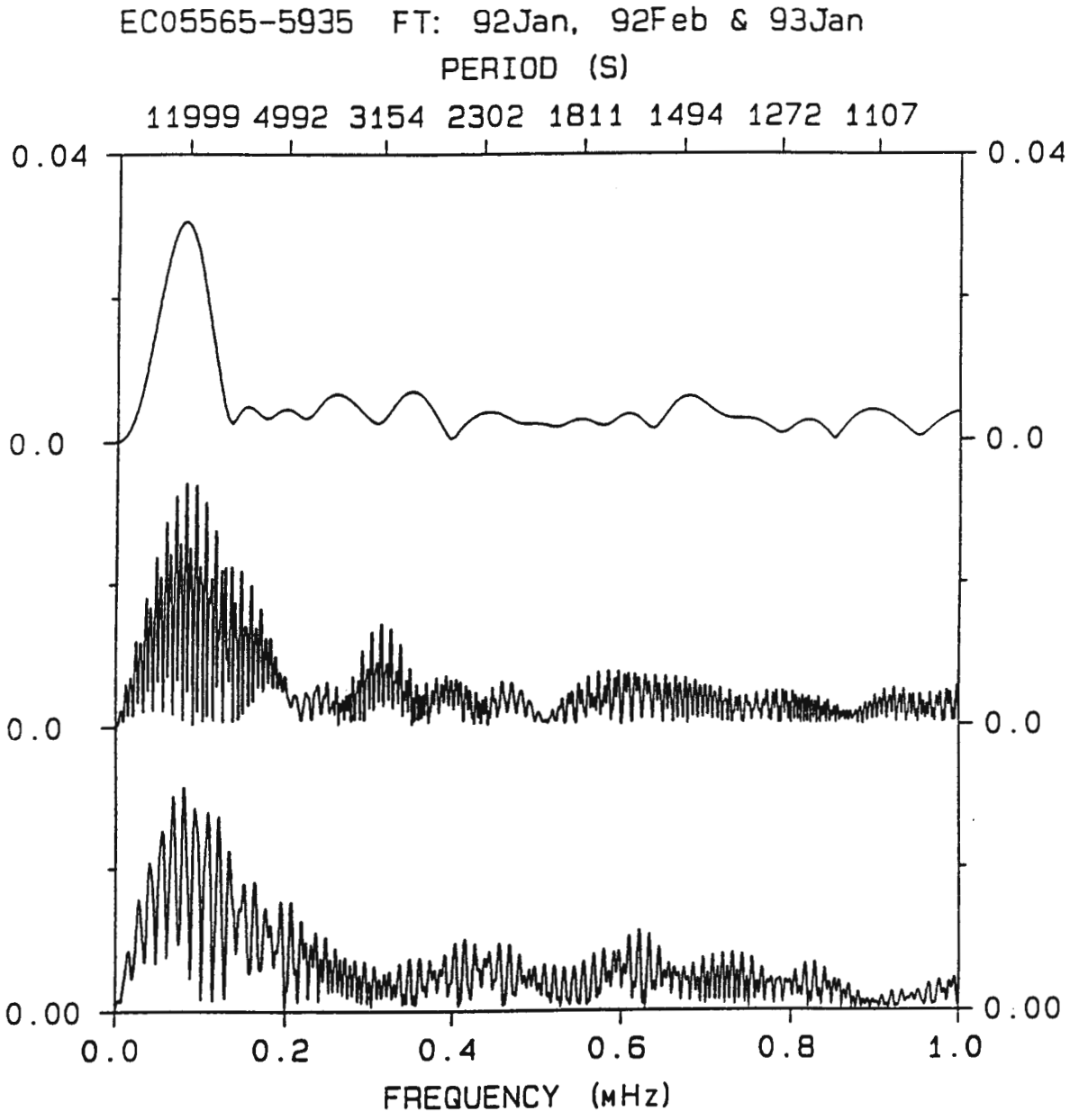

Figure 11. Amplitude spectra of EC05565-5935 for 92Jan (bottom), 92Feb (middle), and 93Jan (top).

and Hutchings 1985). From all the above spectral behaviour, it is clear that EC05565-5935 is a UX UMa star.

Because of the very weak spectral features, it was impossible to obtain sufficient signal-to-noise to derive radial velocities. Thus time-resolved spectroscopy was not attempted.

§7.3.2 Photometry

EC05565-5935 has photometric colours (V=14.31, B-V=0.03, U-B=-0.76) very close to that of EC04224-2014. Twelve HSP-runs were secured which are listed in Table V. A selection is plotted in Figure 10 (the runs S5387-S5408 and S5554 are not shown). Most of the observations showed that the B_w magnitude

Table V. Observing Log of HSP for EC05565-5935

Run	UT Date	Start HJD 2440000.+	Duration hrs	B_w	ΔB_w
S5387	031091	8532.58682	1.4	-	-
S5391	311091	8561.48899	0.7	-	-
S5405	061191	8566.54987	1.3	-	-
S5408	101191	8570.51887	1.5	-	-
S5421	311291	8622.45748	3.0	14.15	0.17
S5422	010192	8623.34354	1.9	14.18	0.19
S5424	020192	8624.46141	1.1	14.33	0.14
S5439	030292	8657.31763	3.0	14.18	0.27
S5441	060292	8659.29511	4.5	14.27	0.25
S5444	070292	8660.33845	2.8	14.22	0.17
S5554	251292	8981.54351	0.7	14.01	0.10
S5569	240193	9012.29695	5.5	13.97	0.20

of the object varied little (~0.3 mag) about the mean of 14.2. The light curves in Figure 10 exhibit rapid flickering activity with a peak-to-peak amplitude of ~15% on a time scale of ~10-20 minutes, superimposed on a slow modulation, a possible signature of the orbital period. This modulation can most easily be seen in the longest run S5569 which lasted for 5.5 hours. Note that there is no evidence for eclipses (Figure 10c). In order to search for a coherent period, the data were divided into three groups, 92Jan, 92Feb, and 93Jan, to calculate Fourier amplitude spectra (Deeming 1975). The 92Jan, 92Feb, and 93Jan contain the data of JD8622-8624, JD8657-8660, and JD9012

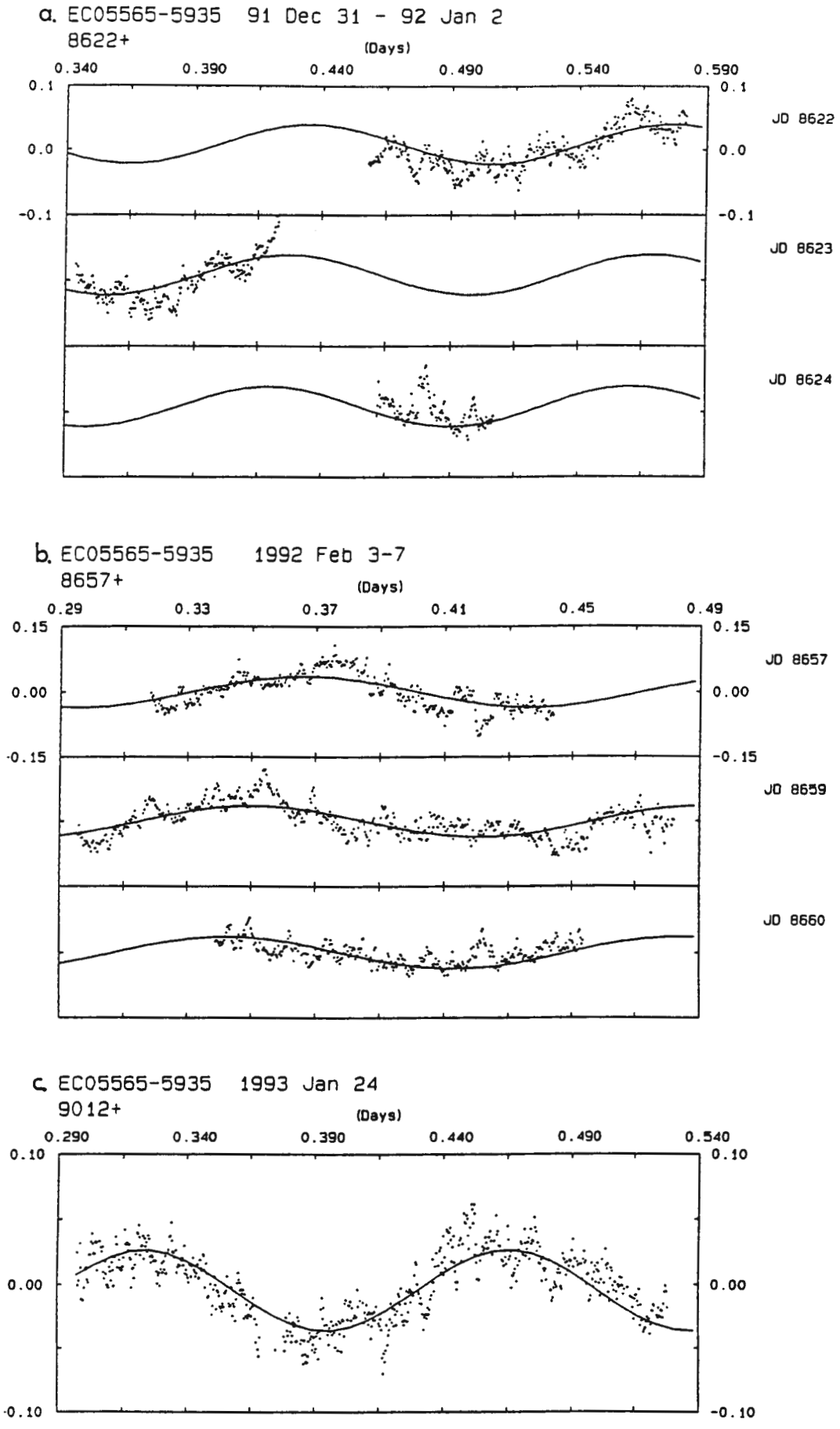

Figure 10. The HSP curves of EC05565-5935 for (a) 92Jan, (b) 92Feb, and (c) 93Jan. The solid lines are a least squares fit of a sinusoid of the mean period 3.4-hr.

In summary, EC04224-2014 is a bright UX UMa star which occasionally declines in brightness and shows an emission spectrum. This spectral variation, absorption/emission transition, is similar to that of VY Scl (Hutchings and Cowley 1984; references therein) and MV Lyr (Voikhanskaya 1988) which show absorption lines in the high state and strong emission lines in the intermediate/low state. Therefore EC04224-2014 is not only a UX UMa star but it may also be a VY Scl star. Note that it has been detected at only a little more than 1 mag below its usual brightness, so the VY Scl classification is not certain.

§7.3 EC05565-5935

§7.3.1 Spectroscopy

The first spectrum of EC05565-5935 with 4Å resolution was obtained on 1988 October 16 and is shown in Figure 7, revealing Balmer lines weakly in emission: the Hß emission line is the clearest feature, and Hγ shows a complex line profile with broad absorption wings; the high Balmer series are barely visible. HeII λ4686Å may be present in the spectrum. On 1990 February 3 and 4, additional spectra with the same wavelength resolution were obtained and are shown in the middle and bottom of Figure 8. Both of these spectra show very weak Balmer lines in absorption; Hγ, Hδ, and Hε are very weak and shallow and Hβ cannot be seen. Two years later, a 4Å resolution spectrum (1992 February 4) and an 8Å resolution spectrum covering λλ4000-7000Å (1992 February 6) were observed and are shown in the top of Figure 8 and Figure 9 respectively. Very weak Balmer emission lines are present in the top of Figure 8. Figure 9 shows almost no features: Hα and Hβ are barely visible, and Hδ probably shows a narrow emission component superimposed on the absorption.

In summary, EC05565-5935 shows two kind of spectral features: very weak Balmer emission lines and broad, weak Balmer absorption lines. It has been observed that emission can temporarily fill in weak absorption lines as in UX UMa (Schlegel, Honeycutt and Kaitchuck 1983) and the UX UMa star BZ Cam (Lu

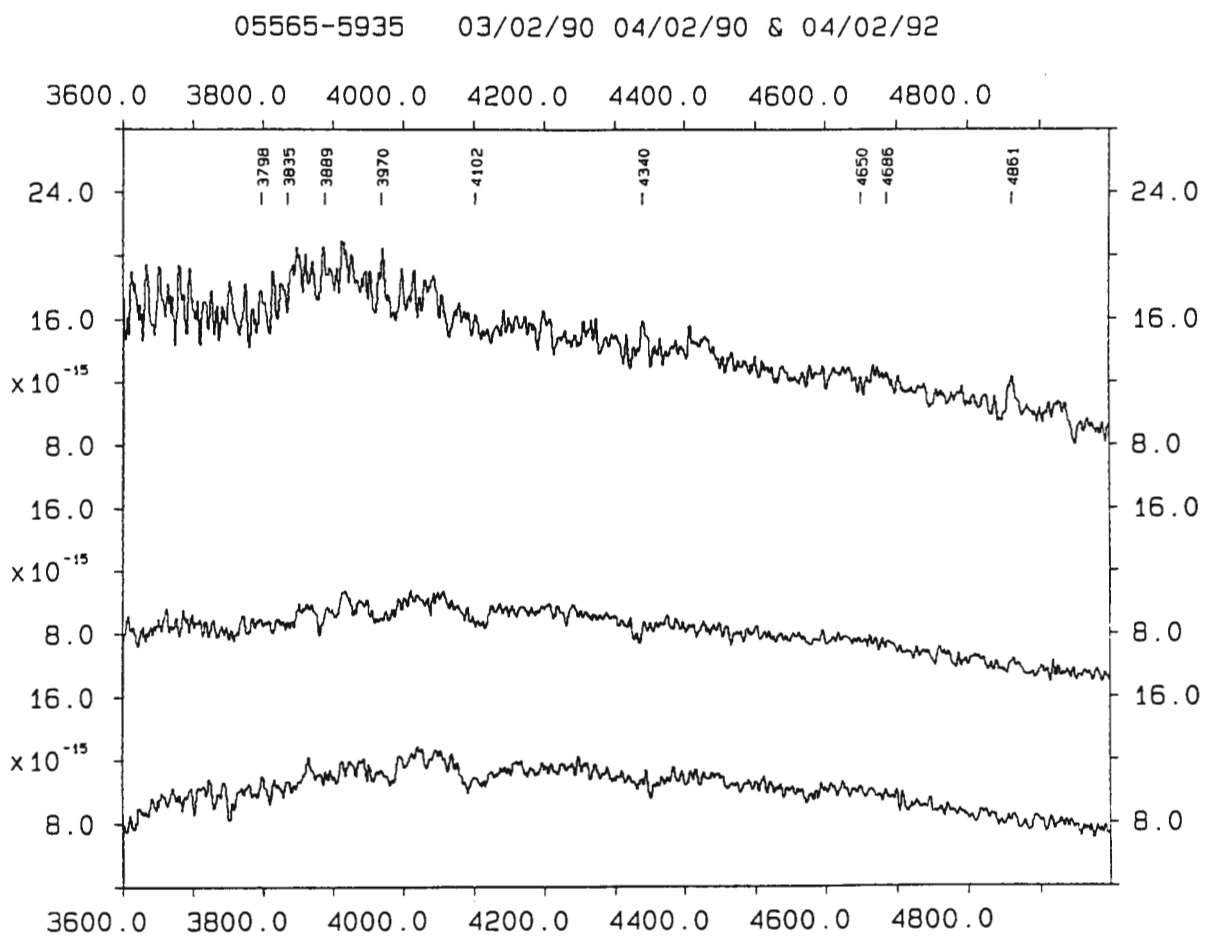

Figure 8. Spectra of EC05565-5935: 1990 Feb 3 (bottom), 1990 Feb 4 (middle), and 1992 Feb 4 (top).

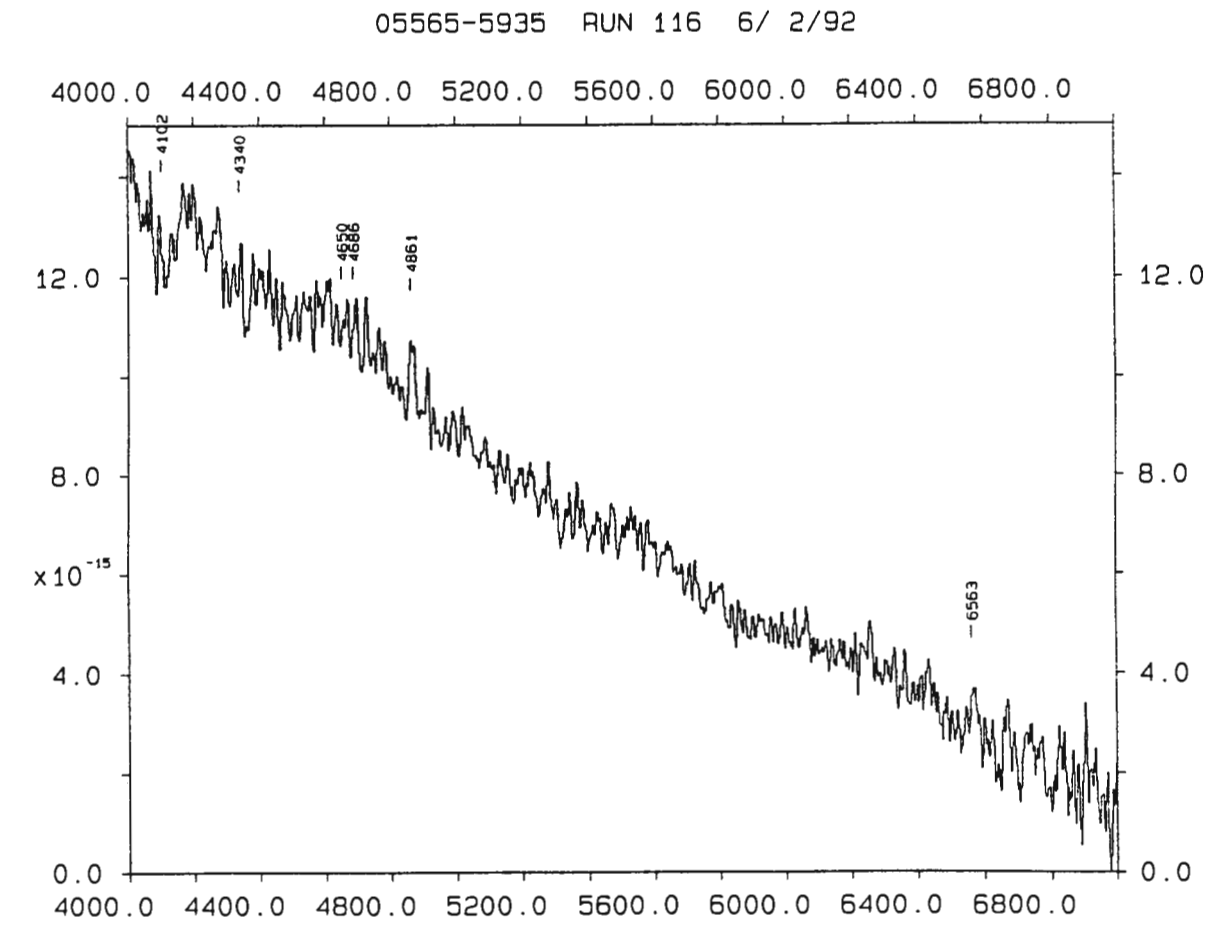

Figure 9. Spectrum of EC05565-5935 taken on 1992 Feb 6 covering λ4000-7000Å.

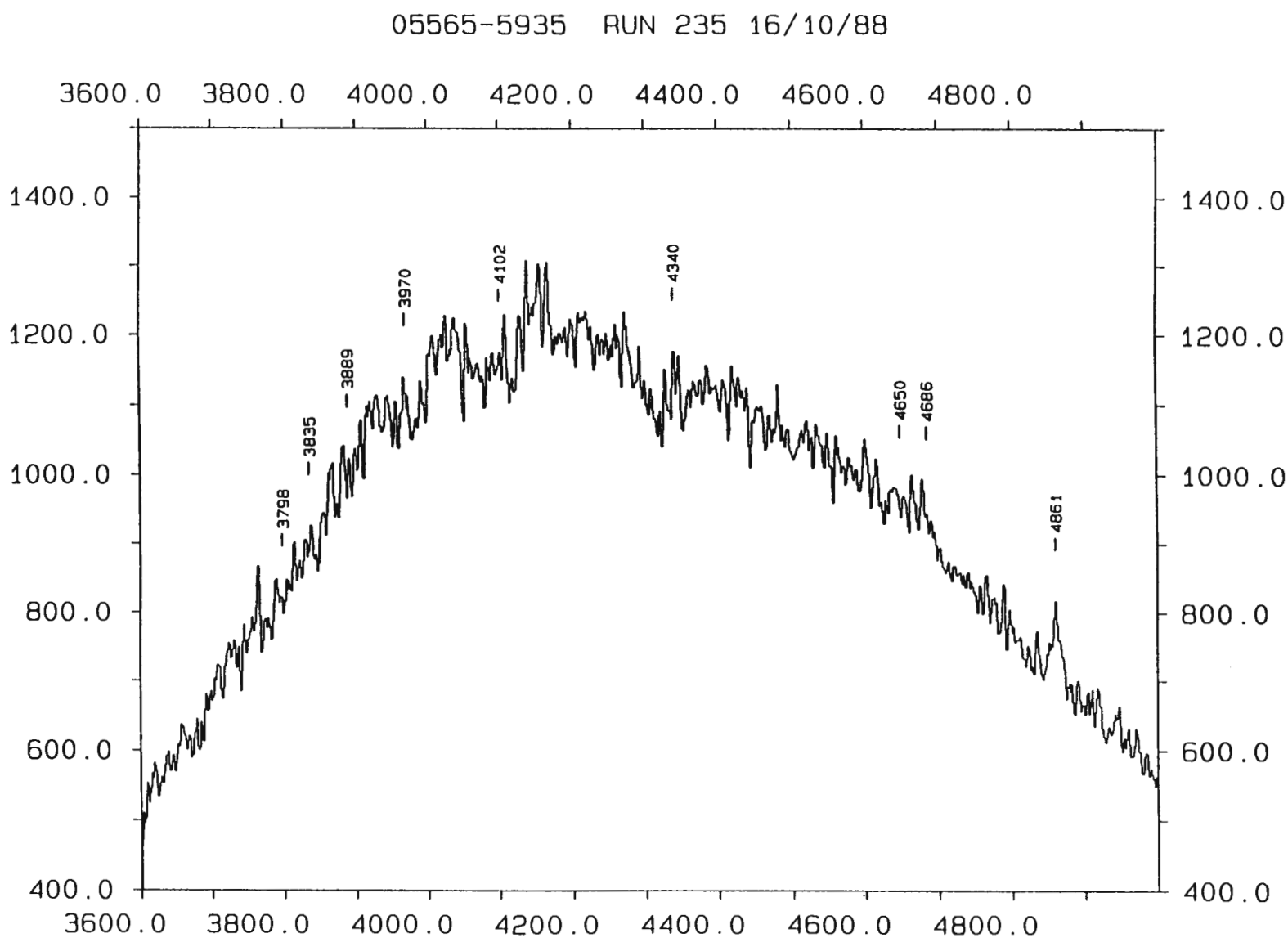

Figure 7. The first spectrum of EC05565-5935 was taken on 1988 Oct 16.

separately by summing all the spectra on that night and the relative radial velocity was determined using the cross-correlation technique. These relative velocities were transformed to the heliocentric velocities using the heliocentric velocity of the templates, 84.4 and 74.3 km/s respectively, and are listed in Table IV. A Fourier amplitude spectrum (Deeming 1975) was calculated from the data of the two nights combined and is shown in Figure 5.

Table IV. Radial Velocities for EC04224-2014

HJD 2440000.+	RV km/s	HJD	RV	HJD	RV
8948.47459	134	8949.34348	64	8949.45053	73
8948.47931	109	8949.34755	120	8949.45553	48
8948.48403	87	8949.35110	152	8949.45909	39
8948.49066	84	8949.35467	137	8949.46267	46
8948.49539	135	8949.35954	85	8949.46624	45
8948.50011	169	8949.36313	112	8949.47108	41
8948.50610	200	8949.36669	96	8949.47465	66
8948.51083	190	8949.37027	231	8949.47822	62
8948.51556	141	8949.37697	171	8949.48180	62
8948.52154	136	8949.38063	179	8949.48665	87
8948.52627	124	8949.38421	117	8949.49021	93
8948.53099	90	8949.38778	173	8949.49379	77
8948.53697	56	8949.39262	142	8949.49737	78
8948.54171	80	8949.39620	176	8949.50219	92
8948.54643	65	8949.39977	197	8949.50577	96
8948.55240	49	8949.40334	179	8949.50934	88
8948.55714	71	8949.40835	120	8949.51292	153
8948.56186	64	8949.41192	37	8949.51783	115
8948.56785	66	8949.41549	141	8949.52139	118
8948.57257	91	8949.41907	76	8949.52497	92
8948.57731	78	8949.42393	39	8949.52853	95
8948.58329	56	8949.42749	68	8949.53337	118
8948.58801	-37	8949.43107	63	8949.53694	46
8948.59274	14	8949.43465	46	8949.54051	44
8948.59874	-15	8949.43968	96	8949.54409	67
8948.60347	14	8949.44337	109		
8948.60819	76	8949.44695	91		

The most likely orbital period (arrowed) in Figure 5 occurs at 0.066 mHz (P_{orb} = 4.2 hrs) but the nearest one cycle/day aliases cannot be ruled out. A sinusoid of the frequency 0.066mHz was fitted to the data of Table IV by least-squares and is shown in Figure 6. The resulting time of largest redshift was JD2448948.501±0.003, the orbital period was $0^d.175\pm0.005$ and the semi-amplitude of the radial velocity curve was 50 ± 5 km/s. Estimates of the radial velocity semi-amplitude in CVs are very unreliable so the value derived here will not be used for a dynamical solution of the system.

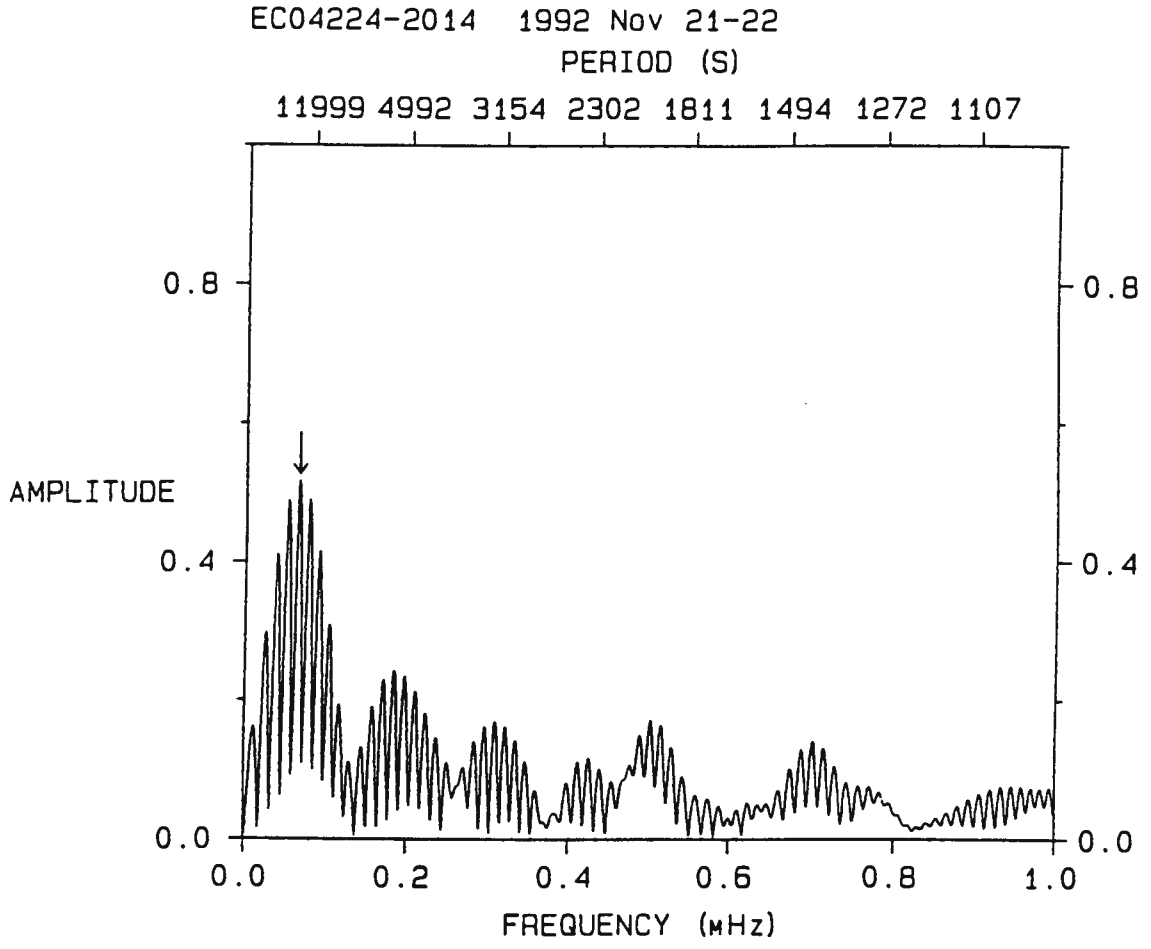

Figure 5. An amplitude spectrum was calculated from the radial velocities obtained during 1992 Nov 21-22.

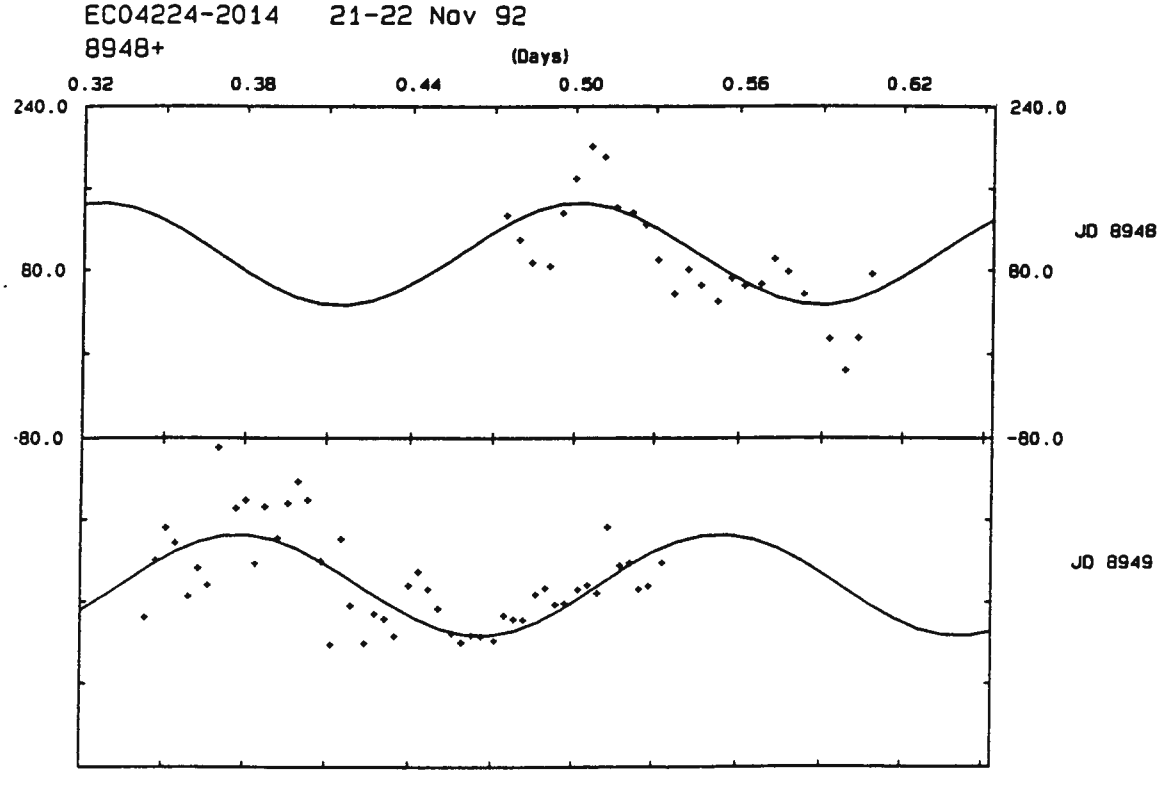

Figure 6. The radial velocity curves of 1992 Nov 21-22. The solid lines are the least-squares fit of the period 4.2-hr.

intensity at wavelength λ and F_c is the fitted continuum level at the same wavelength. The summation was taken over the whole line for the parameter R_{all}, but only over the centre of the line occupied by the emission core for the parameter R_{cen}.

The results are plotted in Figure 4. The top panel shows the HSP-run X0001 binned in 300 seconds bins to match the time resolution of the spectra. Figure 4b shows the behaviour of R_{all} for the four Balmer lines indicated and Figure 4c shows that of R_{cen}. It is clear that the behaviour of R_{cen} is similar to R_{all} and that both are correlated with the light variation. The best correlation with the light variation is shown by Hβ with decreasing correlation up the Balmer series. The quantity R_{all}-R_{cen}, which is a measure of the absorption line wings, was not correlated with the light variation. Clearly the source of the flickering has a significant influence on the emission components of the lines.

The FWHM and FWZI of Balmer lines were calculated and are tabulated in the Table III. The wings of the Balmer emission lines seen on the night of November 21 extend 1200 km/s from the line centre, much less than the absorption lines seen on the following night which extend up to 2400 km/s from the line centre. Assuming that the line width arises from rotational broadening in an accretion disk, it is clear that the absorption line region extends much closer to the white dwarf than does the emission line region.

Table III. FWHM and FWZI of Balmer lines for EC04224-2014

UT Date 1992	Hβ		Hγ		Hδ		Hε	
	FWHM ±2Å	FWZI ±3Å	FWHM	FWZI	FWHM	FWZI	FWHM	FWZI
Nov 21	18	40	20	35	16	35	16	26
Nov 22	40	80	32	70	36	70	-	-

§7.2.3 Searching for an Orbital Period

The orbital period of the system had yet to be determined and as there was no modulation in the photometry, time-resolved spectroscopy was investigated for radial velocity variations. Templates were made for each night

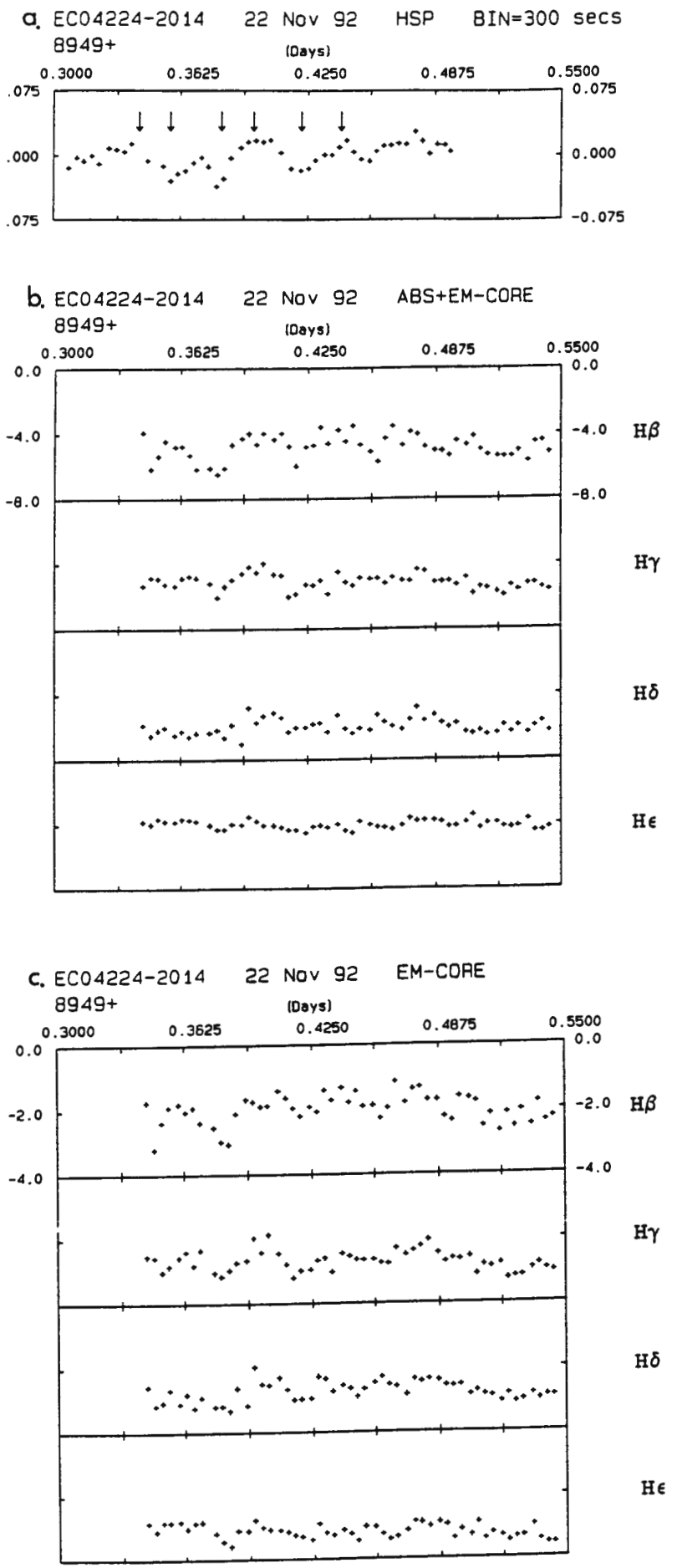

Figure 4. The HSP and the time resolved spectroscopy were simultaneously obtained on 1992 Nov 22. It shows the correlation of the flickering activity and Balmer line depths. (a) Light curve in white light; (b) Balmer line depths; (c) Line depths of central parts of Balmer lines.

calibration with an empirical error of less than 0.3 mag; see discussion in section 2.1.3) on 1992 November 21 and showed a spectrum with broad Balmer emission lines, in complete contrast to the spectra in Figure 1.

In order to study this behaviour, time-resolved spectroscopy (Table II) with a wavelength resolution of 3Å and a time resolution of ~300 seconds was

Table II. Observing Log of Time Resolved Spectroscopy for EC04224-2014

UT Date	Start HJD	Duration (hrs)	B_{mean}
92 Nov 21	8948.4746	3.0	13.0
92 Nov 22	8949.3435	4.4	11.8

secured on the nights of 1992 November 21 and 22. On the second night, HSP observations were simultaneously obtained (Run X0001). The sequence of spectra from 1992 November 21 was binned in orbital phase (using the orbital period derived in the next section) and is shown in Figure 3a. Note that the sequence of spectra on 1992 November 21 does not cover an orbital cycle, so Figure 3a is also a time sequence and has time increasing upwards. The strength of the emission lines underwent a gradual weakening with time, so that the emission lines had almost vanished at the end of the night (Figure 3a). From an estimate of the counts in the wavelength region of λλ4200-4300Å in the individual spectra, a trend of increasing brightness with time can be seen (Figure 3b); the star became ~60% brighter during the run. This estimate is subject to errors due to guiding through a narrow slit. However, we estimate that such errors will be less than 20% showing that the observed brightness increase is intrinsic to the star.

On the following night, the object was back at its typical brightness of B~11.8. The sequence of spectra from this night was binned in orbital phase and shown in Figure 3c. The spectra in Figure 3c show broad Balmer absorption lines with narrow emission cores. HeI λ4471Å is also present in absorption. The emission cores are most prominent in Hß and weaken up the Balmer series. In order to investigate any possible correlation between light variation and spectral variation on November 22, the quantity R, approximate equivalent width, was defined to be $\Sigma(F_\lambda - F_c)/F_c$ where F_λ is the

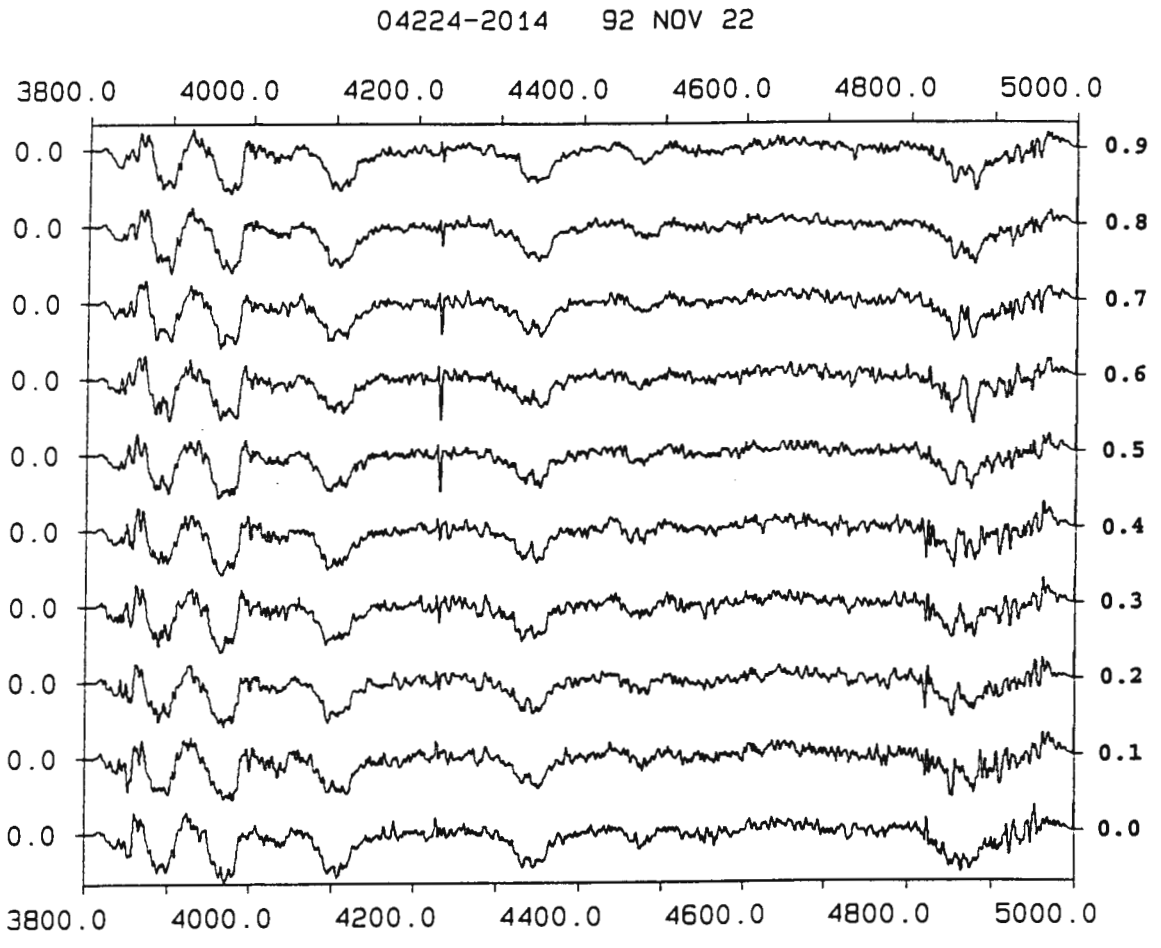

Figure 3c. Phase-binned spectra of EC04224-2014 for 1992 Nov 22. The left ordinate marks the zero intensity and the right ordinate indicates the phases.

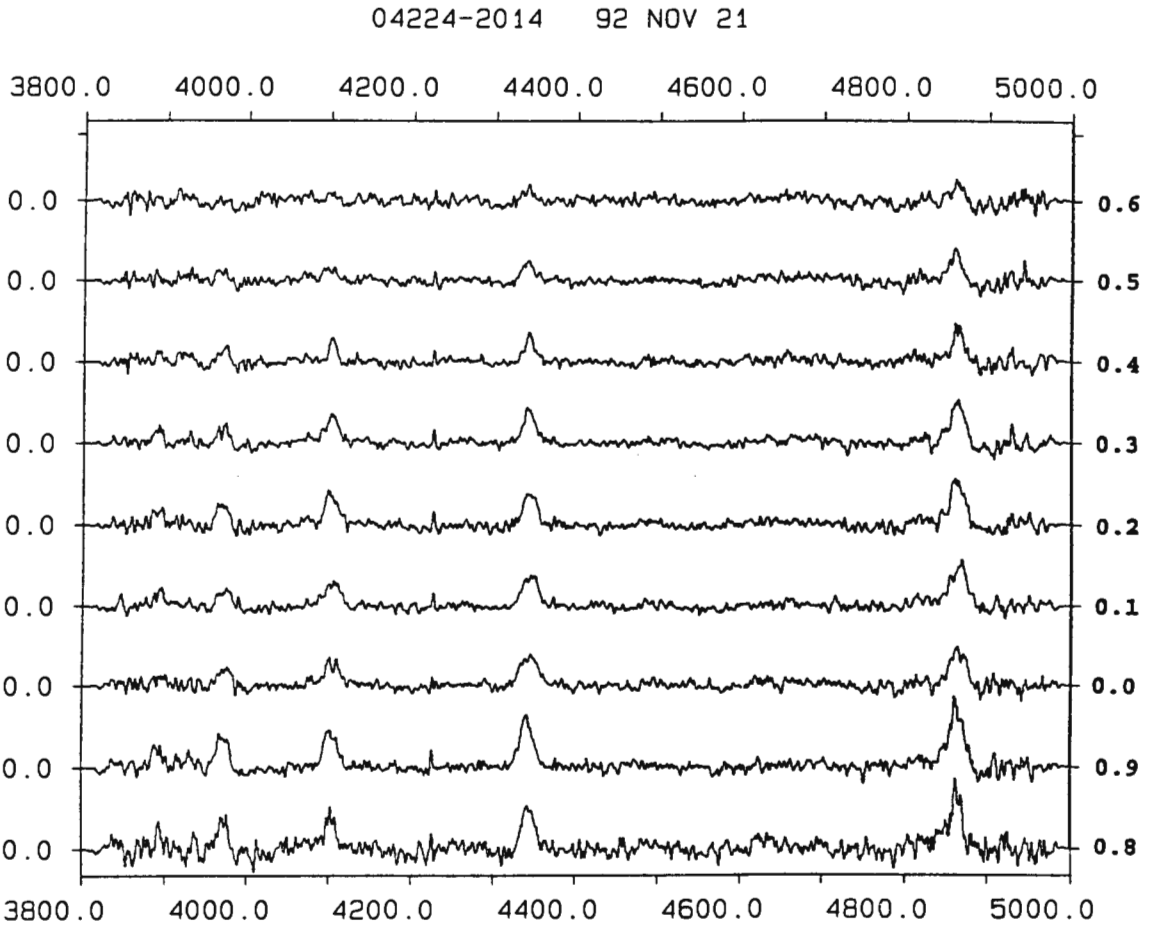

Figure 3a. Phase-binned spectra of EC04224-2014 for 1992 Nov 21. The left ordinate marks the zero intensity and the right ordinate indicates the phases.

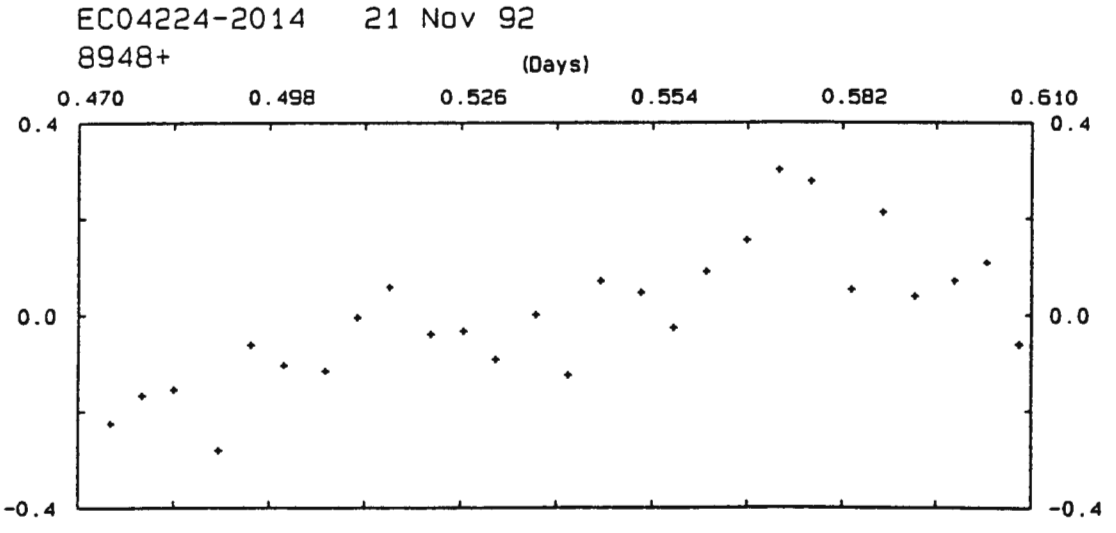

Figure 3b. The plot of counts vs HJD shows the brightness variations during the night of 1992 Nov 21.

Balmer absorption lines on a blue continuum. Emission components are clearly filling in the absorption as Hß is weakly in emission in the top spectrum of Figure 1 and nearly invisible in the bottom spectrum of Figure 1; the strength of Balmer absorption increases up the series, and is strongest in the bottom spectrum. Although the spectra in Figure 1 are consistent with that of a UX UMa star, they are also not dissimilar to spectra of hot DA white dwarfs, so classification as a CV from the spectral features in Figure 1 is not assured.

Eight HSP-runs were obtained which are listed in Table I and plotted in Figure 2. These HSP-runs show rapid flickering variations with a peak-to-peak amplitude of ~10% on a time scale of a few minutes. Therefore this confirms that this object is a CV.

Table I. Observing Log of High-Speed Photometry for EC04224-2014

Run	UT Date	Start HJD	Duration (hrs)	B_w	ΔB_w	
S5450	100292	8663.28773	1.2	11.67	0.05	
S5533	300992	8895.60109	0.7	12.02	0.12	*not shown in Fig 2.
S5541	031092	8898.51683	1.9	-	-	
X0001	221192	8949.30397	4.6	-	-	
X0002	231192	8950.45886	1.3	11.8	0.11	
X0005	261192	8953.42398	4.0	11.9	0.21	
X0007	291192	8956.45751	3.0	11.8	0.12	
S5555	251292	8982.29704	2.6	11.58	0.09	

No convincing evidence for eclipses is visible in any of the runs in Figure 2, the longest of which lasts for 4.6 hours. Thus it is very unlikely that this is a high inclination CV, consistent with the spectroscopic properties of a UX UMa star (almost all of which are not eclipsing). A Fourier amplitude spectrum (Deeming 1975) was calculated for the HSP data of 1992 November 22-29 (the 3rd-6th light curves in Figure 2) and shows no evidence for periodic behaviour with an amplitude greater than 1.5% in the frequency range 0-50 mHz.

§7.2.2 Line Profile Variations and Line Widths

Most of the HSP observations showed that its mean brightness varies between B_w=11.5 and 12.0. However, it was found at B~13 (obtained from the flux

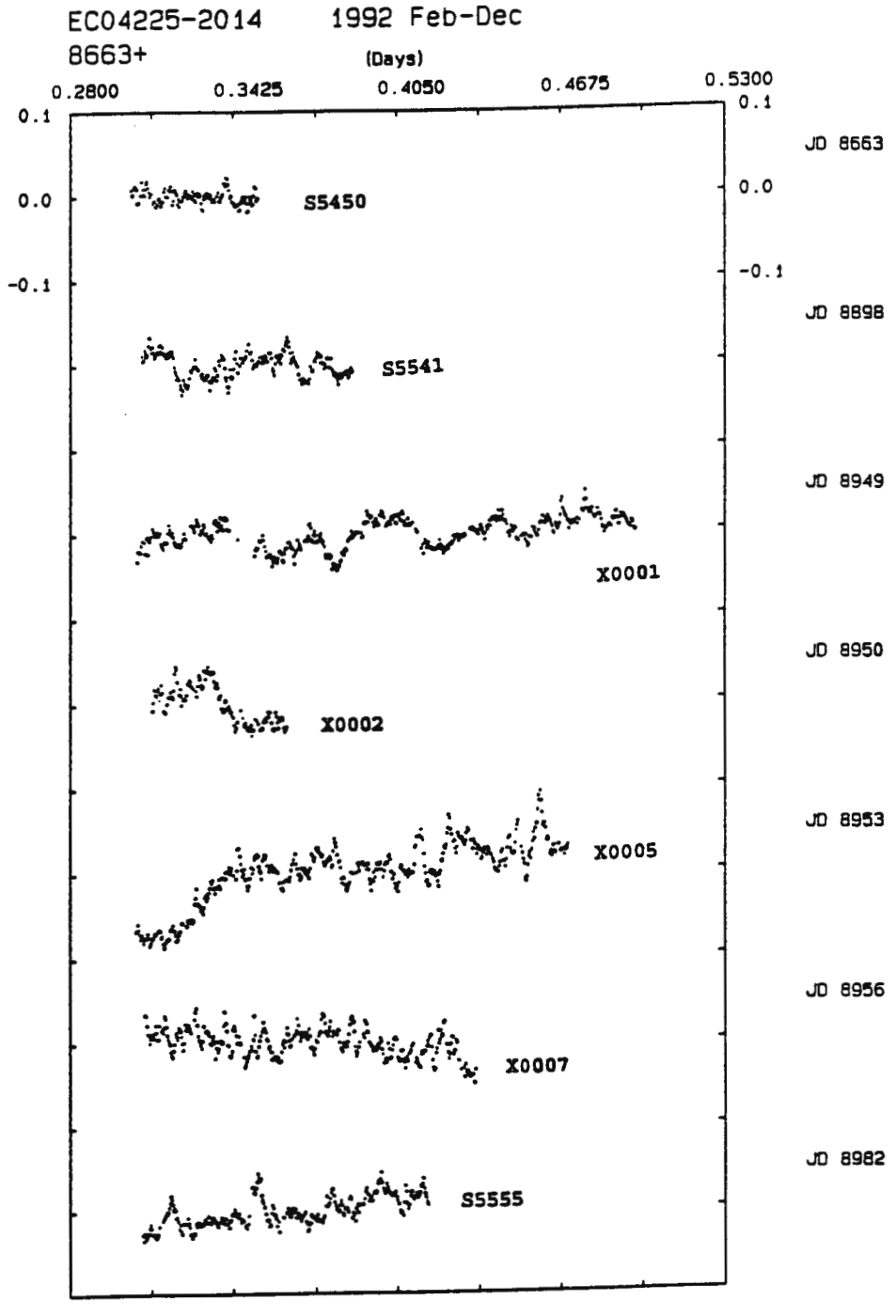

Figure 2. Light curves of EC04224-2014 during 1992 Feb-Dec.

Chapter 7: *Four UX UMa Stars - EC04224-2014, EC05565-5935, EC11588-3142, and EC10560-2902*

§7.1 Introduction

The Nova-like Variables (NLs) were defined in section 3.1.1, and include a wide variety of cataclysmic variables (CVs) which do not exhibit eruptive behaviour. This does not, however, mean that NLs undergo no changes in long-term brightness. In particular, a category of NLs, the VY Scl stars, may spend most of their time in the high state, but occasionally reduce their brightnesses by a magnitude or more for weeks to years (the low state). Note that a VY Scl star may belong to either the UX UMa category or the RW Tri category. The subclass UX UMa is defined by showing broad, shallow Balmer absorption lines in their spectra. Narrow emission cores may also be seen. In contrast, those stars with pure emission line spectra are termed RW Tri stars by Warner (1994).

Many UX UMa stars exhibit no properties which would call attention to themselves in, for example, surveys for X-ray emission, optical variability or emission spectra. Thus, most UX UMa stars are found in colorimetric surveys such as the Edinburgh-Cape survey. In this chapter, four new NLs are presented: EC04224-2014 in §7.2, EC05565-5935 in §7.3 , EC11588-3142 in §7.4, and EC10560-2902 in §7.5.

§7.2 EC04224-2014

§7.2.1 Photometric and Spectroscopic Characteristics

EC04224-2014 was identified as a candidate blue object from the UB plate pair obtained by the UKST on 1989 October 28. The UBV measurements (V=11.4, B-V=0.03, U-B=-0.75) show that it is a genuine blue object. The first spectrum with 4Å resolution was obtained on 1991 November 8 and is shown at the top of Figure 1. A similar spectrum was observed on 1992 February 9 and appears at the bottom in Figure 1. Both of the spectra show shallow, broad

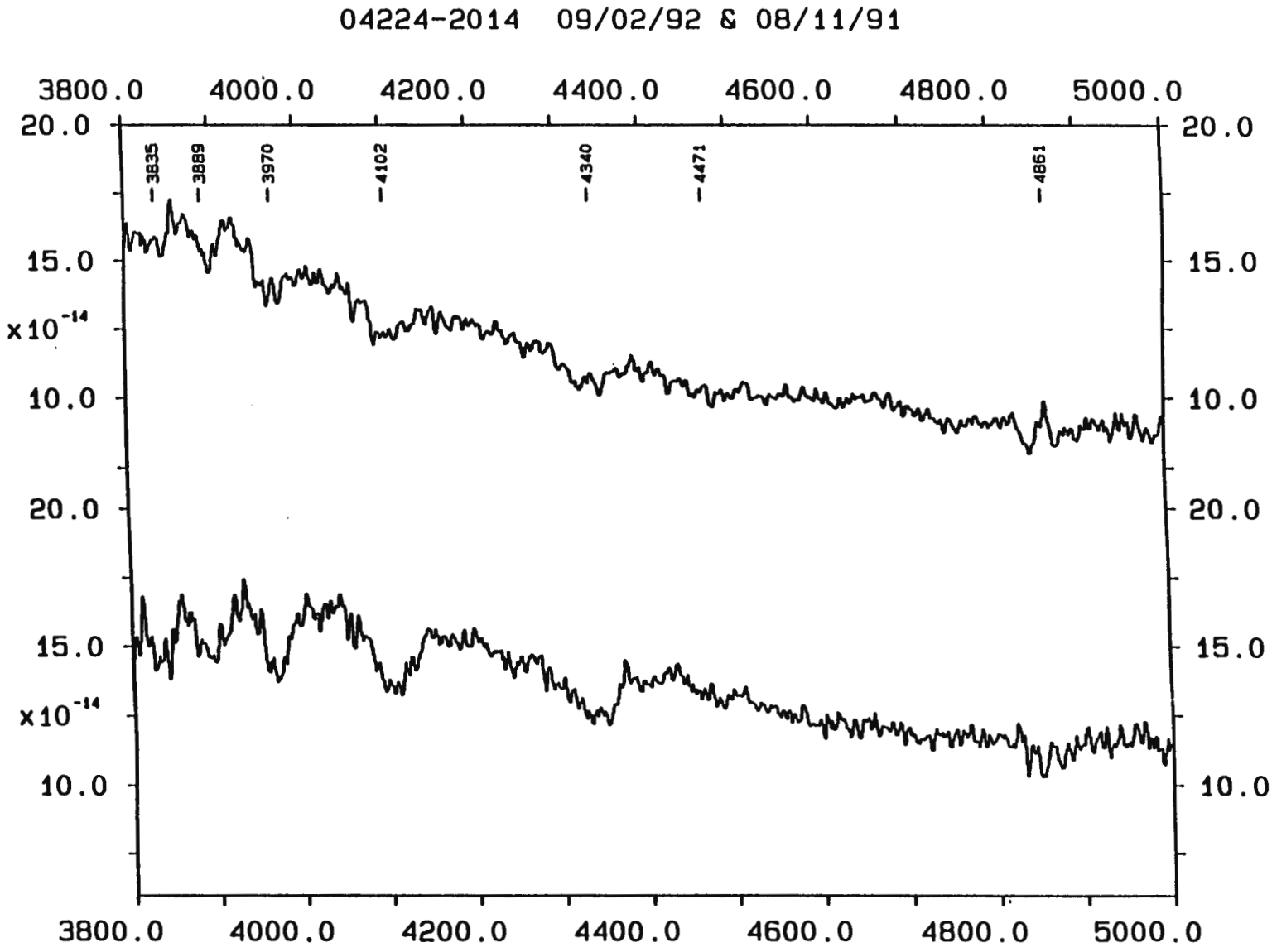

Figure 1. Spectra of EC04224-2014: 1992 Feb 9 (bottom) and 1991 Nov 8 (top).

Warner, B. (1994). *Cataclysmic Variable Stars*, Cambridge University Press, in press.

Wood, J. Horne, K., Berriman, G., Wade, R., O'Donoghue, D., and Warner, B. (1986). *Mon. Not. R. astr. Soc.*, **219**, 629.

Table X. Radial Velocities of EC23593-6724

HJD 2440000.+	RV km/s	HJD	RV	HJD	RV
8944.32361	-45	8944.46255	-1	8948.34004	-9
8944.33064	-33	8944.46965	16	8948.34714	-4
8944.33909	-21	8944.47798	14	8948.35575	2
8944.34613	-12	8944.48503	4	8948.36278	11
8944.35447	7	8944.49334	9	8948.37136	8
8944.36151	-18	8944.50038	27	8948.37841	8
8944.36991	-11	8944.50866	56	8948.38719	-14
8944.37695	27	8944.51569	33	8948.39423	-7
8944.38525	4	8945.29981	-15	8948.40276	-43
8944.39229	22	8945.30828	-6	8948.40980	-13
8944.40061	4	8945.32190	-18	8948.41813	7
8944.40780	0	8945.33762	-10	8948.42517	37
8944.41626	-17	8948.29334	-14	8948.43348	9
8944.42329	-7	8948.30037	7	8948.44061	7
8944.43178	37	8948.30887	-13	8948.44896	40
8944.43888	0	8948.31591	-17	8948.45601	24
8944.44722	-9	8948.32443	-11		
8944.45425	13	8948.33146	-21		

References:

Bailey, J. (1975). *Brit. astr. Ass.*, **86**, 30.

Bailey, J. (1979). *Mon. Not. R. astr. Soc.*, **187**, 645.

Bailey, J., and Ward, M. (1981). *Mon. Not. R. astr. Soc.*, **194**, 17.

Cannizzo, J.K., and Kaitchuck, R.H. (1992). *Scientific American*, **266**, No.1, 42.

O'Donoghue, D., and Soltynski, M.G. (1992). *Mon. Not. R. astr. Soc.*, **254**, 9.

Kaitchuck, R.H., Mansperger, C.S., and Hantzios, P.A. (1988). *Astrophys. J.*, **330**, 305.

Mansperger, C.S., and Kaitchuck, R.H. (1988). *Astrophys. J.*, **358**, 268.

Marsh, T.R., Horne, K., and Shipman, H.L. (1987). *Mon. Not. R. astr. Soc.*, **225**, 551.

Robinson, E.L. (1976). *Ann. Rev. Astron. Astrophys.*, **14**, 119.

Shafter, A.W., and Hessman, F.V. (1988). *Astron. J.*, **95**, 178.

Van Amerongen, S., Damen, E., Groot, M., Kraakman, H., and Van Paradijs, J. (1987). *Mon. Not. R. astr. Soc.*, **225**, 93.

Vogt, N. (1974). *Astron. Astrophys.*, **36**, 369.

Wade, R.A., and Ward, M.J. (1985). in *Interacting Binary Stars*, ed. J.E. Pringle and R.A. Wade, Cambridge University Press, p129.

Warner, B., O'Donoghue, D., and Wargau, W. (1989). *Mon. Not. R. astr. Soc.*, **238**, 73.

The above shows that the B-V colour becomes bluer as the brightness increases but the U-B colour does not vary much. Of course, there are insufficient data to study fully the correlation between colours and brightness. Thus, simultaneous UBV HSP is needed in order to investigate the above colour-brightness relation.

§6.4.3 Search for an Orbital Period

In order to search for the orbital period, time-resolved spectroscopy with 3Å wavelength resolution and 600 seconds time resolution was obtained during 1992 November 17-21 and is listed in Table IX. The sequence of spectra was

Table IX. Observing Log of Time-Resolved Spectroscopy for EC23593-6724

UT Date	Start UT Time h m	Duration hrs	Resolution (FWHM Å)	Coverage Å
92 Nov 17	19 41	4.6	3	3700-5000
92 Nov 18	19 07	0.9	3	3700-5000
92 Nov 21	18 58	3.9	3	3700-5000

used to construct the template (grand sum spectrum) which is shown in Figure 17. Figure 17 shows similar features to that in Figure 15. The relative radial velocities of individual spectra were determined using the cross-correlation technique. The results are listed in Table X and plotted in Figure 18. A Fourier amplitude spectrum (not shown here) was calculated for the data of 1992 Nov 17-18. The amplitude spectrum does not show any convincing periodicity, as can be verified from inspection of the scatter in the top two panels of Figure 18. Another Fourier amplitude spectrum was calculated for the data of 1992 November 21/22 alone and is shown in Figure 19. Figure 19 exhibits a highest peak of 0.139 mHz. A sinusoid of frequency 0.139 mHz was fitted by least squares to the data of 1992 November 21/22 and appears as the solid lines in Figure 18. However, the highest peak in Figure 19 is not significant and the radial velocity variations in Figure 18 are not very convincing evidence for an orbital period of 1.96-hr. The failure to obtain a well-determined radial velocity curve is probably because EC23593-6724 is of low inclination.

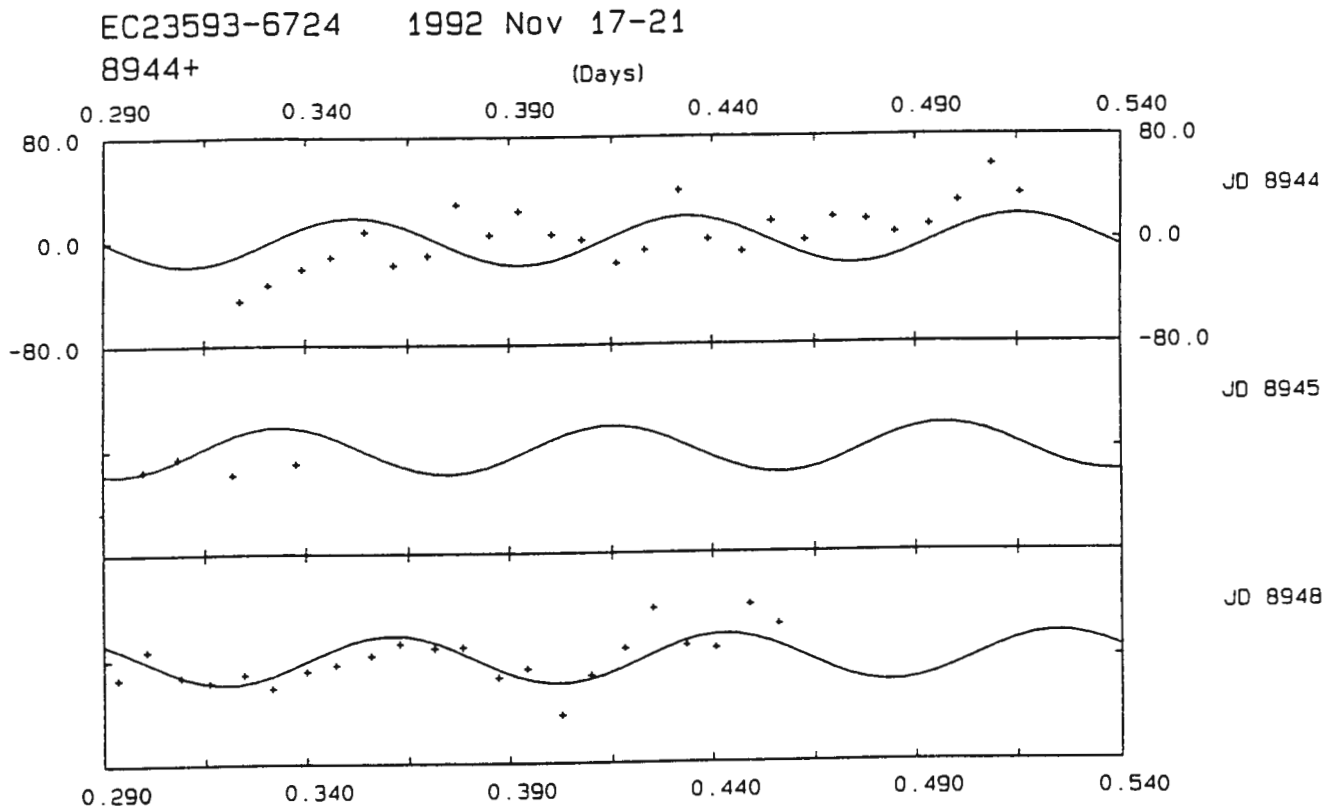

Figure 18. Radial velocity curves of EC23593-6724 obtained on 1992 Nov 17 (top), 18 (middle), and 21 (bottom).

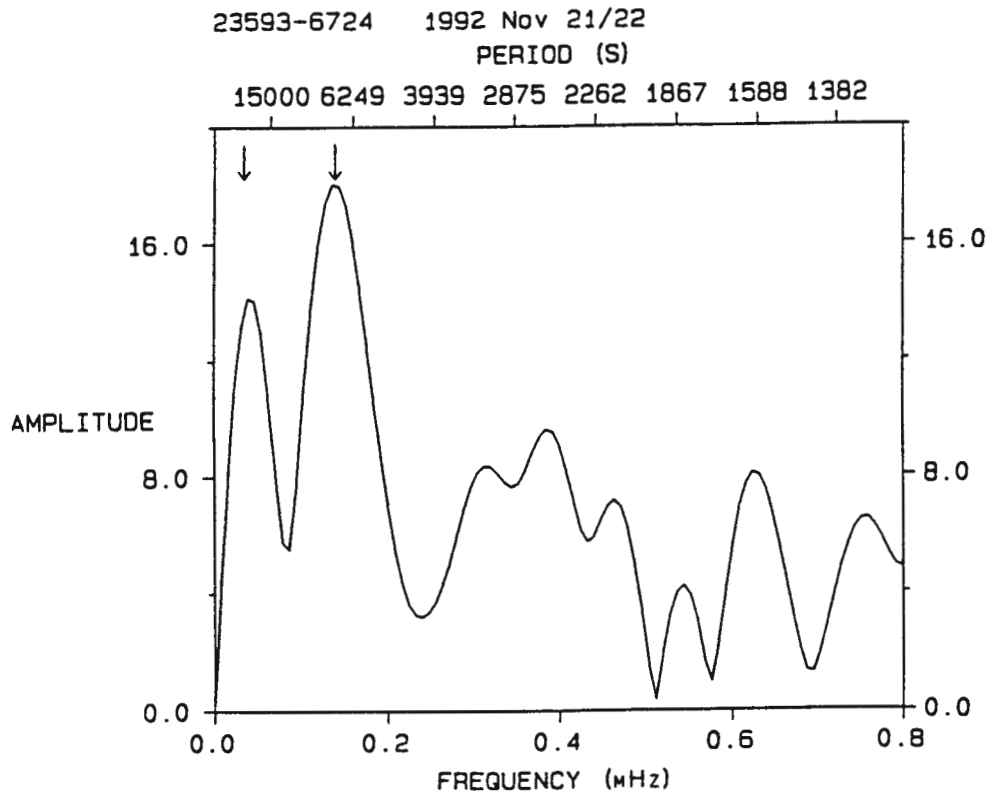

Figure 19. Amplitude spectrum of EC23593-6724 calculated from the radial velocities of 1992 Nov 21/22 show a highest peak of 0.139 mHz.

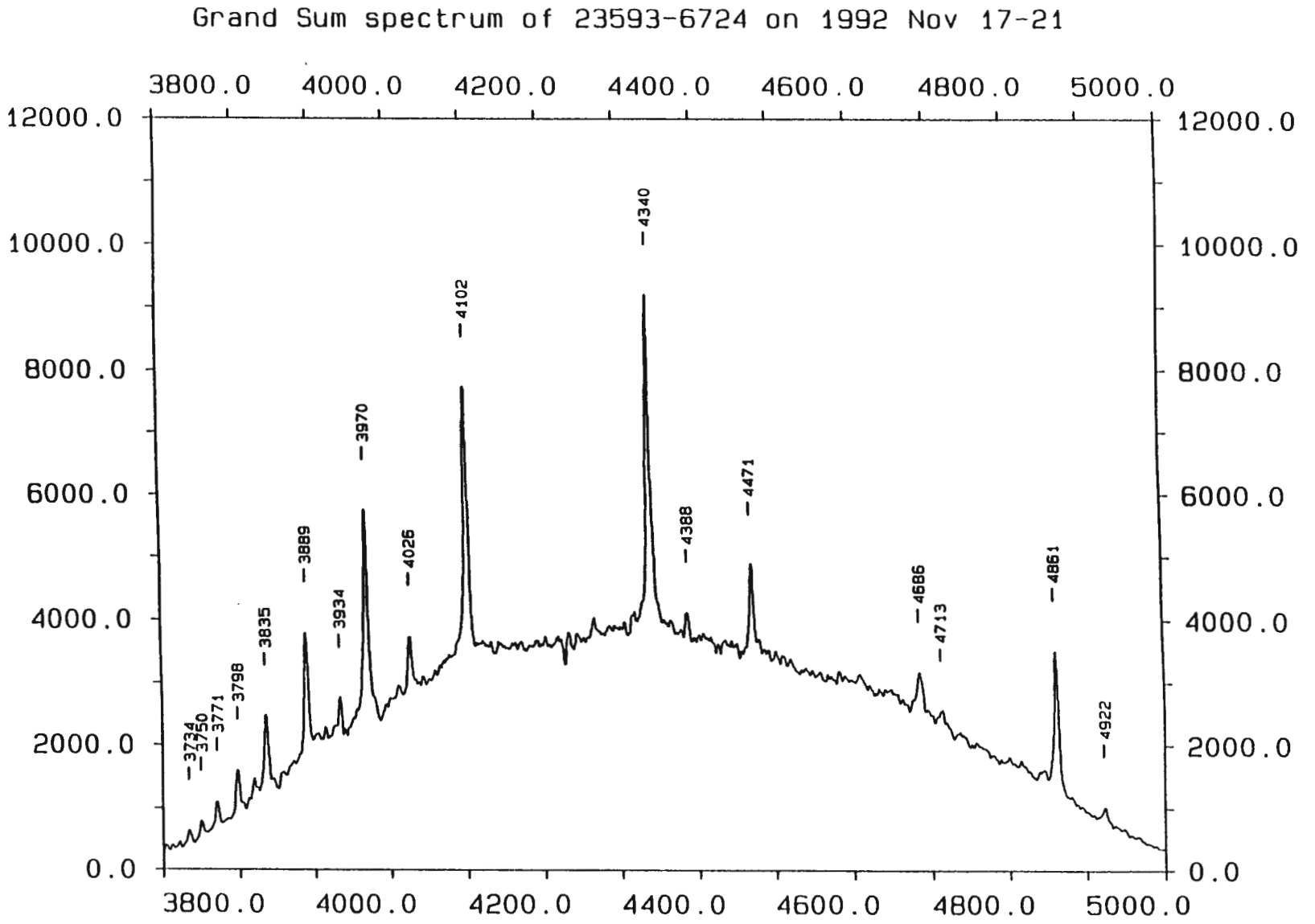

Figure 17. Grand sum spectrum of EC23593-6724 on 1992 Nov 17-21 is the template used for the cross-correlation.

(45Å) of 1992 October 3, which must arise from stronger emission from the inner regions of the disk in 1992 October.

The spectra in Figure 15 are similar to spectra of the SU UMa star YZ Cnc (see Figure 2 of Shafter and Hessman 1988). This suggests that the object is an SU UMa star.

§6.4.2 Photometric Characteristics

Seven HSP-runs were obtained during 1992-1993 and are listed in Table VIII.

Table VIII. Observing Log of High Speed Photometry for EC23593-6724

Run	UT Date	Start HJD 2440000.+	Duration hrs	B_w	ΔB_w
S5542	041092	8899.50295	3.1	14.5	0.86
S5543	041092	8900.34082	4.8	14.7	1.17
X0003	251192	8952.27753	4.0	14.1	0.55
X0004	261192	8953.28435	2.9	14.4	0.54
X0006	291192	8956.28889	3.7	14.5	0.54
S5625	220893	9222.46205	3.0	13.9	0.55
X0012	180993	9249.35907	3.6	14.6	0.75

These data are plotted in Figure 16 and reveal strong, flare-like flickering variations with peak-to-peak amplitudes of ~0.5-1.2 mag on a time scale of a few minutes. No repeatable patterns are found in the light curve: on the night of 1992 October 4 (run S5543 in Figure 16a), the flickering activity underwent a dramatic increase with an amplitude exceeding one magnitude. During 1992 November 25-29, the object showed a flickering amplitude of ~0.5 mag, less active than in 1992 October. Ten months later, the HSP-run X0012 (Figure 16c) was obtained on 1993 Sep 20 showing flickering superimposed on a big hump which lasted for about an hour. Fourier amplitude spectra (not shown here) were calculated for the data in Table VIII and do not show convincing evidence for periodic behaviour with amplitudes greater than 15% in the frequency range of 0-100 mHz.

Four UBV measurements were obtained:

UT Date	HJD 2440000.+	V	B-V	U-B
4 Sep 92	8900.3314	14.59	0.35	-0.91
23 Aug 93	9222.6132	13.89	0.06	-0.94
24 Aug 93	9223.6044	14.17	0.19	-0.89
15 Nov 93	9307.3294	14.06	0.16	-0.99

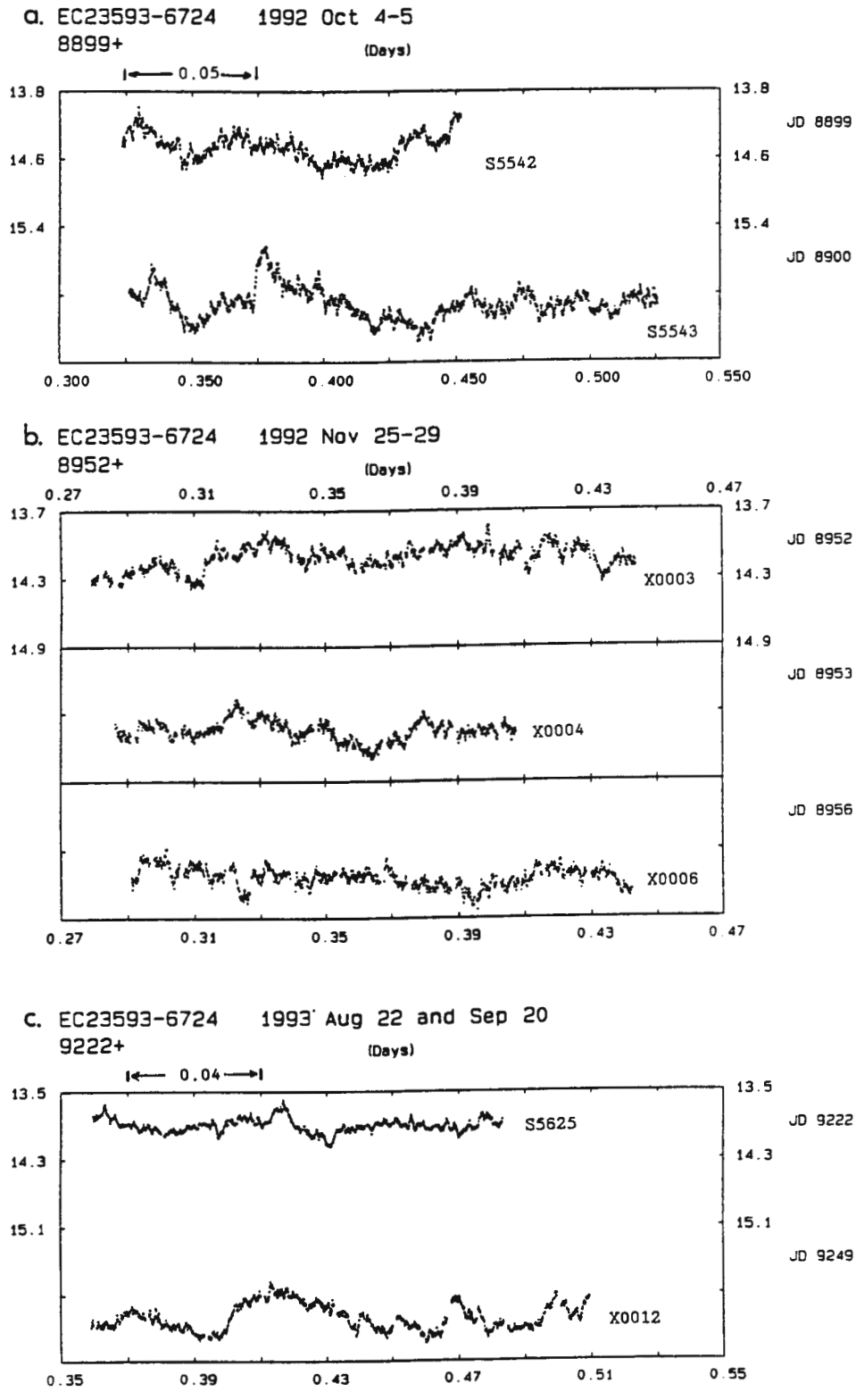

Figure 16. Light curves of EC23593-6724: (a) 1992 Oct 4-5; (b) 1992 Nov 25-29; (c) 1993 Aug 22 and 1993 Sep 20.

§6.3.3 Summary

The characteristics of EC23128-3105 are summarized as follows: (1) the object has an ultrashort orbital period (1.4-hrs) which is characteristic of both the SU UMa and the AM Her stars (see §3.4.1); (2) the light variations of 1991 August showed a significant orbital modulation and a modulation with a period of about half of the orbital period. This photometric behaviour resembles that of VW Hyi (Van Amerongen et al. 1987); (3) the spectrum of EC23128-3105 is characterized by broad, double-peaked Balmer lines in emission and does not show HeII λ4686Å. These spectroscopic properties are typical of a DN, not of an AM Her star which shows strong HeII λ4686Å and the Balmer jump in emission. Although no outbursts were detected which would have allowed us to check that EC23128-3105 shows the outburst properties of an SU UMa star, the above (1), (2) and (3) enable us to place EC23128-3105 in the SU UMa subclass of DN. The system may have a mass ratio in the range of $0.09 \geq M_2/M_1 \geq 0.06$ and a high mass white dwarf.

§6.4 EC23593-6724

§6.4.1 Spectral Characteristics

EC23593-6724 was selected to be a candidate blue object from the UB plate pair on 1990 October 22. The first spectrum with 4Å resolution was obtained on 1992 October 3 and is shown at the bottom of Figure 15. A similar spectrum was secured on 1993 August 19 and also appears in Figure 15. Both of these spectra are characterized by strong Balmer lines, weaker HeI (λ4026Å and λ4471Å), weak CaII λ3934Å and HeII λ4686Å in emission that are produced in a region of the disk which is optically thin in the continuum. In addition to these, HeI λ4388Å and λ4713Å are barely visible. HeI λ4922Å/FeII λ4924Å blend is weakly present as well as the HeI λ5016Å/FeI λ5018Å blend. The Balmer emission lines are resolved up to H13 with very narrow FWHM of ~6Å which suggests the object is probably a low inclination system. Note that the FWZI of 15Å in the spectrum of 1993 August 19 is much narrower than that

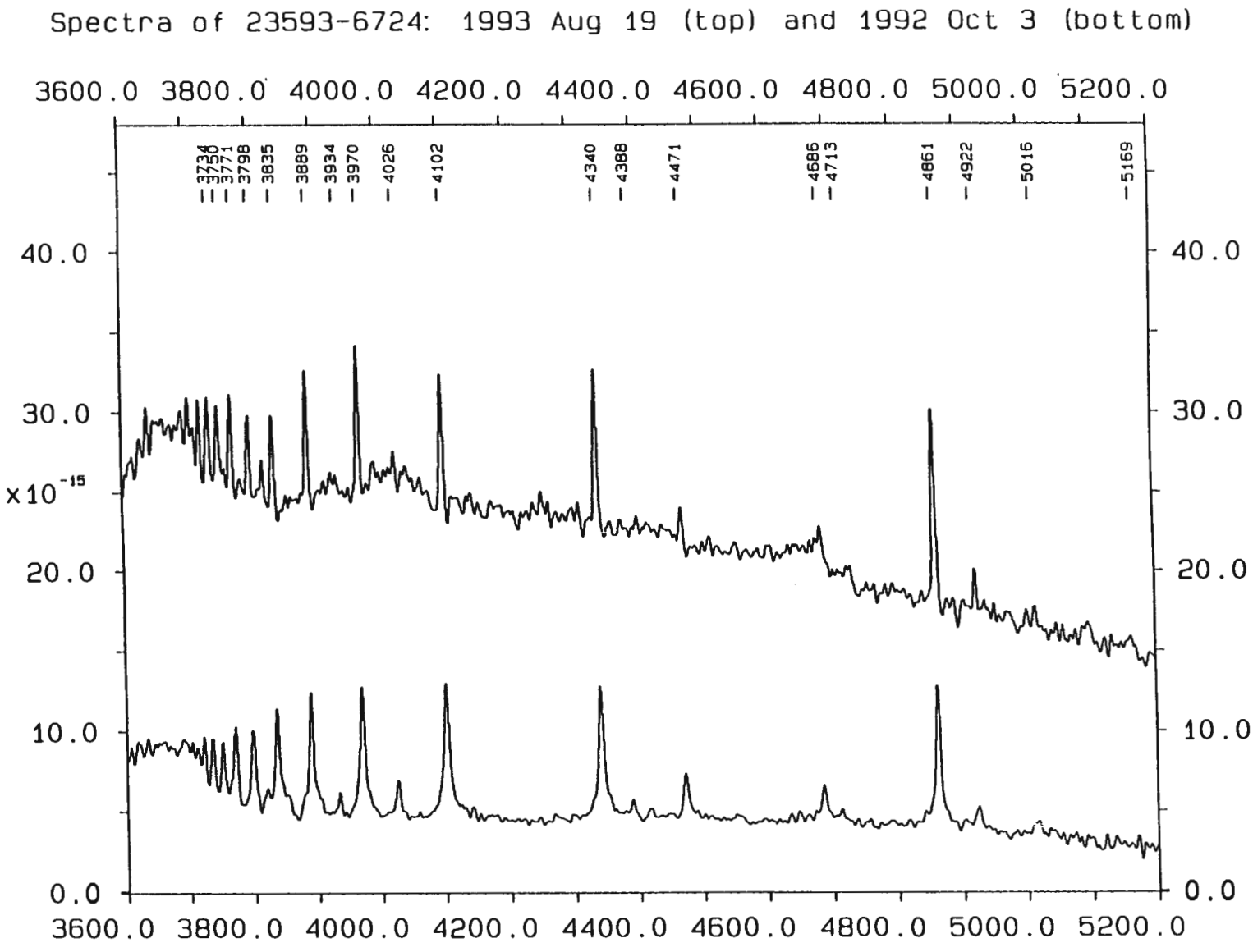

Figure 15. Spectra of EC23593-6724 on 1992 Oct 3 (bottom) and 1993 Aug 19 (top) show strong and narrow emission lines.

1986) and especially VW Hyi (Vogt 1974 and Van Amerongen et al. 1987) are seen in some of the runs (S5355-S5381 and S5397). These humps are not seen in other runs (S5389, S5612 and S5619) and the presence or absence of humps is not related to the mean brightness of the system, which hardly changed for any of the runs in Figure 12. The shape of the light variations of Runs S5355-S5381 is similar to that of VW Hyi (see Figure 1 of Van Amerongen et al. 1987) in quiescence. The light variations of 1991 August 9-11 (S5373-S5381) were converted to B_w-magnitude and binned into 100 orbital phases corresponding to the ephemeris derived on 1991 August 5 in the last section. The result is plotted in Figure 13 and exhibits a significant orbital modulation with a peak-to-peak amplitude of 0.28 mag.

A Fourier amplitude spectrum (not shown here) was calculated for the data of S5373-S5381 (JD8477-8480) and shows a highest peak of 0.043 mHz (6.46 hrs) which arises from low frequency changes in the mean brightness of the system. After removing this frequency from the light curve, a Fourier amplitude spectrum of the residuals was calculated and is shown in Figure 14. Figure 14 exhibits a highest peak at 0.383±0.001 mHz (2607 s) (arrowed). Because the orbital humps in the light curves do not vary sinusoidally, alias patterns at both the orbital period and the first harmonic of the orbital period are visible in Figure 14. In order to determine the correct orbital period (P_{orb}) and photometric period (P_{ph}), the frequencies of the five largest peaks near 0.4 mHz were compared with those of the five prominent peaks near 0.2 mHz. Only three pairs of frequencies were found to be related by the expected 1:2 ratio. The possible values of P_{orb} are 4789, 5071 and 5400 seconds and are consistent with the peaks (4761, 5050 and 5376 seconds) arrowed in Figure 9, within the measurement errors of ~30 seconds. Because these three candidate P_{orb} have approximately the same amplitude, ~4 percent, it is difficult to select a correct orbital period from Figure 9 and 14. The possible P_{ph} are 2387, 2530 and 2688 seconds corresponding to the half of the above candidate P_{orb}. The rest of the data show weak evidence for the photometric period as can be verified from inspection of Figure 12.

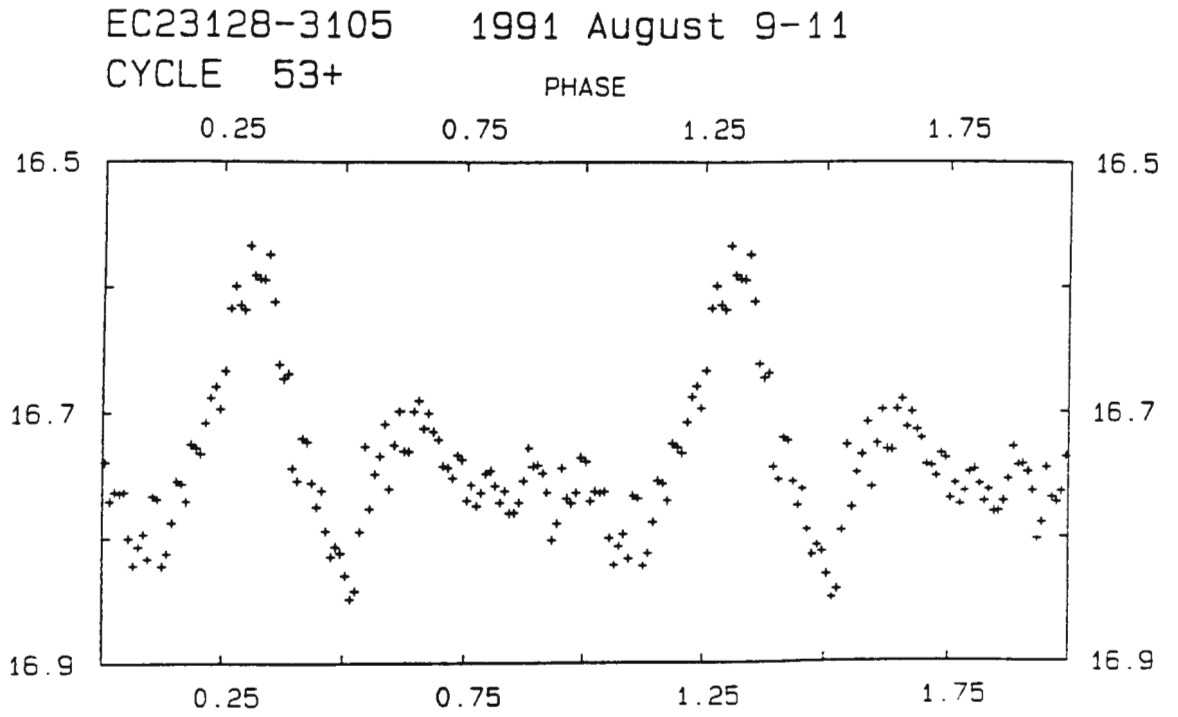

Figure 13. Orbital light curve of EC23593-6724. The ordinate is B_w-magnitude; the abscissa is orbital phase.

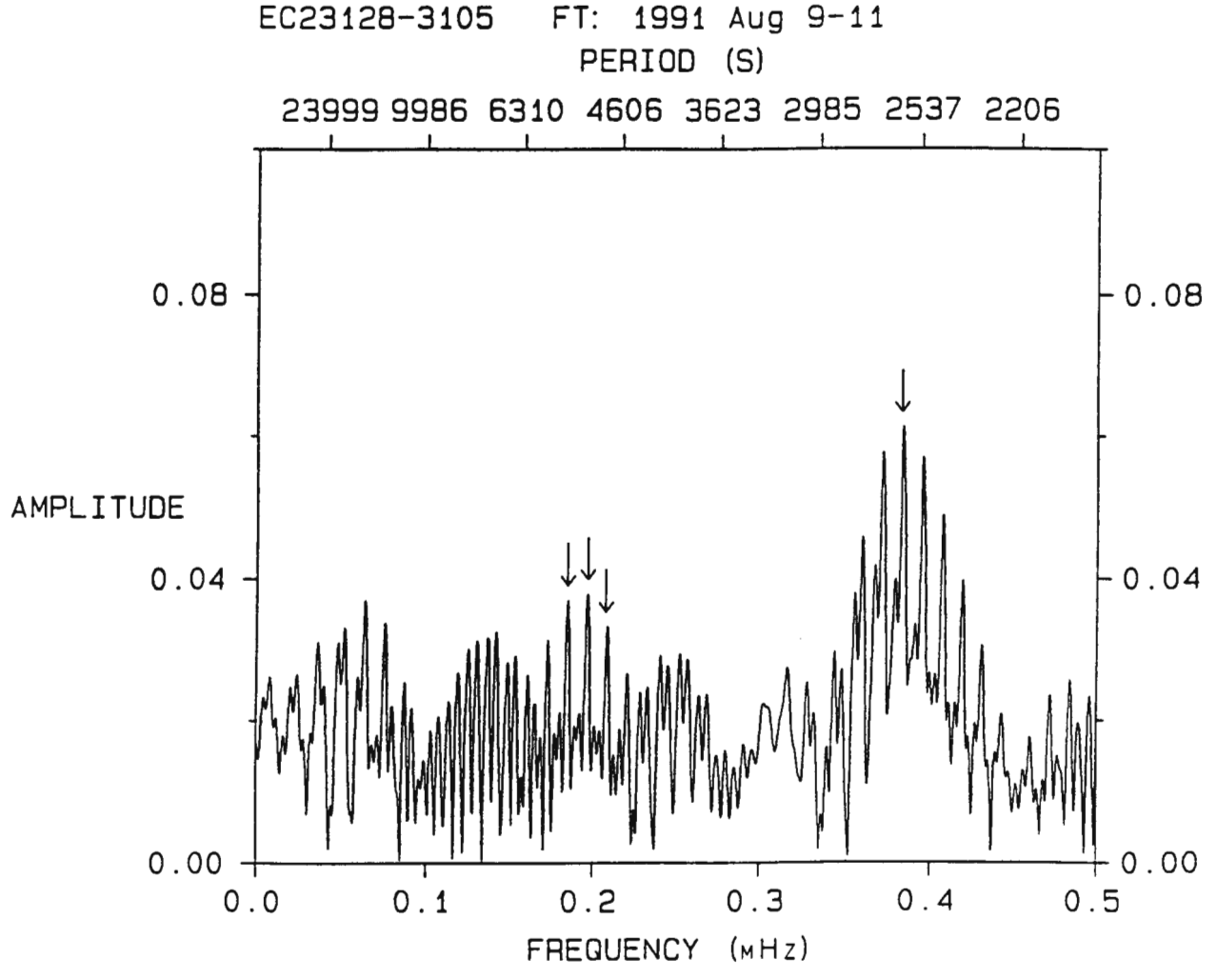

Figure 14. Amplitude spectrum (EC23128-3105) of 1991 August 8-11.

data of Figure 12. The HSP observations show that the object has a mean brightness of B_w~13.1 mag with a small variation of ~0.3 mag from run to run.

Table VI. Observing Log of HSP for EC11588-3142

Run	UT Date	Start HJD 2440000.+	Duration hrs	B_w	ΔB_w
S5449	100292	8662.55861	1.7	13.25	0.16
S5479	090492	8722.40028	1.3	13.07	0.16
S5509	260692	8800.23649	1.7	12.96	0.15
S5513	280692	8802.22920	1.7	13.00	0.10
S5516	290692	8803.22049	1.9	13.00	0.14
S5566	230193	9010.53447	1.3	13.26	0.13
S5568	230193	9011.46418	3.0	13.36	0.16
S5575	190293	9038.47565	2.3	13.27	0.07
S5610	170693	9156.24427	2.8	13.13	0.10

The first spectrum with 4Å resolution (top of Figure 13) was obtained on 1990 February 6 and showed shallow, broad Balmer absorption lines on a blue continuum. The spectral features are stronger than in EC05565-5935. Emission almost fills in Hß and is weaker up the Balmer series; the Balmer absorption increases up the series. In addition to these, HeI λ4471Å in absorption is weakly present in the spectrum. Two years later, EC11588-3142 was observed on 1992 February 5 showing almost no spectral features (bottom of Figure 13). These spectra are typical of a UX UMa star whose spectral properties have been discussed in section 7.3.1.

Since there is no modulation in the photometry, time-resolved spectroscopy was obtained during 1992 March 21-22 (Table VII) in order to search for an orbital period. A series of spectra on both nights was secured with 3Å wavelength resolution and a time resolution of 400 seconds. The template (Figure 14) was constructed summing all the spectra on both nights and showed similar features to the first spectrum except HeII λ4686Å is obviously visible in Figure 14. The relative radial velocity was determined using the cross-correlation technique. The results are plotted in Figure 15. A Fourier

Table VII. Observing Log of Time-Resolved Spectroscopy for EC11588-3142

UT Date	UT Time h m	Duration (hrs)	Resolution FWHM(Å)	Coverage Å
1993 Mar 21	23 12	4.0	3	3600-5000
1993 Mar 22	20 45	2.5	3	3600-5000

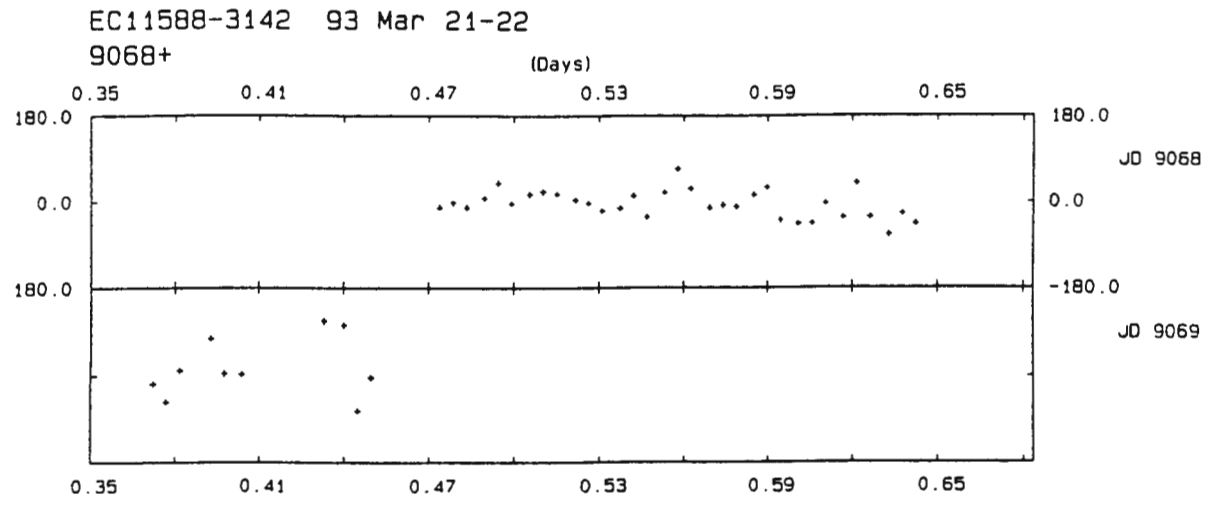

Figure 15. Plot of radial velocities of EC11588-3142 of 1993 March 21-22.

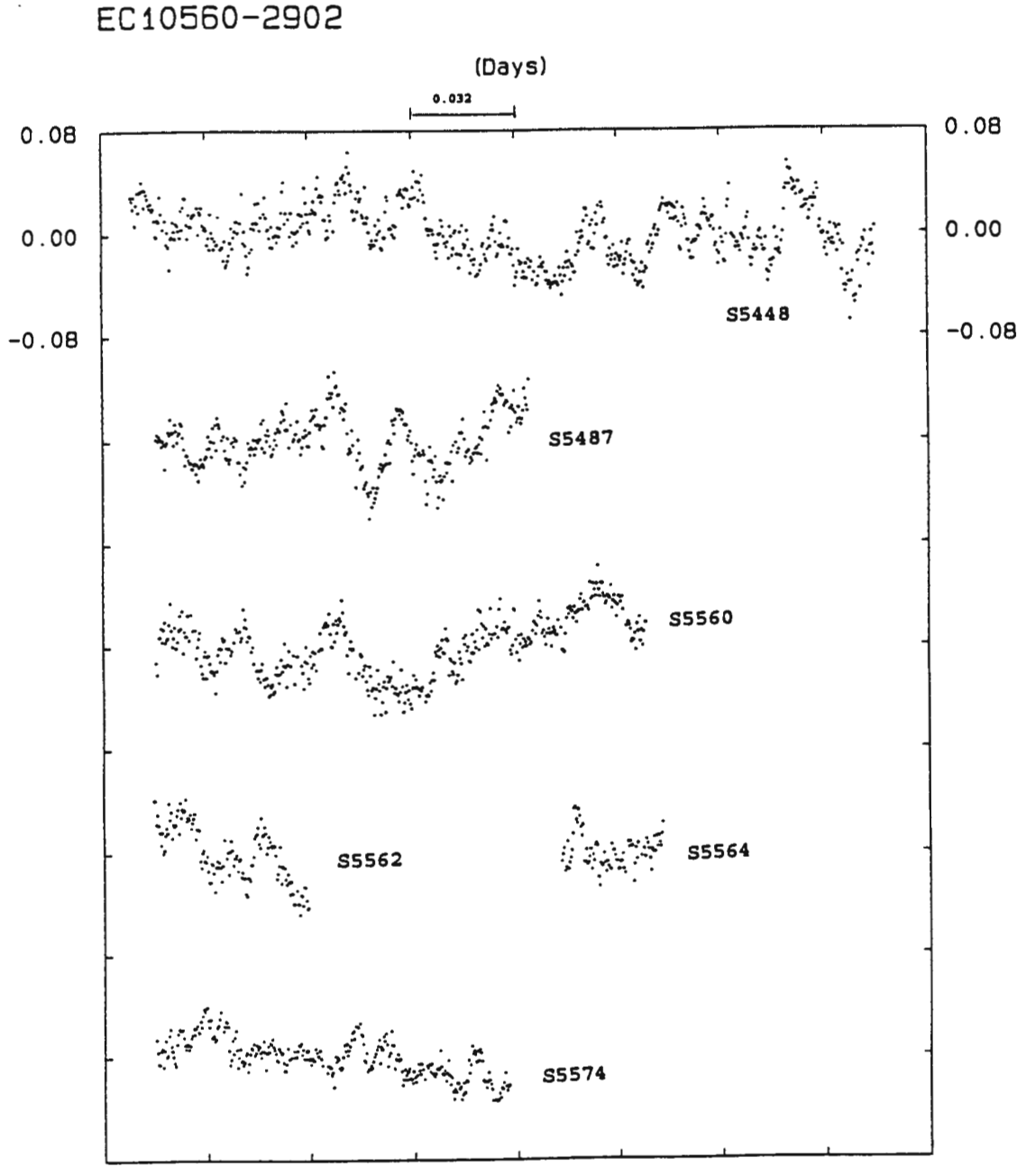

Figure 16. Light curves of EC10560-2902 during 1992-1993.

amplitude spectrum (not shown) was calculated for the radial velocities, and showed no periodicity, which can be verified from inspection of the scatter in Figure 15. Because of the weakness of the spectral features in each individual spectrum, it was impossible to separate the emission component from the absorption profile to pursue the search for an orbital period.

§7.5 EC10560-2902

The photometric colours (V=14.34, B-V=-0.02, U-B=-0.91) of EC10560-2902 are bluer than in the previous three objects and closer to the blackbody line in the two colour diagram, but this cannot assist much in the classification. The HSP observations were made in 1992 and 1993 and are listed in Table VIII

Table VIII. Observing Log of HSP for EC10560-2902

Run	UT Date	Start HJD 2440000.+	Duration hrs	B_w	ΔB_w
S5448	090292	8662.30838	5.5	14.19	0.17
S5487	290492	8742.34801	2.8	14.12	0.15
S5560	190193	9007.41959	3.7	14.06	0.16
S5562	210193	9008.54270	1.2	14.04	0.12
S5564	220193	9009.54903	0.8	14.15	0.08
S5574	180293	9037.43072	2.6	13.99	0.10

and plotted in Figure 16. These data show that the mean B_w varies by ~0.2 mag between B_w=13.99 and 14.19 from run to run. The light curves in Figure 16 show flickering variations with a peak-to-peak amplitude of ~8% on a time scale of ~15-30 minutes. Thus it is clear that this object is a CV. A Fourier amplitude spectrum was calculated for the runs S5560-S5564 and the longest run S5448 (a duration of 5.5 hours), but there is no evidence for an orbital modulation.

The first spectrum with 4Å wavelength resolution was obtained on 1990 May 18 and is shown in Figure 17a. The spectrum showed strong, broad Balmer emission lines which can be resolved up to H11. The high excitation CIII/NIII blend near λ4650Å is also present as well as the HeII λ4686Å emission line which is relatively strong compared to Hβ. A low resolution (8Å) spectrum was observed on 1992 February 7 and is shown in Figure 17b.

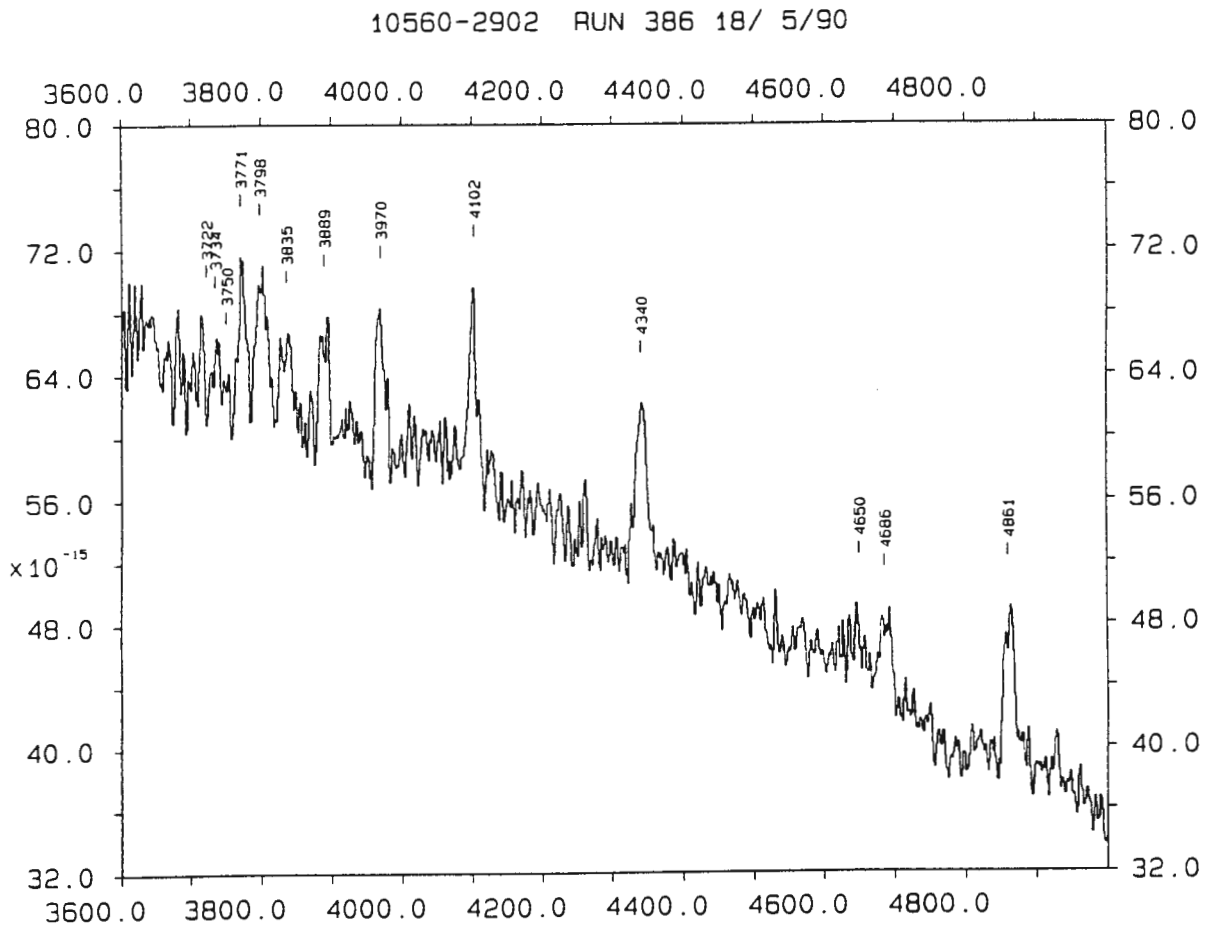

Figure 17a. The first spectrum of EC10560-2902 on 1990 May 18.

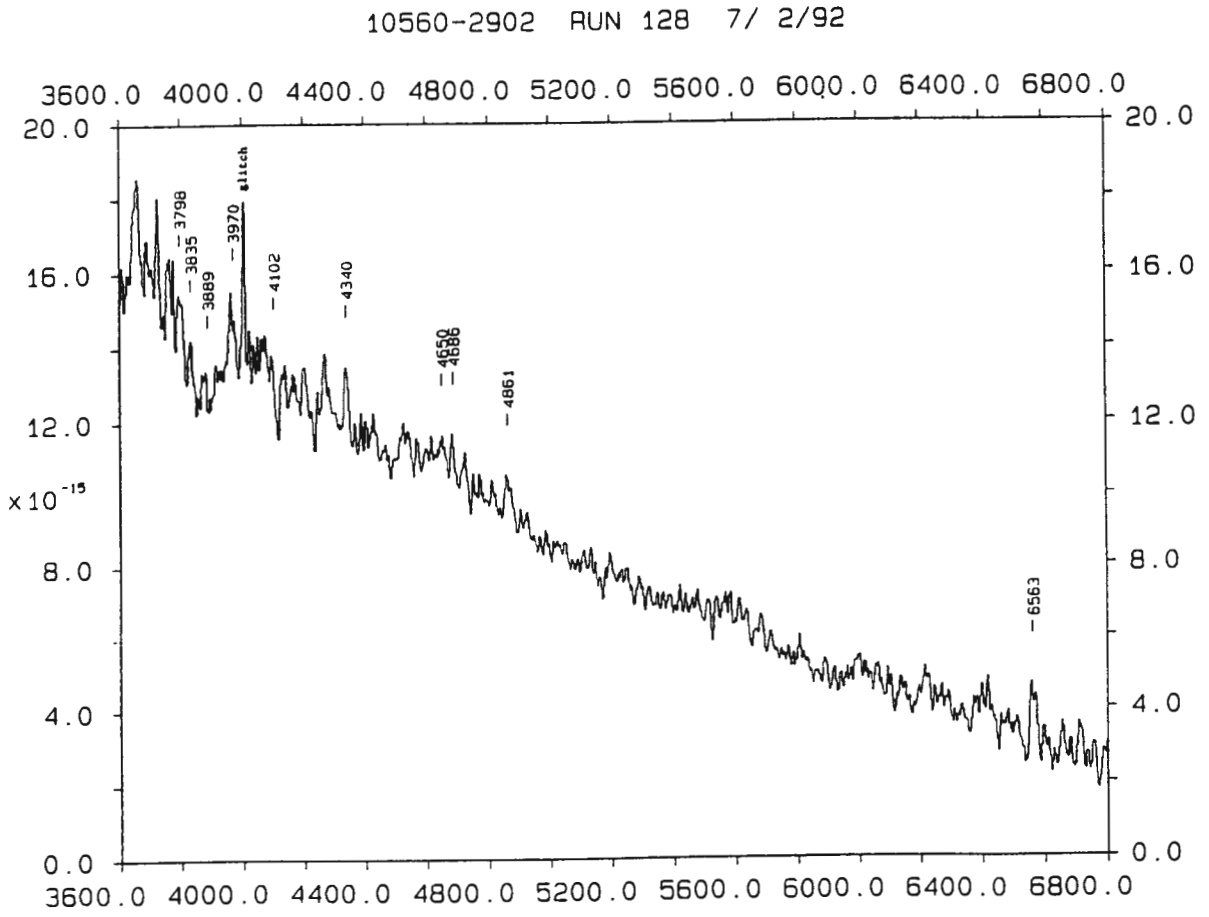

Figure 17b. The spectrum of EC10560-2902 on 1992 February 7.

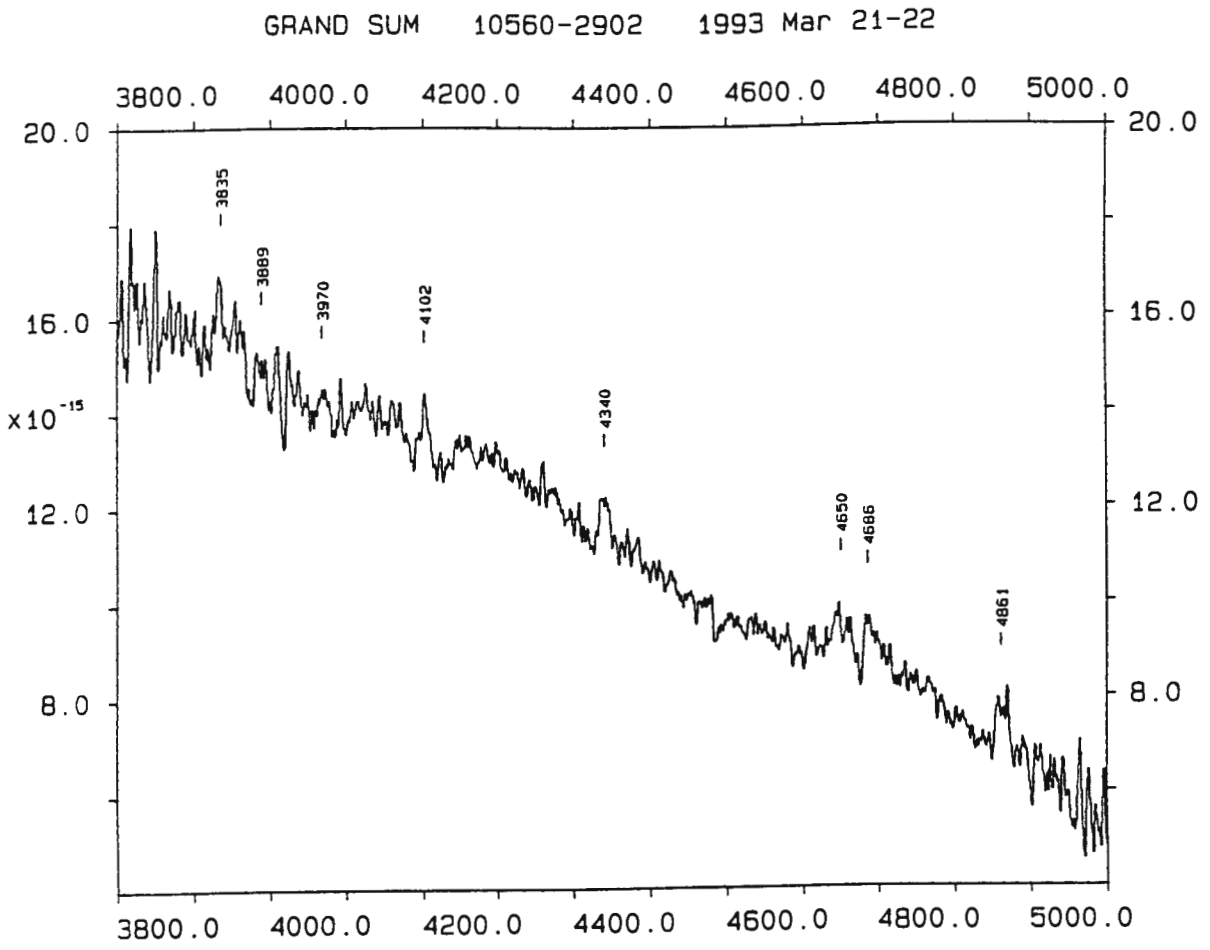

Figure 17c. Grand sum spectrum of EC10560-2902 on 1993 March 21-22.

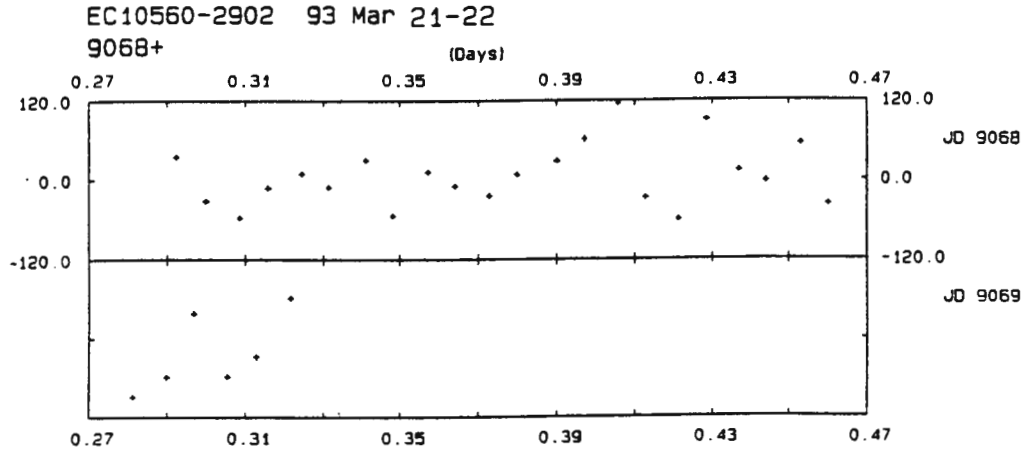

Figure 18. Plot of radial velocities of EC10560-2902 obtained on the nights of 1993 March 21-22.

The low order Balmer lines are barely visible in emission. No other features are definitely present; this spectrum is very different to that shown in Figure 17a.

As there is no modulation in the photometry, time-resolved spectroscopy (Table IX) was obtained during 1993 March 21-22 to search for an orbital

Table IX. Observing Log of Time-Resolved Spectroscopy for EC10560-2902

UT Date	UT Time h m	Duration (hrs)	Resolution FWHM(Å)	Coverage Å
1993 Mar 21	20 48	4.0	3	3600-5000
1993 Mar 22	20 22	1.6	3	3600-5000

period. The sequence of 3Å resolution spectra on both of the nights was summed to construct the template (Figure 17c). The template shows similar features to Figure 17b but the absorption components in Hδ, Hϵ, and H8 are clearer than in Figure 17b. The relative radial velocities were determined using the cross-correlation technique. These data are plotted in Figure 18. A Fourier amplitude spectrum was calculated for the radial velocities but shows no significant signal with a semi-amplitude greater than 30 km/s. This is not surprising from inspection of the scatter in Figure 18. The failure to determine an orbital modulation is due to the very weak features in the individual spectra.

In regard to the sub-classification, although moderate emission lines were seen in the first spectrum (Figure 17a), absorption components were seen in the wings of the high order Balmer lines in Figure 17b and 17c; thus the spectral features of EC10560-2902 are more like a UX UMa star than a RW Tri star which shows pure emission line spectra.

References:

Bailey, J. (1981). *Mon. Not. R. astr. Soc.*, **197**, 31.

Deeming T.J. (1975). *Astrophys. Space Sci.*, **36**, 137.

Hutchings, J., and Cowley, A.P. (1984). *Publ. astr. Soc. Pac.*, **96**, 559.

Haug, K., and Drechsel, H. (1985). *Astron. Astrophys.*, **151**, 157.

Lu, W., and Hutchings, J.B. (1985). *Publ. astr. Soc. Pac.*, **97**, 990.

Schlegel, E.M., Honeycutt, R.K., and Kaitchuck, R.H. (1983). *Astrophys. J. Suppl.*, **53**, 397.

Voikhanskaya, N.F. (1988). *Astron. Astrophys.*, **192**, 128.

Warner, B. (1987). *Mon. Not. R. astr. Soc.*, **227**, 23.

Warner, B. (1994). *Cataclysmic Variable Stars*, Cambridge University Press, in press.

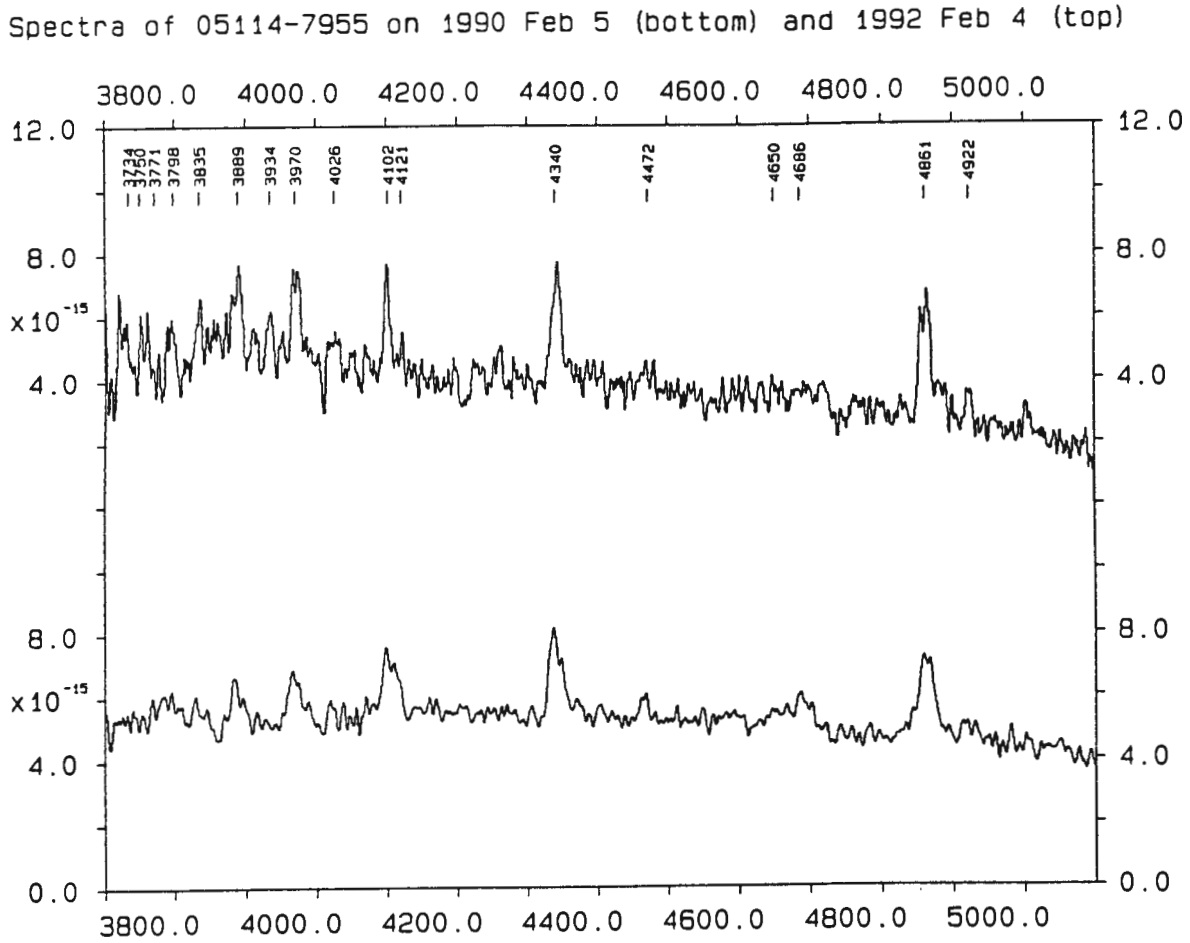

Figure 1. Spectra of EC05114-7955 on 1990 Feb 5 (bottom) and 1992 Feb 4 (top). The ordinate is in erg/cm²/s/Å and the abscissa is in Angstroms.

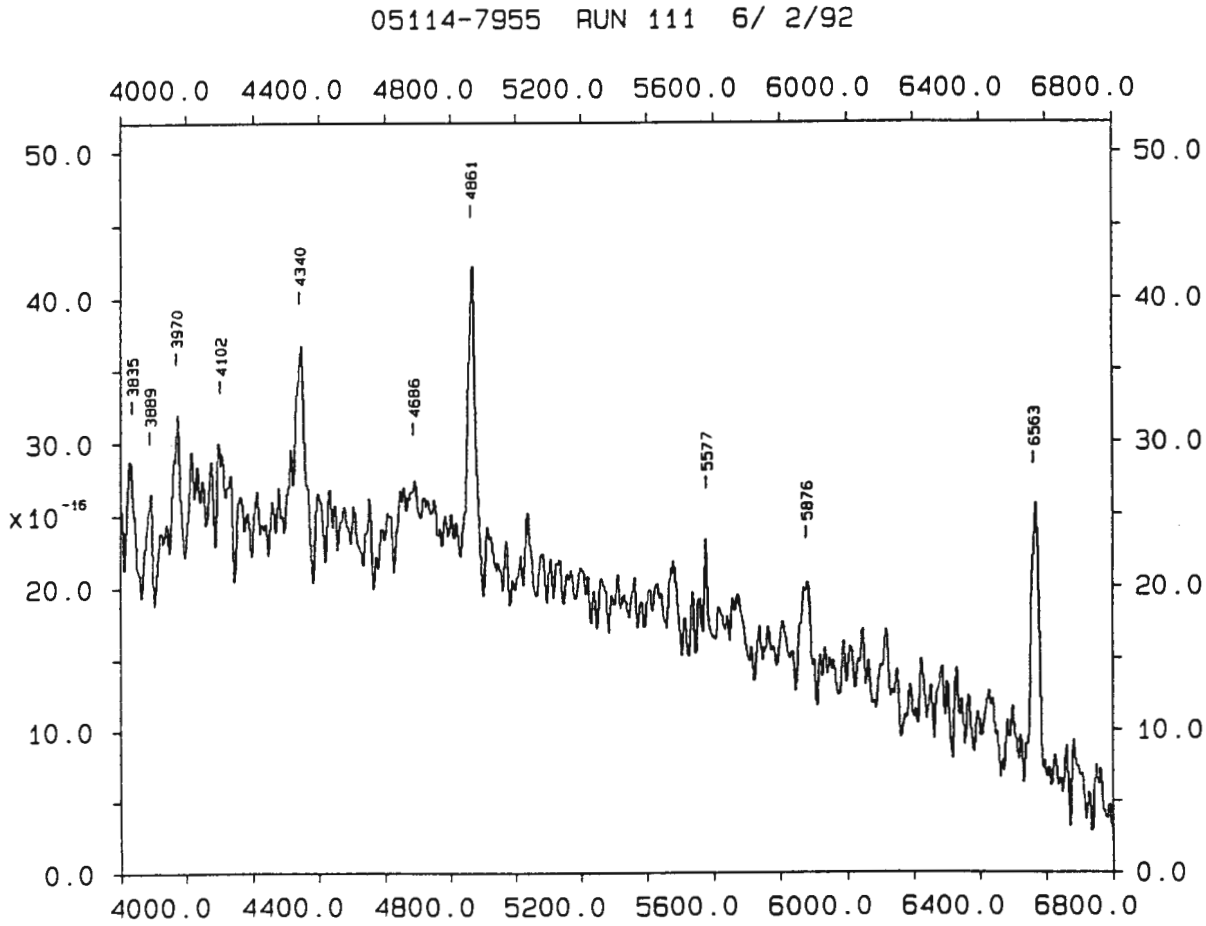

Figure 2. A low resolution spectrum of EC05114-7955 on 1992 Feb 6.

Chapter 8: *Two Peculiar CVs: EC05114-7955 and EC20335-4332*

Two CVs, EC05114-7955 and EC20335-4332, showing peculiar behaviour are presented in this chapter: EC05114-7955 is discussed in section 8.1 and EC20335-4332 is discussed in section 8.2.

§8.1 EC05114-7955

§8.1.1 Spectroscopic Characteristics

EC05114-7955 was spectroscopically observed on 1990 February 5. The spectrum with 4Å resolution covering λλ3700-5100Å is shown in the bottom of Figure 1 and is characterized by broad, double-peaked Balmer lines in emission. There can thus be no doubt that this object is a CV. HeI λ4471Å is visible and HeII λ4686Å in emission is blended with the high excitation lines of CIII/NIII λ4650Å. Two years later, a similar spectrum was obtained and is shown in the top of Figure 1. The Balmer lines are resolved up to H12 and are stronger than that in the bottom spectrum of Figure 1. HeI λ4026Å, λ4121Å, λ4471Å, and λ4922Å in emission are possibly present as well as CaII λ3934Å. An 8Å resolution spectrum covering λλ3800-6800Å was obtained on 1992 February 6 and is shown in Figure 2. The Balmer series, Hα-H9, are present. HeII λ4686Å is visible as well as HeI λ5876Å. No other features are visible. Note that the emission line at λ5577Å is from the night sky. Although HeII λ4686Å and the CIII/NIII λ4650Å blend emission are present in the spectra, the low HeII λ4686Å to Hβ ratio suggest classifying EC05114-7955 as a dwarf nova, such as TY PsA (O'Donoghue and Soltynski 1992).

§8.1.2 Light Variations

UBV photometry of EC05114-7955 was obtained on 1990 February 23 yielding the values V=14.82, B-V=0.24, U-B=-0.78, which places the object slightly above the blackbody line in the UBV two-colour diagram. The HSP-runs secured

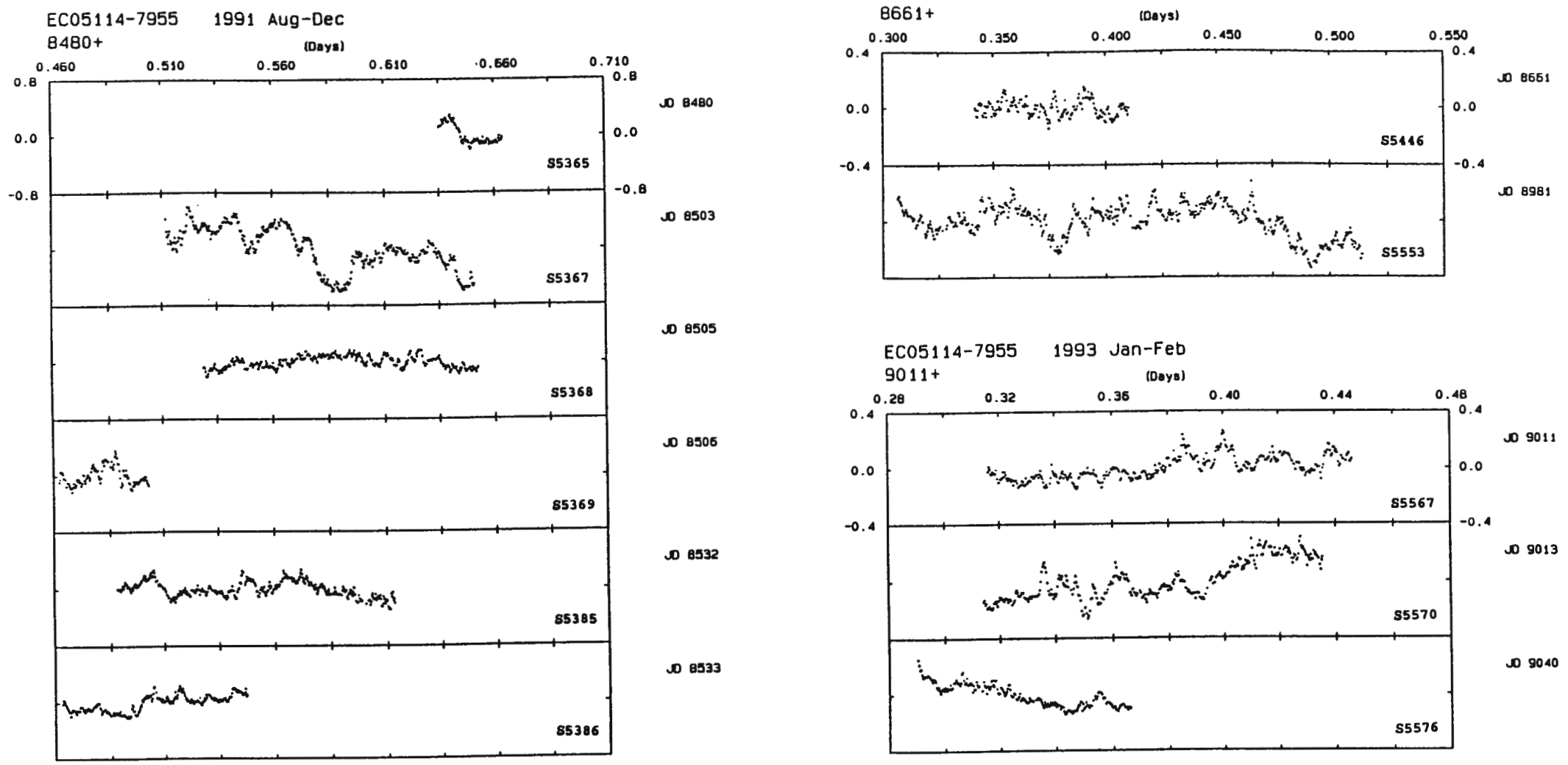

Figure 3. Light variations of EC05114-7955: (a) 1991 Aug-Dec; (b) 1992; (c) 1993 Jan-Feb (for details of HSP-runs see Table I).

during 1991-1993 are listed in Table I and plotted in Figure 3. These data show flickering variations with a peak-to-peak amplitude in the range ~20-40% (except Run S5367) on a time scale of a few minutes. Run S5367 has the largest amplitude variation of 1.7 mag due to a deep minimum in the light curve (2nd panel of Figure 3a); the deep minimum between HJD8503.58-8503.60 lasting for about 28 minutes and having a depth of ~0.85 mag looks like an eclipse but this behaviour was not seen again in the later observations (Figure 3). Fourier amplitude spectra (not shown here) for individual runs were calculated for the data in Table I and show no evidence for rapid oscillations with amplitude greater than 2% in the frequency range 5-50 mHz. In the low frequency range 0-5 mHz, the amplitude spectra exhibit various peaks with amplitudes ≥8%, none of which indicate a coherent period but which arise from the large amplitude of the flickering.

Table I. Observing Log of High-Speed Photometry for EC05114-7955

Run	UT Date	Start HJD 2440000.+	Duration hrs	B_w	ΔB_w
S5365	120891	8480.6345	0.7	15.5	0.54
S5367	040991	8503.5113	3.3	15.8	1.72
S5368	060991	8505.5279	3.0	15.7	0.55
S5369	060991	8506.4617	1.1	15.6	0.65
S5385	021091	8532.4875	3.0	15.7	0.77
S5386	031091	8533.4626	2.0	15.5	0.54
S5446	080292	8661.3413	1.7	15.1	0.30
S5553	241292	8981.3053	5.0	15.0	0.75
S5567	230193	9011.3153	3.1	15.0	0.47
S5570	250193	9013.3133	2.9	15.0	0.67
S5576	210293	9040.2895	1.8	14.8	0.44

Table II. Observing Log of Time Resolved Spectroscopy for EC05114-7955

UT Date	Start UT h m	Duration hrs	Resolution FWHM Å	Coverage Å
91 Nov 9	22 15	4.0	4	3500-5200
92 Feb 8	18 56	4.7	3	3700 5000

§8.1.3 Radial Velocity Variations

Since the photometric data do not show any orbital modulation, time-resolved spectroscopy (Table II) was obtained in 1991 November 9 and 1992

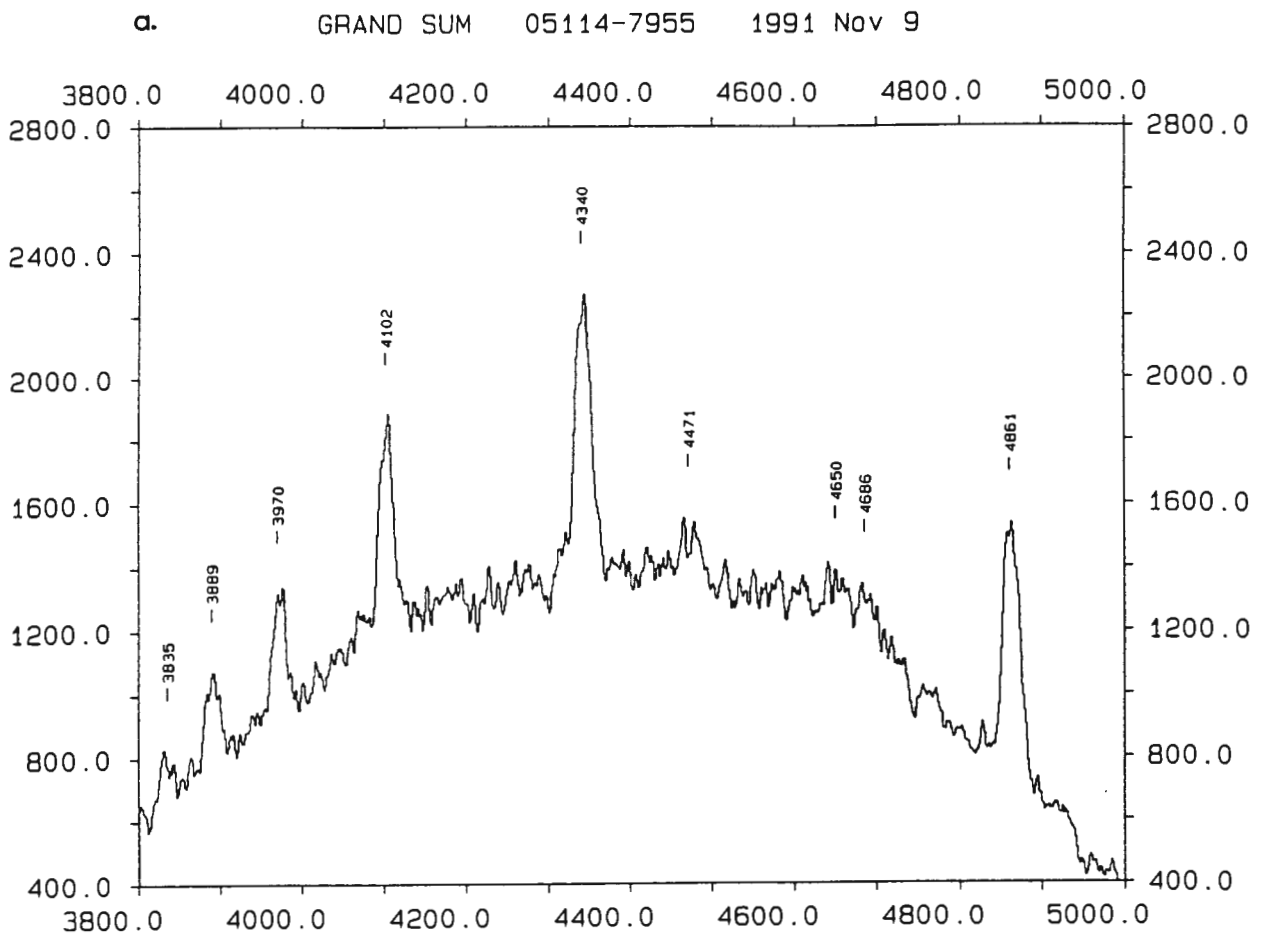

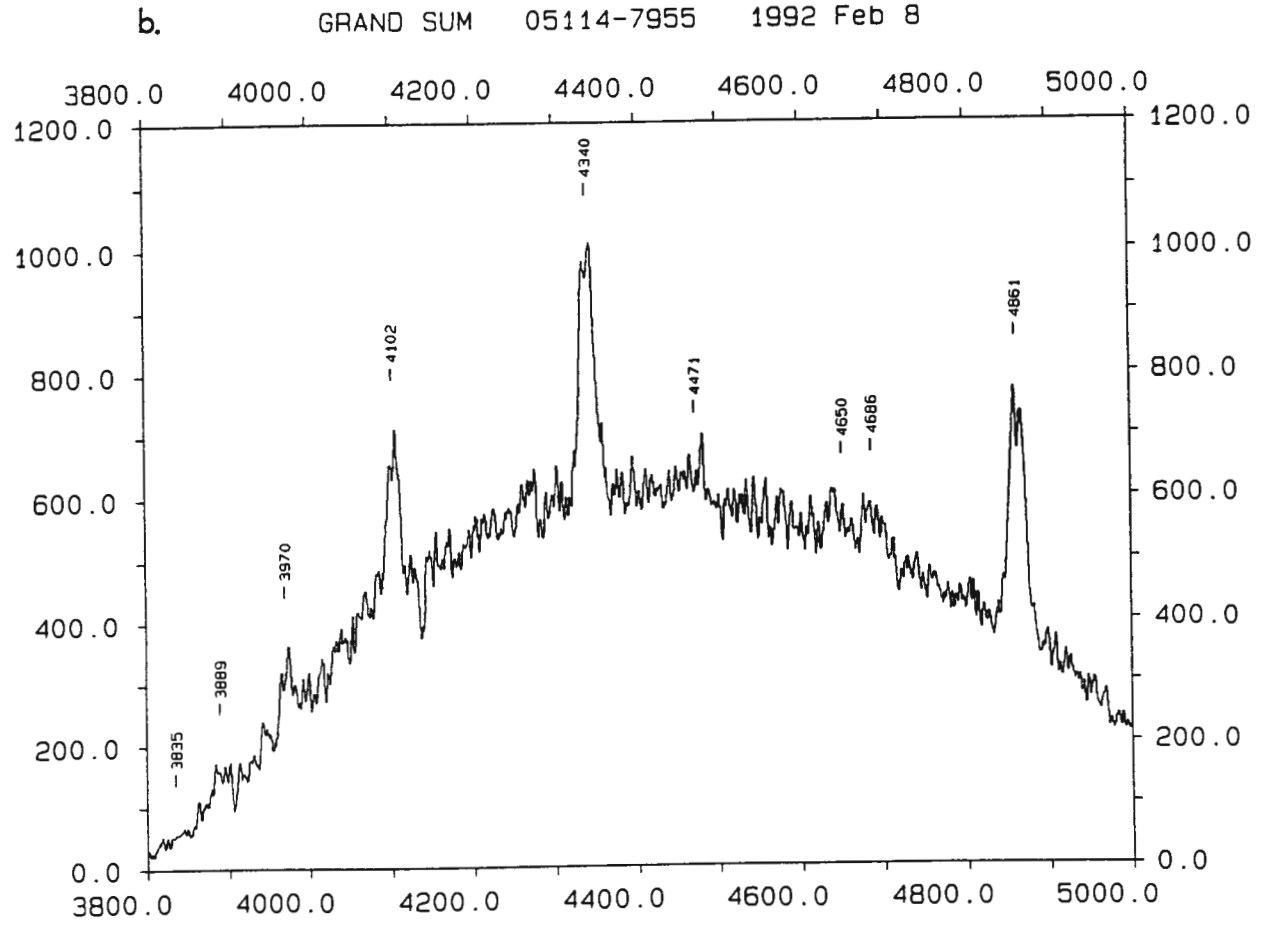

Figure 4. Grand sum spectrum of EC05114-7955 on (a) 1991 Nov 9 and (b) 1992 Feb 8. The ordinate is counts.

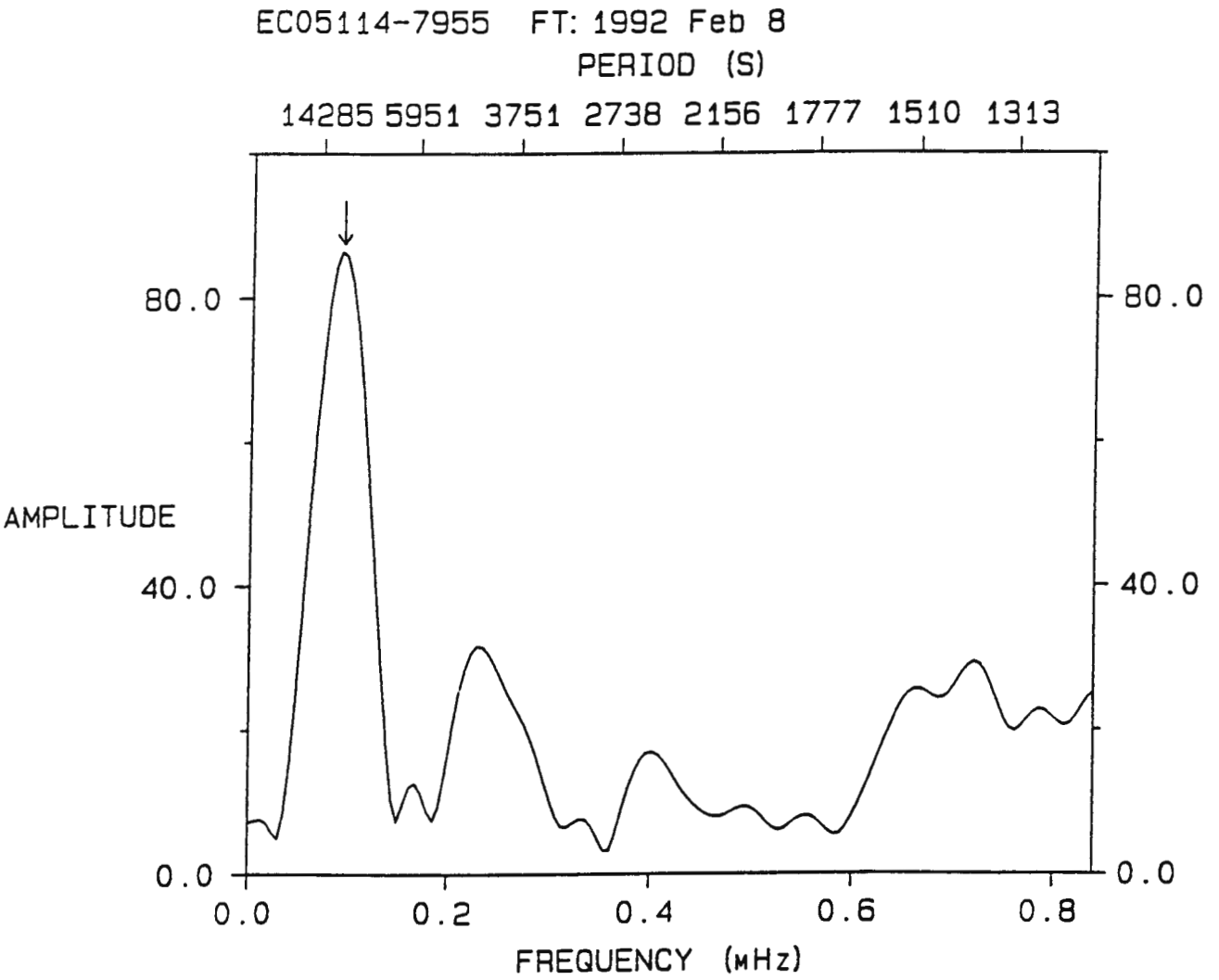

Figure 5. Fourier amplitude spectrum calculated for the radial velocities of EC05114-7955 on 1992 Feb 8. The highest peak occurs at a period of 3.02-hr.

February 8 in order to search for an orbital period. The templates were made for each run separately by summing all the spectra on that night and are shown in Figure 4. The relative radial velocities were determined using the cross-correlation technique and are tabulated in Table III. An amplitude spectrum (Figure 5) was calculated for the data of HJD8861 (1992 February 8) because it has a longer time span. The highest peak in Figure 5 occurs at 0.0918 mHz (0.126 days) (arrowed). In order to derive the best period, an ephemeris for times of largest red shift, and the semi-amplitude K_1, a sinusoid of initial frequency equal to that of the highest peak in Figure 5 was fitted to the HJD8661 data by non-linear least-squares and gave

$$T_0(\mathrm{HJD}) = 2448661.233 \pm 0.003 + 0^{d}.130 \pm 0.014\ E\ ,$$

$$K_1 = 83 \pm 11 \text{ km/s}.$$

All the data in Table III were fitted by least-squares with a sinusoid of period 3.1-hr (0.130 days) and are shown in Figure 6a (Figures 6b,c will be discussed in the next section). The period derived above, 3.1 hrs, also fits the data of 1991 November 9. The sequences of spectra were binned into orbital phases and are plotted in Figure 7 (bottom to top: phase 0.0 to 0.9) which show complex line profiles. The strengths of the Balmer lines seem to vary with orbital phase in Figure 7b. The details of the line-profile and strength variations will be discussed in the next section.

Table III. Relative Radial Velocities of EC05114-7955

HJD 2440000.+	RV km/s	HJD	RV	HJD	RV
8570.42636	119	8570.59171	-165	8661.38675	7
8570.43689	42	8661.28792	-65	8661.39380	-31
8570.45386	-66	8661.29497	-68	8661.40361	6
8570.46440	-82	8661.30201	-89	8661.41066	-81
8570.47702	-121	8661.31136	-47	8661.41771	-11
8570.48756	-23	8661.31841	-18	8661.42632	-130
8570.49976	-37	8661.32546	8	8661.43368	-48
8570.51030	-12	8661.33449	-25	8661.44078	-136
8570.52314	55	8661.34154	27	8661.44924	-31
8570.53368	60	8661.34859	38	8661.45628	22
8570.54566	70	8661.35722	79	8661.46333	-9
8570.55732	61	8661.36427	105	8661.47190	82
8570.56932	36	8661.37132	177	8661.47895	6
8570.57987	21	8661.37970	46	8661.48599	89

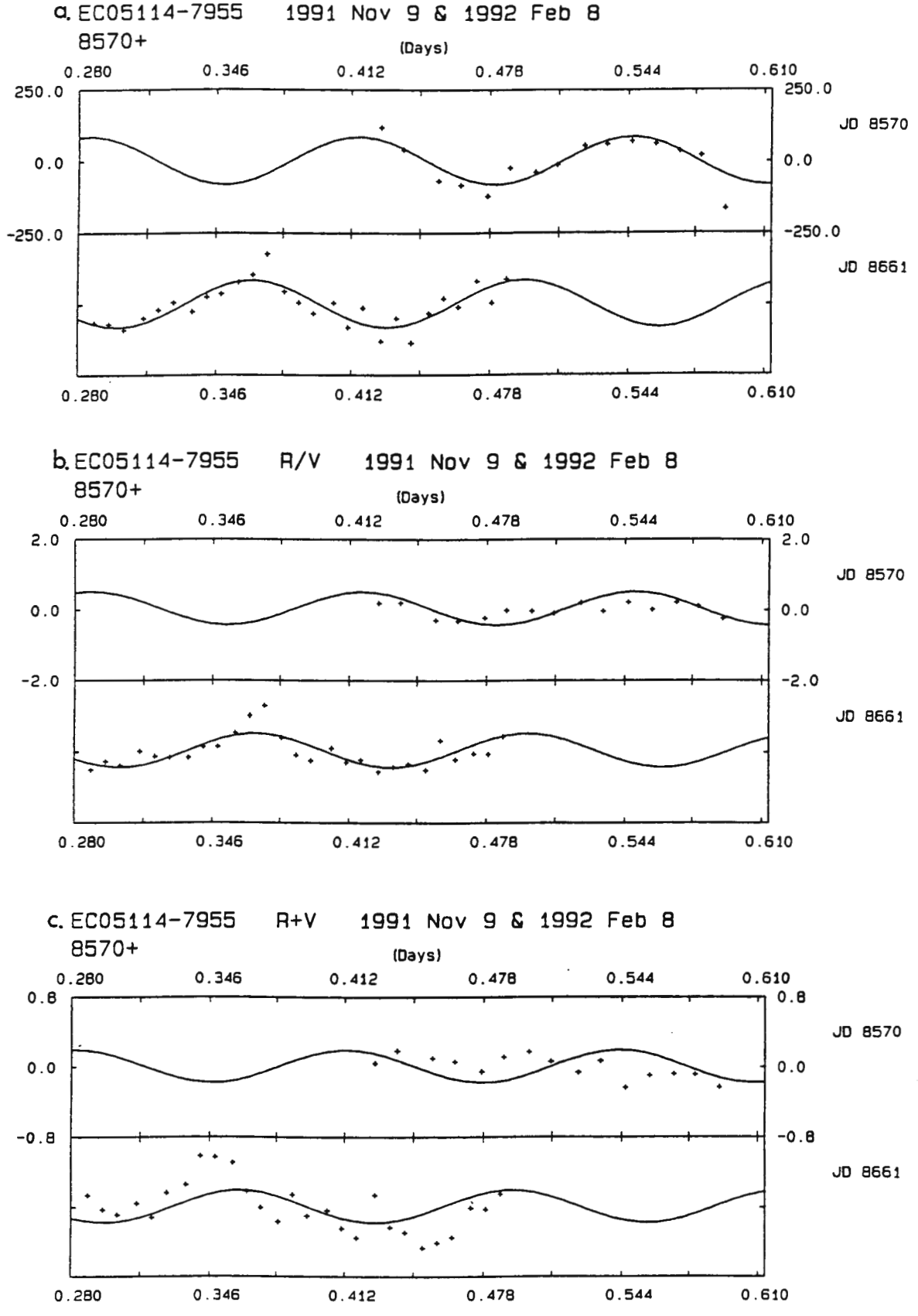

Figure 6. Plots of (a) radial velocity, (b) R/V ratio, and (c) R+V variations.

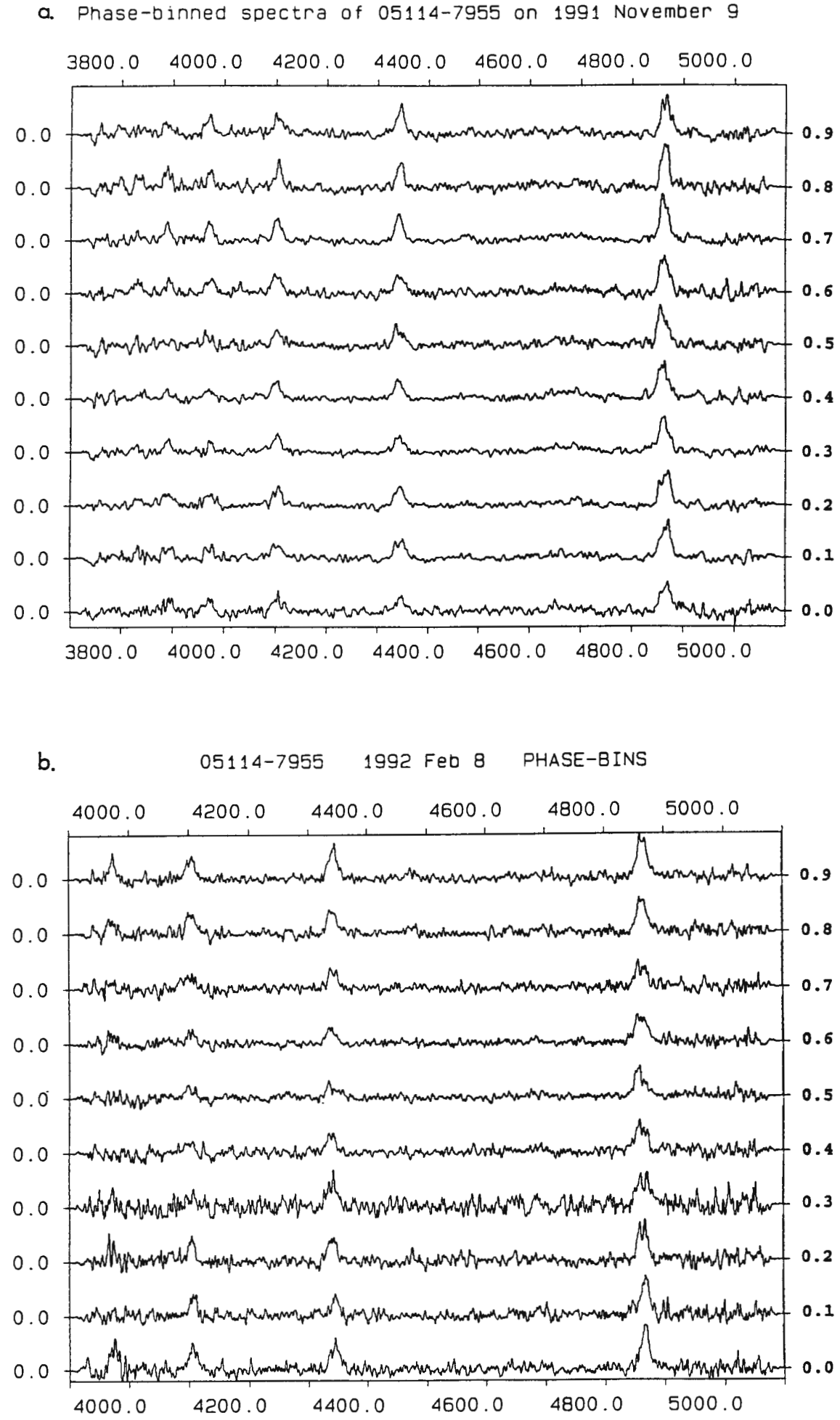

Figure 7. Spectral variations for (a) 1991 Nov 9 and (b) 1992 Feb 8. The ordinate in left-hand side is the relative intensity normalized by the continuum and the ticks mark the zero intensity. The ticks on the right-hand side ordinate mark the orbital phases. The abscissa is in Å.

§8.1.4 Lines Profiles

The grand sum spectra in Figure 4 show similar spectral features to Figure 1 and 2. The Balmer lines in Figure 4a show single-peaked profiles but exhibit double-peaked profiles in Figure 4b. Measurements of full widths at half maximum (FWHM), full widths at continuum level (FWZI), and equivalent widths were made by fitting gaussian profiles to all the strong Balmer lines in Figure 4. The results are listed in Table IV. All widths of the Balmer

Table IV. Balmer emission lines of EC05114-7955

Lines	FWHM ±4Å	FWZI ±4Å	EW ±4Å	FWHM ±2Å	FWZI ±2Å	EW ±2Å
	1991 November 9			1992 February 8		
Hβ	23	42	33	22	45	30
Hγ	22	40	20	21	40	20
Hδ	20	40	14	16	31	11
Hε	16	31	8	16	30	10

emission lines decrease up the series; the higher order Balmer lines have uncertain values due to blended wings. The double peaks in the line profiles have a separation of about 9Å and are the classic signature of Doppler broadening in an accretion disk. They usually appear in highly inclined dwarf novae such as OY Car (Bailey and Ward 1981), Z Cha (Marsh et al. 1987), and TY PsA (O'Donoghue and Soltynski 1992). Assuming the rotation of the accretion disc is Keplerian, then half of the peak-separation represents the projected velocity ~300 km/s of the outer edge of the disc and the FWZI indicates the projected velocity ~1400 km/s of the inner boundary of the disc which possibly extends to the surface of the white dwarf.

The profiles of emission lines in CVs frequently show periodic variations with the orbital motion. This variation is caused by asymmetry in the strength of emission from different parts of the accretion disk. In order to investigate these profile variations, the red/violet (R/V) ratio was measured for Hβ, Hγ, and Hδ separately. The technique of O'Donoghue and Soltynski (1992) was used to evaluate the ratio (R/V) and total equivalent width (R+V). The details have been discussed in Chapter 6 (§6.3.1). The results are plotted in Figure 6b and 6c. The solid lines in Figure 6b and 6c are a least

squares fit of a sinusoid of the orbital period, 3.1-hr. The R/V for the data of 1991 November 9 shows no periodic variations but the R+V exhibits a slight decrease with time. This suggests that the line-emitting region is distributed symmetrically in the disk with respect to the white dwarf. In contrast, the results of 1992 February 8, in both R/V and R+V, reveal a variation at the orbital period in phase with the radial velocity variations: there are minima at phase 0.5, corresponding to the largest blue shift, and maxima at the largest red shift (phase 0.0). The effect can be seen from inspection of the line strengths in Figure 7b. These results imply that the emission line region is distributed asymmetrically in the disk. Compared to the results of 1991 Nov 9, a significant change in the distribution of line emission has occurred. This kind of change has been observed in V2051 Oph (Warner and O'Donoghue 1987). Therefore the semi-amplitude of the radial velocity curve obtained above is not likely to be very reliable, so the value of K_1 will not be used to derive a dynamical solution for the system.

§8.1.5 Discussion

From the large amplitude of the flickering and the low excitation spectrum, EC05114-7955 is similar to a dwarf nova. The CIII/NIII λ4650Å blend in emission is not usually seen in the spectra of DN but is present in the majority of NLs. However, among the known DN, two of them, TY PsA (O'Donoghue and Soltynski 1992) and BV Pup (Vogt 1976), show the CIII/NIII λ4650Å blend. BV Pup also exhibited relatively strong HeII λ4686Å and a low outburst amplitude ~2mag (Szkody et al. 1986). Vogt (1989) suggested that the post-novae may evolve through a "BV Pup stage" before becoming dwarf novae. Although no outbursts have yet been detected, EC05114-7955 has similar spectral features to BV Pup. Thus, EC05114-7955 may be related to BV Pup and is thus a DN; the possibility that it is a NL can't be ruled out. If it is a DN, it would be the only DN with $3 < P_{orb} < 4$ hrs.

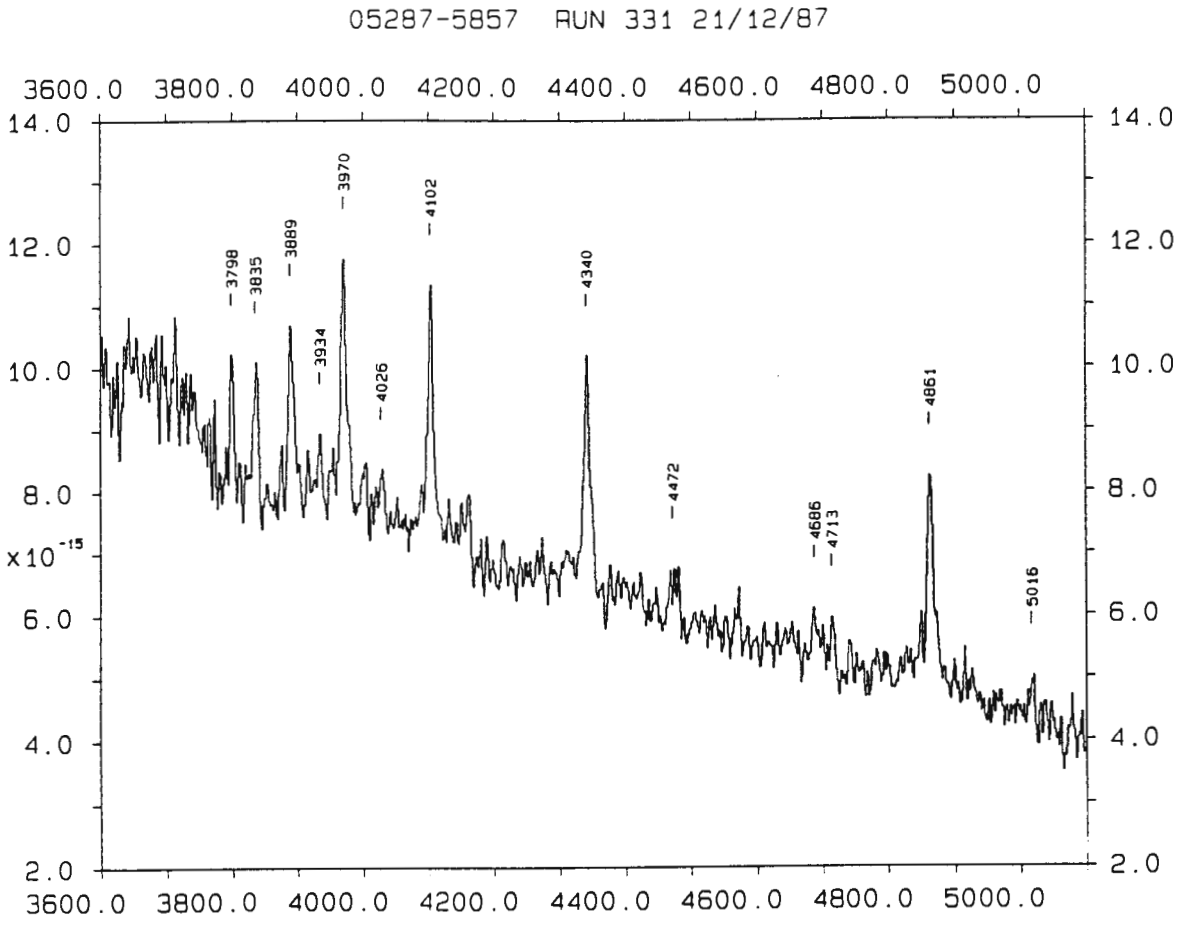

Figure 1. The first spectrum was taken at 14th Bmag on 1987 December 21.

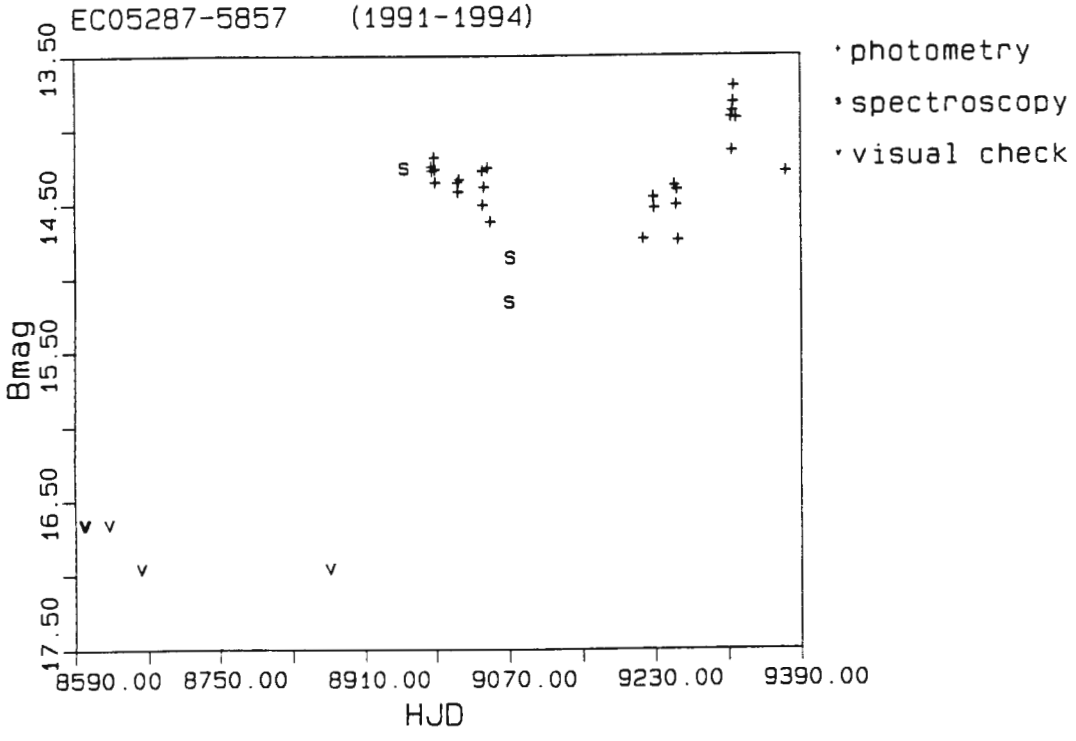

Figure 2. Long term light-variation of EC05287-5857 during 1991-1994. The (+) signs represent the magnitudes obtained by UBV measurements or the mean magnitudes of HSP; if the magnitude is obtained by HSP, the run number of the light curve is labelled in the right-hand side of the (+) sign. The "S" represent the magnitudes derived from the spectroscopic flux; the spectrum is shown in the plot whose Figure number is beside the "S".

Chapter 9: *Photometry and Spectroscopy of a New VY Scl Star EC05287-5857 in the High State*

In cataclysmic variables, two types of rapid oscillations generally appear in outbursting dwarf novae and nova-like variables: dwarf novae oscillations (DNO) and quasi-periodic oscillations (QPO). For dwarf novae, DNO and QPO usually appear half way up the rising branch of the outburst and persist through maximum and disappear about half way down the declining branch (Patterson 1981 and Warner 1988). There are exceptions such as in VW Hyi; DNO were present towards the end of an outburst (Warner and Brickhill 1978). DNO can be coherent for ~100 cycles or more and do not usually have sufficient amplitude to be seen in the light curves. The QPO generally have periods 3-5 times longer than DNO in the same star and are coherent for only a few cycles. In a Fourier amplitude spectrum, QPO generally have their power spread out over a wide range of frequencies which is difficult to detect unless the QPO are obviously visible in the light curves.

So far, no satisfactory theory has yet been given to explain the origin of the DNO and QPO, although a number of models have been considered: (1) a rotating spot at the inner edge of the accretion disk (Bath 1973) or on the surface of the white dwarf (Lamb et al. 1978); (2) non-radial oscillations in the surface layers of the white dwarf (Papaloizou and Pringle 1978) or in the accretion disk (Van Horn et al. 1980); and (3) magnetically controlled accretion from the disk (Warner 1983).

As has been already discussed in section 3.1.1, the VY Scl stars, a category of the NLs, spend most of their time in the high state and occasionally fade to the low state by one or more magnitudes, which is caused by temporary reducing of the rate of mass transfer from the secondary (Warner 1994), for weeks to years. Some of these stars show QPO such as in TT Ari (Hollander and Van Paradijs 1992) and MV Lyr (Borisov 1992). These QPO have periods of a few hundred seconds. They seem to represent periodic behaviour

The presence of humps may be caused by sudden increases in mass transfer rate, because, during the night in which the humps appeared (HJD 9160), the object was ~0.6 mag brighter than in the previous night (HJD 9159). Thus, the cause of the humps in light variations of EC20335-4332 is probably not dissimilar to that of PG0917+342, in which Skillman and Patterson (1993) suggested that superhumps arise from precession of an elliptical disk. To confirm this, further intensive spectroscopy is required.

Comparing the spectra of both EC20335-4332 and PG0917+342, the CIII/NIII λ4650Å emission was seen in the spectra of PG0917+342 (Green et al. 1982) in the fainter state but was invisible in that of EC20335-4332. Thus, from the above discussions, we may conclude that EC20335-4332 is likely a dwarf nova, instead of a nova-like variable.

References:

Bailey, J., and Ward, M. (1981). *Mon. Not. R. astr. Soc.*, **194**, 17.

Dobrzycka, D., and Howell, S.B. (1992). *Astrophys. J.*, **388**, 614.

Green, R.F., Ferguson, D.H., Liebert, J., and Schmidt, M. (1982). *Publ. astr. Soc. Pac.*, **94**, 560.

Hutchings, J.B., and Cote, T.J. (1986). *Publ. astr. Soc. Pac.*, **98**, 104.

Marsh, T.R., Horne, K., and Shipman, H.L. (1987). *Mon. Not. R. astr. Soc.*, **225**, 551.

O'Donoghue, D., and Soltynski, M.G. (1992). *Mon. Not. R. astr. Soc.*, **254**, 9.

Patterson, J., and Moulden, M. (1993). *Publ. astr. Soc. Pac.*, **105**, 779.

Skillman, D.R., and Patterson, J. (1993). *Astrophys. J.*, **417**, 298.

Vogt, N. (1976). in P. Eggleton et al. (eds), *Structure and Evolution of Close Binary Systems*, D. Reidel Publishing Company, p147.

Vogt, N. (1989). in M.F. Bode and A. Evans (eds.), *Classical Novae*, John Wiley and Sons Ltd, Ch12, p225.

Warner, B. (1994). *Cataclysmic Variable Stars*, Cambridge University Press, in press.

was calculated for the residuals and is shown in Figure 11c. The highest peak occurs at 0.1298 mHz (7704s). Two of the above possible P_{hp}, 6711s and 7246s, are consistent with that highest peak (7704s), within the error ~820s. Sinusoids with periods 6711s and 7246s respectively were fitted to the residuals of run X0011. The results are shown in Figure 12. Although the fit of the period 7246s is slightly better than that of 6711s, there is little difference. Therefore, further intensive photometry is required to confirm the P_{hp}.

§8.2.3 Discussion

As mentioned above, the photometric behaviour of EC20335-4332 shows a rapid change in the shape of the light curves within a mean brightness range of less than 1 mag. This kind of behaviour has been observed in the possible intermediate polar TW Pic (Patterson and Moulden 1993) which showed various patterns of light variations at brightnesses, 14.1-14.7 Bmag. Intermediate polars (IPs), by definition (Warner 1994), should be hard X-ray emitters and multi-periodic. Although the photometric characteristics of EC20335-4332 are analogous to that of TW Pic, EC20335-4332 can not be compared with IPs because of the lack of strong HeII λ4686Å and multiple periodicities in the light variations. The hump in the light curve of EC20335-4332 could be similar to the "permanent superhumps" seen in the UX UMa star PG0917+342 (Warner 1994). This star showed humps with peak-to-peak amplitudes ~0.05 mag and a period 1.88-hr (Skillman and Patterson 1993). The hump period of EC20335-4332, ~2-hr, is very close to that of PG0917+342, but the hump amplitude of EC20335-4332, ~0.24-0.50 mag, is much larger than that of PG0917+342. Note that there are few NLs below the period gap. For the SU UMa stars, there is a correlation between the orbital period and the superhump period (P_s): P_{orb} is slightly shorter than P_s. PG0917+342 also has an orbital period 1.73 hrs (Dobrzycka and Howell 1992), shorter than P_{hp}. Thus, if EC20335-4332 is an SU UMa star, its orbital period is predicted to be shorter than 2 hrs.

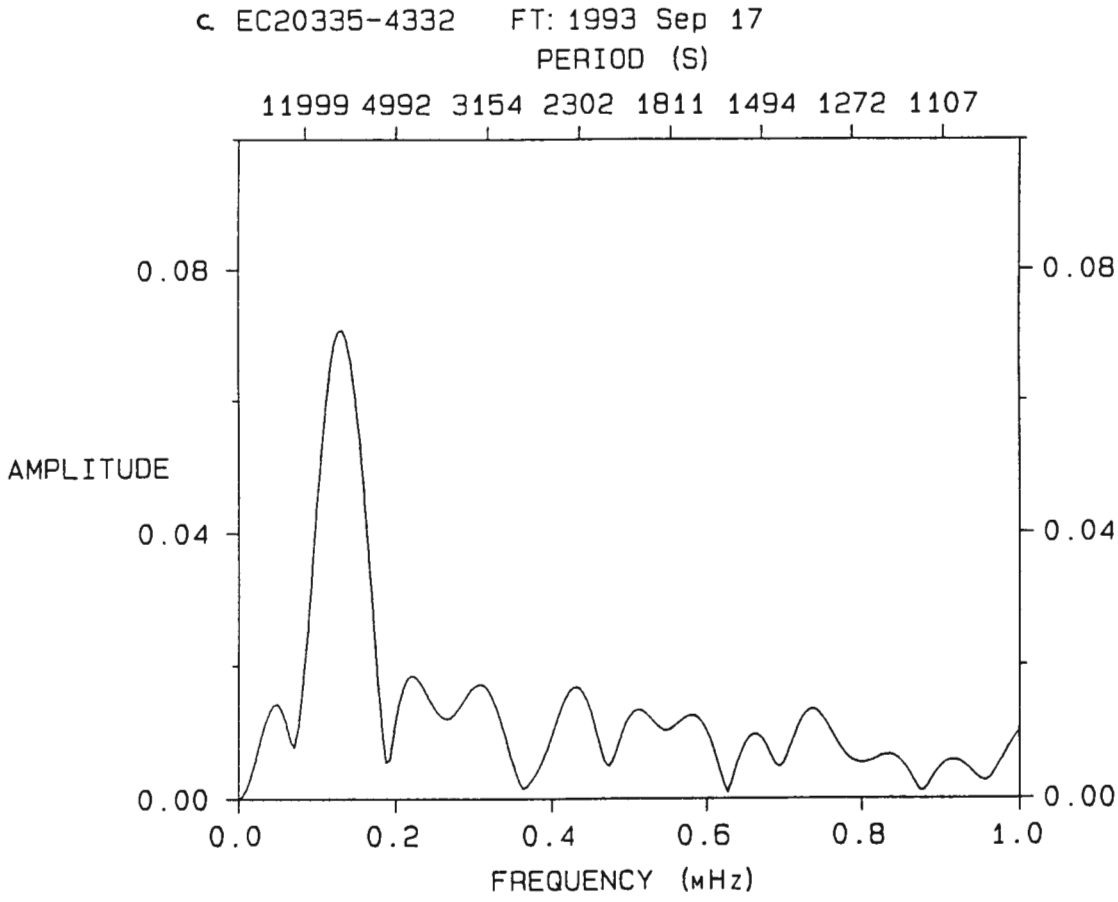

Figure 11. -continued.

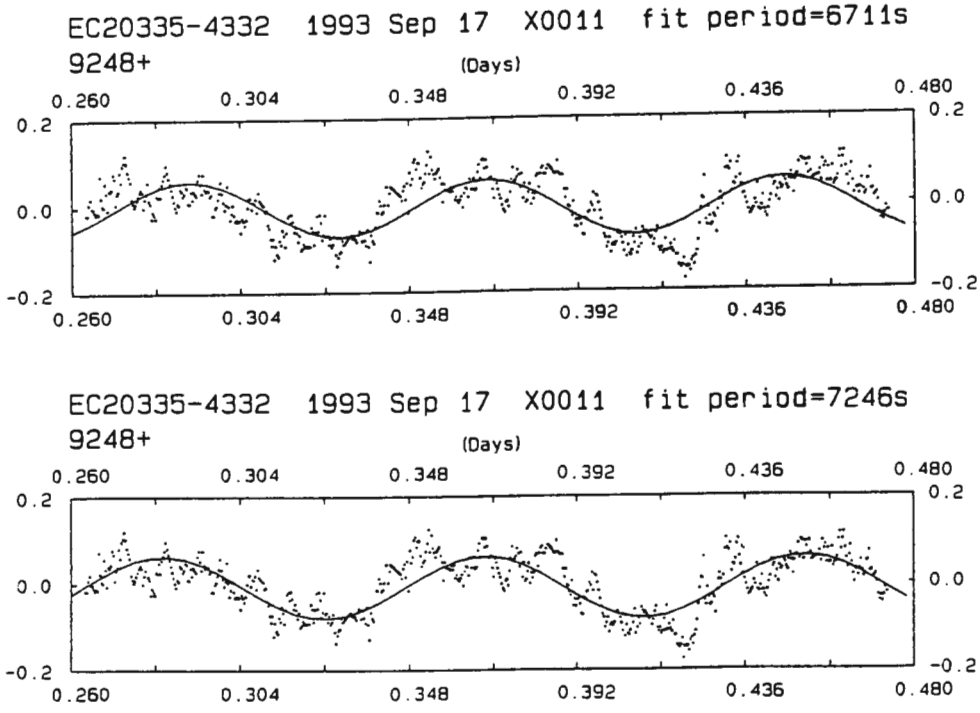

Figure 12. A comparison between fitting sinusoids of period 6711s (top) and 7246s (bottom) to the light curve of run X0011 after removing low frequencies (see text).

Table VI. Observing Log of High-Speed Photometry for EC20335-4332

Run	UT Date	Start HJD 2440000.+	Duration hrs	B_w	ΔB_w
S5611	170693	9156.4249	3.2	15.7	0.31
S5615	190693	9157.5930	1.5	15.4	0.24
S5618	200693	9159.4828	2.3	15.5	0.41
S5622	220693	9160.5052	3.9	14.9	0.40
X0008	120893	9212.3204	4.5		
S5623	210893	9221.2730	0.9	15.0	0.27
S5624	220893	9222.2459	5.0	14.9	0.28
S5626	230893	9223.2351	6.4	15.0	0.28
X0011	170993	9248.2635	5.0	15.8	0.50

(Figure 10b). Fourier amplitude spectra were calculated for the data, S5618-S5622 and S5624-5626, and are shown in Figure 11. The humps in the light curves do not vary sinusoidally, so alias patterns at both the hump period (P_{hp}) and the first harmonic of the hump period are visible in Figure 11. Figure 11a shows a highest peak of 0.127±0.003 mHz but other aliases are of similar amplitude. The diurnal aliases can be ruled out, because their frequencies are not double the prominent aliases in the first harmonic: the frequencies of the six largest peaks near 0.13 mHz were compared with those of the seven most prominent peaks near 0.3 mHz. Only three pairs of frequencies (arrowed in Figure 11a) were found to be related by the expected 1:2 ratio. The possible values of P_{hp} are 6289, 6711, and 7246 seconds with measurement errors ~160 seconds and their first harmonics are 3184, 3425, and 3704 seconds which are consistent with the peaks (3195, 3448 and 3731 seconds) arrowed in Figure 11b, within the measurement errors of ~30 seconds. Among the above three peaks in Figure 11b, the amplitude of the 3448s-peak is much stronger than that of the other two. Thus the period 6711s in Figure 11a is the most likely alias to be the correct value of P_{hp}. This can be verified from the measurement of the interval between the mid-points of the two maxima of the humps in the bottom panel of Figure 10a. The result shows that the interval is ~6652s which is consistent with 6711s.

In Figure 10c, the object seems to show an orbital modulation superposed on a gradual increase in the mean brightness. A straight line was fitted to the data of Run X0011 and then subtracted from the data in order to remove the low-frequency variation in the light curve. A Fourier amplitude spectrum

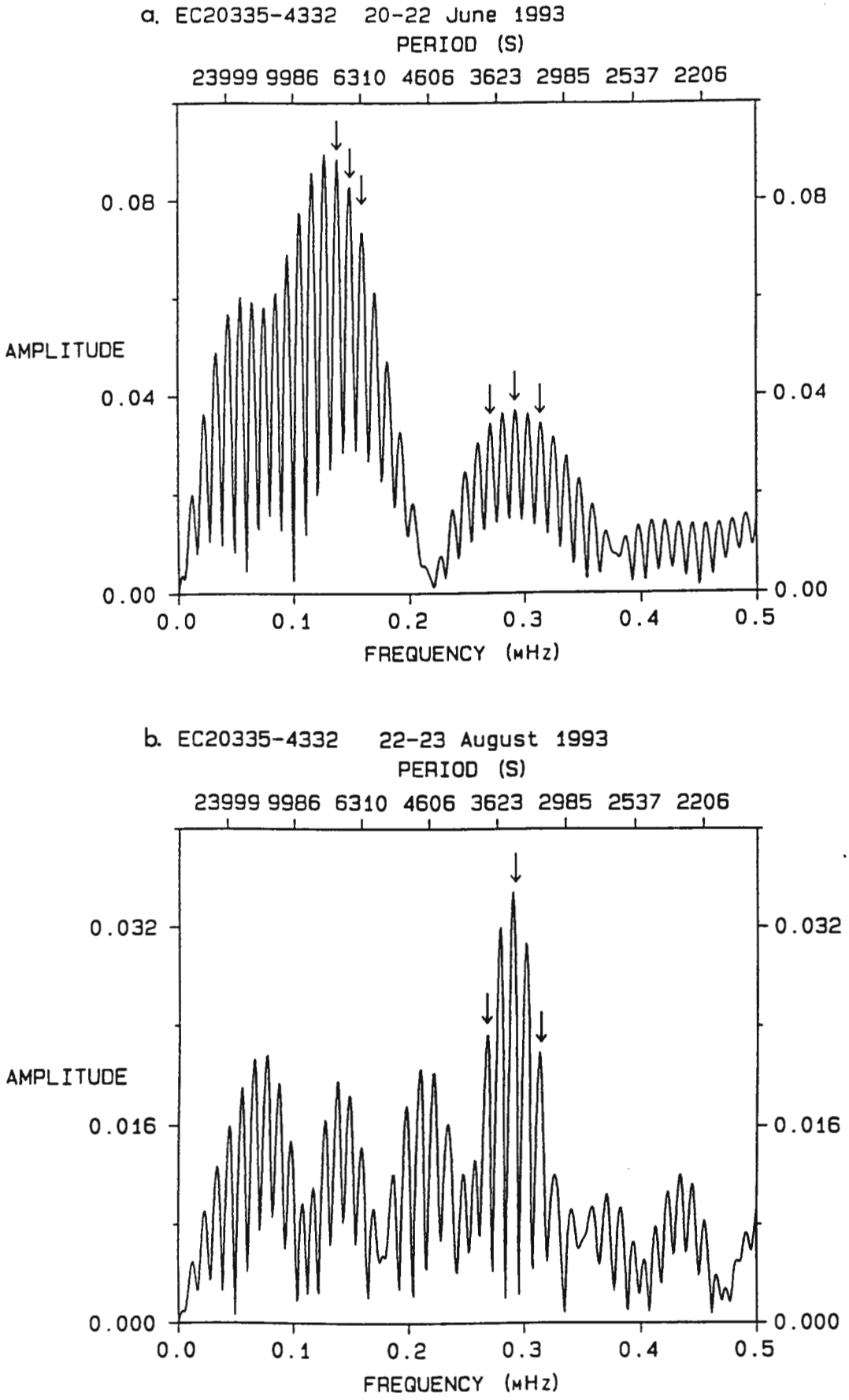

Figure 11. Fourier amplitude spectra of EC20335-4332 for (a) 1993 June 20-22 (runs S5618 and S5622), (b) 1993 August 22-23 (runs S5624 and S5626), and (c) 1993 September 17 (run X0011).

§8.2 EC20335-4332

§8.2.1 Spectral Characteristics

EC20335-4332 was first observed on 1992 May 7. The spectrum (not shown here) is characterized by broad Balmer lines in emission. Thus the object was classified as a CV. About four months later, time-resolved spectroscopy with time resolution of 1200s was obtained on 1992 August 28 (Table V). The sequence of spectra was summed to construct the template shown in Figure 8.

Table V. Observing Log of Time-Resolved Spectroscopy for EC20335-4332

UT Date	Start UT h m	Duration hrs	Resolution FWHM Å	Coverage Å
92 Aug 28	19 50	3.0	4	3600-5000

The grand sum spectrum reveals weak Balmer lines with FWZI~35Å, resolved up to H11. HeI λ4026Å, λ4388Å, and λ4471Å are possibly present. HeII λ4686Å in emission is visible as well as CaII λ3934Å. The radial velocities were determined using the cross-correlation technique. The results are plotted in Figure 9. A Fourier amplitude spectrum (not shown) was calculated for the radial velocities, and showed no periodicity as expected from the scatter in Figure 9. The failure to determine an orbital period is probably due to the very weak features in the individual spectra, the low time resolution, and (perhaps) the low inclination of the system (because the Balmer lines are narrow).

§8.2.2 Light Variations

UBV measurements of EC20335-4332 were obtained on 1991 July 8 and exhibited blue colours, B-V=-0.02 and U-B=-0.71, at V=15.38. The HSP-runs were obtained during 1993 June-September. These data are listed in Table VI and plotted in Figure 10. Figure 10 shows a rapid change, from night to night, in the shape of the light curve without a significant change in the mean brightness (which varies between 14.9-15.8 Bmag). A hump modulation appeared in the light curve with a period of ~2 hours on June 22 (the bottom panel of Figure 10a) but was not seen on the previous night (third panel of Figure 10a) nor in August

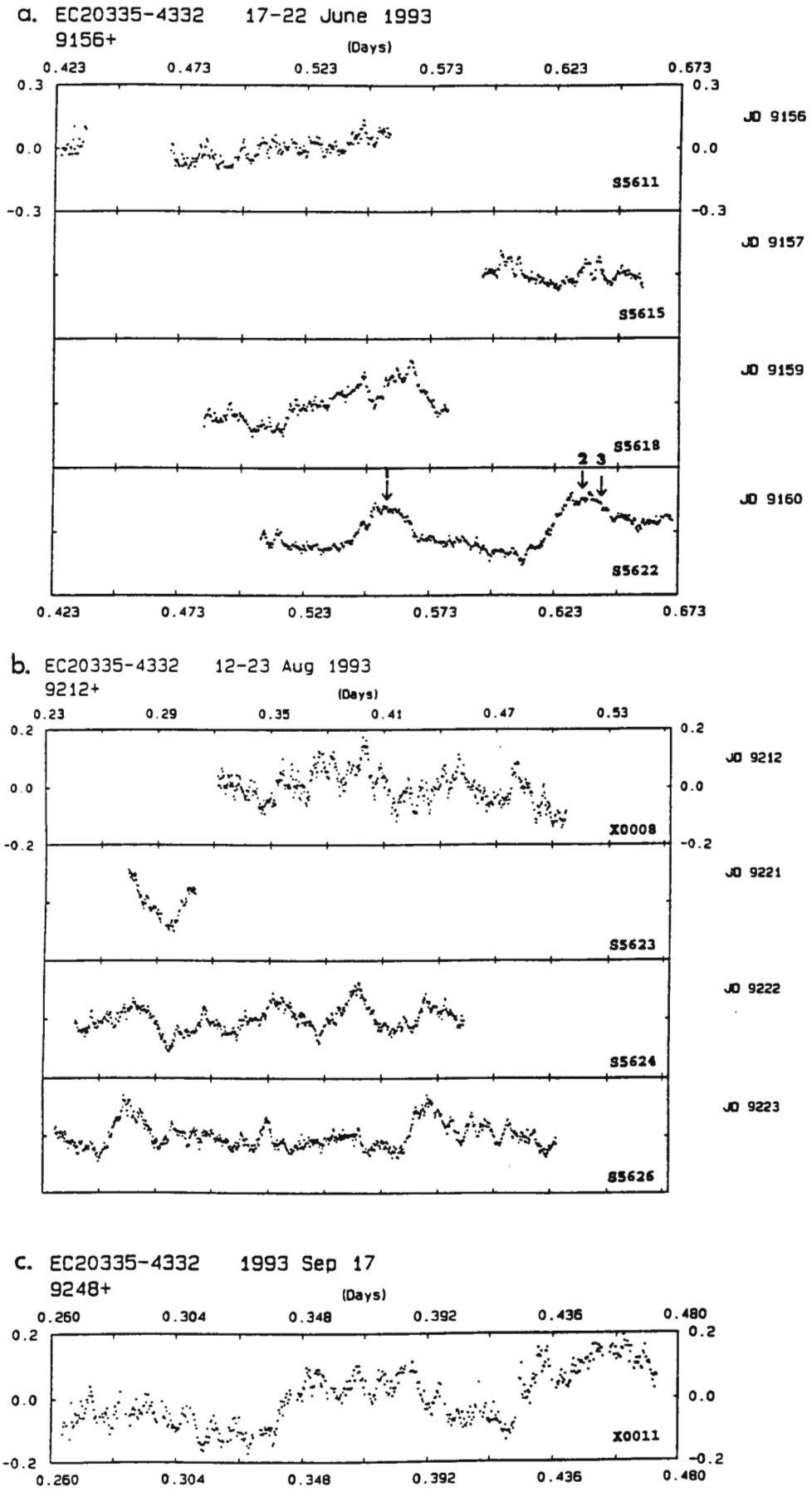

Figure 10. Light curve of EC20335-4332: (a) 1993 June 17-22; (b) 1993 August 12-23. The arrow 1 marks the mid-point (at HJD 9160.5570) of the maximum of the first hump. The intervals between the arrows 1 & 2 and that between 1 & 3 are 6711s and 7246s respectively; and (c) 1993 September 17.

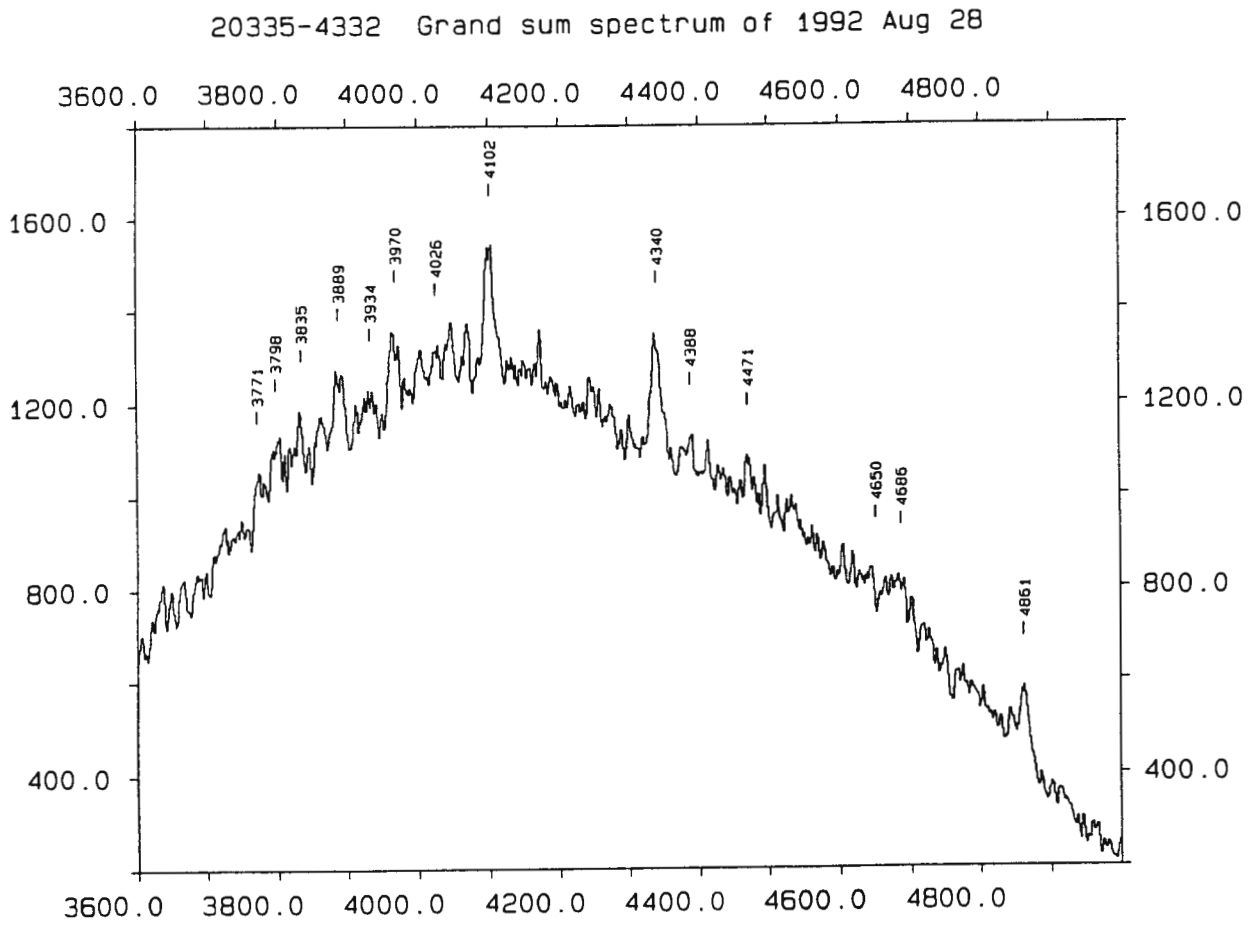

Figure 8. Grand sum spectrum of EC20335-4332 on 1992 August 28. The ordinate is in counts and the abscissa is in Å.

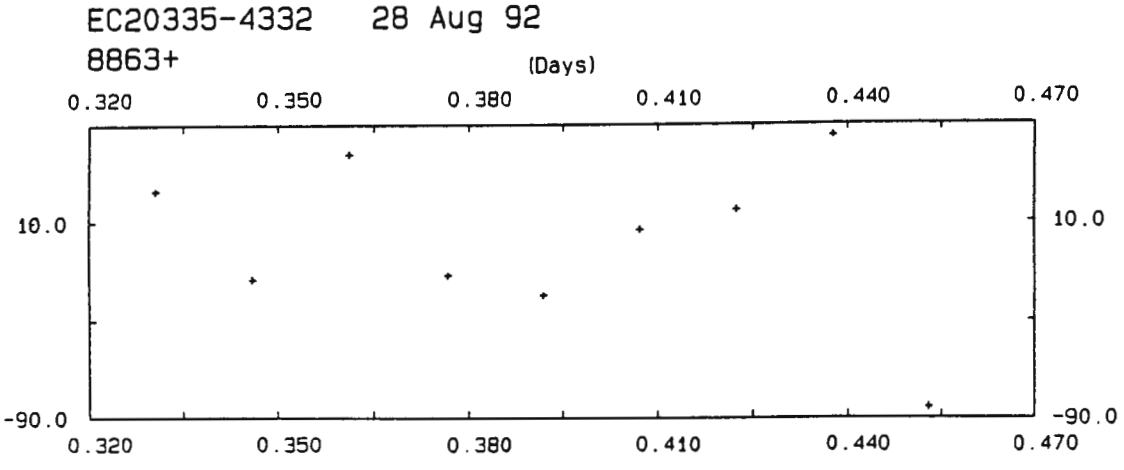

Figure 9. Radial velocities of EC20335-4332.

in the flickering and are of different character to the QPO seen in outbursting dwarf novae.

We will demonstrate that: (1) on a long time scale EC05287-5857 behaves like a VY Scl star; (2) on a time scale of tens of minutes (in the high state), the light variations of EC05287-5857 exhibit brightness oscillations which have coherence lasting for a few cycles.

§9.1 Introduction

EC05287-5857 was selected to be a candidate blue object from a UB plate pair taken on 1987 August 30. This object was spectroscopically identified as a CV on 1987 December 21. The first spectrum (1987 December 21) was obtained at 14th mag and is shown in Figure 1. Strong Balmer lines are present in emission and resolved up to H10. HeI λ4471Å is weakly present as well as HeII λ4686Å. In addition to these, CaII λ3934Å, HeI λ4026Å, λ4713Å, and λ5016Å are barely visible.

§9.2 Long-Term Light Variations

Intensive follow-up work was started in late 1991. The photometric data, obtained from visual inspection, photoelectric photometry, and spectroscopy during 1991-1994 are collected in Table I and plotted in Figure 2. Figure 2 shows that the object was not seen brighter than B~16.5 until 1992 November. Since that time, it has been seen only in the bright state for more than a year. This photometric characteristic resembles that of the VY Scl stars. However, it is also not dissimilar to the behaviour of the Z Cam stars, a category of dwarf novae showing standstills in brightness within 2 mag of the outburst maximum and lasting for tens of days to years. Therefore, the classification is not determinable from the long-term light curve alone. The detailed classification and the photometric and spectroscopic characteristics will be discussed in the following sections.

Table I. Brightness Variations during 1991-1993

UT Date	HJD	B	Measuring Method
91 Dec 4	8594.518	>16.7	visual check
91 Dec 6	8596.548	>16.7	visual check
91 Dec 31	8622.456	>16.7	visual check
92 Feb 4	8657.316	>17.	visual check
92 Aug 31	8865.647	>17.	visual check
92 Nov 23	8949.58103	14.3	spectroscopic flux
92 Dec 22	8979.33920	14.3	HSP
92 Dec 23	8980.35806	14.3	HSP
92 Dec 25	8982.41134	14.2	HSP
92 Dec 26	8983.30098	14.3	HSP
92 Dec 27	8984.36734	14.4	HSP
93 Jan 20	9008.30262	14.4	HSP
93 Jan 21	9009.31128	14.5	HSP
93 Jan 22	9010.29947	14.4	HSP
93 Feb 16	9035.31243	14.3	HSP
93 Feb 17	9036.30408	14.56	UBV photometry
93 Feb 18	9037.28173	14.4	HSP
93 Feb 22	9041.28387	14.3	HSP
93 Feb 25	9044.2725	14.67	UBV photometry
93 Mar 18	9065.28742	15.2:	spectroscopic flux
93 Mar 19	9066.27473	14.9:	spectroscopic flux
93 Aug 12	9211.6441	14.79	UBV photometry
93 Aug 23	9222.6358	14.51	UBV photometry
93 Aug 24	9223.6286	14.58	UBV photometry
93 Sep 15	9245.6306	14.43	UBV photometry
93 Sep 17	9247.6247	14.56	UBV photometry
93 Sep 18	9248.5252	14.46	UBV photometry
93 Sep 19	9249.51255	14.8	HSP
93 Nov 15	9307.4702	13.97	UBV photometry
93 Nov 16	9308.44909	14.2	HSP
93 Nov 17	9309.37871	13.9	HSP
93 Nov 18	9310.35997	13.9	HSP
93 Nov 19	9311.37050	13.8	HSP
93 Nov 21	9313.36703	14.0	HSP
94 Jan 15	9368.3755	14.34	UBV photometry

Table II. UBV Measurements

UT Date	HJD	V	B-V	U-B
93 Feb 17	9036.3041	14.58	-0.015	-0.877
93 Feb 25	9044.2725	14.61	0.067	-0.803
93 Aug 12	9211.6441	14.72	0.071	-0.861
93 Aug 23	9222.6358	14.54	0.031	-0.858
93 Aug 24	9223.6286	14.59	0.012	-0.833
93 Sep 15	9245.6306	14.45	-0.017	-0.830
93 Sep 17	9247.6247	14.56	0.042	-0.682
93 Sep 18	9248.5252	14.49	-0.029	-0.949
93 Nov 15	9307.4702	13.98	-0.004	-0.880
94 Jan 15	9368.3755	14.35	-0.005	-0.847

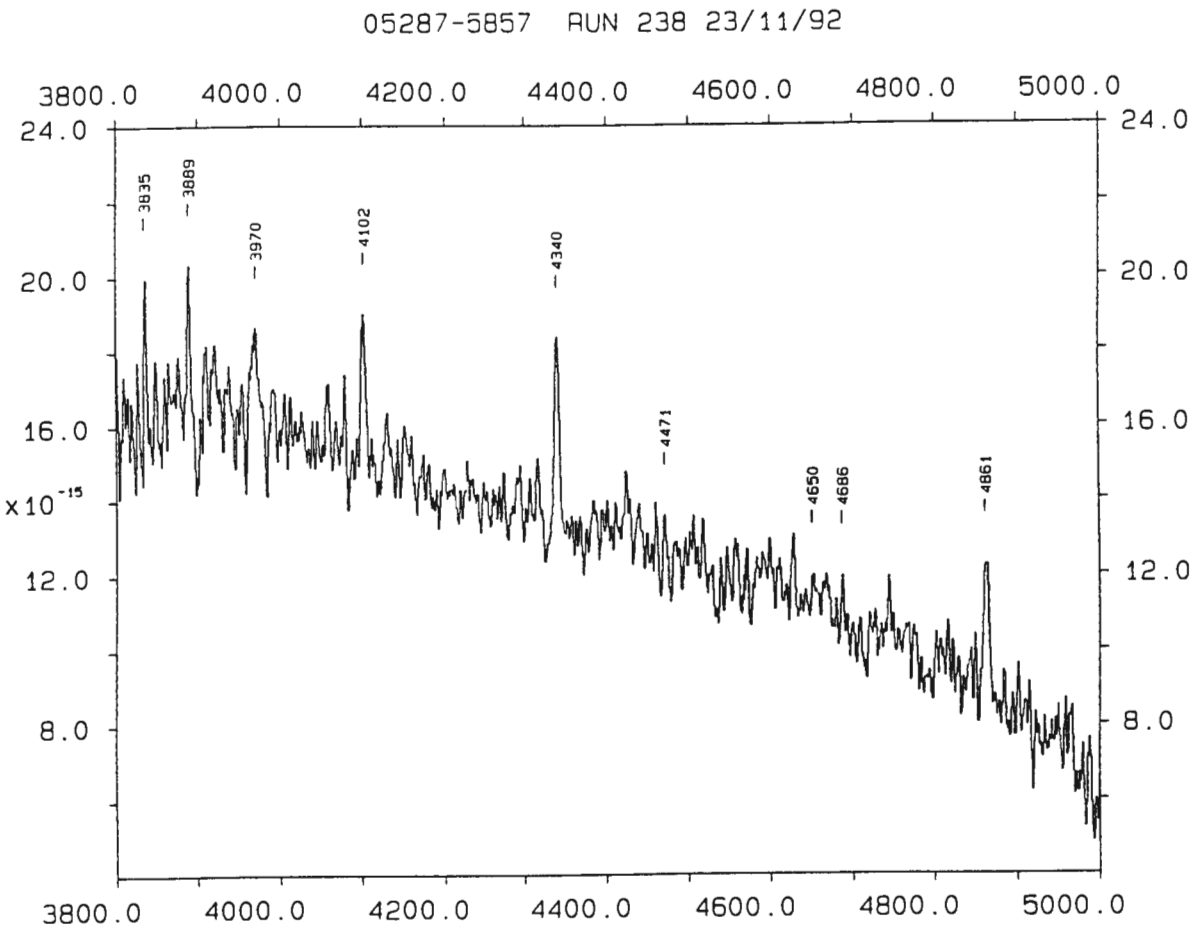

Figure 3. Spectrum obtained on 1992 November 23.

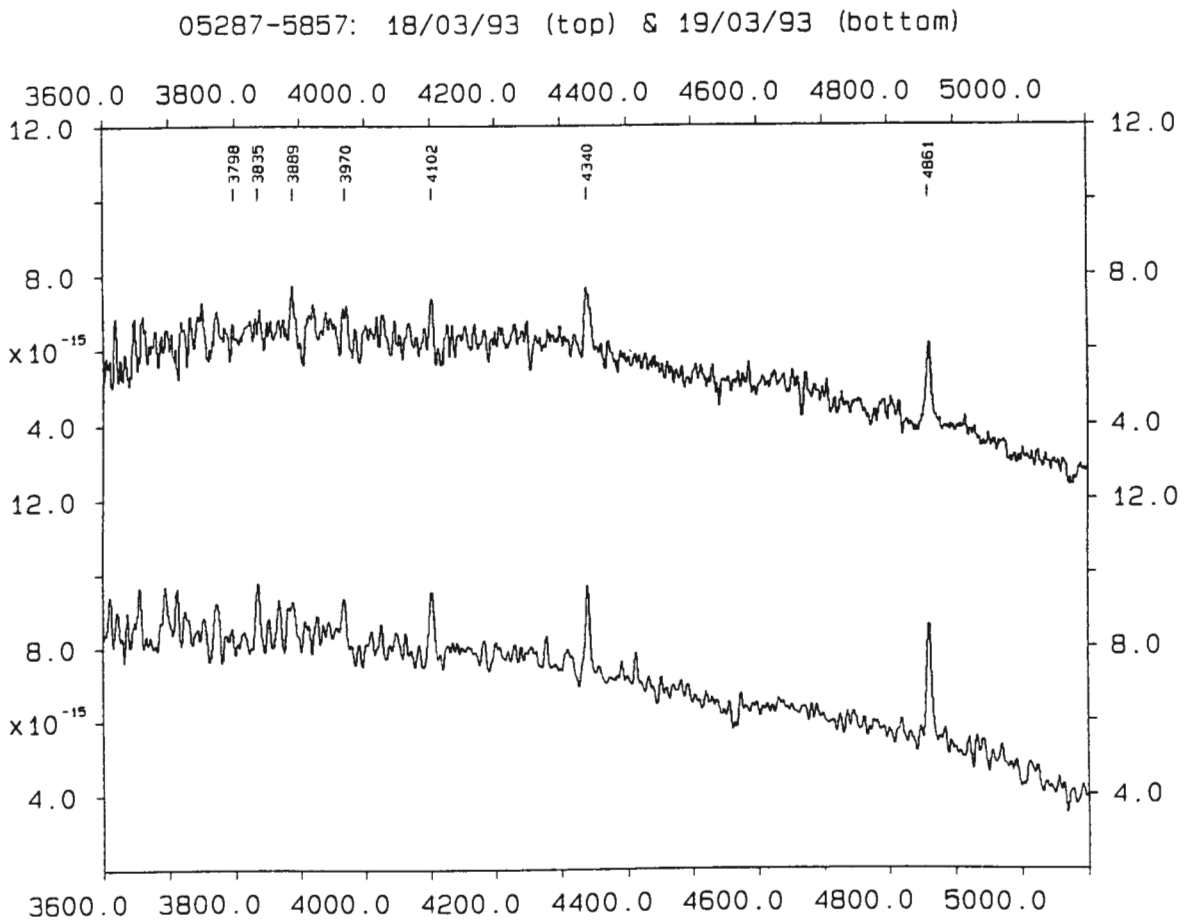

Figure 4. Spectra of 1993 March 18 (top) and 1993 March 19 (bottom).

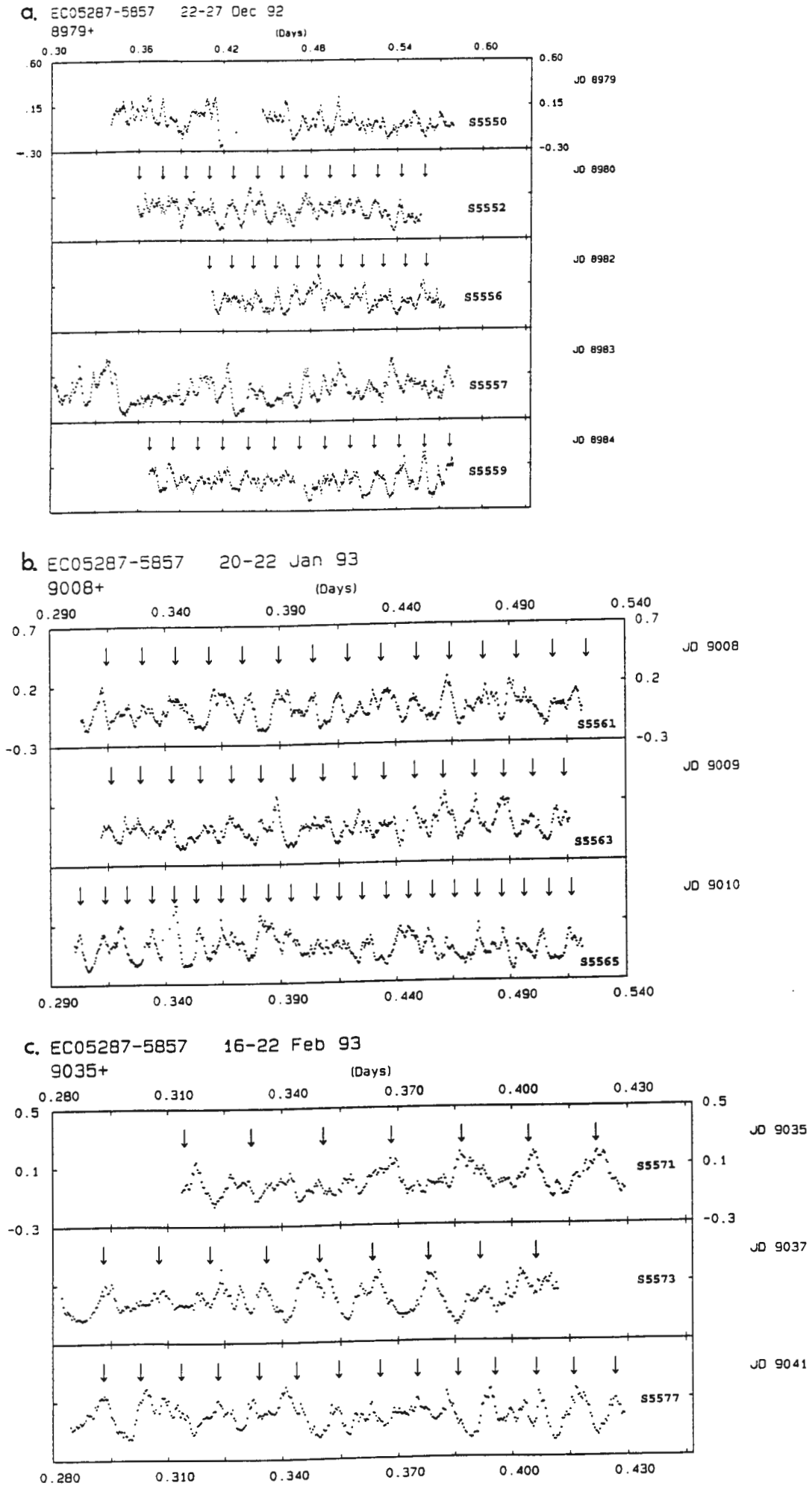

Figure 5. Light variations of (a) 1992 Dec 22-27, (b) 1993 Jan 20-22, (c) 1993 Jan 20-22, (d) 1993 Feb 16-22, (d) 1993 Sep 19, and (e) 1993 November 16-21. The arrows indicate the calculated times of maximum light.

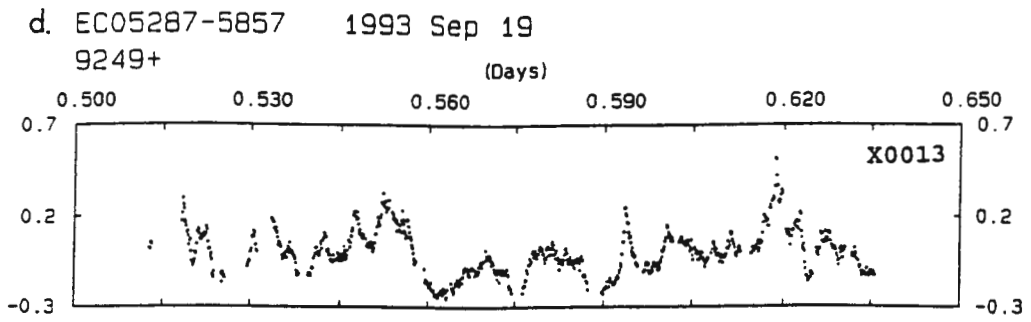

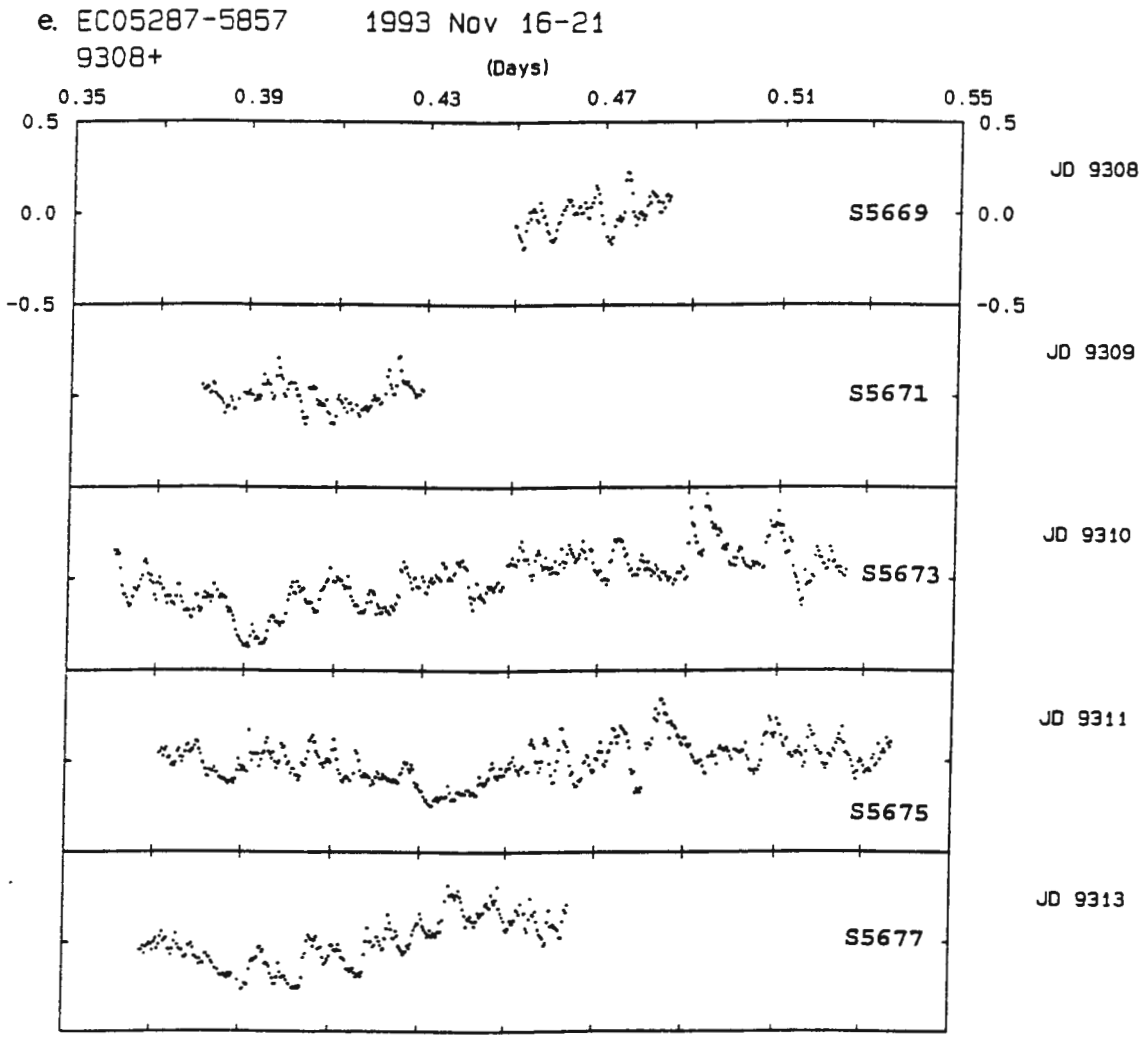

Figure 5. -continued.

§9.3 Spectroscopic Characteristics

As mentioned above, EC05287-5857 was fainter than 17th Bmag between late 1991 and 1992 November. The records in Table I shows that the object became bright some time in the interval 1992 September 1 - November 22 (JD8866-JD8948). On the night of 1992 November 23 (JD8949), the object was detected at 14th Bmag (derived from the spectroscopic flux) and a 3Å resolution spectrum was obtained. The spectrum is shown in Figure 3 and reveals Balmer lines in emission. Comparing the spectrum with that in Figure 1, the widths of the Balmer lines are narrower in Figure 3. No HeI, HeII, and other features are visible in the spectrum.

Two spectra with 4Å resolution were obtained at brightness ≤ 15th Bmag in 1993 March and are shown in the top (March 18) and the bottom (March 19) of Figure 4. The top spectrum in Figure 4 shows weak Balmer emission lines: Hβ and Hγ are clearly present; the rest are barely visible up to H9. On the following night, the Balmer emission lines are stronger and decrease up the series. No other features are visible in the spectrum.

§9.4 Photometric Characteristics

§9.4.1 UBV and High Speed Photometry

UBV measurements were obtained and are listed in Table II. The object has B-V and U-B colours very close to the blackbody line in the UBV two-colour diagram. HSP was obtained during 1992 Dec - 1993 Nov. These data are listed in Table III and plotted in Figure 5. The light curves show rapid flickering variations with a large peak-to-peak amplitude of ~40-60% on a time scale of about 15-26 minutes. The mean brightness of each run varies little about 14.3 Bmag except for the runs of 1993 November which show that the object was at ~13.9 mag, brighter than at any other time (see Figure 2). From the above flickering activity and the spectral features shown in §9.3, the characteristics of EC05287-5857 in the bright state do not resemble those of outbursting dwarf novae; instead, EC05287-5857 is more like a VY Scl star.

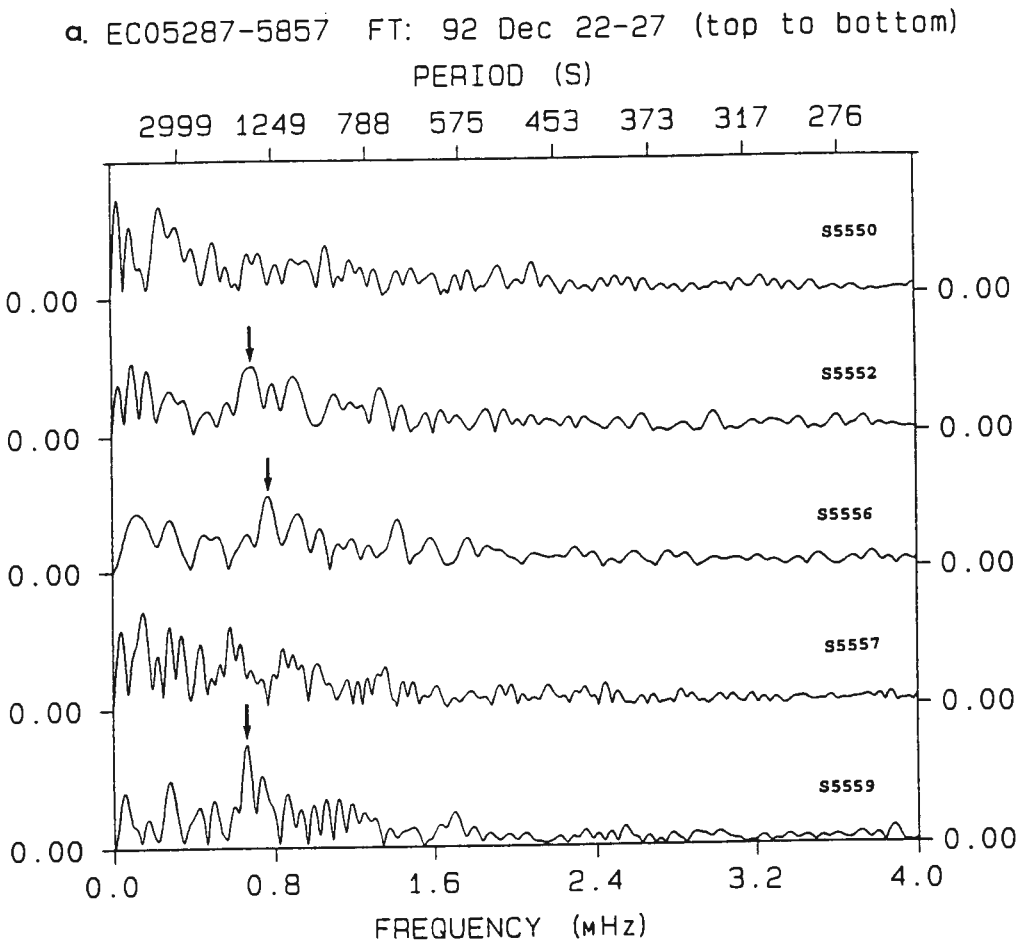

Figure 6. Fourier amplitude spectrum of (a) 1992 Dec 22-27, (b) 1993 Jan 20-22, (c) 1993 Jan 20-22. The arrows mark the period of the QPO.

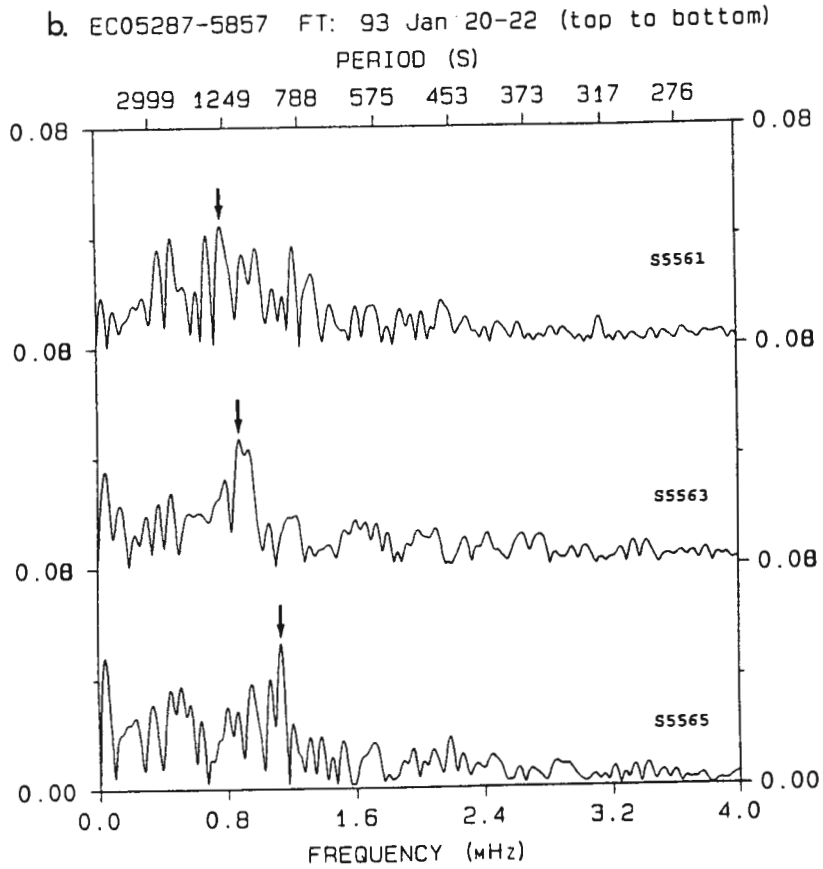

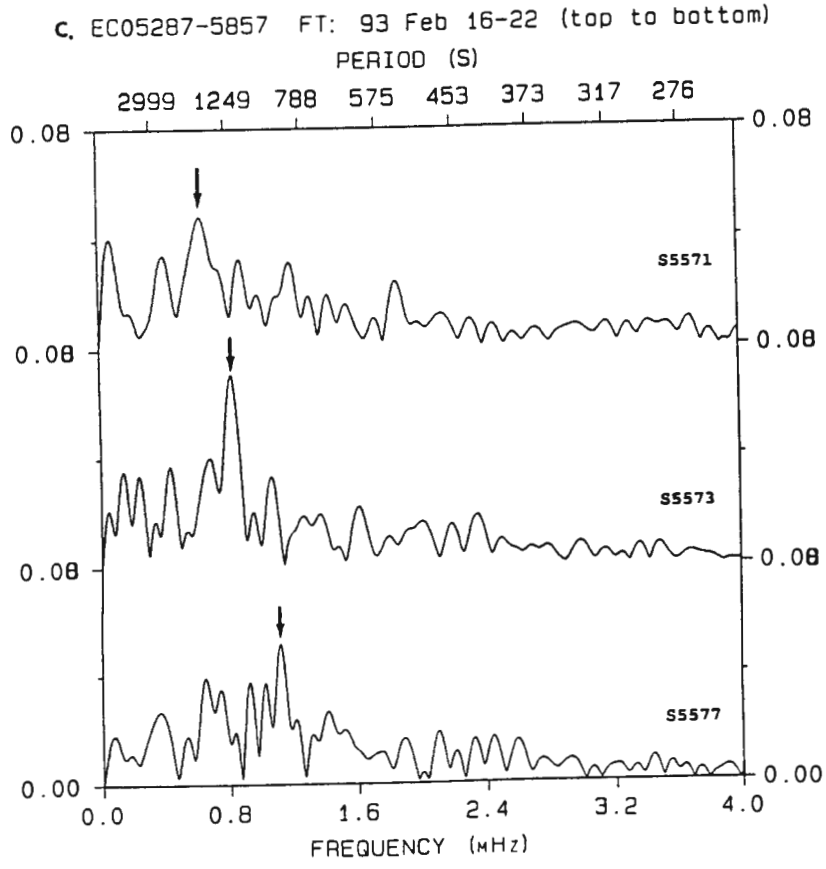

Figure 6. -continued.

Table III. Observing Log of High Speed Photometry

Run	UT Date	Start HJD 2440000.+	Duration hrs	B_w	ΔB
S5550	221292	8979.33920	5.7	14.3	0.6
S5552	231292	8980.35806	4.7	14.3	0.5
S5556	251292	8982.41134	3.8	14.2	0.5
S5557	261292	8983.30098	6.6	14.3	0.6
S5559	271292	8984.36734	5.1	14.4	0.6
S5561	200193	9008.30262	5.2	14.4	0.5
S5563	210193	9009.31128	4.9	14.5	0.5
S5565	220193	9010.29947	5.3	14.4	0.7
S5571	160293	9035.31243	2.8	14.3	0.4
S5573	180293	9037.28173	3.1	14.4	0.4
S5577	220293	9041.28387	3.5	14.3	0.4
X0013	190993	9249.51255	2.9	14.8	0.8
S5669	161193	9308.44909	0.8	14.2	-
S5671	171193	9309.37871	1.2	13.9	-
S5673	181193	9310.35997	4.0	13.9	-
S5675	191193	9311.37050	4.0	13.8	-
S5677	211193	9313.36703	2.3	14.0	-

*Runs S5669-S5677 were taken under poor condition, thus ΔB are not given.

§9.4.2 Quasi-Periodic Oscillations

The light variations of 1992 December - 1993 February seem to have coherent periods. In order to investigate this possibility, Fourier amplitude spectra were calculated for individual runs and are shown in Figure 6. Figure 6 reveals no evidence for any periodic behaviour with amplitudes greater than 1.5% at frequencies ≥ 4 mHz. The top and fourth amplitude spectra (S5550 and S5557) of Figure 6a do not exhibit any coherent periods as can be verified from inspection of the flickering activity in Figure 5a. The other amplitude spectra in Figure 6 show amplitudes of ≥ 2% spreading over the frequency range 0.6-1.2 mHz. The highest peaks (arrowed in Figure 6) in the above frequency range are representative of the QPO time scale for the corresponding runs. A sinusoid of the frequency of these highest peaks in Figure 6 was fitted to the corresponding data of Table II by least squares. The resulting ephemerides are tabulated below:

Run	Frequency mHz	Period (days)	Time of Maximum 2440000.+
S5552	0.696 ± 0.015	0.01662 ± 0.00036	8980.36044 ± 0.00019
S5556	0.772 ± 0.018	0.01499 ± 0.00034	8982.41008 ± 0.00015
S5559	0.662 ± 0.013	0.01746 ± 0.00034	8984.36842 ± 0.00012
S5561	0.777 ± 0.013	0.01488 ± 0.00025	9008.30025 ± 0.00015

S5563	0.880 ± 0.014	0.01315 ± 0.00021	9009.31641 ± 0.00012
S5565	1.138 ± 0.013	0.01017 ± 0.00012	9010.30247 ± 0.00009
S5571	0.643 ± 0.025	0.01799 ± 0.00069	9035.31445 ± 0.00017
S5573	0.823 ± 0.022	0.01405 ± 0.00037	9037.27937 ± 0.00009
S5577	1.122 ± 0.020	0.01032 ± 0.00018	9041.28174 ± 0.00009

The arrows in Figure 5 indicate the times of maximum light corresponding to the above ephemeris of each run. The calculated times of maximum light seem to match the observed times quite well in run S5552. In the runs S5556 and S5559 the oscillations are most coherent in the middle and towards the end of the runs respectively. In Figure 5b, the calculated times of maximum light match only a few peaks in run S5561 and near the end of run S5663. There is poor coherence at the end of run S5565 (the bottom panel of Figure 5b). Figure 5c shows that the coherence in runs S5571 and S5573 is strong but is weak in S5577.

Note that the periods of the QPO vary from run to run in the range 15-26 minutes but also show some repeatability: the QPO frequency (0.77 mHz) in S5561 recurred in S5556. The QPO frequencies 0.66 mHz in S5559 and 1.138 mHz in S5565 are consistent with those in S5571 and S5577 respectively.

Fourier amplitude spectra (not shown here) were calculated for the runs X0013 and S5669-S5677 and show no evidence for rapid, quasi-periodic behaviour of the kind seen in 1992 December - 1993 February. From the above, it is interesting that runs S5550-S5577 which show QPO were obtained at a mean brightness B_w~14.3. Run X0013 was observed at B_w=14.8, about 0.5 mag fainter than in runs S5550-S5577. In contrast to this, runs S5671-S5677 were obtained when the object was about 0.5 mag brighter than during runs S5550-S5577. This suggests that the QPO may occur at a certain brightness and mass transfer rate in this system.

Okuda et al. (1992) presented a radial oscillation model of an accretion disk for QPO. Their results show that longer periods of QPO, 400-740s, will originate from the annuli near the outer edge of the disk, at 50-80% of disk radius. The calculated oscillation-amplitude is less than about 1 percent. Carroll et al. (1985) calculated models of p-modes and g-modes to explain accretion disk oscillations and concluded that all oscillations with period greater than 480s are caused by retrograde waves, which travel in a direction

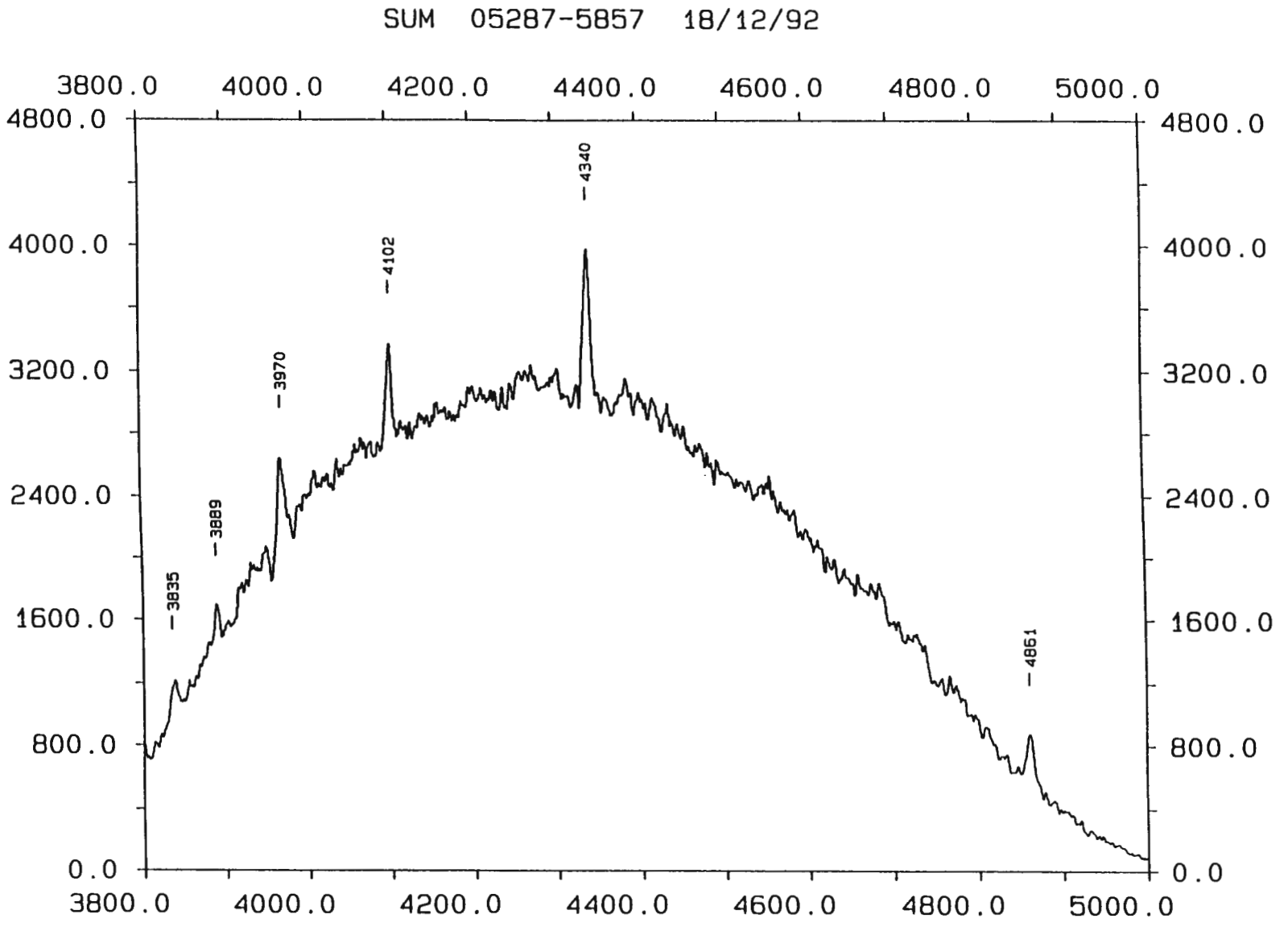

Figure 7. The grand sum spectrum (template) of 1992 December 18.

opposite to disk rotation. The above models are able to explain the periods of QPO of EC05287-5857 but are not able to predict an amplitude as large as the object showed, ~30%. Thus, the occurrence of QPO in the present case may not arise from the mechanism in the models mentioned above. Warner (1994) suggested that "if the QPOs are the result of superposition of many oscillations of disk annuli then the peak power should move to shorter periods at shorter optical wavelengths", because the temperature decreases outwards in the disk. Since the amplitudes of the QPO of EC05287-5857 are quite large, simultaneously UBVRI HSP would be useful to investigate this possibility.

§9.5 Search for Radial Velocity Variations and An Estimate of the Distance

The orbital period of the system has yet to be determined, because there is no orbital modulation in the photometry. In order to search for radial velocity variations, time-resolved spectroscopy (Table IV) with wavelength resolution of 3Å and time resolution of 900 seconds was obtained on 1992 December 18. The sequence of spectra was summed to construct the template which is shown in Figure 7. Table V gives the FWHM and FWZI which were obtained from measuring the Balmer lines in the grand sum spectrum (Figure 7). The Balmer lines are very narrow and the wings extend ~650 km/s from the line centre. This suggests that the object is a low inclination system.

Table IV. Observing Log of Time Resolved Spectroscopy

UT Date	Start UT Time h m	Duration hrs	Resolution (FWHM Å)	Coverage Å
92 Dec 18	21 45	4.08	3	3800-5000

Table V. Line Widths of Balmer Series

Lines	Hβ	Hγ	Hδ	Hε	H8
FWHM (±1Å)	10	9	7	7	6
FWZI (±2Å)	25	17	15	17	10

Radial velocities were measured for individual spectra using the cross-correlation technique. The results are listed in Table VI and plotted in

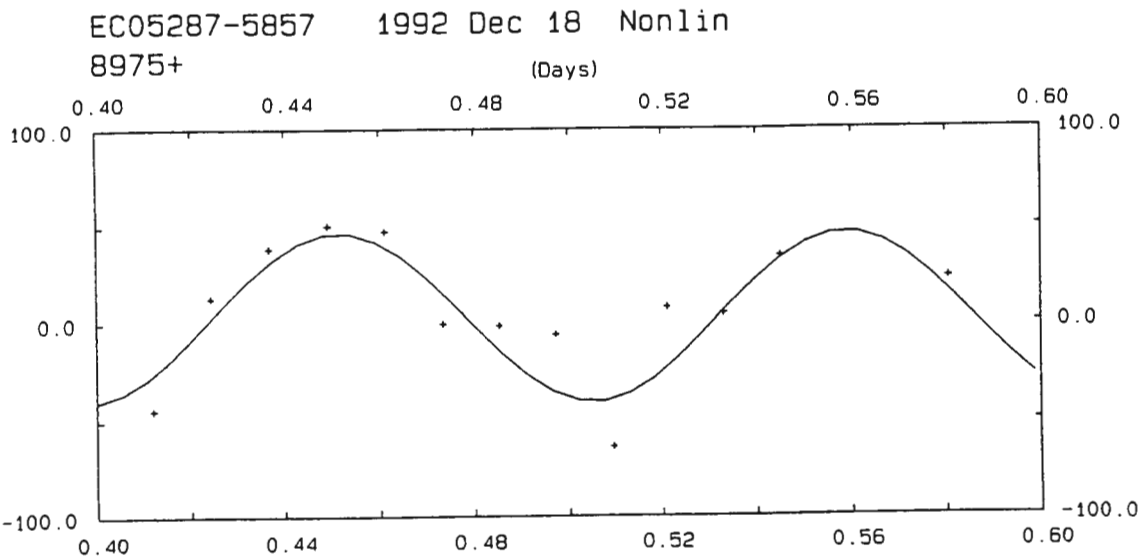

Figure 8. Radial velocity curve. The solid line is a sinusoid of period of 2.57-hr fitted by non-linear, least squares.

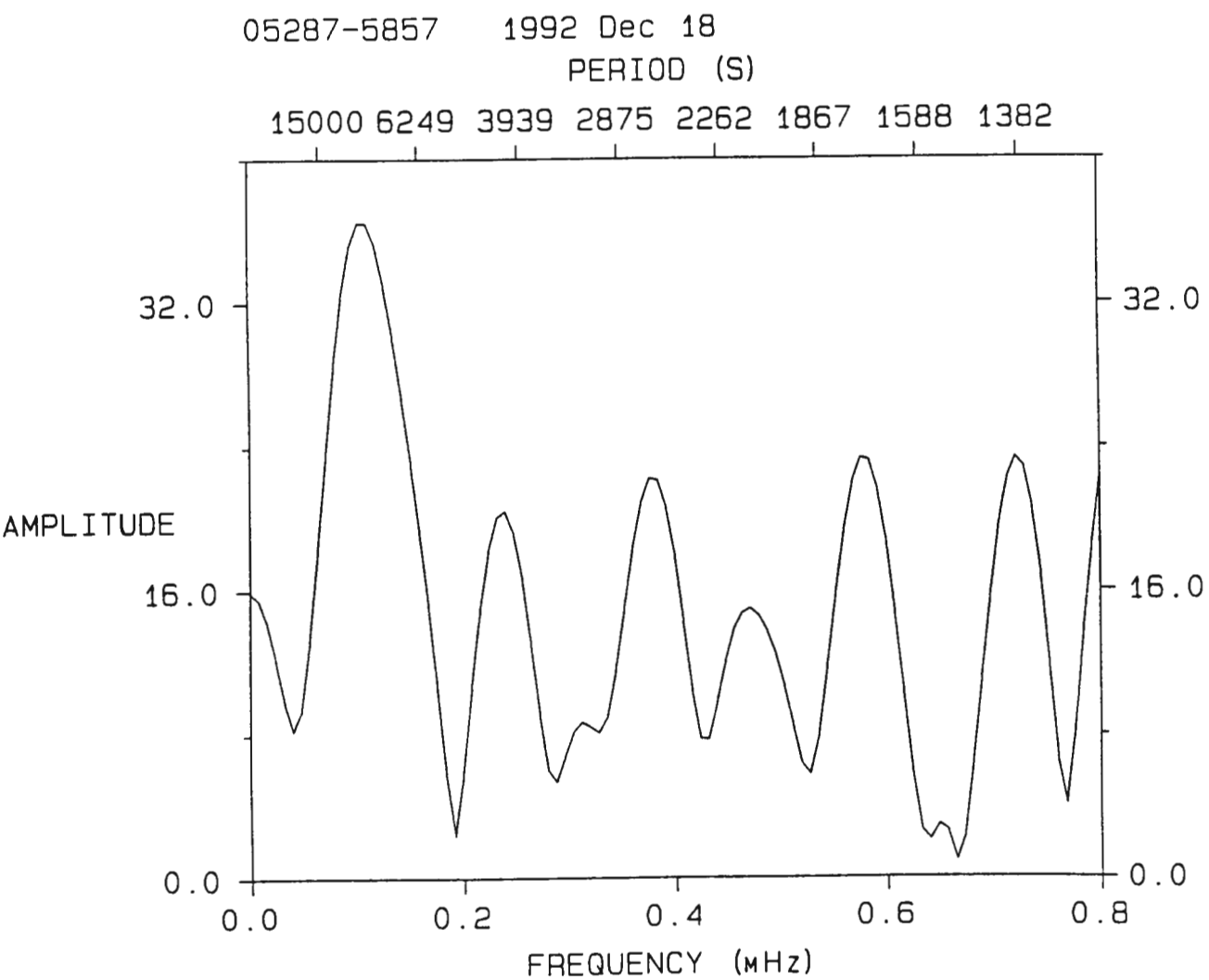

Figure 9. Amplitude spectrum calculated from the radial velocities.

Table VI. Relative Radial Velocity

HJD 2440000.+	RV km/s	HJD	RV
8975.41202	-44	8975.50936	-64
8975.42431	13	8975.52119	8
8975.43669	38	8975.53320	5
8975.44925	50	8975.54504	34
8975.46129	47	8975.55687	-11*
8975.47345	-0	8975.56871	-34*
8975.48526	-1	8975.58058	23
8975.49716	-6		

*deleted from the radial velocity curve.

Figure 8. An amplitude spectrum was calculated for the data in Table V and is shown in Figure 9 in which the highest peak has a frequency of 0.1189 mHz. In order to obtain the best estimate of orbital period, a sinusoid of initial frequency 0.1189 mHz was fitted by non-linear least squares and gave a semi-amplitude of the radial velocity curve of 43±9 km/s, a time of maximum red shift of 2448975.4514±0.0006, and an orbital period $0^d.107\pm0.007$. The solid line in Figure 8 is the non-linear, least squares fit of this period (2.57-hr). This estimate for the orbital period is extremely uncertain: the peak in Figure 9 is not very significant, there are few points in Figure 8 and the fit has large scatter. However, if correct, this would place EC05287-5857 in the period gap of CVs. Thus it is extremely urgent to get more spectroscopy to verify this result. All other VY Scl stars have $3 \leq P_{orb} \leq 4$ hours.

Assuming that the above estimate of the orbital period is correct, with a K-band magnitude of 14.3, a lower limit to the distance of the system can be derived using Bailey's method (Bailey 1981; Warner 1987); the result is 230 pc.

§ References:

Bailey, J. (1981). *Mon. Not. R. astr. Soc.*, **197**, 31.

Bath, G.T. (1973). *Nature Phys. Sci.*, **246**, 84.

Borisov, G.V. (1992). *Astron. Astrophys.*, **261**, 154.

Carroll, B.W., Cabot, W., McDermott, P.N. Savedoff, M.P., and Van Horn, H.M. (1985). *Astrophys. J.*, **296**, 529.

Hollander, A., and Van Paradijs, J. (1992). *Astron. Astrophys.*, **265**, 77.

Lamb, F.K., Pines, D., and Shaham, J. (1978). *Astrophys. J.*, **225**, 582.

Okuda, T., Ono, K., Tabata, M., and Mineshige, S. (1992). *Mon. Not. R. astr. Soc.*, **254**, 427.

Papaloizou, J., and Pringle, J.E. (1978). *Mon. Not. R. astr. Soc.*, **182**, 423.

Patterson, J. (1981). *Astrophys. J. Suppl.*, **45**, 517.

Van Horn, H.M., Wesemael, F., and Winget, D.E. (1980). *Astrophys. J.*, **235**, L143.

Warner, B., and Brickhill, A.J. (1978). *Mon. Not. R. astr. Soc.*, **182**, 777.

Warner, B. (1983). *Int. Astr. Union Colloq.*, **No. 72**, 155.

Warner, B. (1987). *Mon. Not. R. astr. Soc.*, **227**, 23.

Warner, B. (1988). *High Speed Astronomical Photometry*, Cambridge University Press.

Warner, B. (1994). *Cataclysmic Variable Stars*, Cambridge University Press, in press.

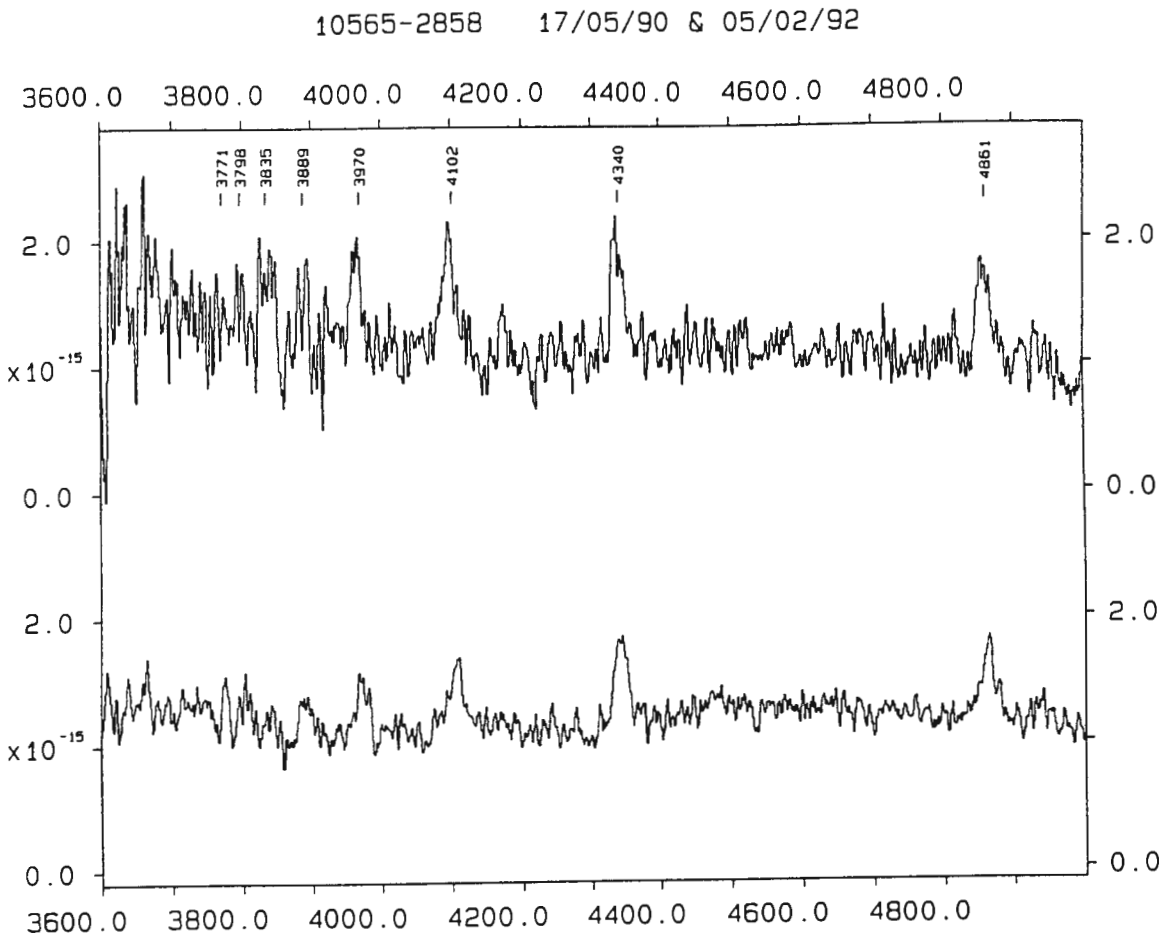

Figure 1. Spectra of EC10565-2858: The bottom panel is the first spectrum obtained on 1990 May 17 and the top spectrum was obtained on 1992 February 5.

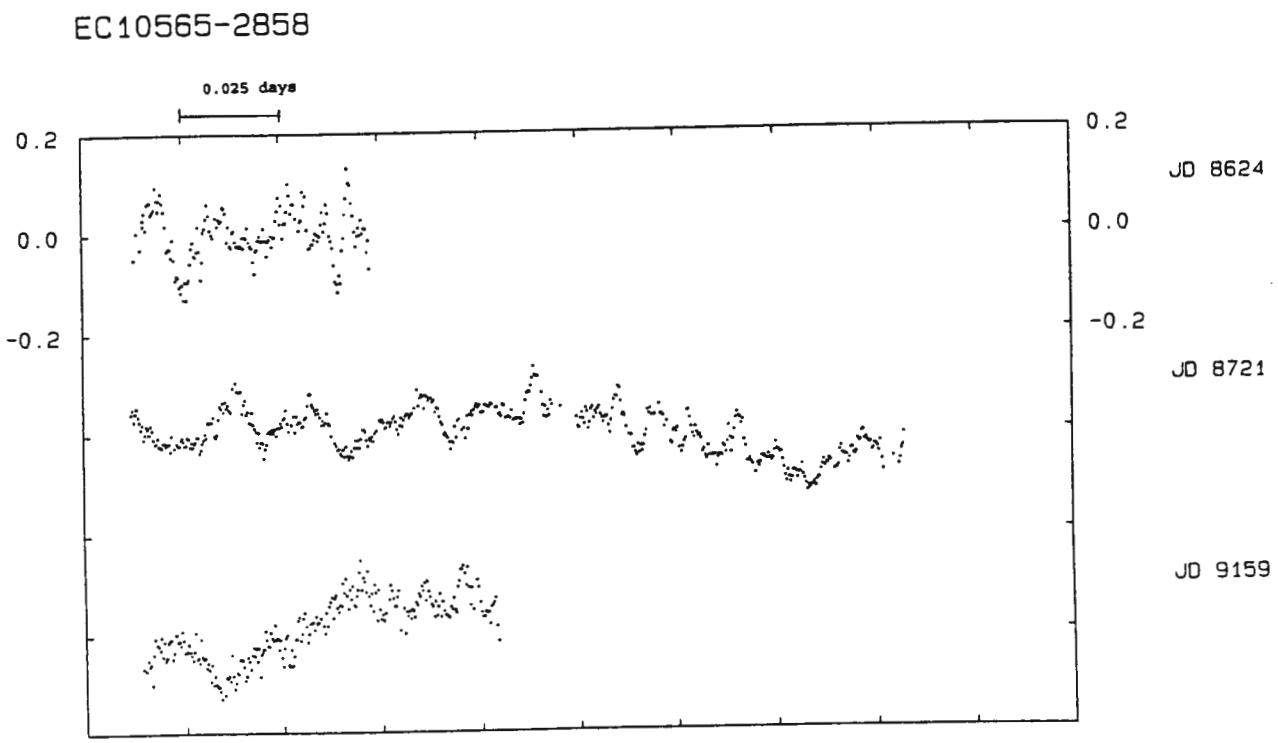

Figure 2. Light curves of EC10565-2858.

Chapter 10: *EC10565-2858 and EC10578-2935*

Two CVs, EC10565-2858 and EC10578-2935, are presented in this chapter. There was not enough information to determine their classification. EC10565-2858 is possibly a dwarf nova and is discussed in section 10.1. EC10578-2935 is possibly a nova-like variable and is discussed in section 10.2.

§10.1 EC10565-2858

The first spectrum with 4Å resolution was obtained on 1990 May 17 and is shown at the bottom in Figure 1. The spectrum shown at the top of Figure 1 was secured with the same resolution on 1992 February 5. Broad Balmer emission lines are present in both of these spectra and resolved up to H9 (Figure 1). No other features are visible.

Due to limitations of telescope time and weather, the HSP observations (Table I) are sparse. Only three light curves (Figure 2) were obtained, all at different brightnesses: the top at B_w~15.79, the middle at B_w~14.97, and the bottom at B_w~16.26. The light curves in Figure 2 all show flickering variations with peak-to-peak amplitudes of ~20% on a time scale of a few minutes.

Table I. Observing Log of HSP for EC10565-2858

Run	UT Date	Start HJD 2440000.+	Duration (hrs)	B_w	ΔB
S5425	030192	8624.52284	1.4	15.79	0.37
S5476	080492	8721.25116	4.7	14.97	0.30
S5616	200693	9159.21396	2.2	16.26	0.34

The photometric and spectral characteristics demonstrate that this object is a CV. It may possibly be classified as a dwarf nova due to the absence of HeII λ4686Å and CIII/NIII λ4650Å.

Since there are large time gaps between these three HSP-runs, a calculation of a Fourier transform was not attempted. Instead, time-resolved spectroscopy (Table II) was obtained on the nights of 1993 March 18-19 in order to search

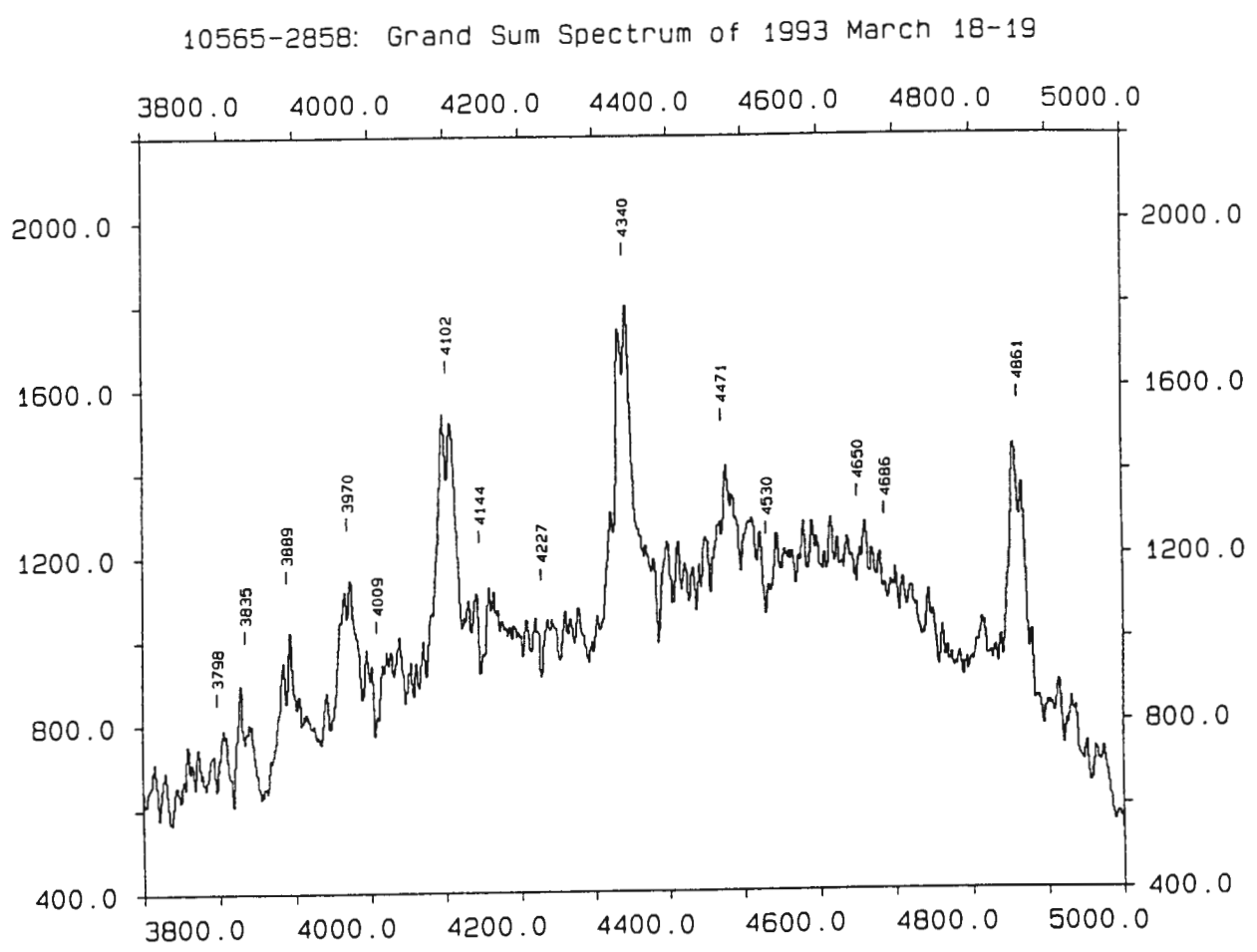

Figure 3. Grand sum spectrum (template) of EC10565-2858 on 1993 March 18-19.

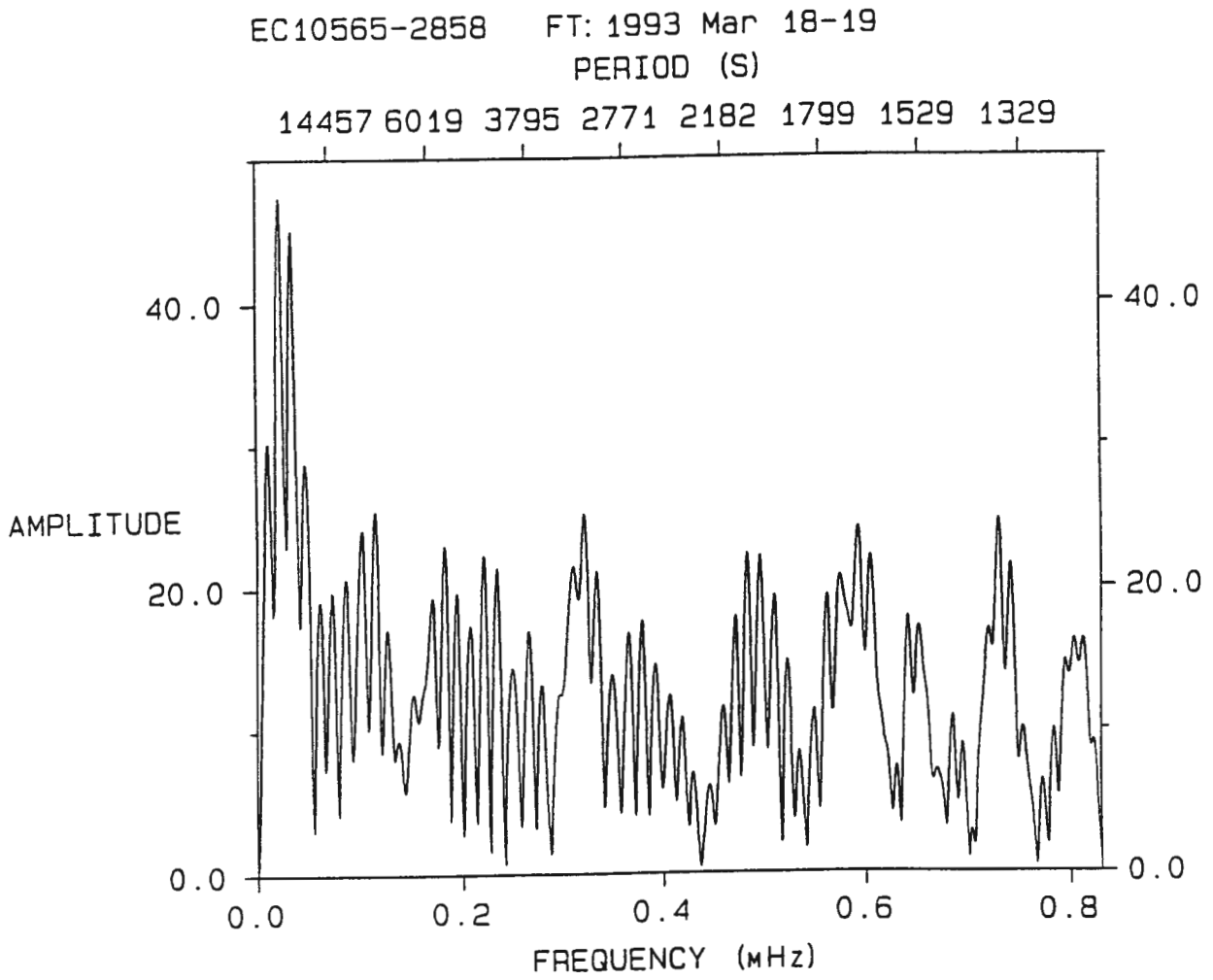

Figure 4. Amplitude spectrum of EC10565-2858 was calculated for the radial velocities which shows two highest peaks, 12.2-hr and 7.9-hr, with nearly

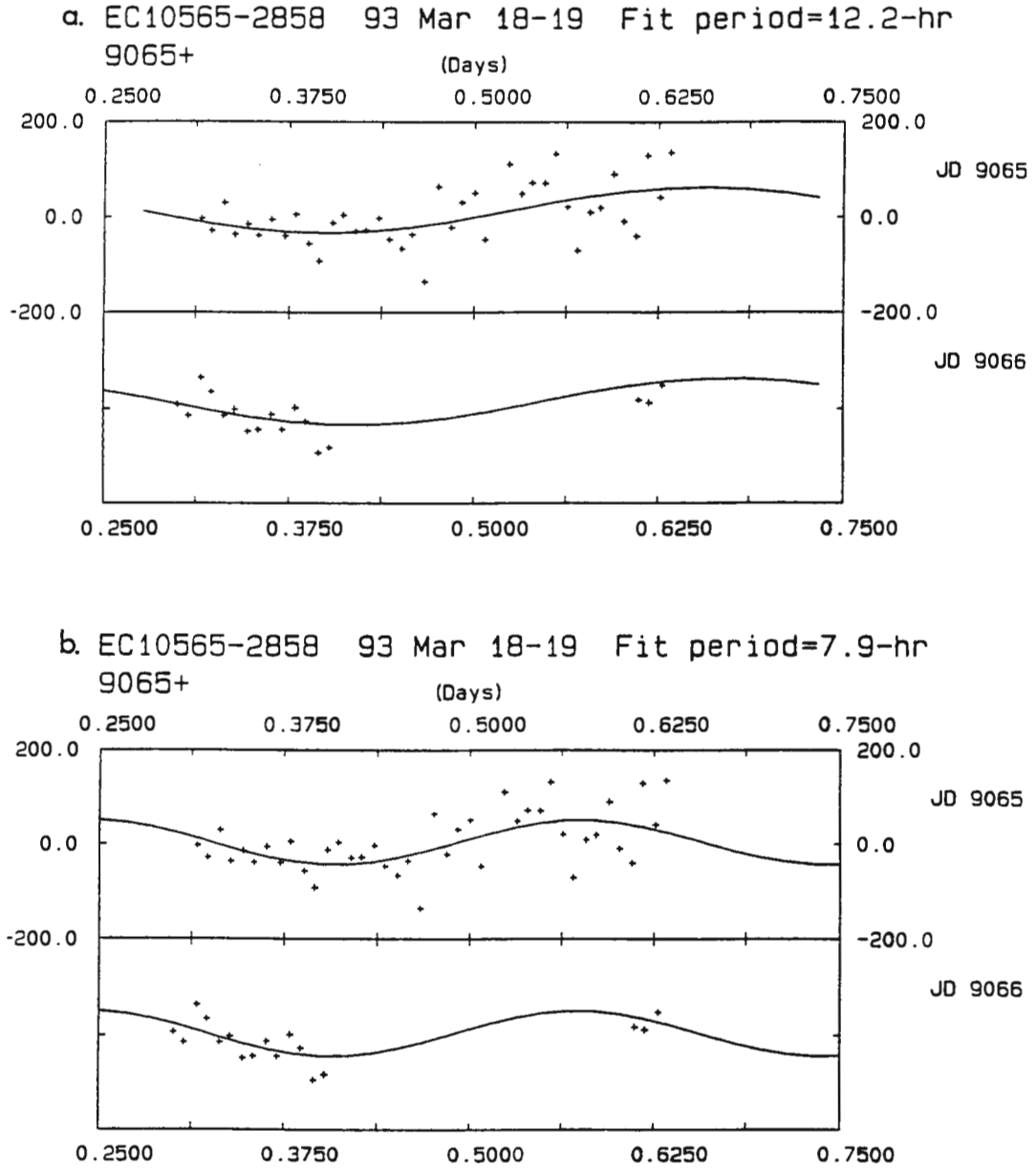

Figure 5. Radial velocity curves fitted by sinusoids of the periods of (a) 12.2-hr and (b) 7.9-hr for EC10565-2858.

Table II. Observing Log of Time-Resolved Spectroscopy for EC10565-2858

UT Date	Start UT Time h m	Duration hrs	Resolution (FWHM Å)	Coverage Å
93 Mar 18	21 33	7.50	4	3800-5000
93 Mar 19	21 00	2.50	4	3800-5000

for an orbital period. The sequence of spectra with 4Å resolution from the two nights' observations were summed to construct the template which is shown in Figure 3. The grand sum spectrum (template) shows clearer features than in Figure 1. The Balmer lines show double-peaked profiles with FWZI~45Å. HeI λ4471Å is visible in Figure 3. The relative radial velocities were determined using the cross-correlation technique and are tabulated in Table IIIa. A Fourier amplitude spectrum was calculated from the data in Table IIIa excluding the asterisked datum which was discarded due to their large deviation. The results are shown in Figure 4 and exhibit a highest peak of 0.0227 mHz (12.2±1.20 hrs) and a second highest peak of 0.0348 mHz (7.98±0.30 hrs), both with an error of 0.0022 mHz. These two peaks are of similar amplitude and are one cycle/day aliases of each other; it is not possible to choose between them. Sinusoids of the above periods, 12.2 and 7.98 hours, were fitted to the data in Table IIIa by least squares and are shown in Figure 5. The results show that the semi-amplitudes, K_1, of the radial velocity curves are about 50 km/s. This value is rather small for a system showing broad line widths ~45Å and double-peaked profiles.

A CV with an orbital period longer than 6-hr may contain a secondary of spectral type late K. Therefore the secondary may be detectable in the spectrum and may affect the determination of K_1 due to its apparent orbital motion in the opposite direction. To investigate this possibility, the grand sum spectrum (Figure 3) was re-examined to search for a K-type spectrum. Some weak absorption lines were identified: TiI λ4009Å/FeI λ4005Å blend, FeI λ4144Å, and CaI λ4227Å. The absorption at λ4530Å could not be identified. This certainly shows that the spectra are contaminated by the secondary and provides support for $P_{orb} > 6$ hrs. Therefore relative radial velocities were re-determined in the following way: the continuum outside the Balmer lines

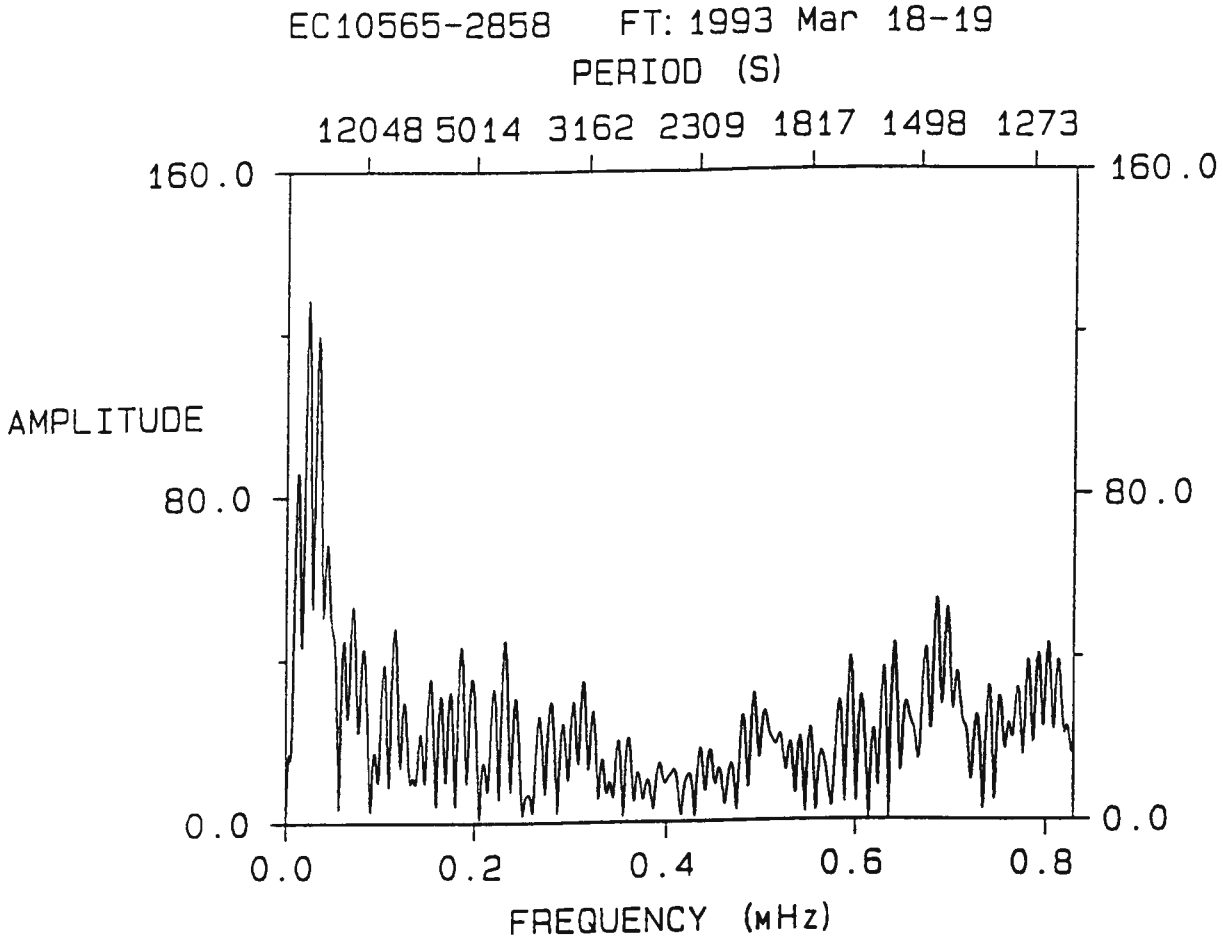

Figure 6. Amplitude spectrum of EC10565-2858 was calculated for the new radial velocities (see text) which shows two highest peaks, 12.09-hr and 8.18-hr.

Table III. Relative Radial Velocities of EC10565-2858

(a) first results

HJD 2440000.+	RV km/s	HJD	RV	HJD	RV
9065.31618	-3	9065.47585	64	9065.63313	135
9065.32322	-28	9065.48441	-21	9066.30023	7
9065.33203	29	9065.49157	31	9066.30728	-14
9065.33907	-36	9065.50013	51	9066.31616	64
9065.34764	-14	9065.50716	-47	9066.32321	34
9065.35469	-38	9065.51579	248	9066.33205	-14
9065.36349	-5	9065.52283	110	9066.33916	-1
9065.37228	-39	9065.53146	49	9066.34775	-47
9065.37940	5	9065.53850	72	9066.35479	-43
9065.38799	-56	9065.54744	71	9066.36356	-12
9065.39503	-92	9065.55449	132	9066.37059	-43
9065.40387	-12	9065.56312	21	9066.37924	1
9065.41101	3	9065.57019	-71	9066.38628	-26
9065.41971	-29	9065.57889	9	9066.39495	-93
9065.42676	-27	9065.58593	19	9066.40205	-81
9065.43535	-2	9065.59478	90	9066.61209	17
9065.44238	-46	9065.60183	-9	9066.61914	11
9065.45101	-66	9065.61039	-40	9066.62805	48
9065.45806	-36	9065.61742	130	9066.63517	460*
9065.46665	-136	9065.62608	42		

(b) final results

9065.31618	-24	9065.47585	87	9065.63313	197
9065.32322	13	9065.48441	-46	9066.30023	28
9065.33203	30	9065.49157	74	9066.30728	10
9065.33907	-55	9065.50013	113	9066.31616	104
9065.34764	-32	9065.50716	22	9066.32321	32
9065.35469	-89	9065.51579	227	9066.33205	55
9065.36349	-35	9065.52283	312	9066.33916	2
9065.37228	-95	9065.53146	98	9066.34775	-120
9065.37940	-32	9065.53850	30	9066.35479	-52
9065.38799	-121	9065.54744	155	9066.36356	-66
9065.39503	-123	9065.55449	325	9066.37059	-6
9065.40387	-28	9065.56312	210	9066.37924	-58
9065.41101	-107	9065.57019	-226	9066.38628	-73
9065.41971	-120	9065.57889	158	9066.39495	-305
9065.42676	-30	9065.58593	73	9066.40205	-167
9065.43535	-68	9065.59478	135	9066.61209	130
9065.44238	-77	9065.60183	5	9066.61914	183
9065.45101	-92	9065.61039	-216	9066.62805	260
9065.45806	-86	9065.61742	193	9066.63517	507
9065.46665	-69	9065.62608	152		

RV > 300 km/s or RV < -210 km/s were deleted from the RV curves.

was set to zero intensity in order to get rid of the contribution by the secondary. The Balmer lines (Hβ-H9) were used to determine the radial velocities by cross-correlation. The results are shown in Table IIIb. A Fourier amplitude spectrum was calculated again and is shown in Figure 6. Figure 6 shows a highest peak of 0.0229 mHz (12.09±0.51 hrs) and a second highest peak of 0.0339 mHz (8.18±0.40 hrs). These two peaks are consistent

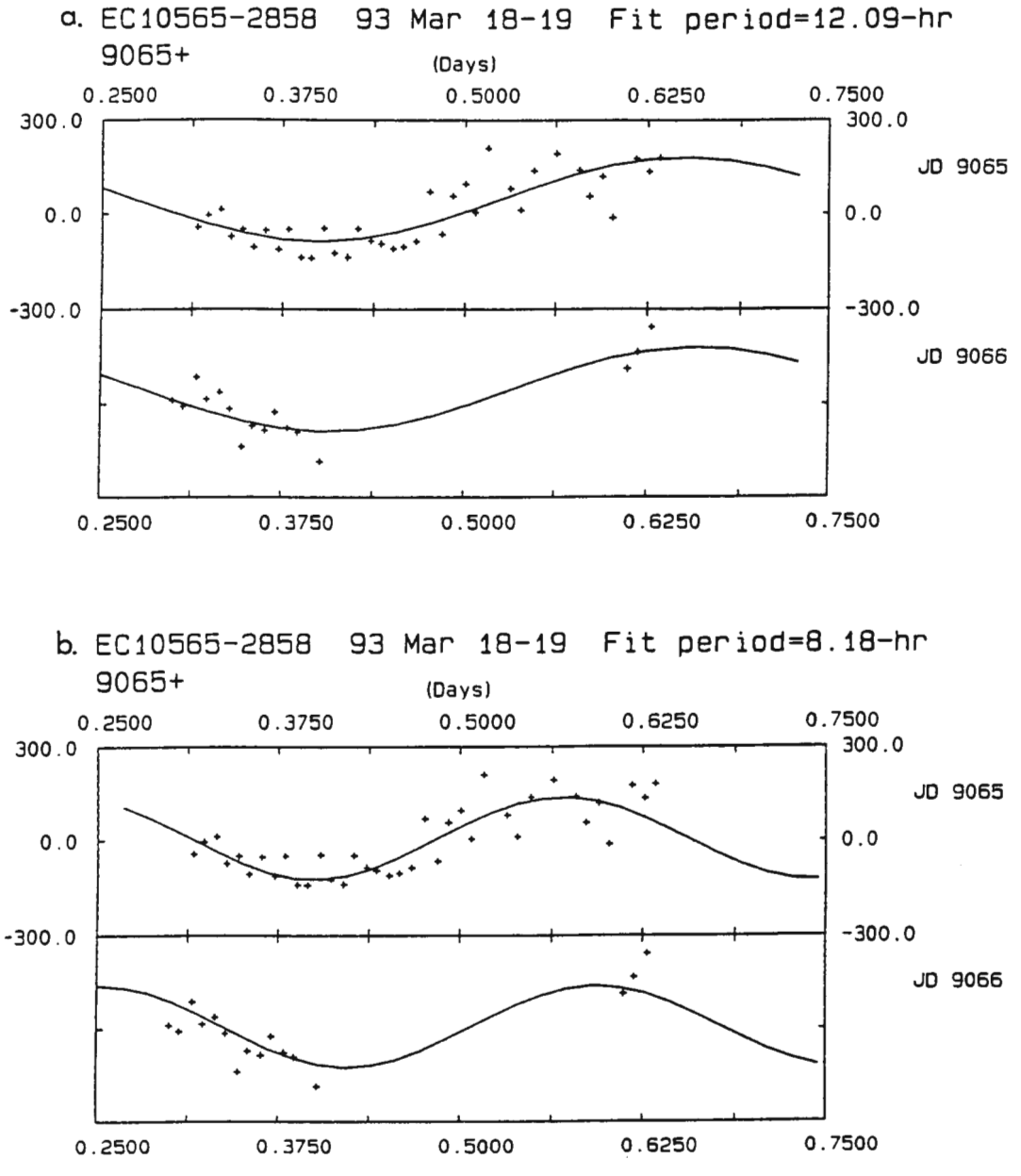

Figure 7. Radial velocity curves were fitted by sinusoids of the periods of (a) 12.09-hr and (b) 8.18-hr for EC10565-2858.

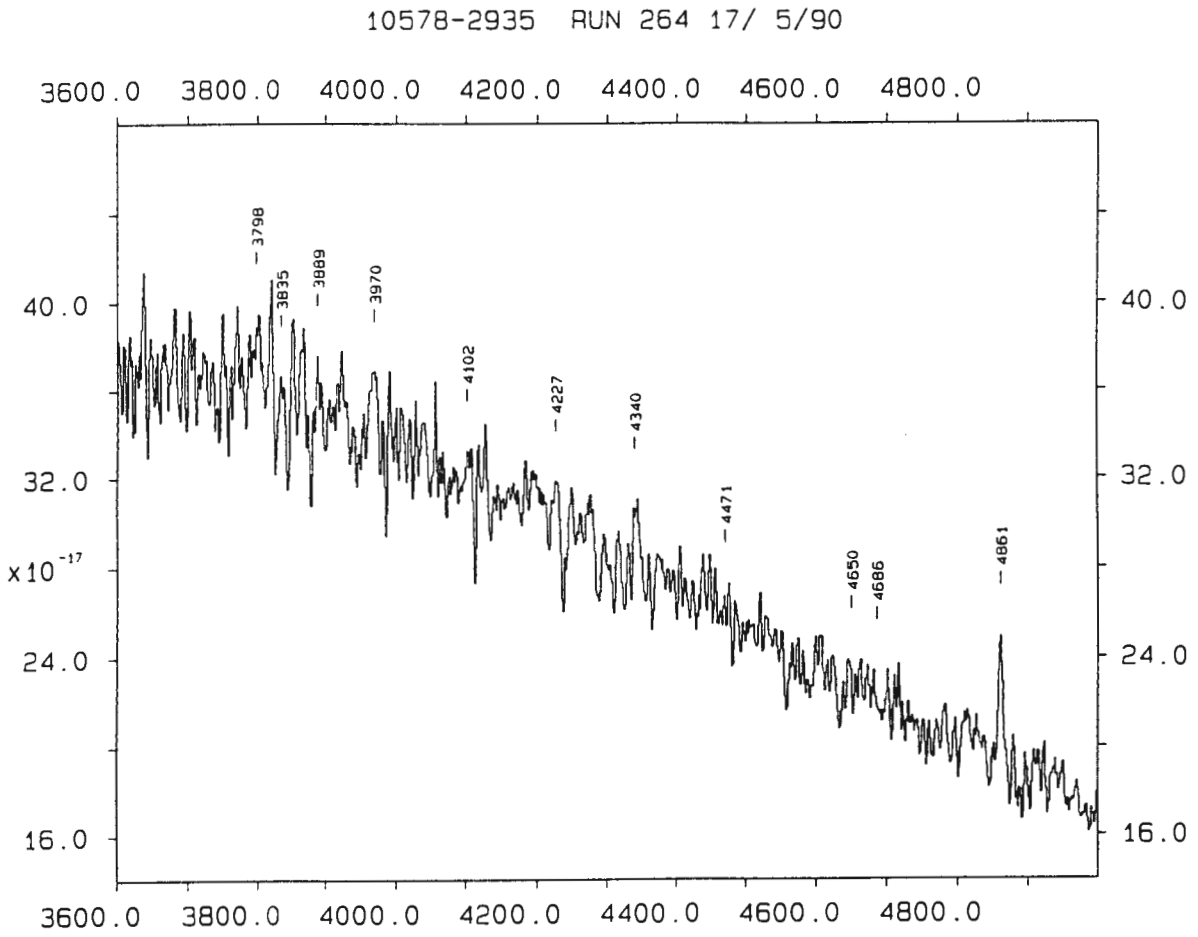

Figure 8a. The first spectrum of EC10578-2935 obtained on 1990 May 17.

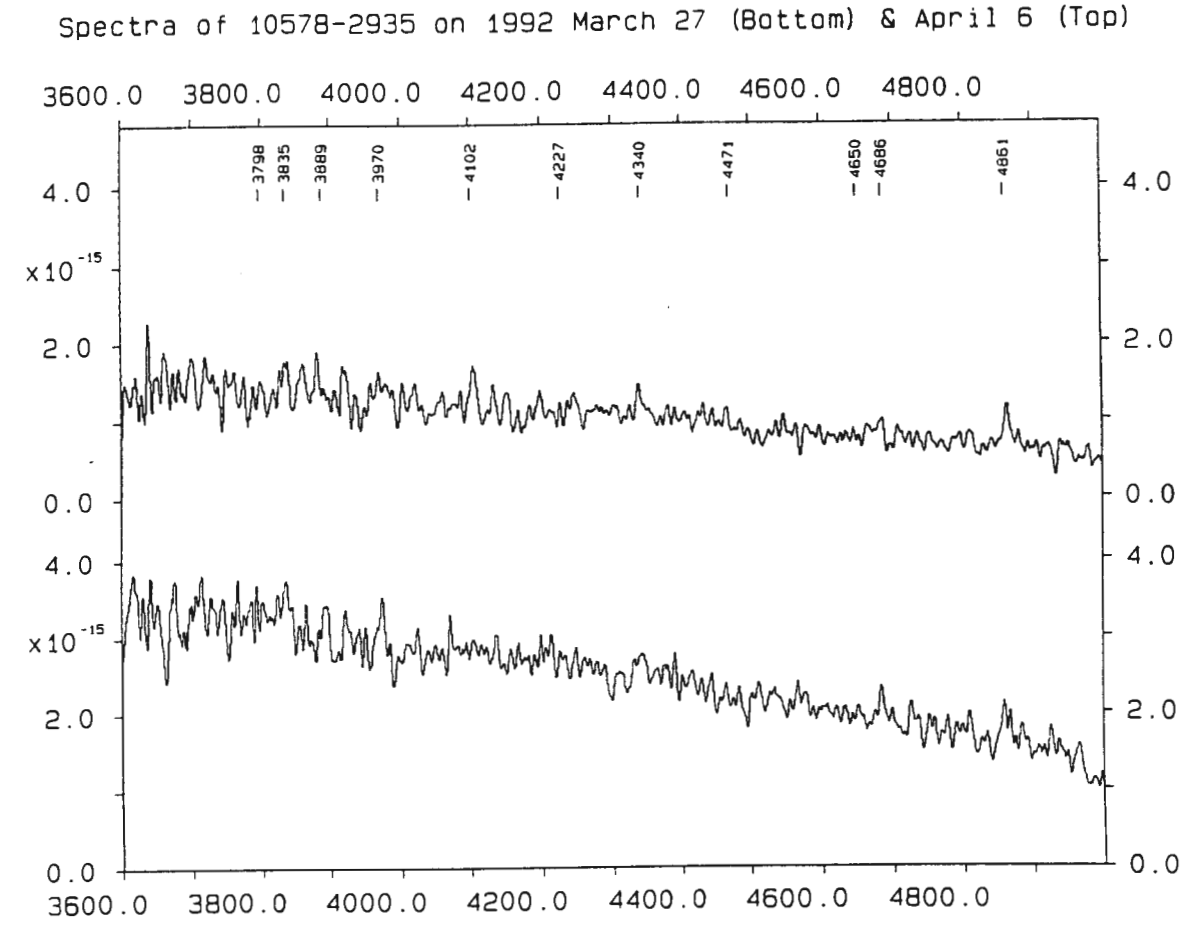

Figure 8b. The bottom spectrum of EC10578-2935 was secured on 1992 March 27 and the top spectrum was observed on 1992 April 6.

with the previous two peaks in Figure 4. The semi-amplitudes obtained from least squares fits to the radial velocity curves (Figure 7) are ~130 km/s which is much larger than the earlier semi-amplitudes of ~50km/s.

The object had UBV colours of V=15.98, B-V=0.40, and U-B=-0.72 on 1990 March 2. The B-V colour is as red as EC19314-5915 (Buckley et al. 1992) which is a triple system containing a late G dwarf and shows B-V=0.41. This confirms that the spectra are contaminated by the contribution of the secondary and that the first value of K_1 determined, ~50 km/s, is then spurious.

For a Roche lobe-filling secondary, the secondary mass M_2 may be derived using the mean empirical M_2-P_{orb} relation (Warner 1994): $M_2/M_\odot = 0.065 \cdot (P_{orb})^{5/4}$, for $1.3 \leq P_{orb} \leq 9$, where P_{orb} is in hours; the resulting M_2 is 0.9 $M_\odot$ if P_{orb}=8.18 hrs. The secondary would then be of spectral type K. For a system with P_{orb} greater than about 10 hrs, the above M_2-P_{orb} relation is no longer valid because the system must contain an evolved secondary (Warner 1994). If the 12.09-hr is the correct P_{orb}, the secondary mass of EC10565-2858 is then not estimable using the M_2-P_{orb} relation and should be derived from a dynamical solution. Thus, time-resolved spectroscopy at red wavelengths is needed in order to obtain the mass ratio of the system and to confirm the absorption lines which were identified in Figure 3.

§10.2 EC10578-2935

The first spectrum with 4Å resolution was obtained on 1990 May 17 and is shown in Figure 8a. Figure 8a shows very weak Balmer lines in emission; Hβ is clearly present but the high Balmer series lines are barely visible. No other features are visible. Two spectra with the same wavelength resolution were obtained in 1992 and are shown in Figure 8b. The spectra in Figure 8b exhibit similar features to that in Figure 8a. HeII λ4686Å is weakly present in emission as well as the Balmer lines (see the bottom in Figure 8b). From the above spectra, the object is probably a CV. This classification is not certain because of the weakness of the spectral features. The UBV

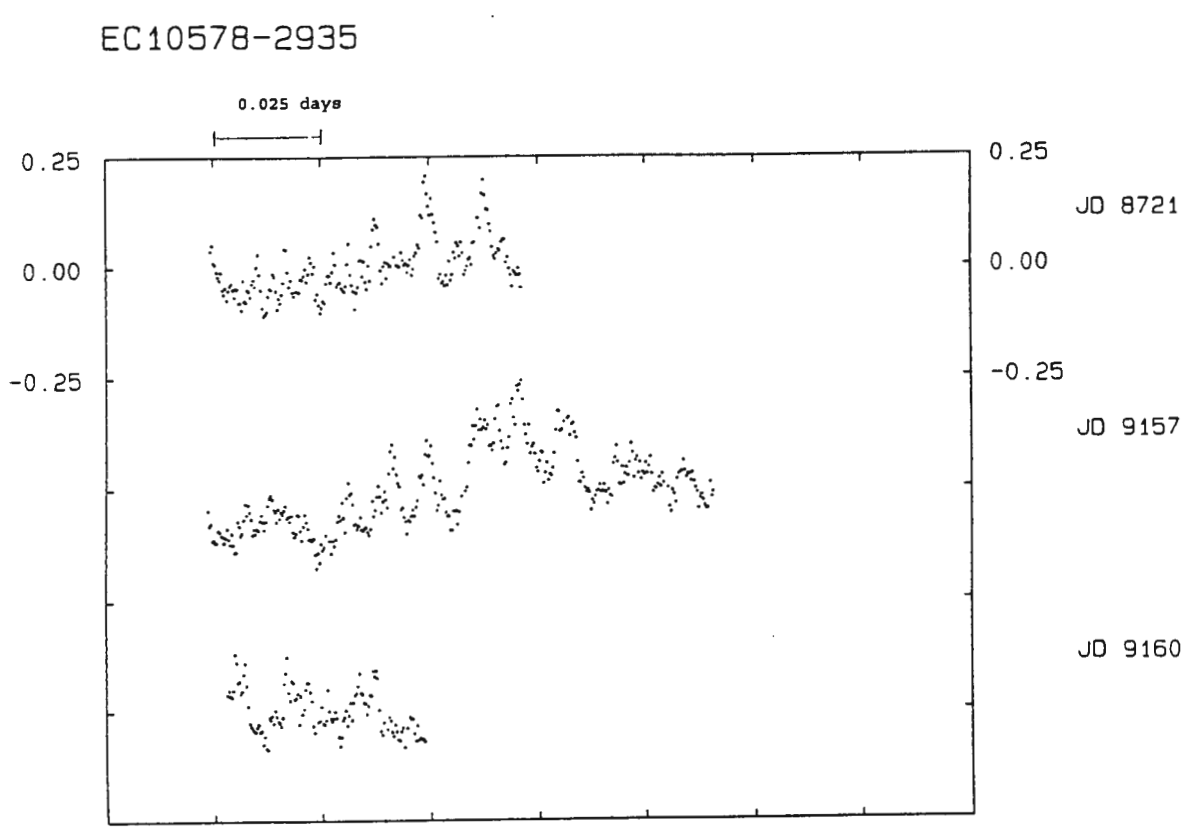

Figure 9. Light curves of EC10578-2935.

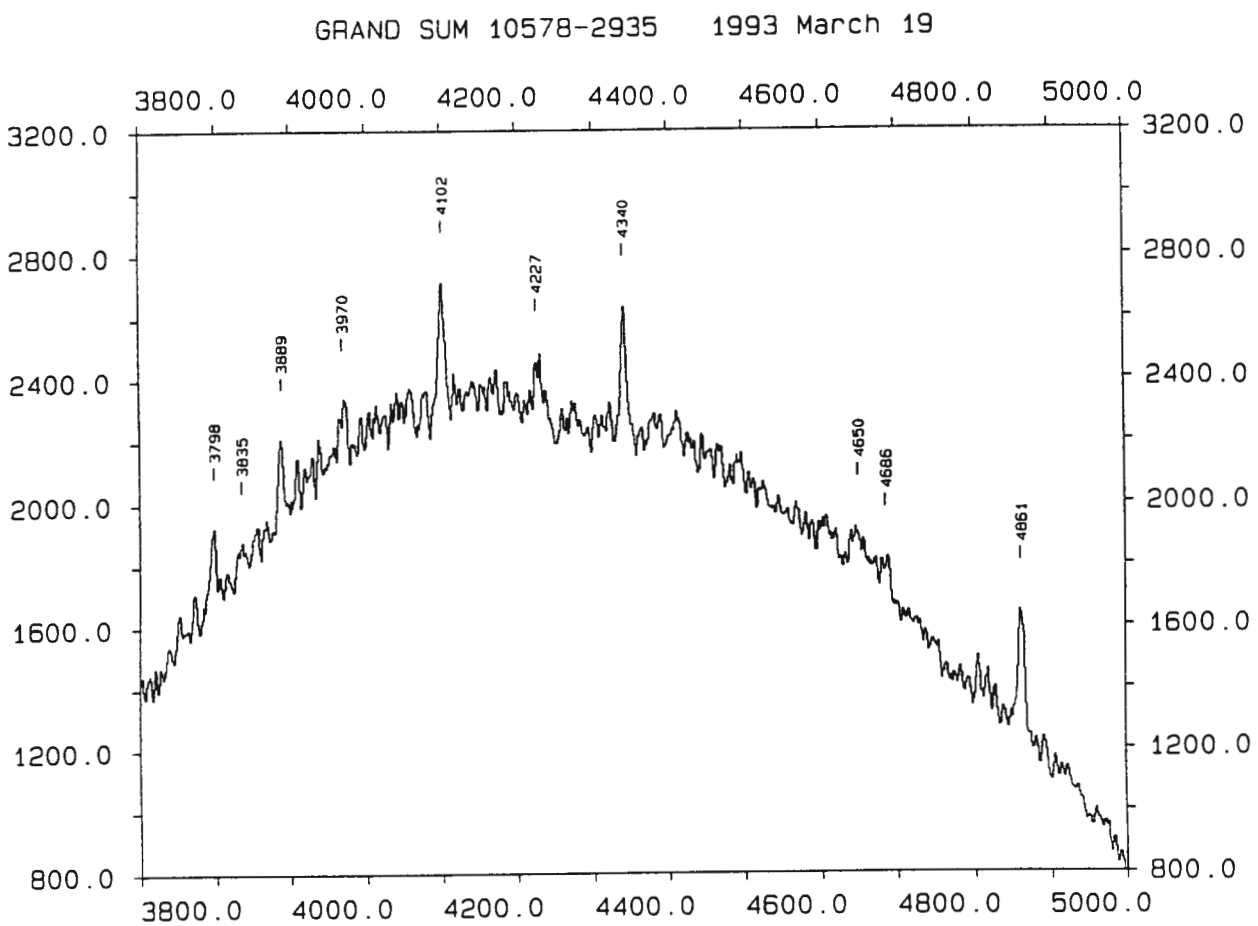

Figure 10. Grand sum spectrum (template) of EC10578-2935 on 1993 March 19.

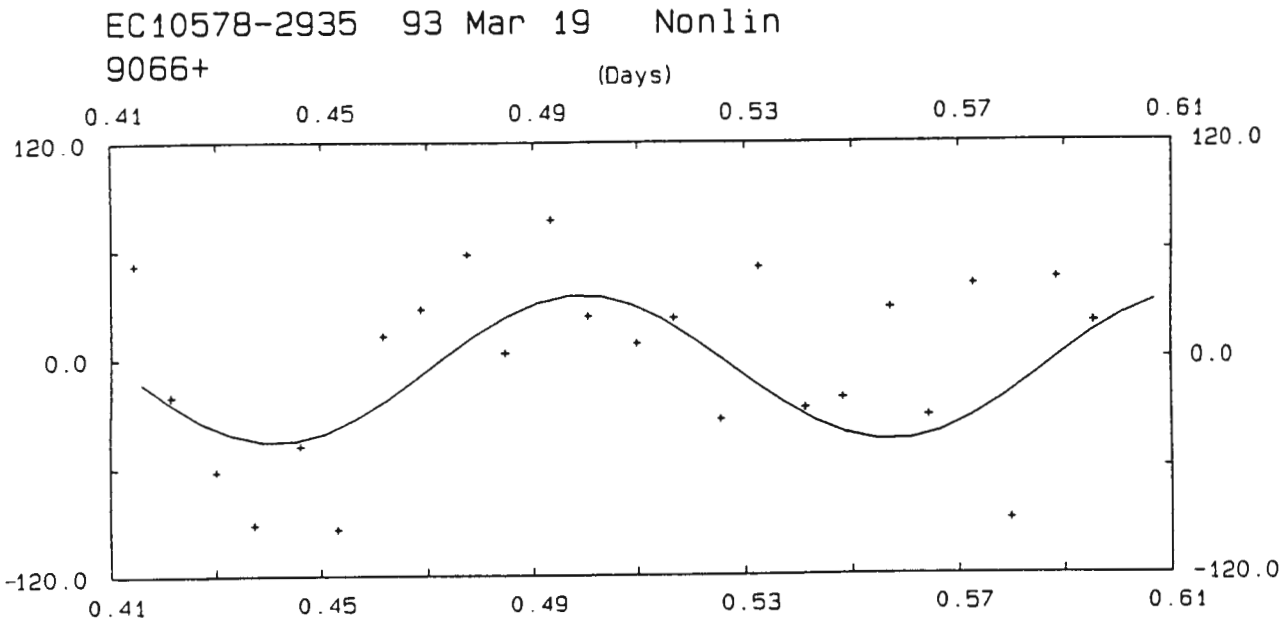

Figure 11. Radial velocity curve of EC10578-2935 was fitted by a sinusoid of the period of 2.8-hr.

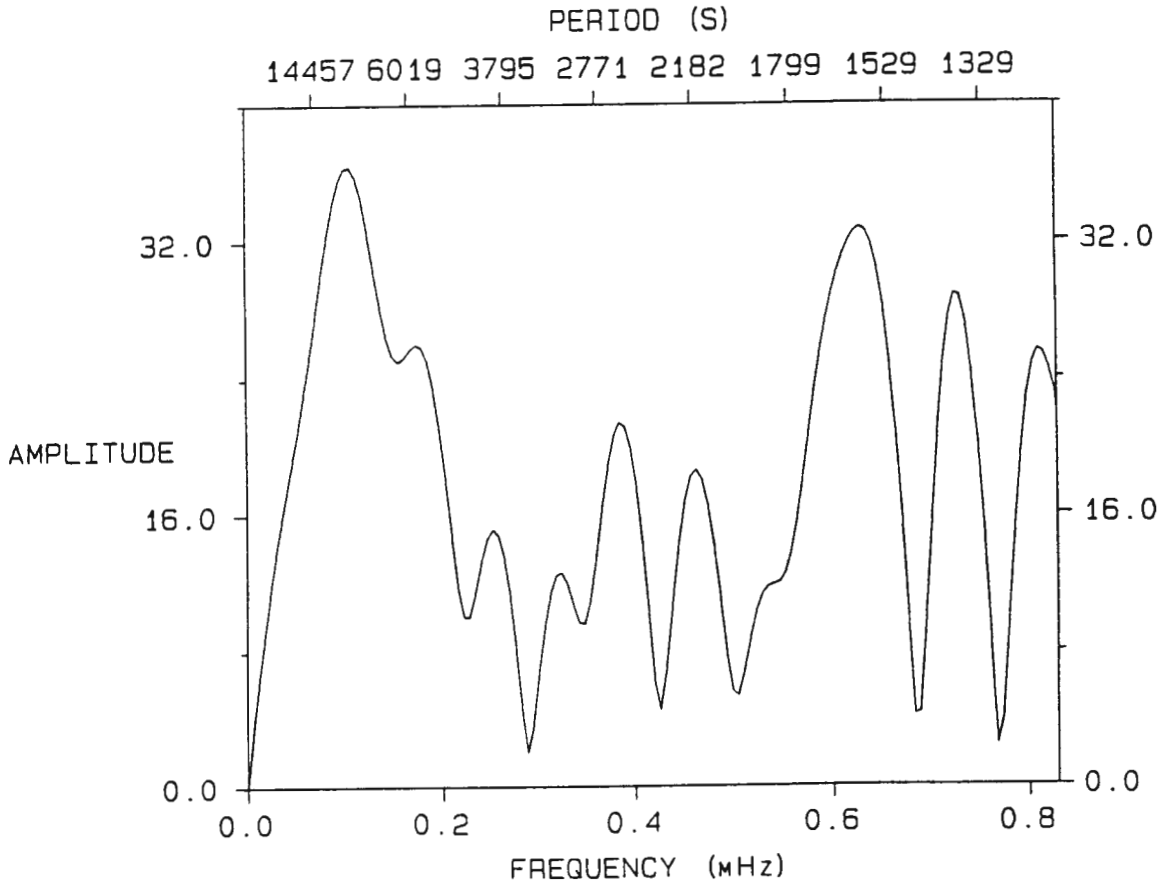

Figure 12. Amplitude spectrum calculated for the radial velocities of EC10578-2935.

measurements show that the object is genuinely blue (V=15.9, B-V = -0.01, U-B = -0.82). Therefore, three HSP runs were obtained and are listed in Table IV. These light curves are plotted in Figure 9 and exhibit rapid flickering activity with a peak-to-peak amplitude of ~25% on a time scale of a few minutes. There is thus no doubt that EC10578-2935 is a CV. However, the light curves in Figure 9 are too short to be used to search for orbital modulations: the longest run only lasted for ~3 hours.

Table IV. Observing Log of HSP for EC10578-2935

Run	UT Date	Start HJD 2440000.+	Duration (hrs)	B_w	ΔB
S5477	080492	8721.46370	1.7	15.78	0.39
S5613	180693	9157.22297	2.8	15.62	0.51
S5620	210693	9160.22746	1.1	15.48	0.30

In order to search for an orbital period, time-resolved spectroscopy was obtained on 1993 March 19 (Table V). A series of spectra was observed with a wavelength resolution of 4Å and a time resolution of 600 seconds. These

Table V. Observing Log of Time-Resolved Spectroscopy for EC10578-2935

UT Date	Start UT Time h m	Duration hrs	Resolution (FWHM Å)	Coverage Å
93 Mar 19	23 44	4.0	4	3800-5000

spectra were summed to construct the template which is shown in Figure 10. The Balmer emission lines are much stronger than in the spectra discussed above, and show narrow profiles with FWZI of ~20Å which suggests that the object is a low inclination system. The CIII/NIII blend λ4650Å is visible as well as HeII λ4686Å, implying that the object is possibly a NL. In addition to these spectral features, a low excitation line, CaI λ4227Å, in emission is seen. This feature is unusual in CV spectra. The cross-correlation technique was used to measure relative radial velocities. The results are listed in Table VI and plotted in Figure 11. A Fourier amplitude spectrum was calculated for the data in Table VI and is shown in Figure 12. The highest peak occurs at a frequency of 0.1056 mHz but it is not very significant. This tentative result will need to be confirmed by more comprehensive spectroscopic observations.

Table VI. Relative Radial Velocities of EC10578-2935

HJD 2440000.+	RV km/s	HJD	RV	HJD	RV
9066.41441	51	9066.47756	57	9066.54113	-27
9066.42146	-20	9066.48461	3	9066.54818	-21
9066.43008	-61	9066.49339	76	9066.55709	27
9066.43726	-91	9066.50050	23	9066.56422	-31
9066.44608	-47	9066.50981	8	9066.57288	40
9066.45313	-93	9066.51686	22	9066.57992	-89
9066.46182	12	9066.52548	-33	9066.58852	43
9066.46887	27	9066.53254	50	9066.59557	19

References:

Warner, B. (1994). *Cataclysmic Variable Stars*, Cambridge University Press, in press.

Division of Labour

The efforts of many people in the Edinburgh-Cape survey have contributed to this thesis. The following is a statement of my contribution.

After I started my Ph.D. study, I soon became involved in the Edinburgh-Cape survey. Thus, I went to the Royal Observatory, Edinburgh (ROE) during 1990 August-1991 April to clear the backlog of blue object selection from the COSMOS data. The selection procedures devised by Dr R.S. Stobie up to that time operated interactively on the ROE VAX within the STARLINK system, but usually suffered from a deficiency of CPU process time in interactive mode. Under the circumstances, the selection of only one field could be done in a day. Therefore I developed an automatic procedure for star/galaxy separation and used the software provided by Dr L. Miller to pair the U and B plates. The selection procedures became fully automatic except for the blue object selection and the visual inspection of the plates. These changes saved ~1/3 of the processing time and enabled a better progress: 1.5-2 fields per day. During my sojourn in Edinburgh, blue object selection of 90 fields were completed, which is comparable to the amount of work done previously during 1986-1990.

Since I returned to Cape Town, I have spent three months per year at the telescope in follow-up photometry and spectroscopy on the cataclysmic variable stars found by the survey. The Phase 2 (i.e. UBV photometry and classification spectroscopy) were almost all obtained by the other members of the Edinburgh-Cape collaboration. I received some assistance in obtaining follow-up observations (Phase 3) from Drs D. Kilkenny, R.S. Stobie, and D. O'Donoghue, especially obtaining simultaneous spectroscopy and photometry: 86% of the photometric data and 68% of the spectroscopic data were obtained by myself and the rest were obtained with the assistance of Drs D. Kilkenny, R.S. Stobie, and D. O'Donoghue. Almost all the Phase 3 data reduction, and all the data analysis, were done solely by me, unless explicitly attributed to others.

Conclusions

This concludes the survey during the past 3 years of the new cataclysmic variables discovered in the Edinburgh-Cape survey. Because of the limited availability of telescope time, exhaustive study of each was not possible. Thus it was not possible to classify all of them definitively; the orbital periods, the most basic datum, remains unknown or uncertain for some of them. This will require much more effort than has been possible from the 330 hrs of Phase 3 photometry and 100 hrs of spectroscopy of the 13 systems.

The results obtained thus far on some of the stars show peculiar behaviour which is difficult to understand in terms of the standard picture of CVs. For example, what are the quasi-periodic oscillations in EC05287-5857 (Chapter 9), what conceals the radial velocity variations of EC23128-3105, and what causes the peculiar brightness variations of EC04030-5801 (Chapter 6)? Thus, further study of a number of the stars is clearly deserved; we conclude with a summary of our suggestions for such effort (see the following Table).

Object	Preliminary results/Future work
Pre-CV:	
EC11575-1845	This binary system has an orbital period 7.86 hrs and shows a large reflection. The dynamical solutions are derived from numerical simulation using Napier's (1968) model. If the effective temperature of the primary is determined, then a unique solution can be obtained from the results of model fits. Thus, IUE observation is required.
Dwarf Novae:	
EC04030-5801	The P_{orb} is predicted to be longer than ~6 hrs. Thus, the secondary is expected to be visible in the optical and a red B-V colour should be seen at quiescence. The outbursts of the system showed an amplitude of ~3 mag and may occur every ~10 months or less. TRS, PHOT, and HSP at quiescence are needed to get the P_{orb}, colours, and flickering activity.
EC23128-3105	The object has an ultrashort P_{orb} of 1.4 hrs and may contain a high mass white dwarf. Further TRS is required to determine an accurate semi-amplitude in order to check whether the system does have such a high mass white dwarf.
EC23593-6724	The object is probably a low inclination system; its B-V colour becomes bluer as the brightness increases. Thus, simultaneous UBV HSP is needed to investigate the above colour-brightness relation.

EC05114-7955 From the large amplitude of the flickering and the low excitation spectrum, the object is probably a DN. But the CIII/NIII λ4650Å in emission is present in the spectrum. Thus, the object may be related to BV Pup. Further SP and HSP are required to understand more about this system.

EC10565-2858 This object is probably a DN due to the absence of HeII λ4686Å and CIII/NIII λ4650Å. Few absorption lines of a K-type spectrum were identified at blue wavelengths. The radial velocity curve shows that the P_{orb} of the system is either ~8 or ~12 hrs. Thus, more comprehensive TRS at red wavelengths is needed to obtain the mass ratio of the system and to confirm the spectral type of the secondary. HSP and long-term brightness variation are also needed to verify the classification.

EC20335-4332 The object is probably a DN and shows a hump period ~2 hrs in the light variations. The humps may arise from precession of an elliptical disk. To confirm the period and cause of the hump, further intensive HSP and SP are required.

UX UMa stars:

EC04224-2014 The P_{orb} is 4.2 hrs. The object is not only a UX UMa star but may also be a VY Scl star. Because it has been detected only a little more than 1 mag below its usual brightness, the long-term brightness variation is critical to confirm the VY Scl classification.

EC05565-5935 The HSP observations show a slow modulation with a period of ~3.4 hrs, which may be the orbital period. Because of its very weak spectral features, it is impossible to obtain the P_{orb} by TRS. Thus, intensive HSP is required to confirm the above determined period.

VY Scl star:

EC05287-5857 From the TRS, the object seems to have a P_{orb} ~2.6 hrs. If correct, this would place the system in the period gap. Thus, it is urgent to get more TRS to verify this result. In addition to this, the object shows the QPO whose periods vary in the range 15-26 mins. Since the amplitudes of the QPO of this object are quite large, simultaneous UBVRI HSP would be useful to investigate the possibility of Warner's (1994) hypothesis for QPO.

Footnotes: SP: spectroscopy; TRS: time-resolved spectroscopy; PHOT: UBV photometry; HSP: high-speed photometry; QPO: quasi-periodic oscillations.